Unconventional superconductivity in the ferromagnetic superconductor UCoGe

Beilun Wu

Communauté
UNIVERSITÉ Grenoble Alpes

THÈSE

Pour obtenir le grade de

DOCTEUR DE L'UNIVERSITÉ GRENOBLE ALPES

Spécialité : **Physique**

Arrêté ministériel du 7 Août 2006

Préparée au sein de **laboratoire Pheliqs de l'Institut de nanoscience et cryogénie (INAC), UGA-CEA, Grenoble**
et de l'école doctorale **de Physique de Grenoble**

Unconventional Superconductivity in the Ferromagnetic Superconductor UCoGe

Présentée par

Beilun Wu

Thèse dirigée par **Jean-Pascal Brison**

Thèse soutenue publiquement le **24/01/2017**,
devant le jury composé de :

Klaus Hasselbach	DR	CNRS Grenoble	Président
Alexandre Buzdin	Prof.	Université de Bordeaux	Rapporteur
Yo Tokunaga	DR	Japan Atomic Energy Agency	Rapporteur
Alain Sakuto	Prof.	Université Paris Diderot	Examinateur
Jean-Pascal Brison	DR	CEA Grenoble	Directeur de thèse

Contents

Acknowledgements

First I'd like to thank Alexandre Buzdin and Yo Tokunaga for having accepted to be the referees of my thesis, and Klaus Hasselbach and Alain Sacuto for being in the jury. Thank you for your big efforts to read the manuscript, and the valuable feedbacks you gave.

Un grand grand merci à Jean-Pascal, mon directeur de thèse, qui a été à mon côté pendant tous ces travaux. Je te remercie pour être si enthousiaste et responsable. Je te remercie aussi pour être si gentil avec moi au tout début de la thèse quand j'étais lent à progresser. Ton rigueur scientifique et ton grand savoir ont toujours été du très bon influence pour moi. C'était une merveilleuse expérience, et un grand privilège en même temps, d'être ton élève.

Merci à Georg, qui mange le plus vite à la table tous les midis. Tes petits cours d'Allemand et tes nombreuses conseils m'ont été très utiles. Merci pour ta sympathie et ta constante patience face à des jeunes étudiants.

Merci à Alexandre Pourret, toujours le premier à chauffer les discussions dans le couloir. Le temps qu'on a passé ensemble, dans les montagnes avec Gaël et Georg, et sur les terrains de badminton, sont pour moi du très beaux souvenirs.

Merci à Daniel, et ta grande expertise expérimentale. Merci pour la correction du manuscript. C'est un grand plaisir d'avoir ton bureau à côté du PPMS.

Merci à Jacques. Bien que tu passe peu souvent au labo, tu continues à nous guider avec tes appels, et ton super charactère à toujours pousser les choses vers le plus loin possible. Tes petits passages dans le labo ont à chaque fois chauffé dramatiquement tout le monde ici. Merci pour tous les encouragements!

Thank you Dai, our dear sample supplier, and a superbe example for working altitude. It is always a big pleasure to do the experiments with you. Hope that in the future Grenoble still has many chances to see you working here.

Merci à mes deux chères camarades, Adrien et Gaël. On a commencé la thèse ensemble et fini (à peu près) ensemble. C'était jamais ennuyant avec vous deux. Les petites discussions qu'on a faites dans le bureau (la plupart du temps inutiles), les petits transfert d'hélium qu'on a fait l'un pour l'autre, ce qu'on s'est moqué de certains personnages, ont fait ce temps-là remplis de rire... et du progrès. Cette période de trois ans ne sera sans doute pas aussi cool si vous n'étiez pas là.

Je veux aussi remercier Jean-Michel, notre technicien incroyable, et à Iulian qui prend sa suite. Efficace et expérimenté, chaleureux et avec du sang froid, vous étiez un support formidable dans le groupe.

Merci à nos amis chimistes au D_5, Christoph, Karine et surtout Gérard, qui m'a passé un échantillon après l'autre de UBe_{13}. On a été sur la bonne voie mais il faut quelqu'un qui prend la suite!

I'd also like to thank Vladimir Mineev, for the great theoretical help, and the many patient explanation you gave. It's always very nice to have a Russian theoretician to

discuss with, although I was with a bit of stress at the beginning.

A big thank to Carley Paulsen from Néel Institut, for our little nice cooperation. I hope that one day you can finally go to Taiwan to see the treasures brought by Chiang Kai-shek.

Je veux aussi remercier Mathieu Taupin, qui m'a passé le travail de conduction thermique quand je suis arrivé et qui m'a beaucoup enseigné à ce moment-là.

There are many many other people in the list: our friends at LNCMI, Gabriel and Ilya, who are always good companions during the night-time experiments; the Japanese visitors, Yusei, Araki san, Harima sensei, and many others, thank you for the nice rice cakes you brought; Getrud Zwicknagl, thank you for many helpful discussions, and the same to Andey Varlamov, who gave me a wonderful book to translate and taught us the four-fruit theory; I'd like also to thank our very rich neighbors from LaTEQS who have helped me in all kinds of occasions, Max, Claude, Marc, François, Jean-Luc, Frédéric, Pierre, Xavier, Louis, Michel, Andreas, Sarah,... excuse me for not listing all your names here.

I'm also grateful to Aifang for helping me with the defense and 'pot' preparation and for many other things. Hope that the new project you are working on will lead to fruitful results.

Et un grand merci aussi à Marielle, toujours prête à nous aider.

Finally I want to thank my parents, to whom I dedicate this thesis. Without their love and their remote support from China, it would not be possible for me to finish the work peacefully here in Grenoble.

Introduction

The ferromagnetic superconductors (UGe_2, URhGe and UCoGe), where superconductivity coexists homogeneously with ferromagnetism, have attracted much attention in the condensed matter community. This thesis is focused on the upper critical field of UCoGe, which is one of the most exotic cases among unconventional superconductors. It shows many features that are anomalous in terms of classical theories of superconductivity.

Thermal conductivity measurements and other experimental methods have been used to confirm these behaviors in H_{c2} of UCoGe, previously observed in resistivity studies. These features can be consistently understood, taking into account a phenomenon specific to the ferromagnetic superconductors: the field dependence of the ferromagnetic fluctuation, which is a strong candidate for the pairing mechanism. Based on such a framework, we analyze the H_{c2} of UCoGe with its normal phase properties, and compare the prediction for the field dependence of the pairing interaction, from Mineev's theory general for all ferromagnetic superconductors, with our experiment. These results strongly prove that superconductivity in these systems originate from ferromagnetic fluctuations.

Independent from the rest of the study, two features in the normal phase of UCoGe are studied, with thermal conductivity and specific heat measurements. The first results on another heavy-fermion system, UBe_{13} are also presented, indicating a promising method to obtain high quality single crystals in this system.

Introduction en français

Les supraconducteurs ferromagnétiques (UGe_2, URhGe et UCoGe), dans lesquels la supraconductivité coexiste de façon homogène avec le ferromagnétisme, ont attiré beaucoup d'attention dans la communauté de la matière condensée. Cette thèse est concentrée sur le champ critique supérieur de UCoGe, un des cas les plus exotiques parmi les supraconducteurs non conventionnels, qui montre de nombreuses caractéristiques anormales par rapport aux théories classiques de la supraconductivité. Des mesures en conductivité thermique et en d'autres méthodes expérimentales ont été utilisées pour confirmer ces comportements de H_{c2} de UCoGe, précédemment observés dans des études en résistivité. Ces caractéristiques peuvent être comprises de façon cohérente, en tenant compte d'un phénomène spécifique des supraconducteurs ferromagnétiques: la dépendance en champ des fluctuations ferromagnétiques, qui est un candidat fort pour le mécanisme d'appariement. Basé sur ceci, nous analysons le H_{c2} de UCoGe avec les propriétés dans la phase normale, et comparons les observations expérimentales avec la théorie de Mineev - une théorie générale valable pour tous les supraconducteurs ferromagnétiques orthorhombic. Ces résultats montrent fortement que la supraconductivité dans ces systèmes provient des fluctuations ferromagnétiques.

Indépendamment du reste de cette étude, le dernier chapitre discute sur deux caractéristiques dans la phase normale de UCoGe, avec des résultats de la conductivité thermique et de la chaleur spécifique. Les premiers résultats sur un autre système de fermions lourds, UBe_{13}, sont également présentés, qui indiquent une méthode prometteuse pour obtenir des monocristaux de haute qualité de ce système.

Chapter 1

Physical background

Ferromagnetism and superconductivity are usually considered as two antagonist phenomena. The internal dipolar field in a ferromagnet should be screened by spontaneous Meissner currents or induce a spontaneous vortex state; and the exchange field would lead to depairing effects on a spin-singlet superconducting state. A good example to illustrate the competition between these two phenomena is $ErRh_4B_4$[1], where the Curie temperature (T_{Curie}) lies below the superconducting critical temperature (T_{sc}). With the appearance of the ferromagnetic order, superconductivity is destroyed (figure 1.1a), except in a very narrow temperature range below T_{Curie} where the two phenomena coexist in the form of a crypto-magnetic state[2, 3, 4]: randomly oriented magnetic domains average out the effect of the dipolar and exchange fields on the scale of the superconducting coherence length ξ_0 (figure 1.1b).

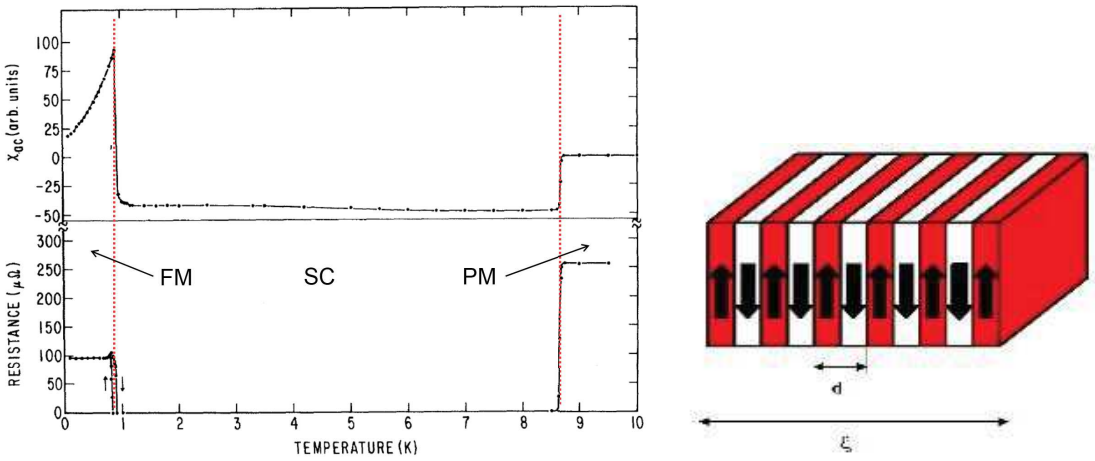

(a) **(b)**

Figure 1.1 | (a): Temperature dependence of ac-susceptibility (χ_{ac}, upper panel) and resistivity (ρ, lower panel) of $ErRh_4B_4$[1]. The red broken lines show the ferromagnetic (FM) and superconductivity (SC) transitions. **(b)**: An illustration of the crypto-magnetic state, figure from Ref.[4].

However, in four uranium-based systems, superconductivity has been discovered recently to coexist with (weak) ferromagnetic order, even though in these systems T_{Curie} is higher than T_{sc}: UGe_2 in 2000[5], URhGe in 2001[6], UIr in 2004[7] and UCoGe in 2007[8]. They have attracted much attention in the condensed matter physics community. Micro-

scopic studies like NMR or muons experiments have proved that the coexistence of these two orders occurs homogeneously in the bulk of these systems (Ref.[9] for UGe_2 and Ref.[10, 11] for UCoGe). This is different from the claims for the coexistence of ferromagnetic order and superconductivity in the Eu based iron pnictide[12], where both orders would exist in different parts of the sample. It is also different from the pseudo coexistence in a crypto-magnetic state[2, 3], as in $ErRh_4B_4$. This is directly seen on the magnetization measurements in UCoGe which displays very little change below T_{sc} [13], and is confirmed by scanning SQUID microscopy which shows that inside the superconducting phase (at $T = 0.2\ \mathrm{K} < T_{sc}$), the size of the magnetization domains is of order μm, much larger than the superconducting coherent length (ξ)[13]. The latter can be estimated with the upper critical field (H_{c2}): for UCoGe, $\xi \sim 5$ nm for $\mathbf{H}//\mathbf{a}$ and $\mathbf{H}//\mathbf{b}$, and $\xi \sim 25$ nm for $\mathbf{H}//\mathbf{c}$.

Very recently, coexistence of ferromagnetism and superconductivity has been reported in thin films of a doped semi-conductor SmN[14]. It is even claimed that this system would be a p-wave superconductor, and a (4f) heavy-fermion. It would then be the first non uranium true ferromagnetic superconductor.

Coming back to the uranium-based systems, UIr, which has a monoclinic crystal structure (thus non-centrosymmetric) and shows superconductivity only under pressure, is not well documented up to now. The other three systems UGe_2, URhGe and UCoGe have orthorhombic symmetry. Figure 1.2 shows their crystal structure. UGe_2 has C_{mmm} space group, while URhGe and UCoGe share the same P_{nma} structure. In all three systems the uranium atoms have a zigzag alignment along the **a**-axis. The arrows on the uranium atoms in figure 1.2 show the direction of the spontaneous magnetization in the ferromagnetic state in these compounds, which is along the **a**-axis in UGe_2 and along the **c**-axis in URhGe and UCoGe.

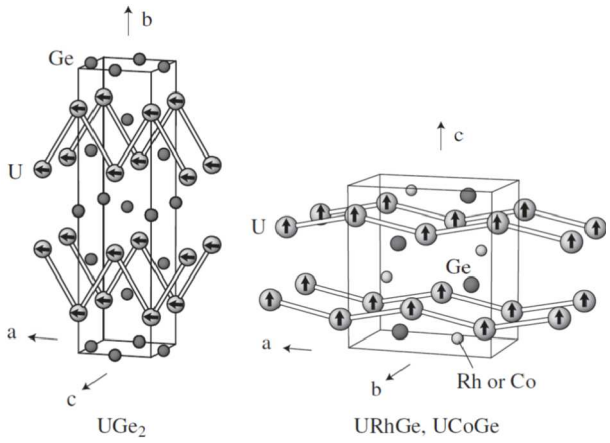

Figure 1.2 | Crystal structure of UGe_2, URhGe and UCoGe. Figure from Ref.[15].

In contrast to the large number of heavy fermion or other strongly correlated electron systems, where superconductivity emerging in the neighborhood of an antiferromagnetic quantum critical point[16, 17, 18, 19], the above mentioned systems are the only examples where superconductivity is found near a ferromagnetic instability (except for SmN, yet to be confirmed[14]). Figure 1.3 presents the pressure-temperature phase diagrams of UGe_2[20, 21], URhGe[22] and UCoGe[23, 24]. Under pressure the ferromagnetic order in UGe_2 and UCoGe decreases, and the Curie temperature becomes zero at a critical pressure (p_c). In URhGe, on the contrary, applying pressure drives the system away from the quantum critical point and T_{Curie} increases. In UCoGe, the superconducting phase

coexists with the ferromagnetic order under pressure below $p_c \sim 1$ GPa, and persists inside the paramagnetic state up to about 4 GPa[25]. The maximum of T_{sc} occurs close to the pressure at which the two transition lines cross. In UGe_2, the superconducting phase lies only inside the ferromagnetic state. A second transition line between two different ferromagnetic states (FM1 and FM2) exists inside the ferromagnetic phase[21], and T_{sc} is maximum around the pressure at which the FM1/FM2 transition temperature is tuned to zero.

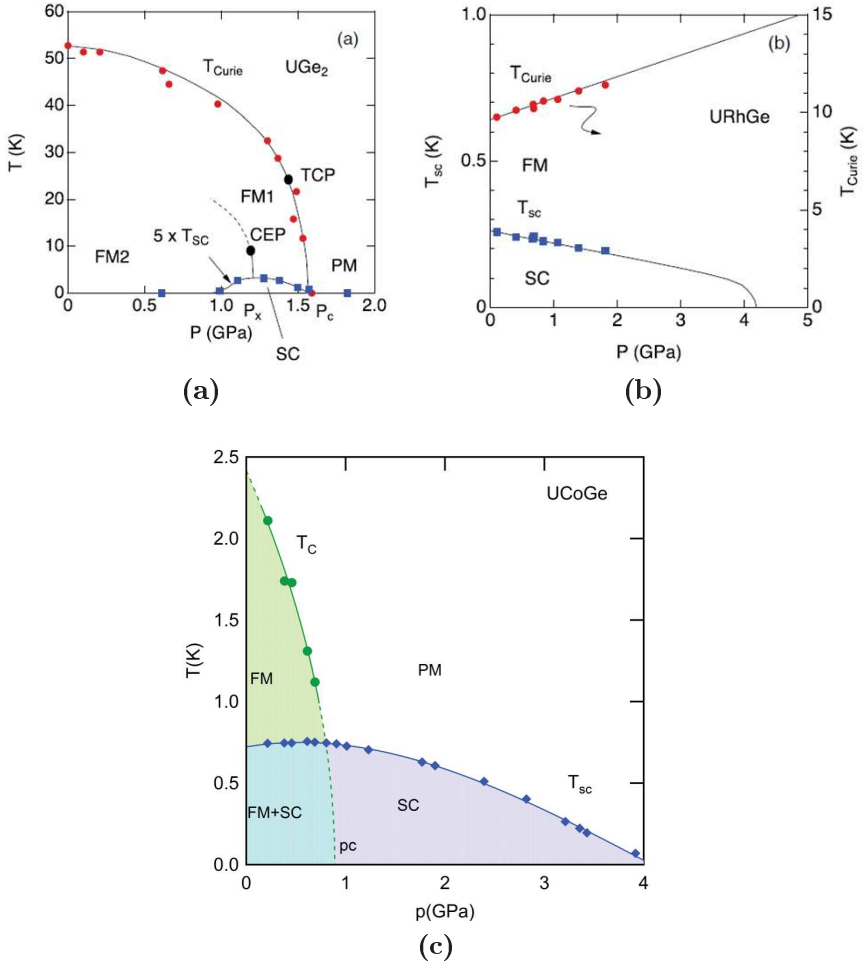

Figure 1.3 | Pressure-temperature phase diagram of UGe_2**(a)**, URhGe**(b)** and UCoGe**(c)**[21, 22, 25].

One might question what kind of new aspects, apart from the change of the magnetic instability, may appear in these ferromagnetic superconductors, compared with the antiferromagnetic cases. In fact, there are indeed new features and puzzles in these systems, some of which could be predicted, and others coming as real surprises. The first (predicted) new feature is p-wave superconductivity.

p-wave superconductivity

Due to the exchange field in the ferromagnetic phase, a p-wave superconducting state with spin-triplet pairing is most likely realized in the uranium-based ferromagnetic superconductors (it will be discussed in detail in Chapter3.3. Other possible candidates for

odd parity triplet superconductivity are the two heavy fermion compounds UPt_3, UBe_{13}, and Sr_2RuO_4).

Generally speaking, if we write the superconducting wave function as a product of the orbital and spin part (possible if the spin-orbit coupling is weak),

$$\Delta^l_{\mathbf{s_1},\mathbf{s_2}}(\mathbf{k}) = g_l(\mathbf{k})\ \chi_s(\mathbf{s_1},\mathbf{s_2}) \tag{1.1}$$

the symmetry of the orbital part is given by: $g_l(-\mathbf{k}) = (-1)^l g_l(\mathbf{k})$, with $l = 0, 1, 2...$ corresponding respectively to s,p,d...-wave pairing states. The letters s,p,d correspond to pairing states with different orbital angular momentum, which are associated with the irreducible representations (IR) of the full rotational symmetry group $\mathcal{SO}(3)$. This is appropriate when the normal state is isotropic, like in the superfluid ^{3}He. In a crystal, superconducting states are classified by the IR of the normal phase symmetry group, but are often still denominated s, p, d-wave states, due to the resemblance in terms of symmetry with the corresponding spherical harmonics ($Y_{lm}(\hat{\mathbf{k}})$, with $m = -l, ..., 0, ...l$), which are the base functions of the l-IR of $\mathcal{SO}(3)$).

The Pauli exclusion principle imposes that the pairing state is antisymmetric with respect to the exchange of the two electrons:

$$\Delta^l_{\mathbf{s_2},\mathbf{s_1}}(-\mathbf{k}) = -\Delta^l_{\mathbf{s_1},\mathbf{s_2}}(\mathbf{k}) \tag{1.2}$$

For a p-wave pairing state $g_l(\mathbf{k})$ is antisymmetric ($l = 1$), and necessarily a spin-triplet state is formed ($S = 1$), with three components, which can be represented on the basis:

$$S_z = \begin{cases} 1, & |\uparrow\uparrow> = \begin{pmatrix} 1 & 0 \\ 0 & 0 \end{pmatrix} \\ 0, & |\uparrow\downarrow> + |\downarrow\uparrow> = \begin{pmatrix} 0 & 1 \\ 1 & 0 \end{pmatrix} \\ -1, & |\downarrow\downarrow> = \begin{pmatrix} 0 & 0 \\ 0 & 1 \end{pmatrix} \end{cases} \tag{1.3}$$

In the presence of a strong spin-orbit coupling, the electron spin is no longer a "good" quantum number. Nonetheless, the electron state are still doubly degenerate if the time reversal symmetry is preserved (Kramer's degeneracy). In such a case the notions of "spin-singlet" and "spin-triplet" superconducting states can continue to be used in terms of "pseudo-spins". In the ferromagnetic state, this is no longer true: Kramer's degeneracy is lifted for opposite "pseudo spins" and there is a band splitting. But if the system still has a center of inversion (which is the case for UGe_2, URhGe and UCoGe), we can still distinguish odd and even parity superconducting states.

A general spin-triplet (odd parity) superconducting wave function can be written as the sum of three components with different (pseudo) S_z:

$$\begin{aligned} \mathbf{\Delta}_{\mathbf{s_1},\mathbf{s_2}}(\mathbf{k}) &= \Delta^{\uparrow}(\mathbf{k})|\uparrow\uparrow> + \Delta^0(\mathbf{k})(|\uparrow\downarrow> + |\downarrow\uparrow>) + \Delta^{\downarrow}(\mathbf{k})|\downarrow\downarrow> \\ &= \begin{pmatrix} \Delta^{\uparrow}(\mathbf{k}) & \Delta^0(\mathbf{k}) \\ \Delta^0(\mathbf{k}) & \Delta^{\downarrow}(\mathbf{k}) \end{pmatrix} \end{aligned} \tag{1.4}$$

or equivalently, in terms of a d-vector:

$$\begin{aligned}\mathbf{\Delta_{s_1,s_2}}(\mathbf{k}) &= (\vec{d}(\mathbf{k}).\vec{\sigma}(\mathbf{k}))\ i\sigma_y \\ &= \begin{pmatrix} -d_x(\mathbf{k}) + id_y(\mathbf{k}) & d_z(\mathbf{k}) \\ d_z(\mathbf{k}) & d_x(\mathbf{k}) + id_y(\mathbf{k}) \end{pmatrix}\end{aligned} \tag{1.5}$$

where σ_i $(i = x, y, z)$ are the Pauli matrices, and

$$\begin{cases} d_x(\mathbf{k}) = -\dfrac{i}{2}(\Delta^{\uparrow}(\mathbf{k}) + \Delta^{\downarrow}(\mathbf{k})), \\ d_y(\mathbf{k}) = -\dfrac{1}{2}(\Delta^{\uparrow}(\mathbf{k}) - \Delta^{\downarrow}(\mathbf{k})), \\ d_z(\mathbf{k}) = \Delta^0(\mathbf{k}) \end{cases} \tag{1.6}$$

For a ferromagnetic state which has an orthorhombic crystal structure, only two possibilities exist for p-wave superconducting state, deduced from symmetry principles[26, 27] and with the hypothesis that strong spin-orbit coupling exists in these systems (orientation of the d-vector is fixed with respect to the crystal axes). They are the A state:

$$\begin{cases} \Delta_A^{\uparrow}(\mathbf{k}) = \hat{k}_x\eta_x^{\uparrow} + i\hat{k}_y\eta_y^{\uparrow}, \\ \Delta_A^{\downarrow}(\mathbf{k}) = \hat{k}_x\eta_x^{\downarrow} + i\hat{k}_y\eta_y^{\downarrow}, \\ \Delta_A^{0}(\mathbf{k}) = \hat{k}_z\eta_z^{0}, \end{cases} \tag{1.7}$$

and the B state:

$$\begin{cases} \Delta_B^{\uparrow}(\mathbf{k}) = \hat{k}_z\zeta_z^{\uparrow}, \\ \Delta_B^{\downarrow}(\mathbf{k}) = \hat{k}_z\zeta_z^{\downarrow}, \\ \Delta_B^{0}(\mathbf{k}) = \hat{k}_x\zeta_x^{0} + i\hat{k}_y\zeta_y^{0}, \end{cases} \tag{1.8}$$

where the η_i and ζ_i are complex numbers. Note that when the $S_z = 0$ component $\Delta^0(\mathbf{k})$ is negligible (which can be imposed by exchange or Zeeman coupling), these forms of the superconducting state will present nodal structures: for the A state, a point node along the z-axis, and for the B state, a line node in the (x, y) plane. When the $\Delta^0(\mathbf{k})$ component is finite, however, these nodes become minimums and the superconducting gap is finite for every $\mathbf{k}$ on the Fermi surface.

Experimentally, for UCoGe the gap node structure has been studied with low temperature thermal conductivity (κ) measurements on different samples, with RRR varying from 16 to 150 and with heat current injected along the three crystal axes[28]. Figure 1.4a presents the temperature dependence of the normalized thermal conductivity (κ/κ_n) on the best sample along each current direction: there is no observable anisotropy of κ in the $T \to 0$ limit between different current directions. Figure 1.4b presents the residual normalized thermal conductivity (at $T = 0$) ($\kappa/\kappa_n(0)$), as a function of RRR (residual resistivity ratio of the samples, which characterizes the sample quality). $\kappa/\kappa_n(0)$ is found to decrease steadily with improving sample quality. From these measurements, there is yet no sign of nodal structures observed in the superconducting gap of UCoGe. Only NMR measurements suggest line of nodes from an observed T^3 behavior of $1/T_1T$ between 0.1 K and T_{sc} [29, 11].

Re-entrant superconductivity

A major surprise in the ferromagnetic superconductors comes from their upper critical field (H_{c2}). The H_{c2} of all three systems present very uncommon and puzzling features.

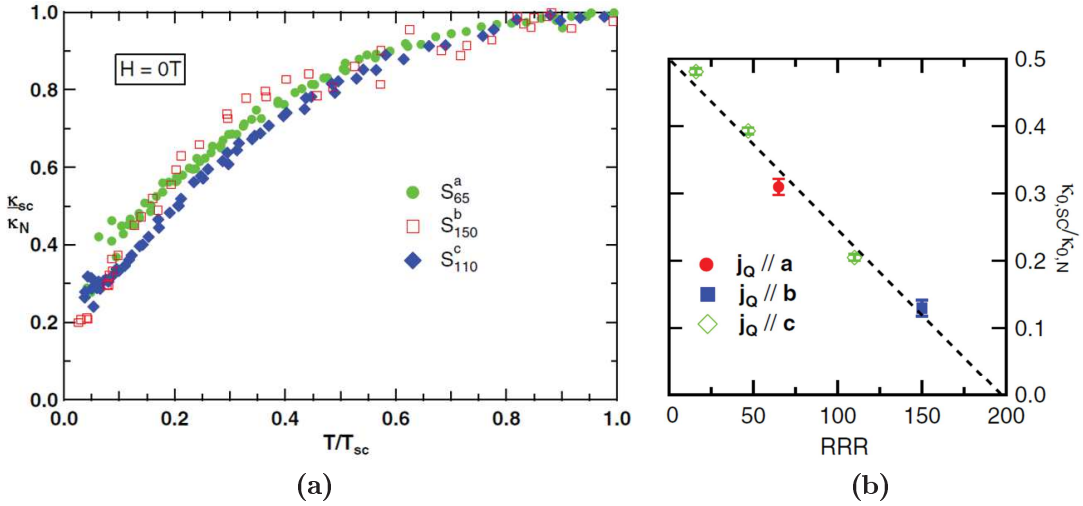

Figure 1.4 | **(a)**: Normalized thermal conductivity (κ/κ_n) of UCoGe as a function of normalized temperature (T/T_{sc}) inside the superconducting state[28], measured along three current directions[28]. The sample notation S^i_x: the sample has a residual resistivity ratio (RRR) that equals x, and κ is measured with heat current injected along the crystal axis i. **(b)**: The normalized thermal conductivity at zero temperature $\kappa_{0,SC}/\kappa_{0,N}$ as a function of RRR[28]. No universal limit that indicates the presence of a superconducting gap node can be observed, even if samples with RRR up to 150 have been measured.

Among them, the most remarkable phenomenon is the re-entrant superconductivity, presented in figure 1.5. In UCoGe (for **H**//**b**)[30] and in UGe_2 (for **H**//**a**)[20, 31], H_{c2} has a special S-shape curvature. In URhGe, for the same field direction (**H**//**b**) as in UCoGe, it appears as a real re-entrant phase: the low field superconducting phase is first suppressed at around 3 T, then a second superconducting phase appears at around 12 T with a transition temperature higher than the T_{sc} at zero field[32]. Moreover, these remarkable phenomena of re-entrant superconductivity in the three cases are associated with field-induced ferromagnetic instabilities. In URhGe and UCoGe, for **H**//**b** (perpendicular to the spontaneous magnetization axis), the maximum of superconducting transition temperature is related to the suppression of the ferromagnetic order (T_{Curie} is tuned to zero by the transverse field)[32, 33, 30]. In UGe_2, the re-entrant superconductivity corresponds to a field-induced transition from a "low ordered moment" phase (FM1) to a "large ordered moment" phase (FM2).

Upper critical field in UCoGe

Apart from the S-shaped H_{c2} for **H**//**b**, H_{c2} of UCoGe also shows many other particularities. Figure 1.6a presents H_{c2} of UCoGe for field along the three crystal axes, determined with resistivity measurements in Ref.[30].

The first remarkable point is the large value of H_{c2} (higher than 16 T for field along the **a** and **b**-axes) compared with its low T_{sc} (0.5 K). High upper critical field is not an exotic phenomenon among heavy fermion superconductors. In these intermetallic systems, the presence of rare earth or actinide ions leads to strong interactions between the f-electrons and the conduction bands. It is usual to have quasiparticle effective masses (m^*) enhanced up to hundreds or even a thousand times the free electron mass, in a large part due to the

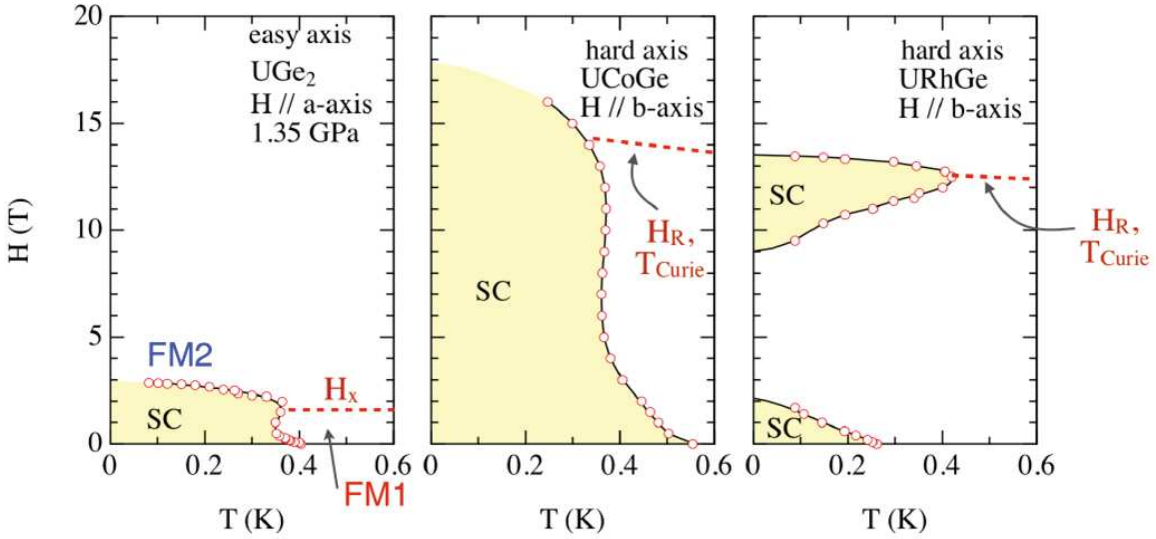

Figure 1.5 | Reentrant sueprconductivity observed in **(a)**: UGe_2 (at 1.2 GPa, for **H**//**a**), **(b)**: URhGe for **H**//**b** and in **(c)**: UCoGe for **H**//**b**. Figure taken from Ref.[34]. The red broken lines correspond to magnetic transitions associated with the re-entrant superconductivity.

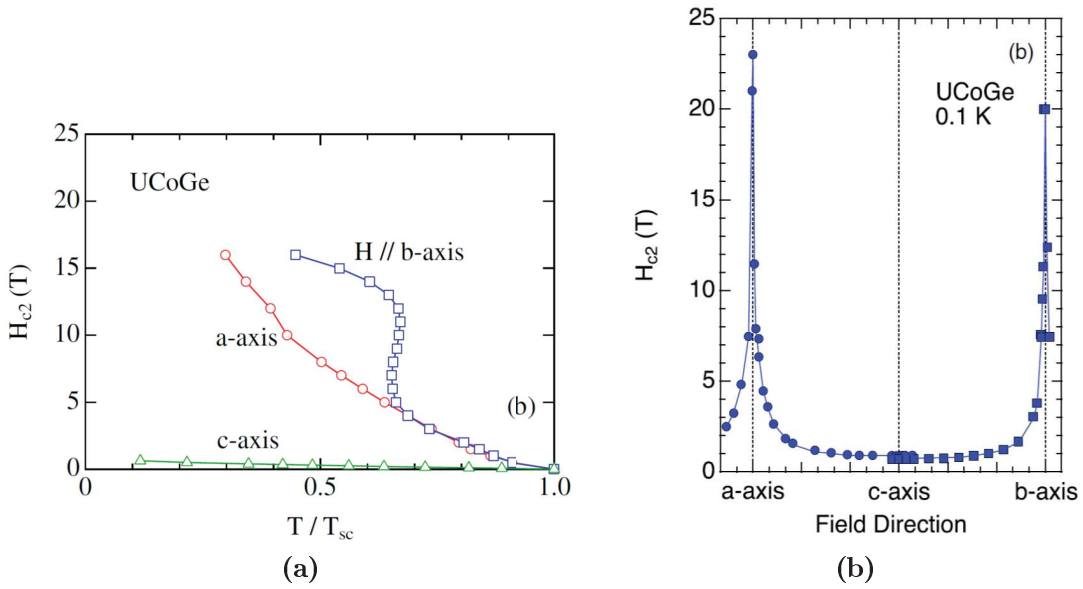

Figure 1.6 | **(a)**: Upper critical field of UCoGe probed with resistivity measurements in Ref.[30]. **(b)**: Angular dependence of H_{c2} in UCoGe, equally obtained with resistivity measurements[35].

Kondo coupling between f-electrons and conduction bands. This means very low Fermi velocities ($v_F \sim (m^*)^{-1}$) and thus a high upper critical field (according to the Werthamer-Helfand-Hohenberg (WHH) theory[36], in a clean superconductor, the orbital limitation for the upper critical field goes like $H_{c2}^{orb} \sim T_{sc}^2 v_F^{-2}$). However, although the Sommerfeld coefficient in UCoGe ($C_p/T = \gamma = 55$ mJ K^{-2} mol^{-1}) indicates a modestly enhanced effective mass m^* (to be compared with examples like UBe_{13}, where $\gamma \sim 1$ J K^{-2} mol^{-1}),

it holds the record for the ratio $H_{c2}(0)/T_{sc}^2$ in all superconducting systems (except for the re-entrant superconducting phase in URhGe).

Secondly, despite the high values of H_{c2} for **H**//**a** and **b**, H_{c2} for **H**//**c** in UCoGe is not higher than 1 T, showing an extremely large anisotropy. Such an anisotropy is observed only in 2D systems, which is not at all the case of UCoGe, where normal phase transport measurements do not show a noticeable variation between different current directions. Equally astonishing is the angular dependence of H_{c2} in UCoGe, presented in figure 1.6b. It is found to be extremely sharp around the **a** or **b**-axis when turning towards the **c**-axis.

Thirdly, apart from the S-shaped H_{c2} for **H**//**b**, for the other two field directions in UCoGe, H_{c2} also presents anomalous upward curvatures (a zoom for **H**//**c** is presented in figure 1.7), in contrast to the usual downward curvature for conventional superconductors, according to the WHH theory[36, 37]. Figure 1.7 shows the evolution of H_{c2} for **H**//**c** under pressure, measured by G.Bastien during his PhD[25]. The upward curvature of H_{c2} for **H**//**c** persists under pressure, and is present both in the ferromagnetic and paramagnetic phase.

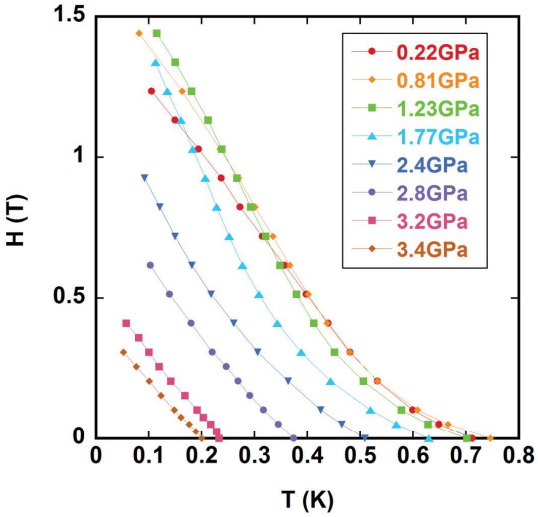

Figure 1.7 | H_{c2} for **H**//**c** of UCoGe under pressure, measured with resistivity in Ref.[25].

Curiously, these particular behaviors of H_{c2} in UCoGe (the upward curvatures and the 2D anisotropy) are not observed in the sister compound URhGe, despite the strong resemblance of the two systems. The H_{c2} of the latter in the low field superconducting phase seems to have a completely usual behavior[38].

Aim of this study

The main focus of this PhD is on the upper critical field of UCoGe, which is considered as one of the most exotic cases among unconventional superconductors. The particular features of H_{c2} in UCoGe mentioned above are the heart of the discussions in Chapter 3 through Chapter 6.

Chapter 3 presents thermal conductivity and other measurements to determine the H_{c2} with bulk sensible probes, and shows the particularities of these behaviors by comparison with classical theories for H_{c2}. Chapter 4 and Chapters 5 demonstrate that these features

are associated with a phenomenon specific to ferromagnetic superconductors: the field dependence of the pairing interactions. These discussions show that H_{c2} for $\mathbf{H}//\mathbf{c}$ in UCoGe can be understood with a suppression of the pairing interactions under field. Such a behavior is compatible with the change of the normal phase properties under field (Chapter 4), and is explained by the theory of V.Mineev[39] (Chapter 5). Meanwhile, the same framework leads to a clear understanding of the difference between the two systems UCoGe and URhGe. This precise understanding of the physical behavior in the simple case of $\mathbf{H}//\mathbf{c}$ in UCoGe and URhGe yields a strong and rare evidence for the nature of the pairing mechanism in these systems.

For $\mathbf{H}//\mathbf{b}$, the situation is much more complex. The application of the theory in Ref.[39] seems to be limited in this case. Chapter 6 reports the experimental findings in the thermal conductivity and resistivity measurements for $\mathbf{H}//\mathbf{b}$ in UCoGe, which give indications of a new physical phenomenon.

Independent from the rest of this study, (the last) Chapter 7 discusses about two particular aspects in the normal phase of UCoGe, and presents also the first results on the other system UBe_{13}. Due to the limited time, these results do not reach full conclusions, but they show the progress and the perspectives for each of these problems.

Before presenting the experimental results and discussions, we will start by introducing the experimental methods used in this study, mainly thermal conductivity and specific heat measurements, in the next chapter.

Chapter 2

Experimental methods

2.1 Thermal conductivity and resistivity measurements

Thermal conductivity is a useful experimental method to study superconducting and other physical properties in metallic or non metallic systems. The most important parts of the experimental results presented in this study are obtained from low temperature thermal conductivity measurements, both on the superconducting and normal phase of UCoGe. Here the general principles of this experimental method will be introduced, followed by a description of the experimental conditions and the set-up used in this study.

2.1.1 Principles

In an isotropic system, the heat current obeys Fourier's relation:

$$\mathbf{j} = -\kappa \, \nabla T \tag{2.1}$$

where κ is, by definition, the thermal conductivity, $\mathbf{j}$ measures the heat current that flows across a unit cross-section perpendicular to the current direction and T is the temperature. In a crystal which does not have cubic symmetry, κ depends on the current direction and gives information on the anisotropy of the system:

$$j_i = - \, \kappa_{ij} \, \frac{\partial T}{\partial x_j} \tag{2.2}$$

There are several mechanisms by which heat can be conducted through a solid. In a metal, heat transport can be carried by the free-moving electrons, but it can also be transmitted by the propagation of other kinds of excitations like phonons, magnetic excitations, etc. In most cases, these different heat channels are considered to be in parallel and independent from each other, so that the total thermal conductivity is the sum of all these contributions:

$$\kappa = \kappa_{elec} + \kappa_{phonons} + \kappa_{magnons} + ... \tag{2.3}$$

In this study, this will be used as a basic assumption for all the thermal conductivity data analyses.

The electronic part of the thermal conductivity (κ_{elec}) can be estimated with a knowledge of the electrical resistivity ρ by using the Wiedemann-Franz (WF) law:

$$\frac{\kappa_{elec.} \, \rho}{T} = L_0 \tag{2.4}$$

where L_0 =2.44.10^{-8} W Ω cm is called the Lorenz number. The WF law is valid when the scattering processes that the electrons undergo influence the thermal and electrical transport in the same way. This is mostly true at low temperature, when the electrons scattering rate is dominated by the elastic scattering from impurities and crystal dislocations, or at high temperature, when scattering is dominated by "high energy" excitations of wave vectors $q \sim \frac{1}{a} \sim k_F$ (a: unit cell length; k_F: Fermi wave vector). For metallic systems with high crystal quality, the deviation from the WF law can be observed at intermediate temperatures, because the inelastic scattering processes due to small wave-vector phonons become important: these processes are much more efficient in restoring the thermal equilibrium than in producing electrical resistance (which requires larger momentum transfers). In such case, the electronic thermal conductivity κ_{elec} will be lower than what is directly estimated with the electrical resistivity values[40].

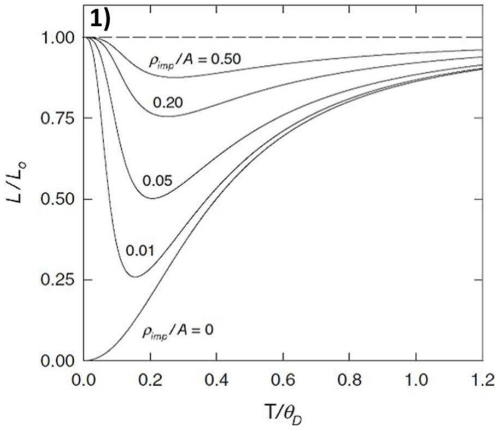

Figure 2.1 | Violation of the Wiedemann-Franz law with the presence of inelastic scattering. Figure from Ref.[41], page 7.

The superconducting transition also leads to a breakdown of the WF law, as the formation of the Copper pair condensate decouples the electrons from heat transfer and κ_{elec} is lowered compared with the normal phase, while the electrical resistivity goes to zero. A more detailed discussion will be presented in Chapter 3.1.

At low temperature, thermal conductivity is sensitive to the propagation of low energy (thermal) excitations in the system, with a resolution of k_BT (of order 0.01 meV at 100 mK). It is thus a good experimental method to probe the excitation spectra in different systems. For example, for a superconductor, low temperature thermal conductivity is used to study the superconducting gap structure and anisotropy. Other thermal properties, such as the specific heat, can give similar information. However, compared with the specific heat, thermal conductivity measurements have two advantages: first, it is a directional probe; second, it is not influenced by the local excitations (like hyperfine excitations of the nuclei, magnetic impurities, ...). The latter have often a dominant effect on the low temperature specific heat measurements, particularly under magnetic field, and may hide the electronic properties from direct observations (as an example, see discussions in Chapter 7.2.2).

2.1.2 General experimental conditions

All the thermal conductivity measurements presented here have been performed in two dilution cryogenic systems. The first one is an old home-made dilution refrigerator equipped with a 8.5 T superconducting magnet. It has a strong cooling power to reach base temperature as low as 7 mK (named the "10 mK dilution" in the following) and can be used for measurements up to 7 K. It has the advantage of being well decoupled from environmental vibrations. The second one allows to cool the system down to about 100 mK, and is equipped with a 15 T superconducting magnet (named the "15 T dilution" after). The 15 T dilution system is further equipped with a pulse-tube Helium-recondensing unit, which allows to perform long-period experiments with very limited Helium consumption. However, it has a poor temperature stability above 1 K, and the mechanical vibrations introduced by the pulse-tube system may add large level of noises to the measurements, which lead to serious heating problems on the thermal conductivity measurements when the temperature is below 150 mK. To overcome these difficulties, extra efforts have been made both from the inside (stiffening the measurement set-up) and from the outside of the cryostat (fixing the tubes of the recondensing system to reduce their vibration amplitude).

The thermal conductivity set-up is described and discussed in the next section. The same set-up is used to measure the sample electrical resistivity during the same experiment, as these data are essential for the quantitative analyses of the thermal conductivity results (section 2.1.4). We are further equipped with an in-situ rotating system which allows precise orientation of the field directions, which will be presented in section 2.1.5.

2.1.3 Thermal conductivity set-up

For the thermal conductivity measurements, the classical "one-heater-two-thermometer" method is used, which is illustrated in the simple scheme in figure 2.2.

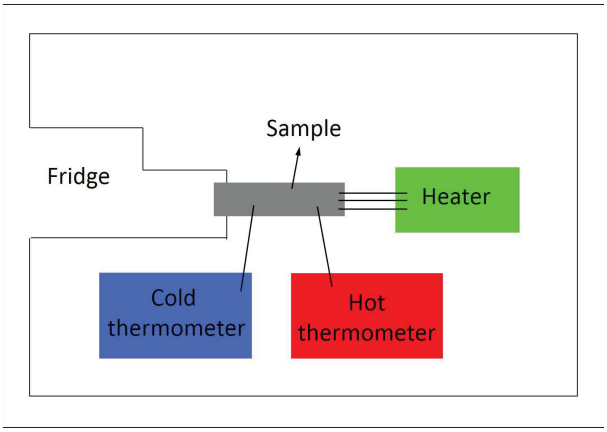

Figure 2.2 | A simple scheme for the thermal conductivity set-up.

To perform such measurements, a bar-shaped sample is fixed to the sample stage at its left end and is thermalized to the system temperature (the dilution fridge temperature). On the right side of the sample, a 10 kΩ resistance heater is used to apply a heating power P on the sample. A heat current then flows along the sample. When a stationary state is reached, the temperature gradient is measured with two carbon Matsushita thermometers.

The constant heating power P is exerted by passing a dc electrical current through the heater, with its voltage accurately measured at the same time. Noting s the section

of the bar-shaped sample, the heat current intensity along the sample is approximately $j = P/s$. The temperature gradient along the sample is given by $\nabla T = (T_{hot} - T_{cold})/l$, with l the distance between the two thermometer contact points. According to Fourier's law (equation (2.1)), the thermal conductivity of the sample κ is then given by :

$$\kappa = \frac{l}{s} \frac{P}{T_{hot} - T_{cold}} \tag{2.5}$$

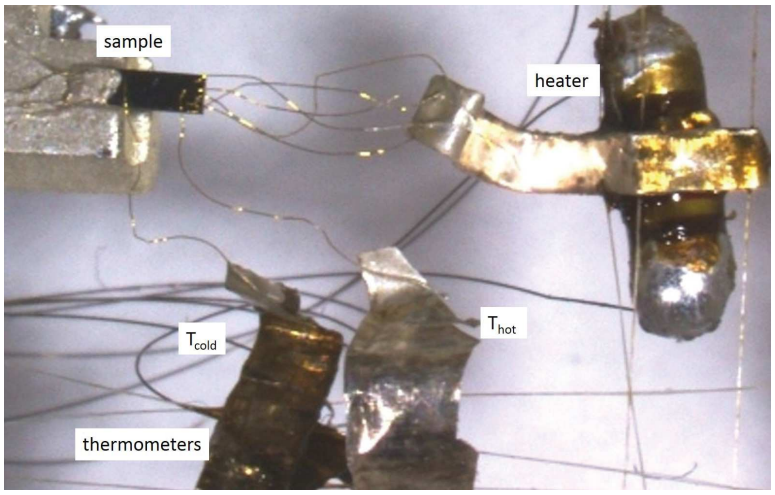

Figure 2.3 | Photo of the thermal conductivity set-up.

The photo in figure 2.3 shows the details of the set-up in practice. The sample is glued to the sample stage with silver paste. Each of the thermometers and the heater is tightly attached to a small silver foil with General Electric varnish. They are electrically decoupled from the silver foil. To reduce the heat leaks, they are suspended only with a few Kevlar wires (30 μm in diameter), which provide sufficient mechanical rigidity while being poor thermal conductors. The thermal and electrical contact between the silver foils and the sample are made by using 15 μm gold wires. They are glued with silver paste on the thermometer or heater silver foils, and are spot-welded on the sample. For the heater, a maximum number of gold wires are mounted for each experiment, so that a good thermal connection between the heater and the sample is obtained. On the cold side, several (4 to 5) gold wires are equally added on the base of the silver paste connection, to guarantee a good thermalization of the sample during the measurements. The thermometers and the heater are measured with Nb-Ti superconducting wires of 50 μm diameter and at least 30 cm in length, so that their thermal conductance through the measuring wires are small enough to be neglected. For measurements performed in the 15 T dilution (thus under high magnetic field), the superconducting wires are no longer suitable for the heater, and are replaced by resistive wires.

The carbon Matsushita thermometers used for the thermal conductivity measurements have the advantage of good sensitivity and quick responses down to lowest temperatures. This is why they are chosen rather than the more usual RuO_2 thermometers. The drawback is that they undergo small changes in their resistance with each cooling-heating cycle and have non negligible magnetoresistances, thus they need to be calibrated for each new measurement.

At the end of each thermal conductivity measurement the thermometer resistances are measured again in a stationary state with the heating power turned off (and the system

temperature adjusted so that the sample temperature remains the same, with a $\Delta T/T$ of order 0.5%). During this period the whole set-up is thermalized to the dilution fridge temperature, and the thermometer resistance data during this time are used both for correcting the residual temperature gradient $T^0_{hot} - T^0_{cold}$ (mainly due to the imperfect calibration laws), and for the thermometer calibration. The value of thermal conductivity is then calculated with:

$$\kappa = \frac{l}{s} \frac{P}{(T_{hot} - T_{cold}) - (T^0_{hot} - T^0_{cold})}, \tag{2.6}$$

where $T_{cold} \sim T^0_{cold}$.

2.1.4 Resistivity measurements

At the end of each thermal conductivity measurement, the electrical resistivity of the sample is also measured. For this the classical four-wire ac method is used. The same gold wires used as thermal contacts between the sample and the thermometers (or the heater) are used as the electrical contacts. This allows to compare the measurements from the two probes with the same geometrical configuration. For the resistivity measurements a small ac current of the order of 100 μA is applied. Any possible heating effects on the sample can be directly detected with the thermometers and can then be corrected.

One disadvantage of measuring the resistivity with the thermal conductivity set-up is that it becomes difficult to reduce the loop area between the voltage wires, so that the noise pickup is large. In a classical resistivity set-up, the two voltage wires are twisted so that the loop area is reduced to a minimum. In our case this is not possible because the two voltage wires pass by separate silver pads, and twisting them would increase the thermal connection between the two thermometers. As a result, the measured resistivity presents some specific resonance frequencies with a dominant quadrature signal at high fields. In practice, to stay far from the resonant frequencies, a very low frequency of 2.33 Hz is used. The resistance value is obtained by averaging the measurements over an 1 minute period.

2.1.5 Field orientation

Superconductivity in UCoGe is known to be extremely sensitive to the magnetic field direction, for field applied along its **a** or **b** axes. When measuring the upper critical field along these two field directions, a precise orientation of the sample in the field becomes a crucial issue.

For thermal conductivity experiments in which the upper critical field for $\mathbf{H}//\mathbf{a}$ and $\mathbf{H}//\mathbf{b}$ are probed, we are equipped with an in-situ alignment system consisting of two (Attocube) piezo-goniometers and one (Attocube) piezo-rotator to orient the sample in the magnetic field. Figure 2.4 shows a photo of the set-up. The two goniometers in the upper part of the photo have perpendicular rotating axes, and each of them has a maximum angle of about 3° in the two directions. The rotator below (behind the square sample stage) has its rotating axis parallel to that of the upper goniometer. It can be turned to any angle between 0° and 360°, which allows to perform complete angular dependence measurements.

An Attocube Inertial Motor Driving Controller ANC150 system is used to control the rotating operations. This is done by sending a series of very short voltage pulses of 30 to

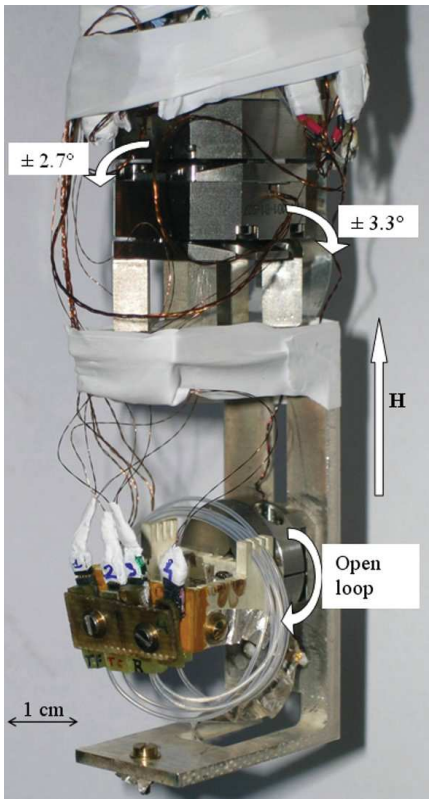

Figure 2.4 | Photo of the alignment system. The upper part of the photo shows two goniometers with perpendicular rotating axes, each of them having a maximum rotating angle of about 3°. On the lower part of the photo, behind the square sample stage lies the piezo rotator which can be rotated completely to 360°.

45 V to the piezo rotator or goniometers, with a "sawtooth profile" triggering the inertial displacements. The resistance of the wires that connect the rotators to the electronics has to be less than 10 Ω, to avoid excessive filtering of the "sawtooth" profile. For this reason, a combination of copper wires and Nb-Ti superconducting wires (in the ^{4}He bath) have been used.

The position of each of the goniometers and the rotator can be followed with a resistive encoder (potentiometer). The resistance ratio of the encoder, that varies from 0 to 1 depending on the position, can be measured with high resolution (at least 10^{-3}) with a Lock-In amplifier. The method is illustrated in figure 2.5a. An ac-signal ($U_0 = 1$ V) is sent into the (total) position resistance, and the position of the goniometer/rotator is indicated by the ratio U_1/U_0. In practice, the position resistance increases strongly at low temperature and under magnetic field: it can reach values higher than 1 MΩ, which is of the same order as the input impedance of the Lock-In amplifier (10 MΩ). As a result, the measurement of the potential ratio is strongly biased. This problem has been overcome by inserting a Femto (DLPVA-100-F-D) voltage pre-amplifier, which has an input impedance of 1 TΩ (see figure 2.5b).

During the experiment the alignment of the sample direction to the magnetic field is set by following the resistance of the sample inside the superconducting transition. For example, for the measurements on UCoGe sample S^c_{16}, to align the crystal **b**-axis along the field, we first set the system temperature at 0.4 K and the magnetic field at 4 T, to be in the resistive superconducting transition. We then use the goniometer 2 (the lower one)

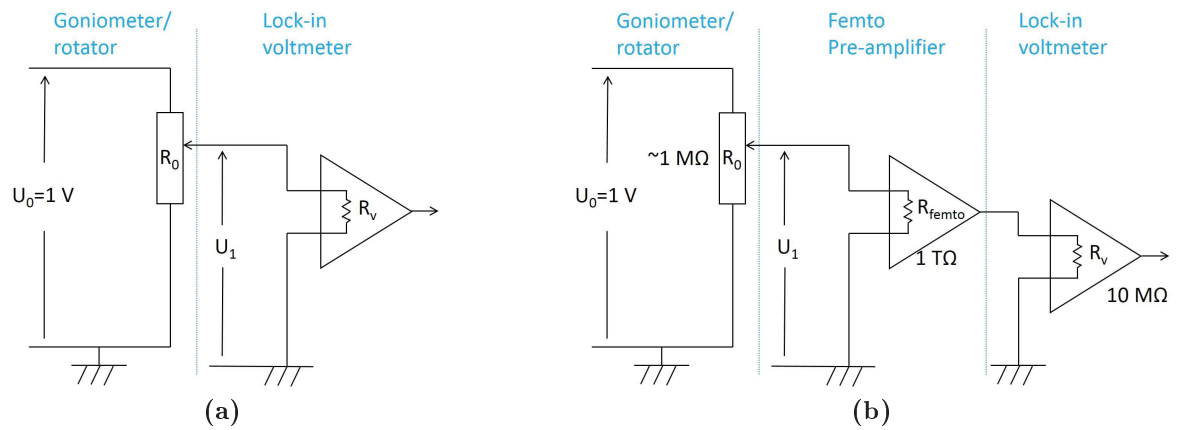

Figure 2.5 | **(a)**: The resistance encoder for the goniometer/rotator position. The ratio U_1/U_0, measured with a Lock-In amplifier (voltmeter), indicates the position. **(b)**: The position resistance ($R_0 \sim 1$ MΩ) similar in order of magnitude to the input impedance of the Lock-in amplifier ($R_v = 10$ MΩ), it is necessary to insert a (Femto) pre-amplifier between the two, which has a sufficiently large input impedance ($R_{femto} = 1$ TΩ).

to rotate the sample so that the field direction is turned in the (**b**,**c**) plane. When the sample **b**-axis is approaching the field direction, the superconducting transition temperature increases, so the sample resistance at 0.4 K decreases. By finding the minimum of the sample resistance at this temperature and field, the field component along the **c**-axis can be accurately eliminated. Figure 2.6a shows the shift of the superconducting transition during such a rotating process, with different colors corresponding to different positions of the goniometer 2, separated by steps typically of 0.01° to 0.05°. Figure 2.6b presents the angular dependence of the resistance of sample S^c_{16} of UCoGe, at $T = 0.4$ K and H =4 T, which allows to find the position of the **b**-axis with a precision of 0.01°.

To complete the orientation of the crystal **b**-axis along the field direction, it is necessary to perform a second step to eliminate small amount of field component along the **a**-axis. To do this, it is necessary to increase the magnetic field up to H =10 T, where the difference between the H_{c2} along these field directions is large, and set the system temperature at $T = 0.4$ K (inside the superconducting transition). We then use the goniometer 1 (upper one) or the rotator to orient in the (**a**,**b**) plane and find the optimal position in the same way we do in the first step. After this we optimize the sample orientation again with goniometer 2 (lower one), to eliminate small field component along the **c**-axis introduced in the second step.

In pratice, the use of this piezo rotating system is also accompanied with some other difficulties.

First, the stress force exerted by the piezo-electric material to perform rotation is very limited even when a maximum voltage (around 60 V) is applied. The goniometer or the rotator will be blocked by a small mechanical resistance to the rotation. This can happen for example if the wires used in the set-up are too rigid.

Second, during the rotating operations, the electrical pulses sent into the rotators dissipate large amount of heat. This increases the temperature of the whole sample stage significantly. Then the sample resistance is strongly modified, due to its sensitivity to temperature variation inside a superconducting transition. As a result, at the end of each

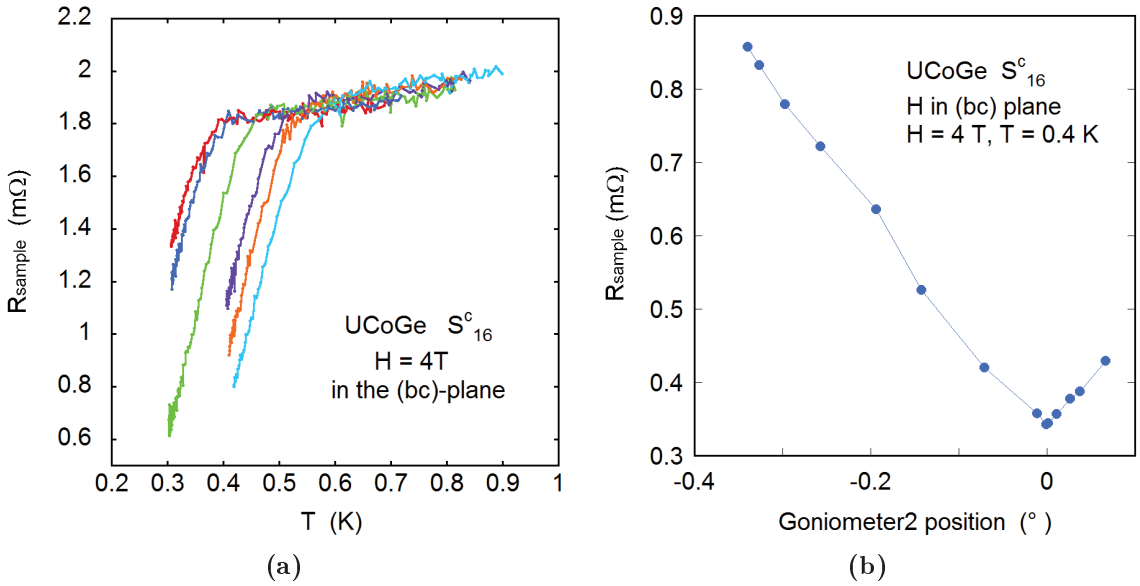

(a) (b)

Figure 2.6 | **(a)**: Shift of the superconducting transition when the field direction is rotated in the (**b**,**c**) plane. Different colors correspond to different positions of the goniometer 2, separated by steps typically of 0.01° to 0.05°. **(b)**: The resistance of sample #1 of UCoGe at $T = 0.4$ K and $H = 4$ T (inside the superconducting transition), as a function of the angle between the field direction and the **b**-axis inside the (**b**,**c**) plane. The resistance of UCoGe is minimum when the field is aligned along the **b**-axis because the H_{c2} is the highest at this position.

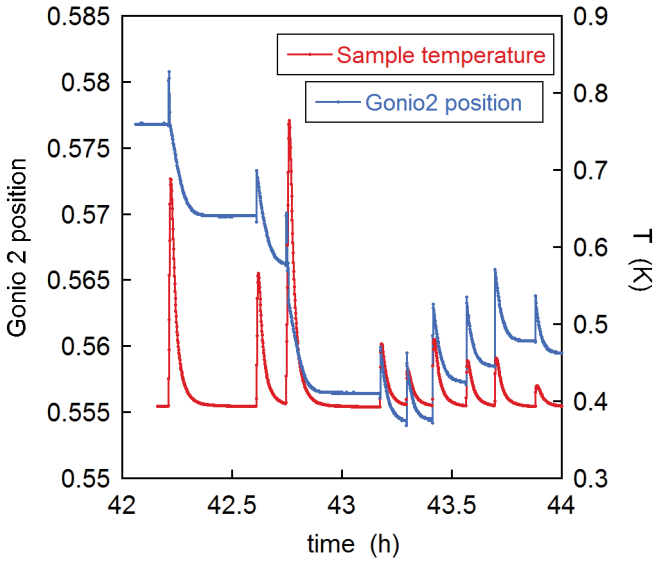

Figure 2.7 | Time evolution of the goniometer 2 position (blue curve, scale on the left) and the increase and relaxing of the sample temperature (red curve, scale on the right) during one part of the rotating processes, as an example.

rotating operation, we have to wait until the sample temperature relax completely to the fridge level to see the influence of field orientation on the sample resistance. This makes the alignment process time-consuming. Figure 2.7 presents the heating effect on the sample

(red curve) as a function of time, when rotating with the goniometer 2 (blue curve for its position). It can be observed that in these rotation steps the sample temperature can rise much higher than the onset of the superconducting transition, and requires typically 10 minutes to relax to the system level. To control this heating effect at a reasonable level, the driving electrical pulses are sent at a low frequency (from 10 to 15 Hz), with an application time that ranges from 10 to 30 seconds. If the pulses are sent with a higher frequency or for a longer time, it is even possible to heat the mixing chamber of the dilution unit, in which case it takes much longer to re-stabilize the system.

2.2 Specific heat measurements

The specific heat C_p is directly related to entropy evolution through $C_p = T(dS/dT)$, thus it is a perfect quantity to characterize phase transitions. For a metal in the normal phase C_p is often composed of an electronic contribution linear in T, and a T^3 phonon contribution: $C_p = \gamma T + \beta T^3$. The linear coefficient γ, named the Sommerfeld coefficient, is related to the electronic density of states. In heavy fermion systems, in general very large γ coefficients are observed due to strong quasiparticle effective mass enhancement($\gamma \propto m^*$).

During this thesis some specific heat measurements have been performed, both in a Physical Property Measurement System (PPMS) and in a dilution cryostat. C_p was measured on two UCoGe samples, in order to study their superconducting and normal phase properties, notably the field dependence of the Sommerfeld coefficient γ (see Chapter 4.3). They were also performed to characterize a series of UBe_{13} samples issued from different growth processes: by studying their superconducting transitions and their Sommerfeld coefficient above T_{sc}, it could be used to select and refine the appropriate method to obtain a high quality monocrystalline sample in this system (see Chapter 7.3).

2.2.1 Method

The classical relaxation method is used for all the specific heat measurements done in this thesis, both in PPMS and in the dilution cryostat. To do this, the sample is glued on an isolated sample stage either with a special glue (for PPMS) or with silver paste (for the dilution). The sample stage, being suspended, is connected to the outside system only with thin metallic wires which serve as heat leaks. A thermometer and a heater are put on the back of the sample stage, and are measured with theses wires.

During the measurement, the sample stage is first heated with a constant heating power P during a period d, and then left relaxing to the temperature of the outside system. Its temperature is measured by the thermometer all along the process, and then fitted with exponential laws to get the specific heat measurements. More specifically, when the temperature of the outside system T_0 is regulated to remain stable, the evolution of the sample stage temperature T is governed by:

$$C_p^{\text{total}} \frac{dT}{dt} = P(t) - K(T - T_0) \tag{2.7}$$

where C_p^{total} is the total heat capacity of the system (sample stage + the sample), K is the thermal conductance of the heat leaks, and $P(t)$ is the heating power at time t. Solving

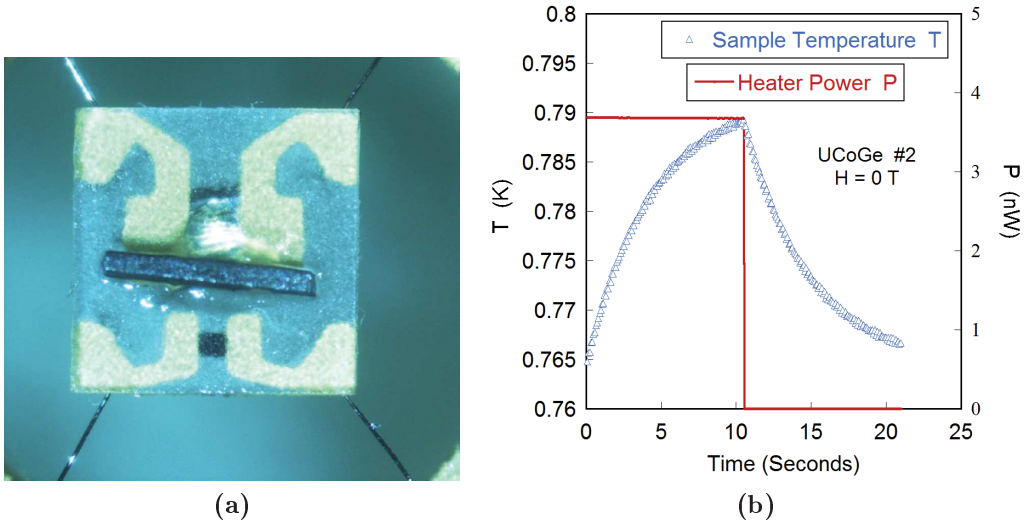

(a) **(b)**

Figure 2.8 | **(a)**: Photo of the PPMS specific heat measurement set-up, with a UBe_{13} sample on it. **(b)**: Time revolution of the sample temperature (blue triangles) during one specific heat measurement with the relaxation time method. The red line shows the power applied by the heater during the measurement.

this equation with the initial condition $T_{t=0} = T_0$, we have:

$$T(t) = T_0 + \int_{t'=0}^{t} \exp(-\frac{t-t'}{\tau}) \frac{P(t')}{C_p^{\text{total}}} \, dt' \tag{2.8}$$

where $\tau = C_p^{\text{total}}/K$ is called the relaxation time. During the measurements with the relaxation method (see figure 2.8b), $P(t)$ is given by:

$$P(t) = \begin{cases} P \, , & \text{for } 0 \leq t \leq d \\ 0 \, , & \text{for } t > d \end{cases} \tag{2.9}$$

Inserting equation (2.9) into equation (2.8) leads to:

$$T(t) = \begin{cases} T_0 + R \left(1 - \exp\left(-\frac{t}{\tau}\right)\right) \, , & \text{for } 0 \leq t \leq d \\ T_0 + R \left(1 - \exp\left(-\frac{d}{\tau}\right)\right) \exp\left(-\frac{t-d}{\tau}\right) \, , & \text{for } t > d \end{cases} \tag{2.10}$$

with $R = \tau P / C_p^{\text{total}}$. Fitting the time evolution of T in figure 2.8b with equation (2.10), one can determine the coefficients τ and R, from which C_p^{total} can be calculated.

The specific heat of the sample can then be obtained, when the heat capacity of the sample stage, which is pre-calibrated before the measurements, is removed from C_p^{total}.

2.2.2 Corrections to the PPMS thermometer calibrations

For the heat capacity measurements performed in the PPMS system, the data analysis is automatically performed by the PPMS program, and the calculated specific heat data can be directly obtained in the resulting data files. However these results present some

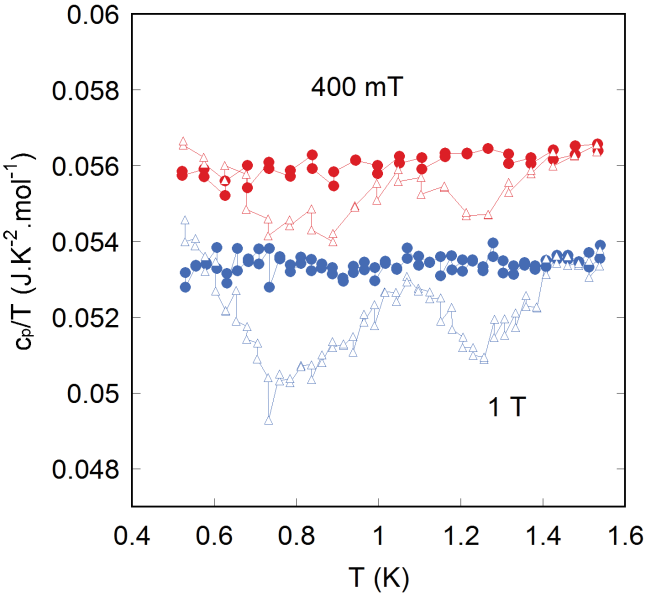

Figure 2.9 | C_p/T as a function of temperature before (open triangles) and after (filled circles) the correction to the PPMS thermometer calibration, at H =400 mT and H =1 T for $\mathbf{H}//\mathbf{c}$ in UCoGe (sample S^c_{16}). It shows clearly that the correction of the thermometer calibration removes the anomalies in the $C_p/T(T)$ curves.

anomalies in the temperature dependence of C_p/T, which are amplified in measurements under magnetic field (see as an example the open triangles in figure 2.9). This leads to serious problems for the quantitative analysis of the Sommerfeld coefficient γ under magnetic field of UCoGe (in Chapter 4.3).

After careful examinations on the PPMS data, we found that these anomalies come from the calibration law of the specific heat thermometer used by the PPMS program. During the thermometer calibration, the PPMS program measures the temperature dependence of the thermometer on several temperature segments. In these different temperature ranges, different currents and different ranges of sensibility are used. This leads to small jumps of the thermometer resistance at the junction of two temperature segments. The PPMS program does not use a calibration law smooth enough to take into account this jump in resistance, leading to these anomalies.

To correct these errors, we took the thermometer calibration table and fit it in a smoother way. To do this, a spline function is used, which, at each temperature, fit the thermometer resistance data at neighboring temperatures with a polynomial (of order 3): it is the same fit as is used to calibrate the thermometers during the thermal conductivity measurements. Then we take the PPMS log file for each specific heat measurement, in which the time evolution of the thermometer resistance and the heating power is registered. The data are re-analyzed with the corrected spline fit for the thermometer calibration, and the values of τ and κ re-calculated to find the C_p results. Figure 2.9 presents the effect of the thermometer calibration corrections, which shows clearly that the anomalies at around 1.2 K and 0.8 K observed in the raw PPMS analyses are completely removed.

Chapter 3

Bulk determination of H_{c2} in UCoGe

As shown in the Chapter 1, the upper critical fields (H_{c2}) of UCoGe has been measured with resistivity, for field along its three crystallographic axes[30]. It is considered as one of the most exotic cases among unconventional superconductors. However, up to now, the only published H_{c2} data in UCoGe have been obtained by resistivity[30, 42]. Confirmation of this exotic behavior requires measurements of H_{c2} with other experimental methods, especially with bulk sensitive probes. This chapter presents bulk measurements of H_{c2} of UCoGe (mainly with thermal conductivity), for magnetic field along the three crystal axes. The results confirm all the particularities of H_{c2} in this system, previously observed in resistivity studies.

3.1 Superconducting transition with different experimental probes

Before presenting our results for H_{c2} in UCoGe obtained with thermal conductivity measurements and other experimental probes, we first discuss different experimental methods used to probe a superconducting transition.

Resistivity

Resistivity (ρ) is the most common experimental tool to probe a superconducting transition, due to the clear signature that it becomes zero in the superconducting phase. However, it has some well-known drawbacks.

First, as soon as some filamentary parts of a massive sample become superconducting, and form a complete (percolating) superconducting path between the two voltage contacts, it will show a complete superconducting transition in resistivity ($\rho = 0$).

A remarkable example is the case of $ZrZn_2$. It was at first claimed to be a superconductor coexisting with a weak ferromagnetic state, according to resistivity and ac-susceptibility results[43]. However, no sign of superconducting transition was observed in specific heat. Later work showed that the observed superconducting transition in this system was due to a superconducting layer of Zn at the sample surface, which was created during the spark erosion cutting of the sample[44].

Apart from this peculiar case, transitions in resistivity in general do correspond to an intrinsic superconducting transition. But it indicates usually a transition temperature higher than the bulk transition. Figure 3.1 shows the superconducting transition probed

with specific heat and resistivity in UCoGe (sample S^c_{16}). The onset of resistivity transition (purple line) at 0.8 K lies much higher in temperature than the bulk superconducting transition in specific heat (red triangles), and the onset of the transition in C_p/T (0.5 K) lies close to the temperature at which the resistivity transition is completed ($\rho = 0$). The filamentary superconducting parts of the sample, which are responsible for the higher T_{sc} in resistivity, are quickly suppressed by an external magnetic field. As a consequence it will have an impact on H_{c2} probed with resistivity (see the discussions in the next section in figure 3.9 and 3.11).

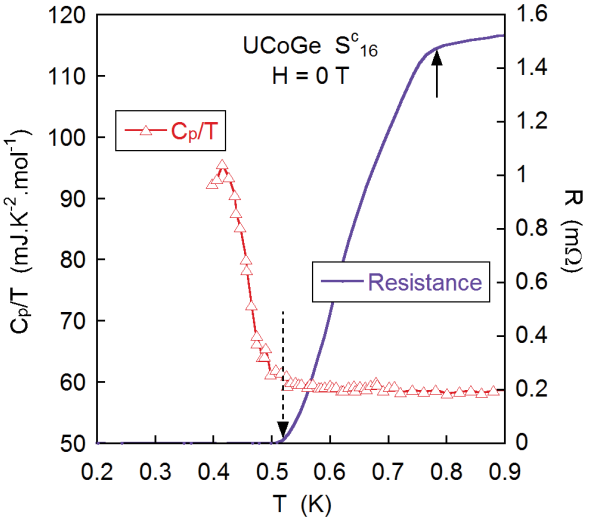

Figure 3.1 | Superconducting transition probed with specific heat (red triangles) and resistivity (purple line) of UCoGe (sample S^c_{16}). The onset of the bulk superconducting transition in specific heat lies close to the temperature at which the resistivity becomes zero (marked by the broken line). The onset of the resistivity transition lies much higher in temperature (marked by the up arrow).

Another complication of the resistivity probe comes from the vortex movements. For a type II superconductor, magnetic field can penetrate into the sample through vortices, each of which carries a quantized magnetic flux ϕ_0. At equilibrium, when interaction between vortices dominate over pinning, they form a periodic lattice (the Abrikosov lattice). Otherwise, the vortex cores can be pinned by defects and impurities.

In the presence of a passing electrical current, the vortices are subject to the Lorentz force coming from the interaction between the charged current and the magnetic flux. When this force is large enough to free the vortex cores from pinning, or to overcome the rigidity of the Abrikosov lattice, the vortices will start to move, which leads finite resistivity inside the superconducting phase.

This is frequently observed for example in cuprates or other high-Tc superconductors. In these systems, large thermal excitations facilitate the depinning of the vortex cores from impurities. The resistivity transition is often observed to be considerably broadened with increasing magnetic field due to the vortex flow[45]. If one takes as a criteria the temperature or field at which the resistivity goes to zero ($T_{\rho=0}$), it will not correspond to the real superconducting transition H_{c2}, but to an irreversibility line H_{irr}, above which the vortices are in motion. Consequently the transition line indicated by resistivity will be lower than the thermodynamic H_{c2}, and show a completely different form[46, 47, 48]. Fig-

ure 3.2 shows the example of an organic superconductor κ-(BEDT-TTF)$_2$Cu(NCS)$_2$[46]. Although its T_{sc} is much lower than in high-Tc superconductors, the transition line H_{irr} probed with resistivity in this compound lies also much lower than the bulk H_{c2} curve, and presents an opposite curvature, very similar to the case of UCoGe for **H**//**c**.

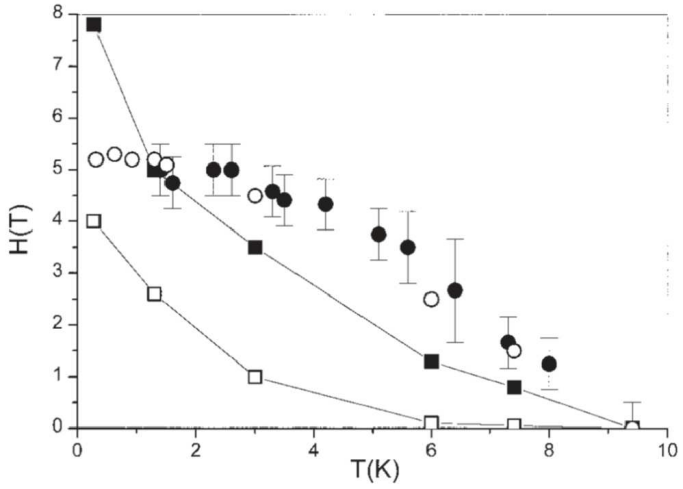

Figure 3.2 | H_{c2} of the quasi 2D organic superconductor κ-(BEDT-TTF)$_2$Cu(NCS)$_2$ obtained by microwave absorption (filled circles) and thermal conductivity (open circles) compared with the fields marking the beginning ($R = R_N$, filled squares) and the end ($R = 0$, open squares, which corresponds to H_{irr}) of the resistive transition.[46]

For these reasons, it is important to measure H_{c2} of UCoGe with a bulk sensitive probe to confirm the results of previous resistivity studies. The two main methods used in this study are specific heat and thermal conductivity.

Specific heat

Specific heat (C_p) is a robust bulk probe for superconductivity since it is a thermodynamic quantity. When the superconducting transition is approached from below the critical temperature (T_{sc}), C_p/T is significantly enhanced and presents a discontinuity at T_{sc}. As an example, figure 3.3 presents the superconducting transition probed with the temperature dependence of C_p/T in UCoGe (sample S_{95}^{ab}) at different magnetic fields along the **c**-axis.

The main difficulty of the determination of H_{c2} with C_p/T comes from the existence of non electronic contributions. When the temperature is below 0.1 K or when the magnetic field is large, nuclear contributions to C_p appear. This is related to the Zeeman or quadrapolar splitting of the nuclear energy levels. These contributions, which behave as $C_p \propto (H/T)^2$, may dominate over electronic contributions, which, together with the broadening of the transition under field, makes the determination of H_{c2} difficult. For superconductors with high critical temperature, the problem appears already at zero field, as C_p can be dominated by the large phonon contribution. In these situations, one needs to subtract accurately these other contributions to observe the superconducting transition. Nonetheless, for most heavy fermion superconductors, these other contributions in C_p are small at temperature around the superconducting transition.

For ferromagnetic systems, there is also an additional experimental difficulty for C_p/T measurements under field perpendicular to the easy axis: most C_p/T set-ups have a

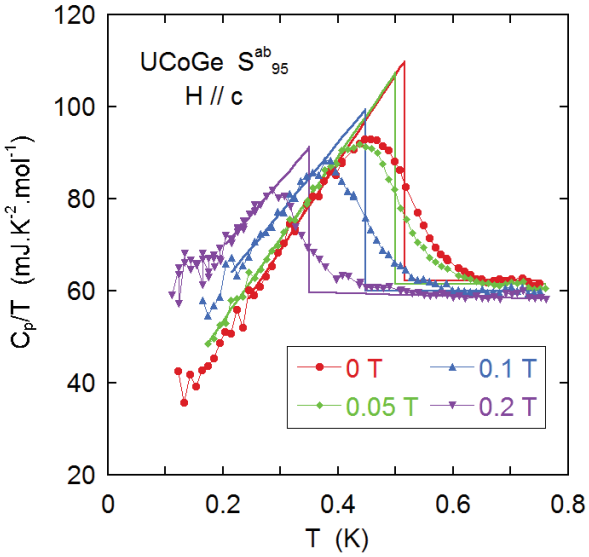

Figure 3.3 | Temperature dependence of C_p/T of UCoGe (sample S^{ab}_{95}), at different magnetic fields along the **c**-axis.

platform suspended by tiny wires for optimal thermal insulation. Then, the torque ($\vec{M} \times \vec{B}$) due to the spontaneous magnetization will change the sample orientation, and may even break the set-up. This is why there are still no direct C_p measurements in URhGe and UCoGe for fields along the **a** or **b**-axis.

Thermal conductivity

The principles of the analysis of the thermal conductivity (κ) measurements have been presented in the previous chapter (section 2.1). When a metal becomes a superconductor, its electrical conductivity becomes infinite, but the electronic part of the thermal conductivity (κ_{elec}) is reduced compared with κ_{elec} in the normal phase, due to the suppression of thermal excitations with gap opening.

The temperature dependence of κ/T inside the superconducting phase is a complex issue. With decreasing temperature, the heat carriers number (the excited quasiparticles) is reduced, leading to smaller thermal conductivity κ_{elec}. On the other hand, since the quasiparticle density becomes smaller, the quasiparticle-quasiparticle scattering rate will decrease too. Meanwhile, as the phonon density is reduced with decreasing temperature, the quasiparticle-phonon scattering rate is also reduced. Thus the scattering rate of quasiparticles is decreased in the superconducting phase, leading to larger mean free paths. The delicate balance of these two opposite effects is difficult to evaluate: quantitative predictions on the behavior of κ/T below T_{sc} usually include only elastic scattering on point defects.

Figure 3.4 shows the temperature dependence of κ/T around the superconducting transition in three UCoGe samples with different quality (indicated by the RRR values in the legend), measured in Ref.[49]. In this study we adopt the same sample notation as in the Ref.[28] and in the thesis of M.Taupin[49]: S^i_x means that the sample has a residual resistivity ratio (RRR) that equals x, and transport properties are measured with current injected along the crystal axis i (for bar-shaped samples). In the two high quality samples (S^c_{100} and S^b_{150}), κ/T is significantly enhanced at low temperature due to suppression

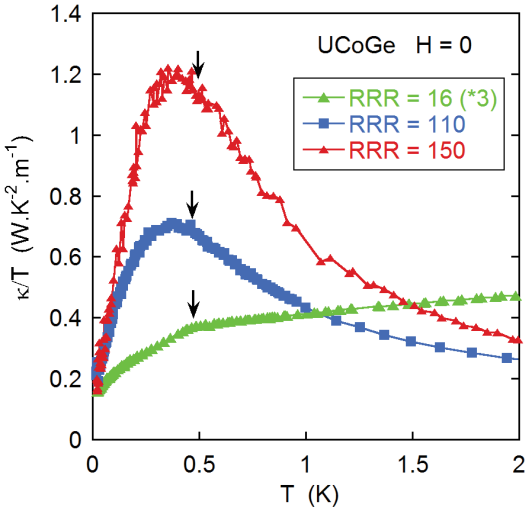

Figure 3.4 | The temperature dependence of κ/T around the superconducting transition observed in three UCoGe samples of different crystal quality (legend indicating their RRR). Red: sample S^b_{150}; blue: S^c_{100}; green: S^c_{16} (κ/T multiplied by 3 for clarity). Data taken from Ref.[49]. The superconducting transition temperature T_{sc} is indicated approximately by the arrow.

of quasiparticle inelastic scattering. It shows a maximum below T_{sc}, which indicates approximately the temperature below which the variation of the quasiparticle density becomes dominant. In these two samples, at T_{sc}, which is approximately indicated by the temperature at which the resistivity goes to zero, κ/T presents only smooth variations.

On the other hand, if the sample quality is poor, the elastic scattering on the impurities or other crystal imperfections will govern the dynamics of the quasiparticles at low temperature. Then the quasiparticle scattering rate will be more or less constant in temperature. In such case κ/T will have a monotonous behavior inside the superconducting phase, and the superconducting transition can be observed as a clear kink (see sample S^c_{16} in figure 3.4).

Therefore, we have chosen a sample of poor quality (sample S^c_{16}, RRR = 16) for our measurements of H_{c2} of UCoGe with thermal conductivity (the same sample as presented in figure 3.4).

3.2 Bulk determination of H_{c2} of UCoGe with thermal conductivity and other measurements

3.2.1 Raw data and analysis procedure

In this study H_{c2} of UCoGe has been measured on sample S^c_{16} with thermal conductivity, for magnetic field along its **a** and **b** axes. The measurements were performed in the 15 T dilution system (Chapter 2.1.2). Careful and precise in-situ field alignments were performed during each experiment (Chapter 2.1.5). Resistivity was measured on the same sample in the same conditions (Chapter 2.1.4). Figure 3.5 and 3.6 show respectively the resistivity and the thermal conductivity of UCoGe (sample S^c_{16}), with magnetic field applied along its **a** and **b** axis.

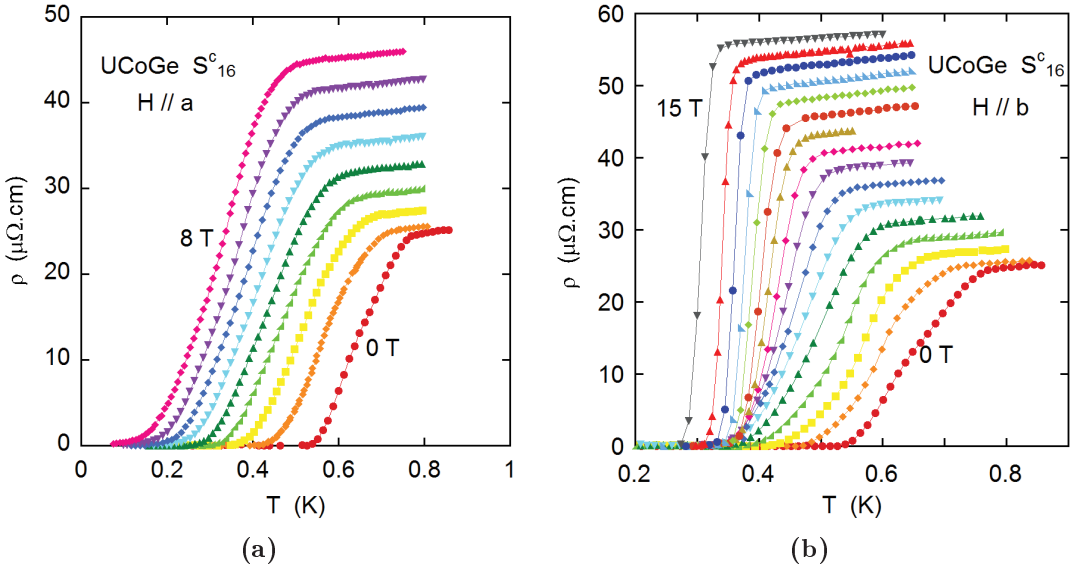

Figure 3.5 | Resistivity (ρ) as a function of temperature of UCoGe (sample S^c_{16}), at different magnetic fields, **(a)**: for **H**//**a**, every tesla from 0 T (the red circles on the right side) up to 8 T (pink diamonds on the left side); **(b)**: for **H**//**b**, every tesla from 0 T (the red circles on the right side) up to 15 T (grey downward triangles on the left side).

Method to determine H_{c2} from the thermal conductivity data

In figure 3.6a and 3.6b the superconducting transition can be clearly observed as a kink in κ/T. However when the magnetic field is large, the signature of the transition becomes small and difficult to detect. In order to obtain the superconducting transition temperature in a precise and controlled way, the following fitting procedure is applied for all the magnetic fields.

- First, the electronic contribution to the thermal conductivity in the normal phase ($\kappa_{qp}^{(n)}$) is estimated with the normal phase resistivity data ($\rho^{(n)}$), by using the Wiedemann-Franz law (equation 2.4) and ignoring the effect of the inelastic collisions (sample RRR = 16). The superscript $^{(n)}$ means normal phase properties, obtained in the whole temperature range by extrapolating the normal phase data:

$$\frac{\kappa_{qp}^{(n)}}{T} = \frac{L_0}{\rho^{(n)}} \tag{3.1}$$

  where $L_0 = 2.44.10^{-8}$ W Ω K^{-2} is the Lorenz number.

- Then we calculate the Lorenz ratio L/L_0, which equals the ratio between total thermal conductivity κ and the normal-phase electronic contribution $\kappa_{qp}^{(n)}$:

$$\frac{L}{L_0} = \frac{\kappa\rho^{(n)}}{L_0 T} = \frac{\kappa}{\kappa_{qp}^{(n)}} = \frac{\kappa_{qp}}{\kappa_{qp}^{(n)}} + \frac{\kappa_{other}}{\kappa_{qp}^{(n)}} \tag{3.2}$$

  It contains two terms. The first one is the normalized electronic contribution, $\kappa_{qp}/\kappa_{qp}^{(n)}$, which should be equal to 1 in the normal phase (when inelastic scattering is negligible) and decrease with temperature in the superconducting phase. The second term arises from the other contributions (phonons, magnons, etc.), $\kappa_{other}/\kappa_{qp}^{(n)}$,

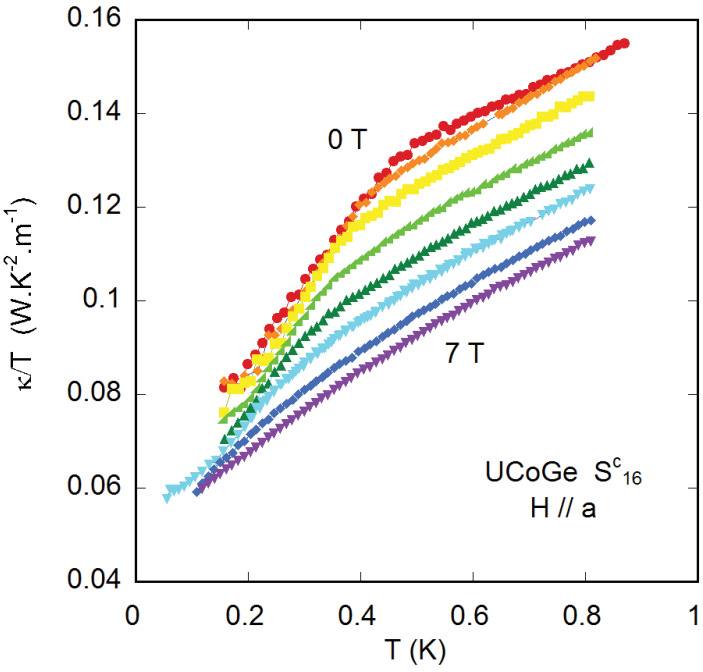

(a)

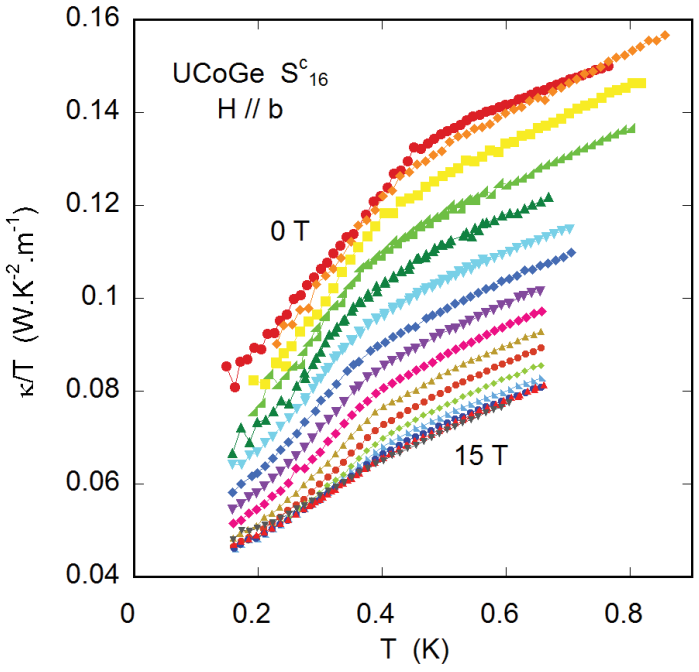

(b)

Figure 3.6 | Thermal conductivity divided by temperature (κ/T) as a function of temperature of UCoGe (sample S^c_{16}) at different magnetic fields, **(a)**: for **H**//**a**, every tesla from 0 T (the red circles on the upper side) up to 8 T (pink diamonds on the lower side); **(b)**: for **H**//**b**, every tesla from 0 T (the red circles on the upper side) up to 15 T (grey downward triangles on the lower side).

which should in principle exhibit only a smooth change in the neighborhood of the superconducting transition.

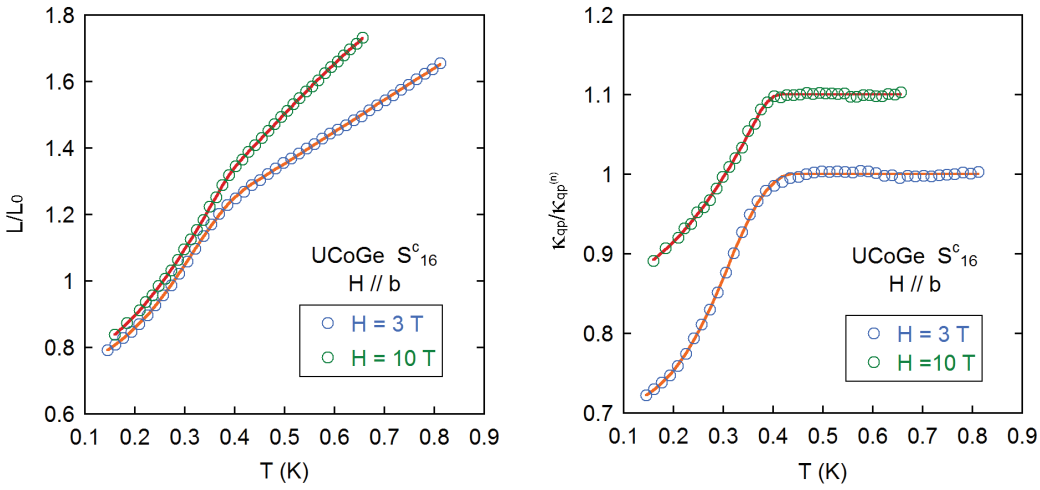

(a) **(b)**

Figure 3.7 | **(a)**: The Lorenz ratio L/L_0 as a function of temperature, obtained from the measurements at 3 T and 10 T for $\mathbf{H}//\mathbf{b}$. The solid lines present the corresponding fit $F_{other}(T) + F_{qp}(T)$ (explained in the text). **(b)**: The normalized quasiparticle contribution to thermal conductivity $\kappa_{qp}/\kappa_{qp}^{(n)}$ as a function of temperature, obtained from the measurements at 3 T and 10 T for $\mathbf{H}//\mathbf{b}$. The solid lines present the corresponding fit $F_{qp}(T)$.

- Finally for each field, the ratio in equation (3.2) as a function of the temperature is fitted as the sum of two functions: for the "other contributions", a polynomial of order 3 that extrapolates to zero at $T = 0$ is used : $F_{other}(T) = aT+bT^2+cT^3$; for the electronic part, we use a piecewise function $F_{qp}(T)$, which equals 1 for $T > T_{sc}$, and decreases linearly with T below T_{sc}. The superconducting transition temperature T_{sc} then comes as a non-linear parameter of the fit and its relative error can be directly obtained with the fit. In practice, in order to improve the fit quality, a few more parameters have been introduced to describe a (quadratic in T) smearing around T_{sc}, and for $T \to 0$.

As two examples to illustrate this method to find the superconducting transition from the thermal conductivity results, the figures 3.7a and 3.7b present respectively the Lorenz ratio L/L_0 and the normalized quasiparticle contribution to thermal conductivity $\kappa_{qp}/\kappa_{qp}^{(n)}$, as a function of temperature, obtained from the measurements at 3 T and 10 T for $\mathbf{H}//\mathbf{b}$. The solid lines present the corresponding fit for comparison.

The resistivity results are also fitted to obtain the transition temperatures. For this, a piecewise function is used, with $\rho = 0$ for $T < T_{\rho=0}$, and ρ increases linearly with T for $T_{\rho=0} < T < T_{onset}$ (inside the transition), and $\rho = \rho_0 + AT^2$ for $T > T_{onset}$ (in the normal phase). The non-linear parameters $T_{\rho=0}$ and T_{onset} give respectively the completeness and the onset of the resistivity superconducting transition. Like in the thermal conductivity

case, the smearing of the transition at temperatures around $T_{\rho=0}$ and T_{onset} are corrected.

For **H**//**b**, although the transition signal in κ/T becomes less significant at high field, the fit functions up to the highest field measured (15 T). For **H**//**a**, however, this determination of T_{sc} with thermal conductivity fails for $H > 5$ T, because the effect of the superconducting transition becomes too weak.

For the case of **H**//**c**, thermal conductivity and resistivity measurements had already been performed on sample S^c_{16} in the PhD studies of L. Howald and M. Taupin[50, 49] We confirm it with ac-susceptibility (χ') measurements on the same sample, presented in figure 3.8. (The χ' measurements were performed with a SQUID magnetometer by Carley Paulsen at Néel Institute in Grenoble.) The superconducting transition temperature at each field is determined by the intersection of linear interpolations of the χ' data both in the superconducting phase and in the normal phase.

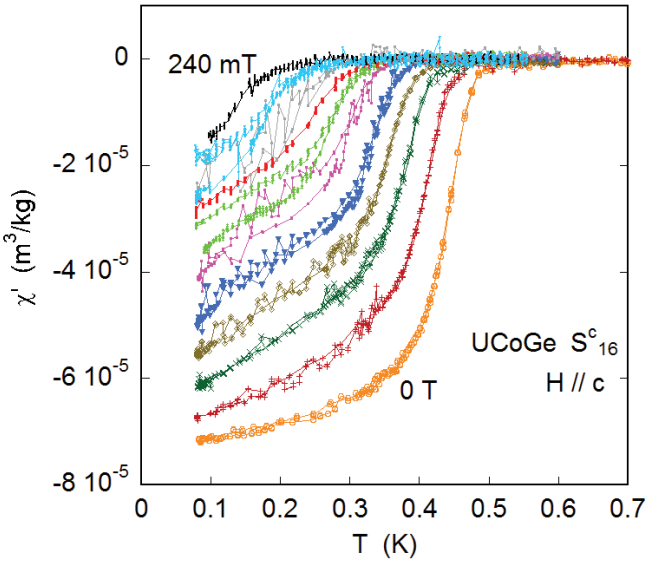

Figure 3.8 | The temperature dependence of ac-susceptibility (χ') in UCoGe, measured equally on the sample S^c_{16}, for different fields between 0 and 0.24 T along the **c**-axis.

To probe the H_{c2} along this **c**-axis, specific heat measurements have equally been performed, on a high quality UCoGe sample S^{ab}_{95} (square shaped sample in the (**a**,**b**) plane). The data are presented in figure 3.3 in the previous section.

The H_{c2} results of UCoGe obtained from all these measurements will be presented and discussed in next section.

3.2.2 Results: bulk upper critical field in UCoGe

Figure 3.9 displays the H_{c2} of UCoGe obtained from thermal conductivity and resistivity measurements on sample S^c_{16}, for magnetic field parallel to **c**-axis and **a**-axis. Figure 3.11 displays the H_{c2} for **H**//**b**. Figure 3.9a presents equally the H_{c2} probed with ac-susceptibility measurements, in good agreement with the thermal conductivity result.

For all three field directions, when the magnetic field is small, the resistivity transition ($T_{\rho=0}$) is about 0.1 K higher than the bulk determination. Most likely this comes from filamentary superconducting paths with higher critical temperature than the bulk of the sample. When magnetic field is increased, the large increase in the resistivity T_{sc} is quickly suppressed, and the bulk superconducting transition occurs when the resistivity transition is complete ($\rho = 0$).

For **H**//**a**, the bulk H_{c2} shows essentially a linear behavior up to 5 T, with a slight upward curvature. For **H**//**c**, the bulk H_{c2} also shows an upward curvature down to the lowest measured temperature (50 mK), and shows no sign of saturation even at $T = T_{sc}/10$.

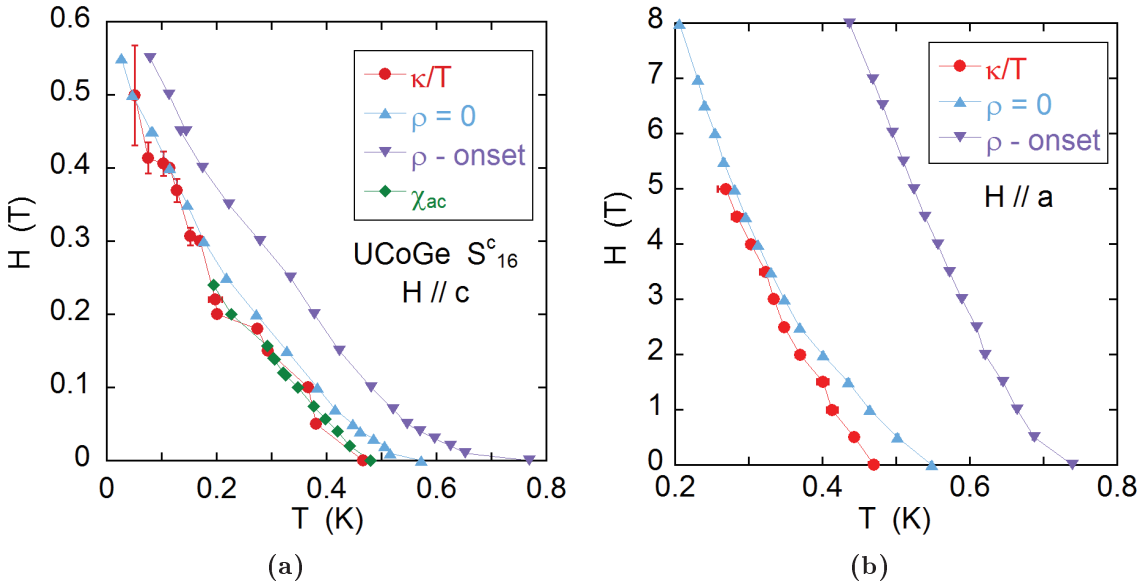

Figure 3.9 | H_{c2} of UCoGe for field along the **c**-axis **(a)**, and along the **c**-axis **(a)**, probed with thermal conductivity (red circles), resistivity (blue and purple triangles) and ac-susceptibility measurements (green diamonds) on sample S^c_{16}. The thermal conductivity measurements for **H**//**c** had been performed during the PhD studies of L. Howald[50] and M. Taupin[49].

Figure 3.10 presents the bulk H_{c2} of UCoGe for **H**//**c** probed both with thermal conductivity and specific heat on several samples of diverse crystal quality. κ/T measurements have been performed on sample S^c_{16} and S^c_{47} in the PhD studies of L. Howald[50] and M. Taupin[49]. C_p/T is measured on sample S^{ab}_{95} in this study, and the raw data are presented in figure 3.3. The upward curvature of H_{c2} down to the lowest measured temperature is observed in all three samples. Such an upward curvature down to (at least) T_{sc} /10 is at odds with the classical behavior of H_{c2} when it is controlled by the orbital limit, and it will be discussed in detail in the next section.

The comparison between the three samples shows that $H_{c2}(0)$ for **H**//**c** in UCoGe presents a large dispersion: it can be different by a factor 2 from one sample to another. However, despite the difference in the determination of T_{sc} with different experimental probes, the bulk T_{sc} is always found to be around 0.5 K, and shows much smaller sample dispersion. Note that for a usual superconductor with orbital limitation, $H_{c2}(0)$ should scale like $H_{c2}(0) \propto T_{sc}^2$. This shows again that the H_{c2} in UCoGe is anomalous.

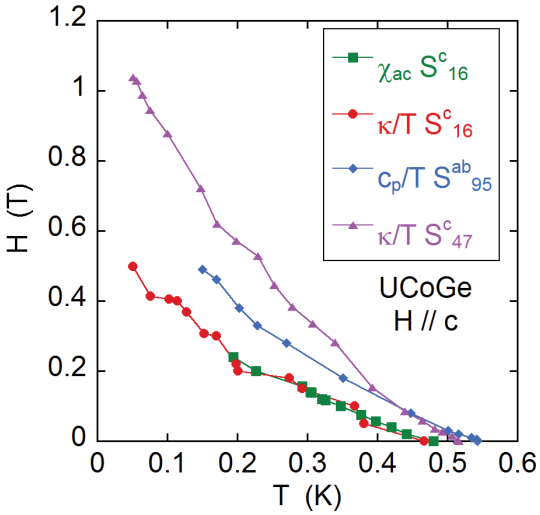

Figure 3.10 | Bulk H_{c2} along the **c**-axis in UCoGe measured on different samples and with different experimental methods. The different curves corresponds to H_{c2} probed with thermal conductivity (and confirmed by ac-susceptibility results) on sample S^{c}_{16}, with specific heat on sample S^{ab}_{95} and with thermal conductivity on sample S^{c}_{47}. The thermal conductivity measurements had been performed in Ref.[50, 49].

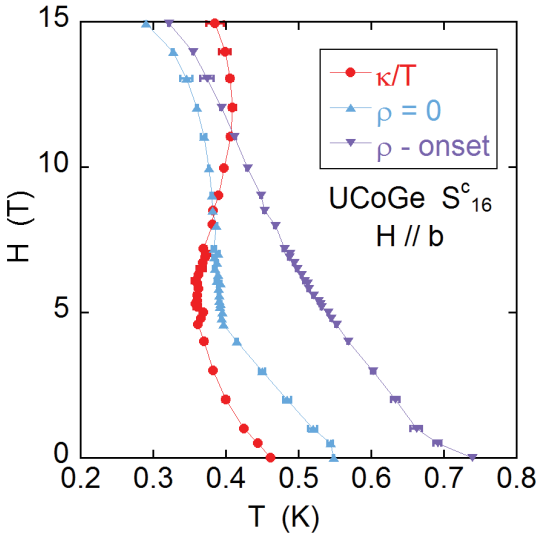

Figure 3.11 | H_{c2} for field parallel to **b**-axis, probed with thermal conductivity (red circles) and resistivity measurements (blue and purple triangles), measured on the sample S^{c}_{16}.

For **H**//**b** (figure 3.11), the S-shape H_{c2} observed in resistivity measurements is confirmed by the bulk measurement, and it appears even in a more robust way. Surprisingly, unlike the case of **H**//**a** and **H**//**c**, the bulk (thermal conductivity) transition temperature becomes larger than the resistive transition ($\rho = 0$) for fields above 8 T, and becomes even higher than the onset of the resistivity transition for fields above 12 T. This crossing of the bulk H_{c2} with the resistivity determination is another unusual phenomenon, as a bulk superconducting sample is expected to have many percolating superconducting

paths and so a higher H_{c2} measured by resistivity. This peculiar situation requires more investigations, and will be discussed separately in Chapter 6.

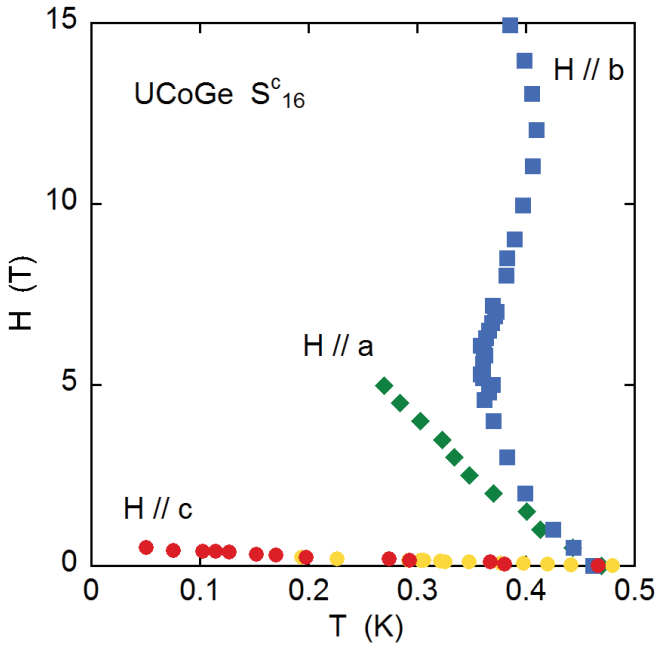

Figure 3.12 | H_{c2} of UCoGe with thermal conductivity measurements performed on sample S^c_{16} for magnetic field all its three axes (green diamonds for **H**//**a**, blue squares for **H**//**b** and red circles for **H**//**c**). The yellow circles correspond to the H_{c2} for **H**//**c** obtained from ac-susceptibility measurements on the same sample. The data are the same as in (figure 3.9 and 3.11).

Figure 3.12 summarizes the H_{c2} of UCoGe probed with thermal conductivity along the three axes **a**, **b** and **c**, measured on the same sample S^c_{16}. Our results confirm all the features observed in the H_{c2} measured with resistivity in Ref.[30] (figure 1.6a), including the S-shape H_{c2} for **H**//**b**, the large anisotropy between the easy magnetization direction (**H**//**c**) and the transverse field directions (**H**//**a** and **b**), and the unusual upward curvatures in H_{c2} in all three field directions. It also unveils new phenomenon at high fields for **H**//**b**.

3.3 Discussions on the H_{c2} of UCoGe

This section will discuss about some of the particular features in H_{c2} of UCoGe, presented in figure 3.12. We will begin with a brief introduction of the main effects that control the H_{c2} of a classical superconductor.

3.3.1 Basic mechanisms controlling H_{c2}

The orbital limitation

A type II superconductor is characterized by the penetration of the magnetic field into the sample in form of vortices. Each of the vortices contains a quantized magnetic flux ϕ_0 created by supercurrents circulating around, and a "non superconducting" core

which has a diameter of order $\xi_(T)$, the superconducting coherence length. Outside the core of an isolated vortex, the magnetic field (and the superconducting current) decays exponentially on a length scale corresponding to the London penetration length λ_L, and the sample remains superconducting. The orbital limitation can be seen as the magnetic field for which the vortex cores fill the whole sample space, thus:

$$H_{c2}^{orb} \; . \; 2\pi\xi(T)^2 = \phi_0 \tag{3.3}$$

This formula can be deduced from the Ginzburg-Landau theory (Ref.[51], from page 171). In the presence of a magnetic field, the density of the Ginzburg-Landau free energy for the superconductivity can be written as:

$$F = F_n + \alpha(T - T_{sc})|\psi|^2 + \frac{\beta}{2}|\psi|^4 + \frac{1}{2m}|(-i\hbar\nabla - \frac{2e}{c}\mathbf{A})\psi|^2 + \frac{B^2}{2\mu_0} \tag{3.4}$$

where ψ is the superconducting order parameter, F_n is the part of free energy independent of the superconducting transition, and α, β are positive coefficients. To obtain the equilibrium state, we minimize the free energy $\mathcal{F} = \int F d\mathbf{r}$ with respect to small variations of $\delta\psi(\mathbf{r})$ and $\delta\mathbf{A}(\mathbf{r})$, which gives the Ginzburg-Landau equations:

$$\begin{cases} \alpha\psi + \beta|\psi|^2\psi + \dfrac{1}{2m}\left(-i\hbar\nabla - \dfrac{2e}{c}\mathbf{A}\right)^2\psi = 0 \\ \mathbf{j} = \dfrac{e\hbar}{im}(\psi^*\nabla\psi - \psi\nabla\psi^*) - \dfrac{4e^2}{mc}\psi^*\psi\mathbf{A} \end{cases} \tag{3.5}$$

Close to H_{c2} the amplitude of the superconducting order parameter $|\psi|$ is small, and we can keep only the first order terms in ψ. The GL equations can then be linearized to give:

$$\frac{1}{2m}\left(-i\hbar\nabla - \frac{2e}{c}\mathbf{A}\right)^2\psi = -\alpha\psi \tag{3.6}$$

and $\nabla \times \mathbf{A}$ equals the external field $\mu_0\mathbf{H}$ throughout the sample because the supercurrent $\mathbf{j}$ is negligible (it is expressed only with terms of order $|\psi|^2$, equation (3.5)). The equation (3.6) is formally identical to the Schrödinger equation for a particle of charge $2e$ and mass m in a uniform magnetic field. As a solution, it has constant velocity v_z along the magnetic field, and has quantized circular movements in the plane perpendicular to the field, with frequency $\omega_c = \frac{2eH}{m}$. $-\alpha$ being an eigenvalue of equation (3.6), we have:

$$-\alpha = \frac{1}{2}mv_z^2 + \hbar\omega_c(n + \frac{1}{2}) \tag{3.7}$$

The maximum of H, which corresponds to H_{c2}, is given by the level $v_z = 0$ and $n = 0$, thus gives $-\alpha = e\hbar H/m$. As $\xi(T)$ is defined in the GL theory as $\xi^2(T) = \hbar^2/2m|\alpha|$, this leads to $H_{c2}(T) = \phi_0/2\pi\xi(T)^2$.

The temperature dependence of $\xi(T)$ for T close to T_{sc} can also be deduced from the GL theory (with the relation to ξ_0 determined by the microscopic BCS theory):

$$\begin{cases} \xi(T) = 0.74\ \xi_0\ \left(1 - \dfrac{T}{T_{sc}}\right)^{-1/2} \\ \xi_0 = 0.18\ \dfrac{\hbar v_F}{k_B T_{sc}} \end{cases} \tag{3.8}$$

Inserting equation (3.8) into (3.3) we have, for T close to T_{sc},

$$H_{c2}^{orb} = \alpha_0 \frac{T_{sc}(T_{sc} - T)}{< v_f >^2} \tag{3.9}$$

where $< v_f >$ corresponds to the averaged Fermi velocity in the plane perpendicular to the field direction, and α_0 is a numerical factor that equals :

$$\alpha_0 = \frac{\phi_0 k_B^2}{2\pi\hbar^2 \ (0.18 * 0.74)^2} = 3.2.10^8 \text{ T K}^{-2} \text{ m}^2 \text{ s}^{-2} \tag{3.10}$$

Deriving the equation (3.9) allows to extract the averaged Fermi velocities $< v_f >$ from the experimentally accessible initial slope of upper critical field ($dH_{c2}/dT|_{H=0}$).

$$\left.\frac{dH_{c2}^{orb}}{dT}\right|_{T_{sc}} = -\alpha_0 \frac{T_{sc}}{< v_f >^2} \propto T_{sc}.m^{*2} \tag{3.11}$$

Paramagnetic limitation

For a spin-singlet superconductor, or a spin-triplet state with an $S_z = 0$ component, the upper critical field can further be limited by the paramagnetic limitation (named also the Pauli limitation H_p), due to the tendency for the electron spins to align parallel to the field direction which breaks the spin-opposite pairing state. The Pauli limitation comes into play when the Zeeman splitting between the spin-up and down electrons becomes comparable with the superconducting gap. At $T = 0$ it is given by:

$$H_p(0) = \frac{\sqrt{2}\Delta(0)}{g\mu_B} = 1.85 \ T_{sc} \tag{3.12}$$

with H_p in Tesla and T_{sc} in Kelvin. In equation (3.12) we have used the BCS relation for the superconducting gap $\Delta(0) = 1.76 \ k_B T_{sc}$ and the gyromagnetic factor g is taken to be 2 (free electron value).

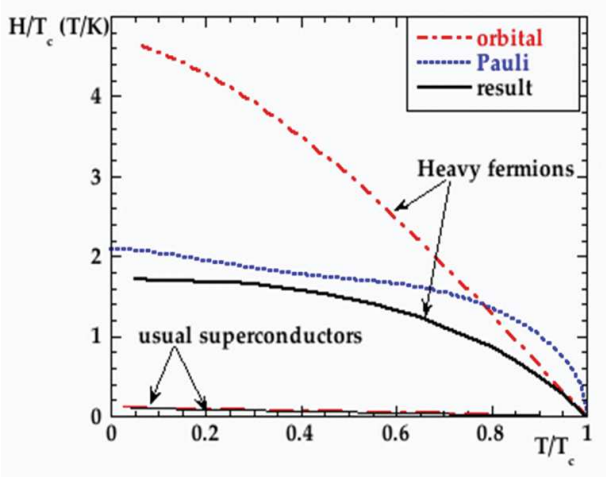

Figure 3.13 | Typical behavior of H_{c2} with orbital limitation and Pauli limitation in classical superconductors (simple metals) and heavy fermion superconductors.

Figure 3.13 shows the consequence of the two above-mentioned effects on the H_{c2} of classical superconductors (simple metals) and of heavy fermion systems. The Pauli limitation, being independent of the density of states or of the Fermi velocity of the system, appears in a universal way, controlled only by the critical temperature T_{sc}. On the other hand, drastic difference can be present in the orbital limitation between different superconducting systems. In the case of simple metals (those which are type II superconductors), the electrons have an effective mass m^* close to a free electron mass (m_e) and their Fermi velocity is large (of the order of 10^6 m/s). The orbital limitation is small and usually dominates other effects in H_{c2}. However, in heavy fermion systems, the quasiparticle effective mass can reach 100 to 1000 times m_e, and the Fermi velocity in these systems can be as low as of the order of a few 10^3 m/s. The orbital limitation in such cases has a much higher value, and if the superconducting order parameter is further a spin-singlet state, the Pauli limitation can play an important role on H_{c2}.

It also needs to be mentioned that, for T close to T_{sc}, as the superconducting gap depends on temperature as (BCS theory):

$$\Delta(T) \sim 3.2 k_B T_{sc} \left(1 - \frac{T}{T_{sc}}\right)^{\frac{1}{2}} \tag{3.13}$$

The Pauli limitation $H_p(T) \propto \Delta(T)$ will increase vertically at $T = T_{sc}$. Thus in the proximity of T_{sc}, H_{c2} is always governed by the orbital limitation, even in heavy fermion systems where Pauli limitation can be dominant at low temperature.

3.3.2 Discussion on the H_{c2} in UCoGe

We now turn to the case of UCoGe, to show how particular is the H_{c2} in this system in terms of classical theories of superconductivity.

Absence of Pauli limitation

	UGe_2 (1.2 GPa)	URhGe	UCoGe
M_0		0.4 μ_B	~ 0.05 μ_B
B_{int}		0.08 T	~ 0.01 T
T_{sc}	0.8 K	0.25 K	0.5 K
$H_p(0)$ for g=2	~ 1.6 T	~ 0.5 T	~ 1 T
$H_{c2}(0)//\mathbf{a}$	~ 2 T	2 T	> 20 T
$H_{c2}(0)//\mathbf{b}$	~ 3.5 T	1.3 T	> 20 T
$H_{c2}(0)//\mathbf{c}$	7 T	0.6 T	$0.5 - 1$ T
T_{Curie}	35 K	9.5 K	2.5 K
B_{exch}	~ 50 T	~ 14 T	~ 3.5 T

Table 3.1

The first point to consider in the case of a ferromagnetic superconductor is the influence from the spontaneous magnetic moment. Without demagnetizing effects, this corresponds to an internal magnetic (dipolar) field $\mathbf{B}_{int} \sim \mu_0 \mathbf{M}$. The values of the spontaneous moment $\mathbf{M}$ and the corresponding $\mathbf{B}_{int}$ for URhGe and UCoGe[15] are listed in the table

3.1. In both systems $\mathbf{B}_{int}$ is much smaller than the experimentally observed H_{c2}. In URhGe, the presence of the internal magnetic field can be observed as a vertical segment near $H = 0$ in the H_{c2} along the **c**-axis (spontaneous magnetization axis)[38]. In UCoGe, $\mathbf{B}_{int}$ corresponds to a field around 10 mT and is barely noticeable experimentally (except for the ac magnetic susceptibility and dc magnetization measurements in Ref.[52, 13], which suggest that no Meissner state exists in UCoGe, and a self-induced vortex state is probably realized).

However, the coexistence of superconductivity and ferromagnetism also leads to a splitting of the spin up and down electrons due to the ferromagnetic interactions, which can be attributed to an effective exchange field B_{exch}. It should be at least of order $B_{exch} \simeq (k_B T_{Curie})/\mu_B$[53]. For a spin-singlet superconductor, or a triplet state with a $S_z = 0$ component, this exchange field B_{exch} will influence H_{c2} through Pauli limitation.

Table 3.1 summarizes the Pauli limitation (H_p) for the three ferromagnetic superconductors UGe_2, URhGe and UCoGe (estimated with the value of T_{sc} according to equation 3.12), the (minimum) exchange field B_{exch} estimated with $B_{exch} \simeq (k_B T_{Curie})/\mu_B$, and the experimental upper critical field along the three field directions. It shows that both the measured upper critical fields and B_{exch} are by far higher than the estimated H_p in these systems. As a consequence, the influence from the Pauli limitation is absent, and a spin-singlet pairing state is practically ruled out. Instead a (triplet) p-wave superconducting state with "equal spin pairing" ($|\uparrow\uparrow>$, $|\downarrow\downarrow>$) configuration most likely takes place.

Jaccarino-Peter effect

It needs to be mentioned that, an absence of Pauli limitation, deduced from a much higher H_{c2} compared with H_p, does not necessarily implies a spin-triplet superconducting state. An exotic example for this is the Jaccarino-Peter effect[54] observed in some strong paramagnet-superconductors. Figure 3.14 presents an example of this effect in the pseudoternary series $Eu_xSn_{1-x}Mo_6S_8$[55]. In this case, the orbital limitation is very high (more than 25 T at $T = 0$, represented by the red broken line). But superconductivity is strongly suppressed by the Pauli limitation, due to the large exchange field associated with Eu ions, leading to a $H_{c2}(0)$ around only 1 T. With increasing magnetic field, the exchange field controlled by the polarization of the Eu ions can be balanced by the external field. The resulting suppression of the Pauli limitation then leads to the re-establishment of superconductivity in the high-field-low-temperature region.

In UCoGe and URhGe, although there has been yet no experimental sign for it, the possibility of a compensation of B_{exch} by the external field has been mentioned. For example such an effect has been proposed for URhGe when the magnetic field is applied along the **b**-axis, to explain the re-entrance superconductivity, based on a dual model in which ferromagnetism is due to the localized 5f electrons, and superconductivity is due to the itinerant 5f electrons, which would couple antiferromagnetically to the localized moment[56]. However, even if such a scenario indeed happens, the situation is different from the original Jaccarino-Peter effect. It has been argued[38] that in the low field superconducting phase of URhGe, the Pauli limitation is absent and H_{c2} is only due to the orbital limitation (and an equal-spin-pairing superconducting state is realized). At the re-entrant field H_R along the **b**-axis, if the B_{exch} is compensated by the external magnetic field, it will be possible that superconductivity re-appears with a $S_z = 0$ component, contrasting with the low field superconducting phase. Nonetheless, this compensation of B_{exch} and the resulting suppression of the Pauli limitation, is not sufficient to explain the

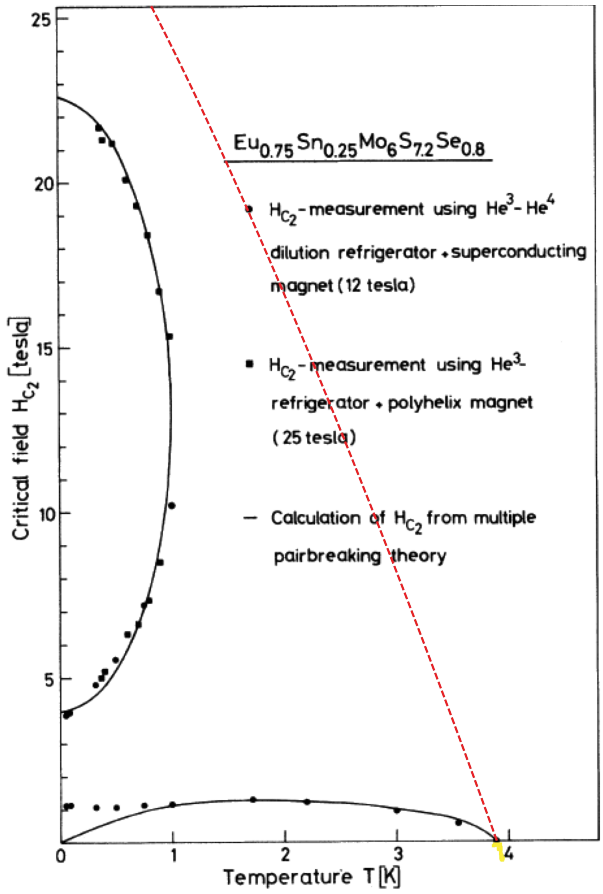

Figure 3.14 | Magnetic field induced superconductivity in the strong paramagnet $Eu_xSn_{1-x}Mo_6S_8$ series[55], which is explained by the Jaccarino-Peter effect. The red line describes the orbital limitation in this system, corresponding to the initial slope given by the calculations in the reference: -9 T/K.

re-entrant superconducting phase: the orbital limitation, which suppresses superconductivity in the low field phase, also needs to be strongly enhanced at fields near H_R.

Anisotropy and angular dependence

The initial slope of H_{c2} in UCoGe along the three field directions can be estimated with a good accuracy from our thermal conductivity measurements, contrary to the resistivity measurements (due to filamentary superconductivity at low fields). $dH_{c2}/dT|_{H=0}$ is found to be about -1 T/K along the **c**-axis, more than 20 times smaller than along **a** and **b**-axes (around -20 T/K for both of them). If H_{c2} were governed uniquely by the orbital limitation, according to equation (3.11) $dH_{c2}/dT|_{H=0}$ would be inversely proportional to the square of the Fermi velocity averaged in the plane perpendicular to the field direction, which can be approximately taken as:

$$\begin{cases} \left(dH_{c2}^{orb}/dT\right)_{H=0}^{a} & \propto & \dfrac{1}{< v_F^b >< v_F^c >} \\ \left(dH_{c2}^{orb}/dT\right)_{H=0}^{b} & \propto & \dfrac{1}{< v_F^a >< v_F^c >} \\ \left(dH_{c2}^{orb}/dT\right)_{H=0}^{c} & \propto & \dfrac{1}{< v_F^a >< v_F^b >} \end{cases} \tag{3.14}$$

where $\left(dH_{c2}^{orb}/dT\right)_{H=0}^{i}$ is the initial slope of H_{c2} for field along the **i**-axis and $< v_F^j >$ is the averaged Fermi velocity along the **j**-axis. Thus the 20 fold anisotropy between the $dH_{c2}/dT|_{H=0}$ along the **c**-axis and along **a**, **b**-axes would mean that $< v_F^a >$ and $< v_F^b >$ are similar in magnitude, but $< v_F^c >$ is 20 times smaller than in the other two directions. This happens typically for a 2D system, where the in-plane Fermi velocity is much larger than that in the perpendicular direction. However, in UCoGe transport studies show a barely noticeable anisotropy in the normal phase. For example, according to the resistivity measurements in Ref.[57], performed on a cubic-shaped sample with current injected along the three crystal axes, the difference in the quadratic coefficient A ($\rho = \rho_0 + AT^2$) between different current directions is found to be no more than a factor of 1.5. The practically isotropic Fermi velocity in UCoGe is thus not compatible with the large anisotropy in H_{c2}, in terms of orbital limitation.

Apart from the averaged Fermi velocities $< v_F^j >$, anisotropy in the orbital limitation can also come from an anisotropic superconducting order parameter. For a superconducting state that presents nodal structure in the superconducting gap, H_{c2}^{orb} will be enhanced when the magnetic field is applied perpendicular to the gap nodes. For example, for a (p-wave) superconducting order parameter with a polar gap structure presented in figure 3.15a, the H_{c2}^{orb} will be higher when the magnetic field is applied along the antinodal direction (**H** along the **z**-axis) than when the field is in the nodal plane (**H** in the (**x**, **y**) plane). Scharnberg and Klemm[58] calculated the H_{c2}^{orb} associated with several p-wave superconducting order parameters (from an isotropic system in the normal phase) whose gap structure has either the planar nodal form (figure 3.15a) or the point nodal form (figure 3.15b). The anisotropy in H_{c2}^{orb} associated with these gap structures is not more than a factor 2, which is far from enough to explain the H_{c2} anisotropy in UCoGe.

The anisotropy of H_{c2} in UCoGe is even more surprising if we look at its angular dependence. Figure 3.17a presents the angular dependence of H_{c2} with field direction turned from the **a**-axis to the **c**-axis and from the **b**-axis to the **a**-axis[30]. Both of them show that turning magnetic field a few degrees away from the **a** or **b**-axis, is enough to change completely the behavior of the whole curve. Figure 3.17b presents the angular dependence of H_{c2} at $T = 0.1$ K from the **a** or **b**-axis to the **c**-axis[35]. It shows that H_{c2} is extremely sensitive to field component along the **c**-axis and presents very sharp angular dependence around the two transverse field directions. Such a behavior does not seem to fit any simple trigonometric relationship.

Figure 3.16 shows the angular dependence of H_{c2} calculated with a CBS p-wave order parameter[59], which presents the gap structure in figure 3.15a. Comparison between these calculations and the case of UCoGe shows that the angular dependence of H_{c2} in UCoGe cannot be fitted easily with that of a p-wave superconducting order parameter.

As a conclusion, the huge anisotropy in H_{c2} in UCoGe, along with its sharp angular dependence, cannot be explained by the Fermi velocity variation along different crystal axes, and the anisotropic orbital limitation for a p-wave superconducting order parameter.

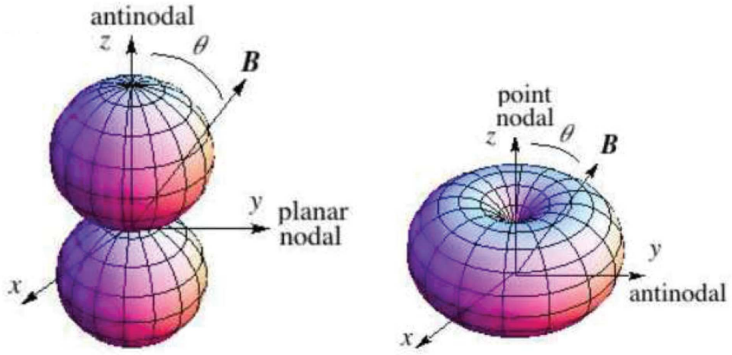

Figure 3.15 | **(a)**: p-wave superconducting gap with a line node. Realized for example for a CBS state: $\Delta_0 \hat{k}_z$. **(b)**: p-wave superconducting gap with a point node. Realized for example for a ABM state: $\Delta_{0\pm}(\hat{k}_x \pm i\hat{k}_y)$. Figure taken from Ref.[59]

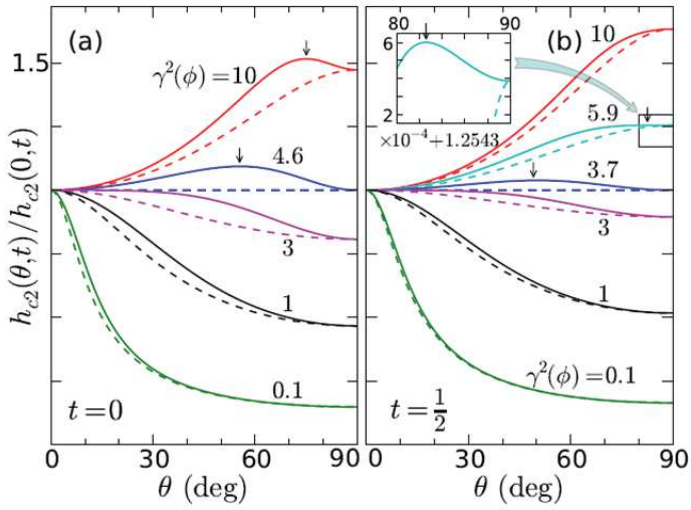

Figure 3.16 | Angular dependence of H_{c2} calculated with an p-wave CBS order parameter[59], based on Scharnberg-Klemm theory[58]. **(a)**: At zero temperature ($t = 0$). **(b)**: At $T = T_{sc}/2$ ($t = 1/2$). The curves for different values of $\gamma^2(\phi)$ correspond to superconductivity associated with different forms of (ellipsoidal) Fermi surface, with $\gamma^2(\phi) = 1$ (black curve) corresponding to a spherical case.

Thus the classical orbital limitation is not sufficient to account for these behaviors in UCoGe.

Anomalous upward curvatures

We then discuss the unusual curvatures presented in the H_{c2} of UCoGe for three field directions.

The remarkable S-shape curvature of H_{c2} for $\mathbf{H}//\mathbf{b}$ reminds us of the field-induced reentrant superconducting phase observed in URhGe, for the same field direction. It gives an indication that the formation of superconductivity is strengthened under magnetic field in this field direction. We will discuss this case in more detail in Chapter 6.

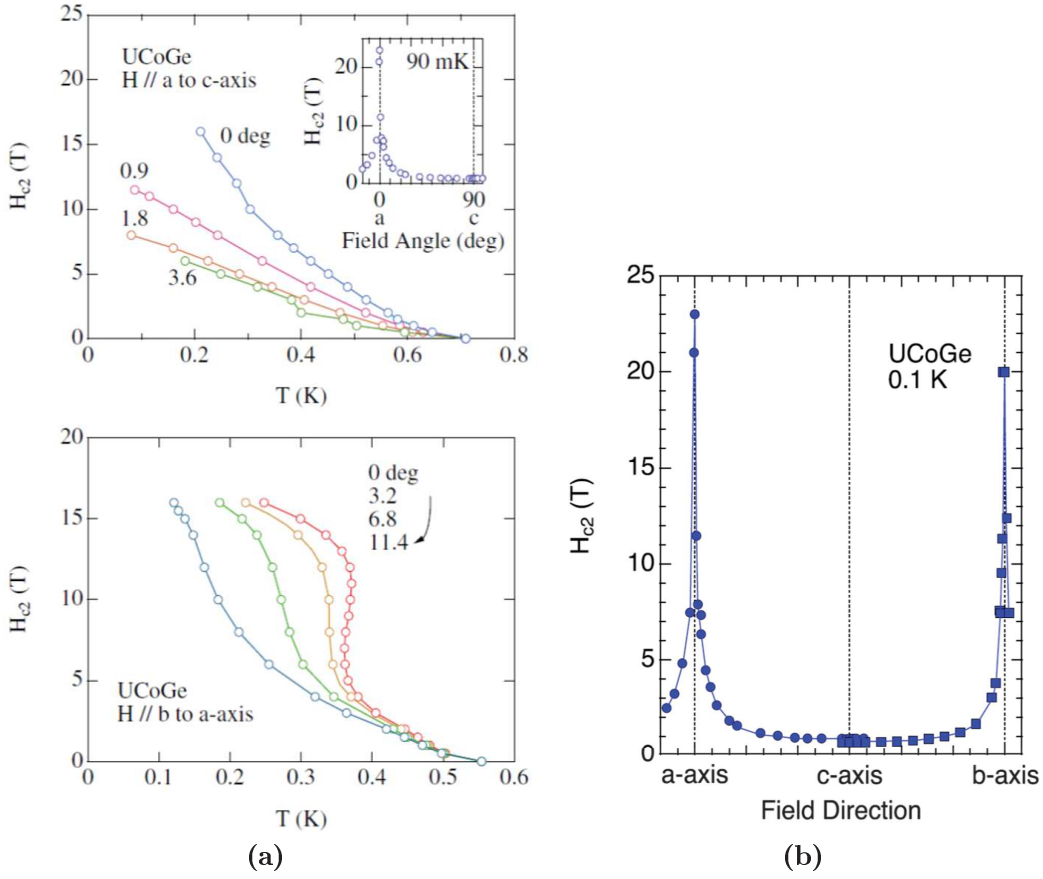

Figure 3.17 | Angular dependence of H_{c2} of UCoGe measured with resistivity[30, 35].

What is equally remarkable, is the upward curvature observed in H_{c2} for $\mathbf{H}//\mathbf{c}$ and for $\mathbf{H}//\mathbf{a}$. For $\mathbf{H}//\mathbf{c}$ it persists down to the lowest measured temperatures (50 mK by κ/T and 10 mK by resistivity, in the PhD thesis of M.Taupin[49]). For $\mathbf{H}//\mathbf{a}$, according to the resistive H_{c2} in figure 1.6 it continues up to 16 T[30]. In both cases, there is no observable sign of inversion of this curvature. This again is completely unusual in terms of classical theory of superconductivity. Figure 3.18 shows the H_{c2} in the weak-coupling WHH theory[36, 37], which presents a downward curvature in the whole temperature range. In more complicated cases, when an anisotropic superconducting order parameter is considered[58], or when (moderate) strong coupling effects are taken into consideration[60], H_{c2} may present some deviations from the WHH behavior, but in general continues to present a downward curvature.

In many superconducting systems, especially in high-Tc superconductors, resistivity or ac-susceptibility measurements indicate a transition line that present an upward curvature in the whole temperature range. However, in these systems there is a strong influence from the vortex motions, which leads to finite dissipation inside the superconducting phase. As is explained in section 3.1, these transition lines do not correspond to the real superconducting transition H_{c2}, but to an irreversibility line H_{irr}, above which the vortices are depinned and are in motion. When the H_{c2} is probed with more robust and bulk sensible experimental methods, a classical downward curvature is usually found[46, 47, 48]. Our bulk measurements of H_{c2} have proved that the situation is different in UCoGe, and the anomalous curvatures of H_{c2} in this system is a robust property of the superconducting

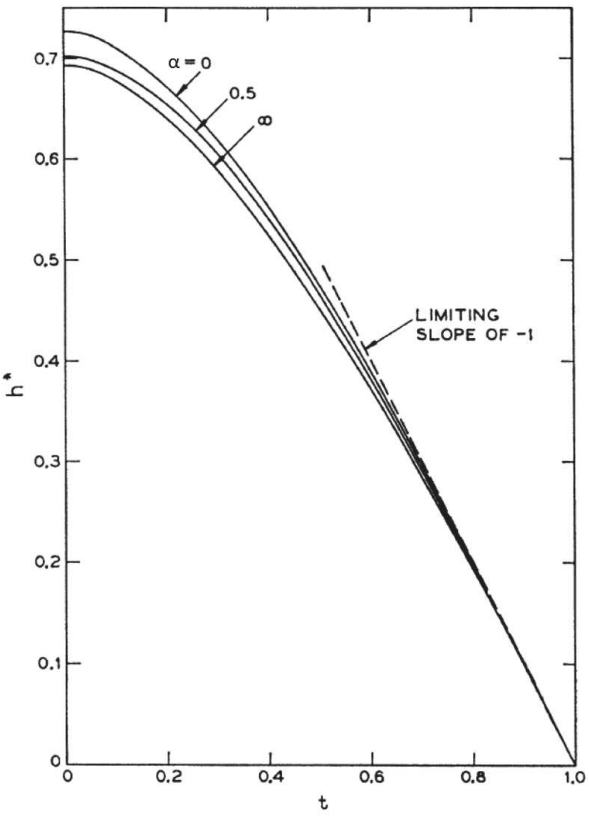

Figure 3.18 | Classical behavior of the upper critical field (with orbital limitation) according to the WHH theory[36]. The parameter α characterizes the purity ($\alpha = 0$ is the clean limit, $\alpha = \infty$ is the dirty limit).

transition.

However, there are other cases where the bulk H_{c2} can present unusual upward curvatures. Here we discuss some of the main possibilities for such a phenomenon:

Strong coupling effects. Increasing the superconducting coupling strength will lead to deviations of H_{c2} from the classical WHH behavior. Figure 3.19 presents the influence of such an effect on H_{c2}, calculated with a strong coupling model with an Einstein phonon spectrum[60]. The pairing strength is characterized by a coupling constant λ. Up to λ value of order 1, the calculated H_{c2} remains close to the WHH behavior (which corresponds to $\lambda << 1$). Significant deviation occurs when λ is further increased, with the appearance of an upward curvature. This effect is for example used in Ref.[61] to explain the special form of H_{c2} in UBe_{13} (the authors estimate a $\lambda \sim 14.5$ in that system). However, in all the cases in figure 3.19, when the temperature is low enough ($T < 0.2\ T_{sc}$), the classical downward curvature is recovered, which is contrary to what is observed in UCoGe for **H**//**c**. What is more, for the H_{c2} curvature to be significantly modified by the strong coupling effects, a λ as large as 5 is needed, but in UCoGe the modest specific heat jump at the superconducting transition at zero field ($\Delta C/C \sim 0.6$, in contrast to the case of UBe_{13}, where $\Delta C/C = 2.5$) indicates that it is unlikely to be the case.

Multiband superconductivity can also lead to upward curvature in H_{c2}. This is observed for example in MgB_2[63]. Figure 3.20 shows another example, the transition metal borocarbide YNi_2B_2C[62], whose H_{c2} is explained with the calculation based on

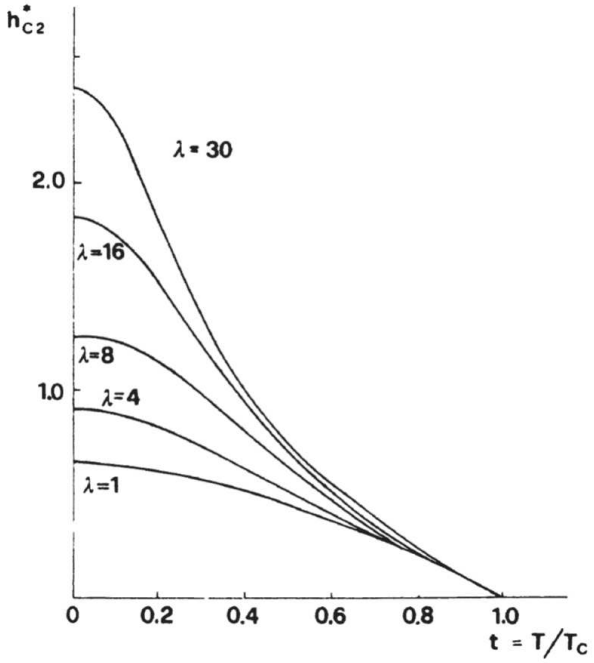

Figure 3.19 | Influence from the strong coupling effect on the form of H_{c2}, calculated with an Einstein phonon spectrum[60].

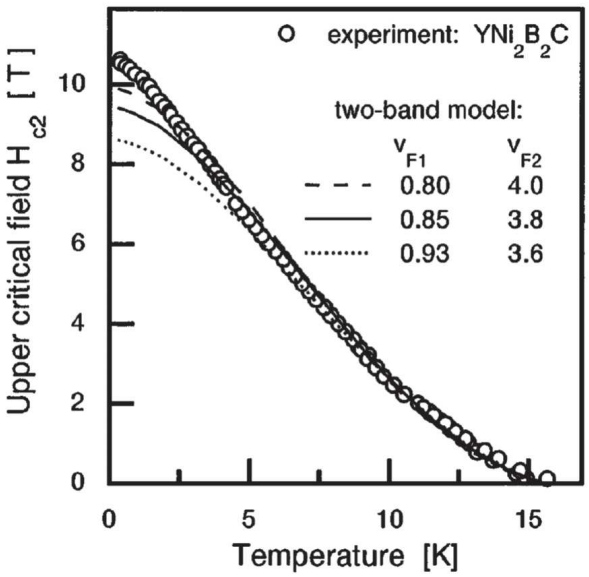

Figure 3.20 | Experimental upper critical field in the transition metal borocarbide for **H**//**c** in YNi_2B_2C (circles), fitted with a two-band model (broken and solid lines)[62] . The legend gives the Fermi velocities used in the two band model are given in unit of 10^7 cm/s.

a two-band model. In UCoGe, sign of multiband superconductivity has indeed been observed in low temperature thermal conductivity measurements[28]. However, as seen in figure 3.20, the multiband superconductivity typically leads to a small upward curvature in some intermediate temperature range, which can unlikely explain the strong upward

curvature in the H_{c2} for $\mathbf{H}//\mathbf{a}$ in UCoGe. Moreover, as in the strong coupling case, such an effect will not produce an upward curvature down to the lowest temperature, contrary to what is observed in UCoGe.

Conclusion

We have shown that many features in the H_{c2} of UCoGe, confirmed by bulk measurements, are in strong disagreement with expectations from the classical theories for H_{c2}. Curiously, none of these features are observed in the sister compound URhGe.

In the next two chapters, we will see how, including a completely new phenomenon in these compounds, it is possible to explain in a consistent way the above features in the H_{c2} of UCoGe, and the difference between UCoGe and URhGe.

Chapter 4

Field-dependent pairing strength

4.1 Pairing mechanism in ferromagnetic superconductors and magnetic fluctuations

In conventional superconductors the attractive interaction responsible for the Cooper pairs is mediated by the exchange of phonons. Identification of this pairing mechanism was first done by the isotope effect in the mercury metal[64], where the superconducting critical temperature (T_{sc}) varies with the isotopic mass of the element. This demonstrated that superconductivity involves the lattice. An even more precise proof for the phonon-mediated pairing mechanism came from the analysis of the tunneling spectra[65], which would be successfully explained with the knowledge of the phonon spectrum, by the strong-coupling Eliashberg theory (see Parks, Chapter 11[66]).

In unconventional superconductors, there are numerous qualitative indications suggesting that the pairing mechanism may come from a magnetic or other electronic origin. In most cases in these systems, no clear signature for the pairing mechanism has been observed in the tunneling spectra (when they could be obtained), and the main method to address the question of the pairing mechanism, is to associate the appearance of a superconducting phase with an electronic instability, by tuning the system with pressure, doping or magnetic field.

In a magnetic medium, an attractive pairing interaction between the electrons can be mediated by the magnetic background (DeGennes, page 104[51]). Consider two electrons (quasiparticles) in the presence of a magnetic background. An electron i, situated at $\vec{r}$ with a spin $\vec{S}_i$, interacts with the local magnetization $\vec{M}(\vec{r})$ according to:

$$H_i = -\tau \vec{S}_i . \vec{M}(\vec{r}) \tag{4.1}$$

where τ is a constant measuring the coupling strength. For low frequency interactions, this leads to a perturbation of the magnetic medium expressed via the static susceptibility tensor as:

$$\delta M_\alpha(\vec{r'}) = \sum_\beta \chi_{\alpha\beta}(\vec{r} - \vec{r'}) \tau S_{i\beta} \tag{4.2}$$

For a second electron j situated at $\vec{r'}$ with a spin $\vec{S}_j$, its interaction V with δM is :

$$V(\vec{r} - \vec{r'}) = -\tau \vec{S}_j . \delta\vec{M}(\vec{r'}) = -\tau^2 \sum_{\alpha\beta} S_{j\alpha} \chi_{\alpha\beta}(\vec{r} - \vec{r'}) S_{i\beta} \tag{4.3}$$

And with a Fourier transformation, this leads to :

$$V(\vec{q}) = -\tau^2 \sum_{\alpha\beta} S_{j\alpha}\chi_{\alpha\beta}(\vec{q})S_{i\beta} \tag{4.4}$$

When diagonalized, the three principal values of the susceptibility tensor are in principal all positive. If the spin S_i and S_j are parallel, the resulting interaction V in equation (4.4) will be negative. For the other spin configuration (S_i and S_j are antiparallel), $V(\vec{q})$ is positive, thus the formation of a paired state (with an attractive interaction) requires that the superconducting wave function changes sign on the Fermi surface[67].

Magnetically mediated pairing was first proposed to explain the p-wave superfluidity in ^{3}He[68]. In many heavy fermion or other strongly correlated electron systems, superconductivity is found to emerge around an antiferromagnetic quantum critical point[69, 19, 17], which suggests that the pairing mechanism is associated with the critical magnetic fluctuations. The situation is similar in the ferromagnetic superconductors UGe_2, URhGe and UCoGe [5, 22, 24], where superconductivity is observed near a ferromagnetic instability. They are considered as examples for the theoretically predicted p-wave superconductivity in a weak itinerant ferromagnet[70]. The belief that superconductivity in these systems has ferromagnetic origin is further strengthened by the phenomenon of re-entrant superconductivity observed in all three systems (figure 1.5 in the introduction). Such phenomena, different from the Jaccarino-Peter effect as discussed in Chapter 3.3.2, are considered in many studies[39, 56, 33, 34, 71] to be related to the enhanced magnetic fluctuations around a field-induced ferromagnetic instability.

An important experimental characterization of the magnetic fluctuations in UCoGe comes from the nuclear magnetic resonance (NMR) studies[72, 57]. In NMR measurements in Ref.[57], the nuclear spin-lattice relaxation rate $1/T_1$, which detects low energy dynamic spin fluctuations perpendicular to the magnetic field, has revealed the presence of Ising-type longitudinal fluctuations along the **c**-axis. What is more, the angular dependence of $1/T_1$ measured with the magnetic fields rotating in the (**b**, **c**) plane (figure (4.1)) shows that the amplitude of the spin fluctuations along the **c**-axis scales with the field component along the **c**-axis. This proves that the longitudinal fluctuations are strongly suppressed by a magnetic field along the **c** axis, but remain almost unchanged under transverse magnetic fields ($\mathbf{H}//\mathbf{b}$, up to 3.5 T in their measurements).

The presence of spin fluctuations in UCoGe, along with their very anisotropic field dependence, is equally observed indirectly in numerous other physical properties. For example, in previous thermal conductivity studies in the normal phase of UCoGe, an extra contribution to the heat conduction κ/T has been detected. It was found to be strongly suppressed by magnetic field along the **c**-axis. This contribution of κ/T is considered to come from itinerant magnetic fluctuations[28] (see also Chapter 7.1). A strong negative magnetoresistance is also observed for $\mathbf{H}//\mathbf{c}$ at temperature around T_{Curie}, in almost every measured UCoGe sample, regardless of its quality. This indicates the important role in transport properties of the scattering process due to the magnetic fluctuations, which are strongly suppressed under field along the **c**-axis. In specific heat, the Sommerfeld coefficient (γ) is also observed to be strongly field dependent for magnetic field along the **c**-axis, which will be discussed in more detail in section 4.3.

Based on the NMR study the authors of Ref.[57] made the important first step to associate the strong anisotropy of the H_{c2} in UCoGe with the suppression of magnetic

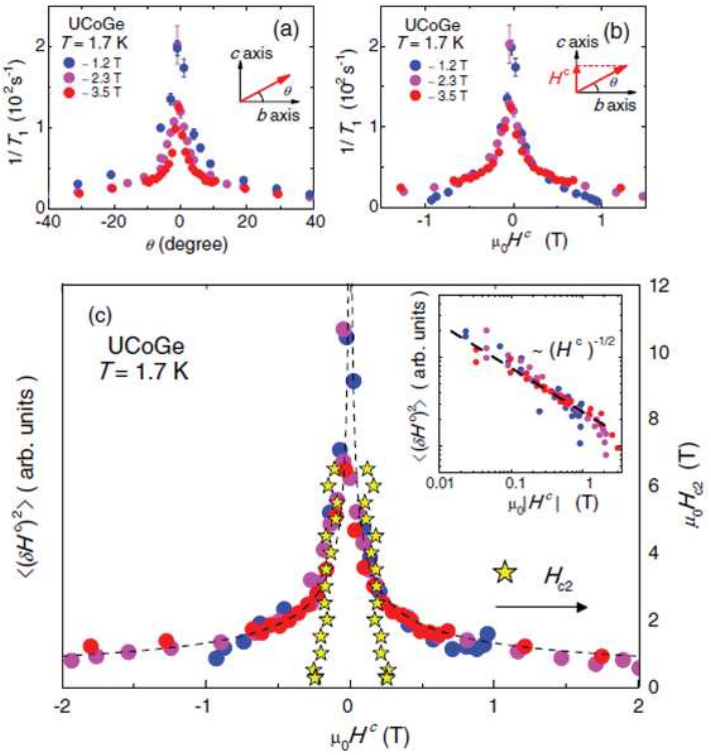

Figure 4.1 | Angle dependence of $1/T_1$ (a) in the (**b**, **c**) plane measured in three different magnetic fields at 1.7 K. When plotted against the field component along **c**-axis ($H^c = H.\sin\theta$), all the $1/T_1$ results (b) and the extracted magnetic fluctuations along the **c**-axis $< (\delta H^c)^2 >$ (c) collapse into a single curve (red, blue and pink circles). The yellow stars present the H_{c2} results for **H**//**c**, featuring that the superconducting phase in the narrow H^c region where the $< (\delta H^c)^2 >$ are not strongly suppressed.

fluctuations by field along the easy magnetization axis. They propose an empirical law to describe the field dependence of the magnetic susceptibility $\chi^c(\vec{q}, i\Omega_n)$ (Ising type along the **c**-axis):

$$\chi^c(\vec{q}, i\Omega_n) = \frac{\chi_0}{\delta(H^c) + q^2 + |\Omega_n|/\gamma_q} \qquad \delta(H^c) = h_{ex}^2 + c'\sqrt{H^c} \tag{4.5}$$

where γ_q is approximately $v_F.q$ and the coefficient c' is a free parameter of order $\mathcal{O}(1)$. For p-wave superconductivity mediated by the longitudinal spin fluctuations, the pairing interaction will be proportional to $\chi^c(\vec{q}, i\Omega_n)$, and it will strongly decrease under field **H**//**c**. This strong suppression of the pairing interaction for **H**//**c** is used to explain the huge anisotropy of H_{c2} between the **c**-axis and the two transverse field directions[73]. However, in Ref.[73] the authors could not make quantitative comparison with experimental data, neither can the empirical form in expression (4.5) be justified.

In the following we will discuss H_{c2} in UCoGe, with this hypothesis that the pairing interaction in this system is sensitive to the external magnetic field.

At first sight, it seems counter-intuitive that when the pairing strength is suppressed by the magnetic field, H_{c2} develops an upward curvature as observed for **H**//**c** in UCoGe: if the pairing strength decreases with field, H_{c2} would be lowered more significantly when

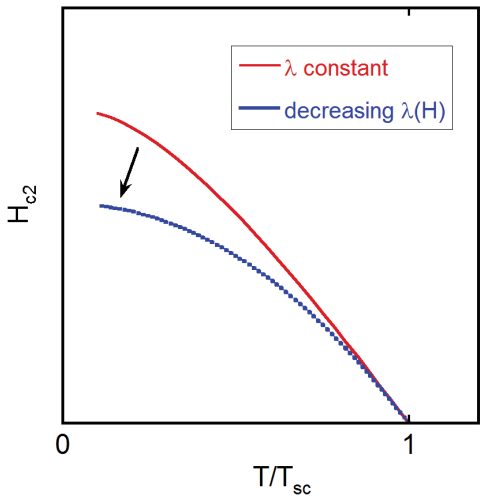

Figure 4.2 | Influence of a field-dependent pairing interaction (λ) on the H_{c2}: an intuitive image.

T approaches 0, and thus present an even stronger downward curvature than the usual case, as illustrated in figure 4.2. In the next section, the effect of a field-dependent pairing strength on the H_{c2} will be discussed explicitly, based on a simplified scheme. It explains why the above intuition can be misleading, and confirms that a decrease of the pairing strength can indeed explain the upward curvature behavior for $\mathbf{H}//\mathbf{c}$ in UCoGe, as well as the 20-fold anisotropy.

4.2 Field dependence of the pairing strength

At the first place, it will be helpful to do some "back of the envelop" calculation to illustrate the influence of a field-dependent pairing strength $\lambda(H)$ on H_{c2}.

In a weak-coupling scheme, the superconducting critical temperature T_{sc} is related to the pairing strength (λ) by:

$$T_{sc} \sim \Omega \exp\left(-\frac{1}{\lambda - \mu^*}\right) \tag{4.6}$$

where Ω is a characteristic frequency of the pairing interaction (in the case of conventional superconductivity, it is proportional to the Debye temperature for the phonons), μ^* is a parameter that characterizes the Coulomb repulsion, and λ characterizes the superconducting pairing strength. For strong coupling superconductors, there is no simple analytical relation that associates T_{sc} and λ. However, T_{sc} is still a function of Ω, λ and μ^*.

Like other unconventional superconductors, UCoGe is in the clean limit. According to the Ginzburg-Landau theory (and the classical WHH theory[36, 37] for H_{c2}), for a superconductor in the clean limit, H_{c2} for T close to T_{sc} is given by (equations (3.3) and (3.9) in Chapter 3.3):

$$H_{c2}^{orb} = \alpha_0 \frac{T_{sc}(T_{sc} - T)}{< v_f >^2} \tag{4.7}$$

where $< v_f >$ is the averaged Fermi velocity in the plane perpendicular to the field direction and α_0 is a numerical constant.

When the pairing strength λ depends on the magnetic field, the critical temperature T_{sc}, defined as the superconducting transition temperature at zero field, will also be a function of magnetic field. In such a case, if one derives the equation (4.7) to get the initial slope of H_{c2}, it is necessary to take the field dependence of $T_{sc}(\lambda(H))$ into account. What is more, the Fermi velocity v_F will also be field dependent as the quasiparticle mass (m^*,$v_F \propto (m^*)^{-1}$) is renormalized by the pairing interactions (see in the next section for more details, equation (4.12)). Differentiating equation (4.7) along the H_{c2} curve taking these additional field dependences into account, we have,

$$\left.\frac{dT}{dH}\right|_{H_{c2}} = -\frac{< v_f >^2}{\alpha_0 T_{sc}} + \frac{dT_{sc}}{dH} + \frac{H}{\alpha_0}\frac{d}{dH}\left(\frac{< v_f >^2}{T_{sc}}\right) \tag{4.8}$$

At $H = 0$, the last term on the right side in equation (4.8) equals zero, and:

$$\left.\frac{dT}{dH}\right|_{H_{c2},H=0} = -\frac{< v_f >^2}{\alpha_0 T_{sc}} + \frac{dT_{sc}}{d\lambda}\frac{d\lambda}{dH} \tag{4.9}$$

The (inverse of the) initial slope of H_{c2} is then determined by two terms: the usual orbital term (first term), and an additional term arising from the field dependence of $\lambda(H)$ (the second term). If $d\lambda/dH = 0$, there is no change of the initial slope compared with the normal WHH theory (equation(3.11)), and the intuitive picture in figure 4.2 is correct. But if $d\lambda/dH = 0$ is finite (and < 0), the initial slope ($(dH_{c2}/dT)_{T_{sc}}$) is decreased by the suppression of λ. And if this term is dominant, $H_{c2}(T)$ may be determined essentially by $T_{sc}(H)$, and much smaller than the orbital limitation. This is why the suppression of λ with H can so strongly affect the anisotropy and the curvature of H_{c2} in UCoGe.

Before going further, here is a brief comment on the NMR results[57, 73]. According to the field dependence of the dynamic spin susceptibility in equation (4.5), the pairing strength λ will depend on the field component along the **c**-axis (H^c) as:

$$\lambda(H^c) \propto \frac{1}{c'\sqrt{H^c} + h_{ex}^2 + q^2 + |\Omega_n|/\gamma_q} \tag{4.10}$$

which is a smooth function of $\sqrt{H^c}$: $\lambda(H^c) = f\left(\sqrt{H^c}\right)$. This H^c dependence will result in an infinite derivative of λ for at zero field, for $\mathbf{H}//\mathbf{c}$:

$$\begin{aligned}\frac{d\lambda}{dH} &= \frac{1}{2}\, f'(\sqrt{H})\, \frac{1}{\sqrt{H}} \\ &\to -\infty \text{ when } H \to 0\end{aligned} \tag{4.11}$$

In such a case, the second term in equation (4.9) will be infinite, and the initial slope of H_{c2} will be zero. This is not consistent with the experimental bulk H_{c2} for $\mathbf{H}//\mathbf{c}$ in UCoGe, presented in the previous chapter (figure 3.10).

4.3 Comparison with normal state properties

The quasiparticle effective mass m^* (and equivalently, the Fermi velocity $v_F \propto (m^*)^{-1}$) is renormalized by the pairing interactions, according to:

$$\begin{cases} m^* = m_b(1+\lambda) \\ v_F = \dfrac{v_F^b}{1+\lambda} \end{cases} \tag{4.12}$$

where m_b (v_F^b) is the band mass of the quasiparticles (band Fermi velocity), renormalized by all the interactions except the pairing interactions for superconductivity.

For a superconductor in the weak coupling limit ($\lambda << 1$), this leads to a negligible effect. But when the pairing strength is strong, it is possible for the field dependence of λ to be reflected in a number of measurable normal phase quantities (if a Fermi liquid), such as the (Pauli) magnetic susceptibility χ_p, the Sommerfeld coefficient of the specific heat γ ($C_p = \gamma T$, if the phonon contribution is negligible), or the quadratic coefficient A of the temperature dependence of resistivity ($\rho = \rho_0 + A.T^2$):

$$\begin{cases} A \propto (m^*)^2 \propto (1+\lambda)^2 \\ \gamma \propto m^* \propto 1+\lambda \\ \chi_p \propto m^* \propto 1+\lambda \end{cases} \tag{4.13}$$

In UCoGe, although the normal phase properties follow roughly the classical behaviors of a Fermi liquid, it is not easy to analyze them quantitatively. The difficulty arises from the proximity of the Curie temperature ($T_{Curie} \sim 2.5$ K) to the superconducting transition ($T_{sc} \sim 0.5$ K). For the A coefficient of resistivity, this leads to a very short temperature range to fit ρ. Meanwhile, when T approaches T_{Curie}, the scattering from the enhanced magnetic fluctuations strongly influence the transport properties, and the temperature dependence of ρ deviates from the T^2 law. For the magnetic susceptibility, it is generally difficult in heavy fermion systems to distinguish local and itinerant contributions. For these reasons we choose the more robust thermodynamic quantity C_p to study the normal phase properties of UCoGe, assuming that a constant C_p/T reflects the quasiparticle (Sommerfeld) contribution.

Specific heat measurements and $\gamma(H)$

When T approaches T_{Curie}, C_p/T is enhanced due to fluctuations around the ferromagnetic transition. To obtain the Sommerfeld coefficient γ correctly, we measured the temperature dependence of C_p/T from 1.6 K down to the onset of the superconducting transition (to stay far from the T_{Curie} anomaly), at different magnetic fields for $\mathbf{H}//\mathbf{c}$, on sample S_{16}^c (the same sample used in thermal conductivity measurements). Figure 4.3a presents some of the $C_p/T(T)$ results. For fields close to 0 T, where the increase of C_p/T near T_{Curie} is important, we fit the whole curve (T ranging from 0.6 K to 1.6 K) with an empirical law: $C_p/T = \gamma + \delta.\exp(-T_0/T)$, to get the value of γ. For fields above 0.1 T, where the anomaly at T_{Curie} almost disappears and the exponential term of the fit becomes negligible, γ is taken as the mean value of C_p/T in this temperature range. The corresponding fits are presented with the solid lines for each field in figure 4.3a.

Figure 4.3b presents the obtained field dependence of γ, for $\mathbf{H}//\mathbf{c}$ in UCoGe. $\gamma(H)$ decreases more than 10% (-6 mJ K^{-2} mol^{-1}) within a narrow field range (H below 0.5 T). In a larger field range for $\mathbf{H}//\mathbf{c}$ in UCoGe, γ presents variations due to the evolution of the Fermi surface. However, these effects should be negligible below 0.5 T, and it is reasonable to consider that this strong decrease of the specific heat below 0.5 T would be due to the variation of the pairing interactions λ. (The results of C_p/T measurements up to 16 T for $\mathbf{H}//\mathbf{c}$ in UCoGe will be discussed in Chapter 7.2.)

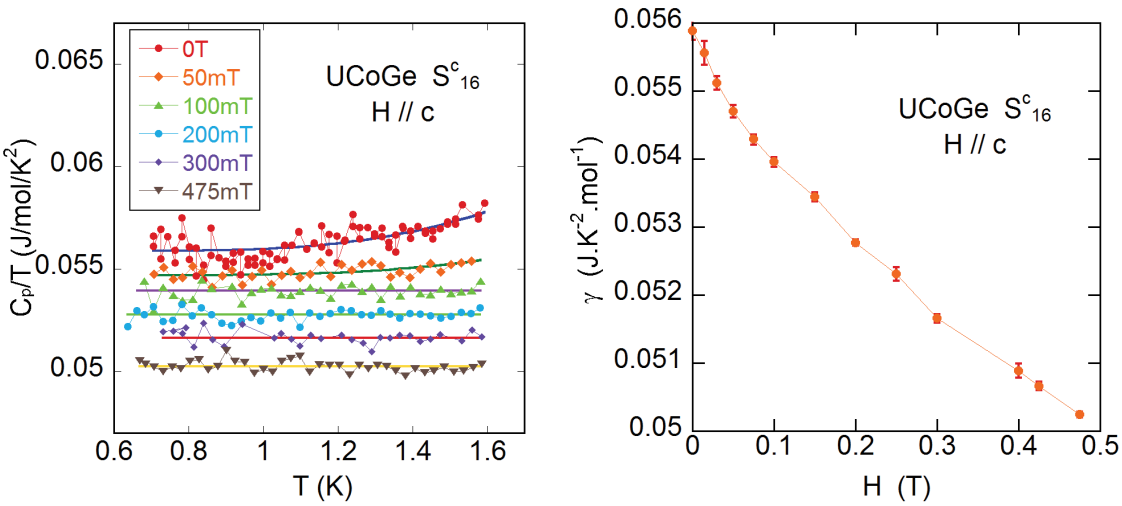

(a) (b)

Figure 4.3 | **(a)**: Temperature dependence of C_p/T of UCoGe, at different magnetic fields for $\mathbf{H}//\mathbf{c}$, measured on sample S^c_{16}. The solid lines show the fits to obtain the Sommerfeld coefficients γ. For fields close to 0 T, C_p/T is fitted with a function $C_p/T = \gamma + \delta.\exp(-T_0/T)$ with T_0 typically around 8 K. For fields above 100 mT, γ is obtained with the mean value of the C_p/T data in the whole temperature range. **(b)** : $\gamma(H)$ for $\mathbf{H}//\mathbf{c}$ of UCoGe, obtained from the data in (4.3a). The error bars are given directly by the fit.

Estimation of $\lambda(0)$

According to equation (4.13), if we associate the field dependence of C_p/T with only the variation of the pairing interaction $\lambda(H)$, we have $\gamma \propto (1+\lambda)$, and:

$$\lambda(H) = \frac{\gamma(H)}{\gamma(0)}(1+\lambda(0)) - 1 \tag{4.14}$$

This allows to calculate $\lambda(H)$ with the $\gamma(H)$ data, if the pairing strength at zero field $\lambda(0)$ is known. With the $\gamma(H)$ presented in figure 4.3b, which has a finite slope at $H = 0$, $\lambda(H)$ will equally have a finite slope at $H = 0$, contrary to the empirical form proposed in the NMR study[57, 73] (equation 4.10).

The value of $\lambda(0)$ can be estimated roughly in the following way. Consider that T_{sc} depends on λ following the BCS expression:

$$T_{sc}(H) = \Omega \exp\left(-\frac{1}{\lambda(H) - \mu^*}\right) \tag{4.6}$$

Deriving the equations (4.14) and (4.6) with respect to H, we have:

$$\begin{cases} \left.\dfrac{d\gamma}{dH}\right|_{H=0} = \dfrac{\gamma(0)}{1+\lambda(0)} \left.\dfrac{d\lambda}{dH}\right|_{H=0} \\ \left.\dfrac{dT_{sc}}{dH}\right|_{H=0} = \dfrac{T_{sc}(0)}{(\lambda(0)-\mu^*)^2} \left.\dfrac{d\lambda}{dH}\right|_{H=0} \end{cases} \tag{4.15}$$

In the equations (4.15), the values of $(d\gamma/dH)_{H=0}$ can be deduced from the data in figure 4.3b. According to equation (4.9) in the previous section, if the effect of $\lambda(H)$ suppression

under field is dominant, we can neglect the orbital contribution to the initial slope of H_{c2}, and $(dT_{sc}/dH)_{H=0}$ can be obtained from the initial slope of H_{c2}. By combining these two equations, we get an estimation of $\lambda(0)$ of order 0.5. Such a "medium pairing strength" is consistent with the modest specific heat jump at the superconducting transition in this compound.

4.4 Estimation of $\lambda(H)$ from H_{c2} with strong coupling calculations

Having confirmed by the C_p/T measurements, that a decrease of $\lambda(H)$, and a finite value of $d\lambda/dH$ at $H = 0$, are compatible with the experimental data in the normal phase, we now try to extract $\lambda(H)$ for the three field directions in UCoGe, from the experimental H_{c2} results in figure 3.12.

In conventional superconductors, it is possible to calculate from first principles the pairing strength λ provided that the phonon-mediated pairing mechanism is well established and that the phonon spectrum is known. In UCoGe, however, such a task is impossible at the present stage, because the ferromagnetic background and even the electronic band structure in this system remain largely unknown.

For this reason, instead of searching for a theoretical model that might reproduce the experimental H_{c2} behavior, in the first place we choose to address the problem in a reverse way: we will depart from our measured H_{c2} curves, and try to extract the field dependence of λ required to reproduce the experimental data.

4.4.1 Method

The principle of the method is simple: we calculate a series of H_{c2} curves, each one associated with a fixed value of the pairing strength λ, with the help of a (conventional) theoretical model for strong-coupling superconductivity[60]. Then the experimental H_{c2} data are compared with the whole series of calculated H_{c2} curves, to extract the λ needed at each magnetic field to reproduce the experimental results.

More specifically, the strong coupling model used for the upper critical field calculations is the one described in Ref.[74]. It simply evaluates H_{c2} with a conventional microscopic model assuming an Einstein spectrum for the interaction density:

$$\alpha F(\omega) = \frac{\lambda\Omega}{2}\,\delta(\omega - \Omega) \tag{4.16}$$

The main parameters for the calculation are the same as mentioned for equations (4.6) and (4.7). The superconducting transition is controlled by: the characteristic frequency of the pairing interaction Ω, the pairing interaction coupling constant λ, the Coulomb repulsion constant μ^*, and the Fermi velocity v_F which determines the orbital limitation. As is discussed in Chapter 3.3.2, in UCoGe the Pauli limitation is absent and a triplet "equal spin pairing" state is most likely realized. So in our s-wave calculation, we impose the gyromagnetic factor g to be zero which suppresses the Zeeman splitting. A precise computation for the Coulomb interaction parameter μ^* remains a formidable task even in the case of simple metals. However, its value varies typically between 0.1 and 0.15. In our case, we fix μ^* at 0.1, and consider it to be independent of the magnetic field. The characteristic frequency of the pairing interaction Ω is also supposed to be independent

of magnetic field: anyway the variation of λ will have a much stronger effect on T_{sc} than that of Ω. v_F is of course renormalized by the pairing interaction: $v_F = v_F^b/(1+\lambda)$. The band Fermi velocity v_F^b, which is renormalized by all the interactions other than those mediating superconductivity, is supposed to be field independent.

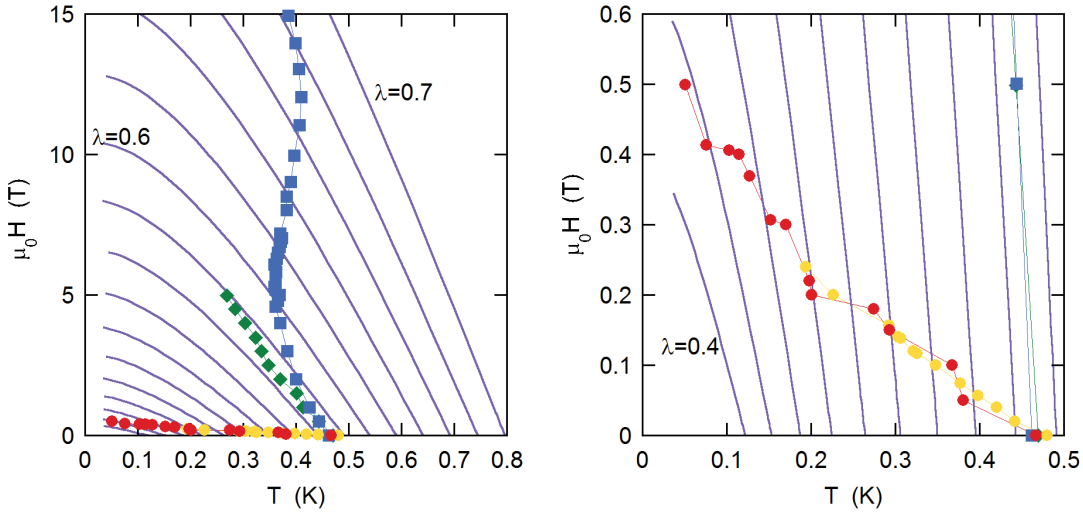

Figure 4.4 | **(a)**: The series of H_{c2} calculated with the strong coupling model, each time with a fixed coupling strength λ that varies from 0.4 up to 0.7 in steps of 0.02 from left to right (one out of two of the calculated curves are presented), and with the Fermi velocity v_F renormalized accordingly. The other parameters for the calculations are fixed as explained in the text. The experimental H_{c2} in figure 3.12 are equally presented for comparison. Blue squares: **H**//**b**; green diamonds: **H**//**a**; red and yellow circles: **H**//**c**. **(b)**: Zoom of the low field region for **H**//**c**.

In practice we first calculate H_{c2} with the strong-coupling model with λ fixed at $\lambda(0)$. (A free parameter, it is roughly estimated to be 0.5 in UCoGe in the previous section. It will be further adjusted with comparison to the specific heat data as explained later.) By comparing the H_{c2} curve with the experimental data, the main parameters for the calculation can be fixed: Ω is adjusted to give the critical temperature T_{sc} at zero field (with $\lambda = \lambda(0)$); v_F^b is adjusted so that the obtained H_{c2} has an initial slope $((dH_{c2}/dT)_{T=T_{sc}})$ matching that of the experimental H_{c2} for **H**//**a**. (We know, a priori, that λ remains almost constant for **H**//**a** in UCoGe, because the magnetic state is little changed in this field direction: for example, T_{Curie} remains unchanged in magnetic fields up to 10.3 T for **H**//**a** [75].) Then, with the other parameters μ^*, Ω and v_F^b fixed, we calculate the H_{c2} for a series of values of λ. The resulting series of H_{c2}, presented in figure 4.4a, are then compared with the experimental H_{c2} to get $\lambda(H)$.

Comparison with specific heat measurements

The $\lambda(H)$ for **H**//**c** obtained in this method, can be compared with the $\lambda(H)$ obtained from the specific heat measurements in figure 4.3, calculated with equation (4.14). The value of $\lambda(0)$, roughly estimated at 0.5, is a free parameter for both sides. In order to adjust its value in a more precise way, we redo the calculations starting from different

$\lambda(0)$. Figure 4.5 shows that a good match is obtained with $\lambda(0) = 0.57$, between the $\lambda(H)$ from the calculations based on H_{c2} and that from the normal phase properties.

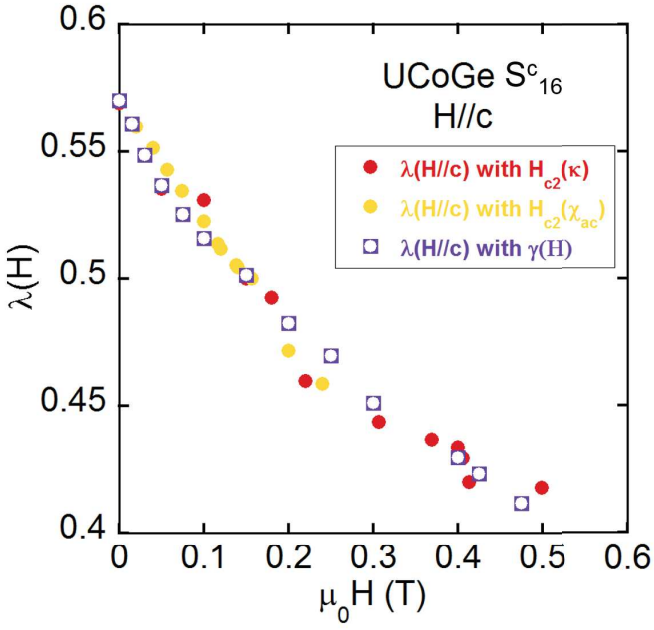

Figure 4.5 | $\lambda(H)$ for $\mathbf{H}//\mathbf{c}$ in UCoGe (sample S^c_{16}) obtained from the experimental H_{c2} data based on strong coupling H_{c2} calculations within a specific microscopic model[60], compared with $\lambda(H)$ for $\mathbf{H}//\mathbf{c}$ calculated with the Sommerfeld coefficient (γ) according to equation (4.14), with $\lambda(0) = 0.57$. Red circles: $\lambda(H)$ obtained from the H_{c2} probed with the thermal conductivity (κ). Yellow circles: $\lambda(H)$ obtained from the H_{c2} probed with the ac-susceptibility (χ). Violet squares: $\lambda(H)$ obtained from $\gamma(H)$. The free parameter $\lambda(0)$ has been adjusted for the consistency between the two.

4.4.2 Results and discussions

Figure 4.6 displays $\lambda(H)$ for three field directions obtained from the strong coupling calculations and the experimental H_{c2} data. It can be observed that for fields along the two transverse axes **a** and **b**, the upward curvature of H_{c2} corresponds to an increase in the coupling strength λ. For $\mathbf{H}//\mathbf{a}$ λ is essentially constant up to 5 T, with only a slight increase of order 1.5% due the barely visible upward curvature. For $\mathbf{H}//\mathbf{b}$, the increase of λ with field is observed at smaller fields due to the stronger curvature of H_{c2} in this direction. The pronounced "S-shape" is reproduced by a $\sim 20\%$ monotonous increase of λ up to 15 T. For fields along the easy magnetization axis **c**, on the contrary, the upward curvature is induced by a very strong suppression of λ (of nearly 30%) in a narrow field range (below 0.5 T), which results in a small upper critical field along this field direction.

4.4.3 Approximations made in the process

The above analysis process is based on several simplifications. The main assumptions are listed below:

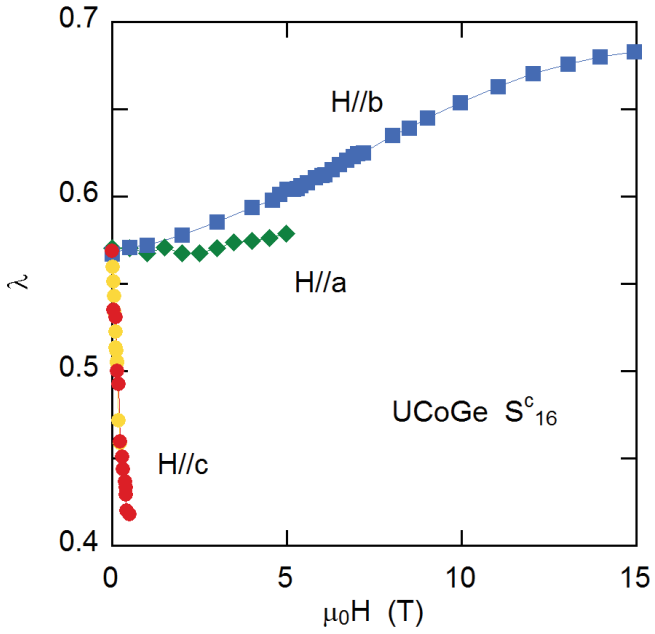

Figure 4.6 | λ(H) for the three crystallographic directions by comparing the experimental H_{c2} with the calculated in figure 4.4.

- **s-wave superconducting state**
  In our study we calculate the H_{c2} using a simple s-wave (nodeless gap) superconducting model. The triplet-pairing nature of UCoGe is taken into account only through the omission of the Pauli limitation, by imposing the g factor at 0. The main assumption here is that the orbital limitation is little different between s and p-wave superconductors, except for a small "renormalization" of the average Fermi velocity.

- **Isotropic Fermi velocity**
  The orbital limitation of the H_{c2} is controlled by the Fermi velocity averaged in the plane perpendicular to the magnetic field direction. Thus anisotropy of H_{c2} can be induced by a non-isotropic Fermi velocity in the normal phase. In UCoGe, no remarkable anisotropy is observed in the normal phase transport properties, so that the observed anisotropy in H_{c2} has to come from mainly another origin. Thus in the above analysis the Fermi velocity at zero field is supposed to be isotropic.

- **Einstein-type spectrum in the strong coupling model**
  The strong coupling calculations for H_{c2} performed here are based on a specific microscopic model with a Dirac function in the interaction density spectrum[60]. Using more realistic pairing interaction spectrum may lead to deviations from the present results, both in the form of calculated H_{c2}, and in the λ-dependence of T_{sc}. However, it is expected that it should lead only to small quantitative corrections to the value of $\lambda(0)$, but would not change the whole interpretation we make, because UCoGe is only in an intermediate coupling regime.

4.5 Conclusions

This chapter shows explicitly how a field dependent pairing interaction can influence the H_{c2}. In case where the tuning of pairing interaction by the magnetic field is strong, both the initial slope and the whole curvature of H_{c2} will be modified. We demonstrate that in UCoGe a strong suppression of the pairing interaction under field along the **c**-axis can indeed account for the huge anisotropy of H_{c2} and the upward curvature in H_{c2} in this field direction. Moreover, due to the renormalization of the quasiparticle effective mass by the pairing interaction, such an effect is reflected in the normal phase properties, for example, in the strong decrease of the Sommerfeld coefficient of the specific heat under $\mathbf{H}//\mathbf{c}$. Finally, we address the question in a reverse way. Starting from the experimental H_{c2} results obtained from the bulk measurements in Chapter 3, we use a microscopic strong-coupling model to obtain the field dependence of the pairing interaction in UCoGe, for the three field directions.

In the next chapter we will see how this field dependence of the pairing interaction can be compared with existing theory[39].

Chapter 5

Mineev's theory

The discovery of the ferromagnetic superconductors UGe_2, URhGe and UCoGe, and especially the field induced re-entrant superconducting phase in URhGe, have excited numerous theoretical investigations on magnetically mediated superconductivity [76, 77, 27, 78, 73, 56, 39]. However, a realistic microscopic description of the superconductivity in these systems is a complicated issue, not only because the pairing mechanism is not fully established, but also due to their complex magnetic background. First, although photoelectron spectroscopy results[79], and the small ordered moment in these systems can be interpreted as pointing to the itinerancy of the $5f$ electrons, the itinerant or localized nature of the ferromagnetism in these systems is not firmly established, and in particular a dual behavior of the $5f$ electrons may occur. Second, the band structure in these systems is also badly known. The situation is particularly complicated in UCoGe, where different band structure calculations agree poorly with each other[80, 81, 82] and show big discrepancy with experimental ARPES results[82]. Finally, the magnetic excitation spectrum has been well studied with neutron scattering measurements only in UGe_2 [83, 84]. In UCoGe neutron measurements barely succeed to detect the magnetic fluctuations, but are unable to determine their spectrum[85].

The approach for the ferromagnetism proposed by V. Mineev[39] is based on the Landau free energy formalism, and is valid for all systems, both itinerant or localized. This chapter will discuss the field dependence of the pairing interaction in UCoGe based on this theory, and compare with the analysis of the experimental data presented in chapter 4, both for the case of $\mathbf{H}//\mathbf{c}$ and $\mathbf{H}//\mathbf{b}$. The sister compound URhGe will also be discussed within the same theoretical framework.

5.1 Outline of Mineev's theory

The model in Ref.[39] gives a general description of the magnetic state for all the ferromagnetic superconductors, based on the Landau free energy formalism in an orthorhombic system. Under magnetic field $\mathbf{H}$, the free energy can be written as:

$$\mathcal{F} = \int dV (F_M + F_\nabla), \tag{5.1}$$

where F_M is the magnetic energy density

$$\begin{aligned} F_M = {} & \alpha_z M_z^2 + \alpha_y M_y^2 + \alpha_x M_x^2 + \beta_z M_z^4 \\ & + \beta_{xy} M_x^2 M_y^2 + \beta_{yz} M_z^2 M_y^2 + \beta_{xz} M_z^2 M_x^2 - \mathbf{M}.\mathbf{H} \end{aligned} \tag{5.2}$$

with M_i the i-component ($i = x, y, z$) of the magnetic moment $\mathbf{M}$, and F_∇, which depends on the gradient of $\mathbf{M}$, is expanded as:

$$F_\nabla = \gamma_{ij}^{\alpha\beta} \frac{\partial M_\alpha}{\partial x_i} \frac{\partial M_\beta}{\partial x_j} \tag{5.3}$$

In the exchange approximation, only the diagonal terms of the γ tensor are considered

$$\gamma_{ij}^{\alpha\beta} = \delta_{\alpha\beta}\delta_{ij}\gamma_{ii} \tag{5.4}$$

We further suppose that it is isotropic: $\gamma_{ii} = \gamma$.

The z direction is chosen to be the spontaneous magnetization axis (**c**-axis in UCoGe and URhGe) and the coefficient α_z is temperature dependent and is associated with the Curie temperature T_{Curie}:

$$\begin{aligned} &\alpha_z = \alpha_0(T - T_{Curie}), \text{ with } \alpha_0 > 0 \\ &\alpha_x > 0, \quad \alpha_y > 0 \end{aligned} \tag{5.5}$$

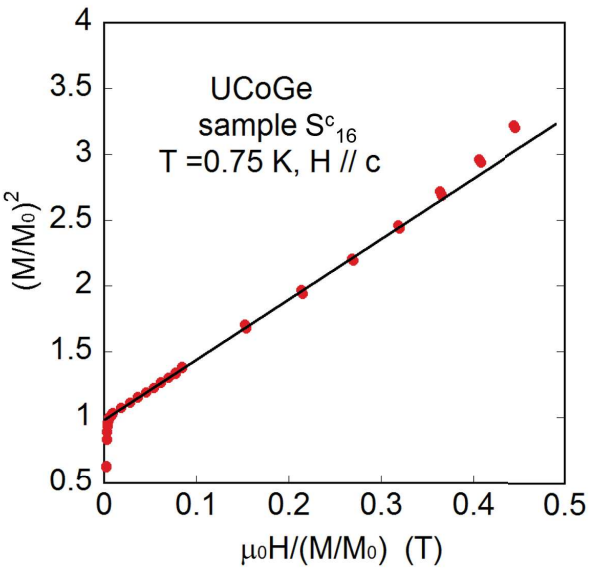

Figure 5.1 | Arrott plot for UCoGe for field along **c**-axis, measured on sample S^c_{16}, at $T = 0.75$ K. Deviation from the linear behavior starts at field above 0.6 T. The magnetization measurements were performed by C. Paulsen at Néel Institute in Grenoble.

The equilibrium state is obtained by minimizing the Landau free energy $\mathcal{F}$ (equation (5.1)), which leads to equations of $\mathbf{M}$ as a function of the applied magnetic field. In particular, for $\mathbf{H}//\mathbf{z}$ this gives:

$$\begin{aligned} &M_z^2 = -\frac{\alpha_0(T - T_{Curie})}{2\beta_z} + \frac{H}{4\beta_z M_z} \\ &M_x = 0, \quad M_y = 0 \end{aligned} \tag{5.6}$$

As a consequence, at $H = 0$, a finite spontaneous magnetization is present ($|M_z| > 0$) if $T < T_{Curie}$. Equation (5.6) implies equally that if the Landau approach is valid, the Arrott plot for magnetic field along **c**-axis (where M_z^2 is plotted as a function of H/M_z)

will have a linear behavior. To check this point, the field dependence of the magnetization of the UCoGe (sample S_{16}^{c}, the same sample used for the thermal conductivity measurements) has been measured, for field applied along the **c**-axis (presented afterwards). It is well known that magnetic properties in UCoGe show a large dispersion on different samples. For example, the Curie temperature in UCoGe ranges from 2 to 3 K. Thus it is crucial to use measurements performed on the same sample to compare the magnetic and superconducting properties. Figure 5.1 presents the Arrott plot at 0.75 K (just above the onset of the superconducting transition), which shows that the linear behavior is nicely followed for field up to about 0.6 T. Thus in the field range in which the superconducting properties of UCoGe is discussed (below 0.5 T on sample S_{16}^{c}), the Landau free energy expression in equation (5.2) describes well the magnetic state of this system for $\mathbf{H}//\mathbf{c}$.

Differentiating further equation (5.1) with a small field variation ($\delta\mathbf{H}$) leads to the magnetic susceptibility $\chi_{ij} = \partial M_i/\partial H_j$ at finite fields. In particular, for $\mathbf{H}//\mathbf{z}$, only the diagonal terms of the susceptibility tensor are non zero, and are given by:

$$\begin{cases} \chi_{xx}(\mathbf{k}) = \dfrac{1}{2(\alpha_x + \beta_{xz}M_z^2 + \gamma_{ij}k_ik_j)} \\ \chi_{yy}(\mathbf{k}) = \dfrac{1}{2(\alpha_y + \beta_{yz}M_z^2 + \gamma_{ij}k_ik_j)} \\ \chi_{zz}(\mathbf{k}) = \dfrac{1}{2(\alpha_z + 6\beta_zM_z^2 + \gamma_{ij}k_ik_j)} \end{cases} \tag{5.7}$$

Thus the magnetic susceptibilities (χ_{ii}) are expressed as functions of $\mathbf{M}(\mathbf{H})$. Moreover, due to the gradient terms in the Landau free energy (F_∇), the magnetic susceptibilities are momentum dependent. This $\mathbf{k}$ dependence is only valid for small $\mathbf{k}$, as the Landau expression of F is valid only with smooth spacial variations.

Possible forms of the p-wave superconducting order parameter in an orthorhombic ferromagnetic superconductor have been derived from symmetry principles (equation (1.7) and (1.8)) in Ref.[26, 27].

The general form of a triplet pairing order parameter is written as the sum of three components with different S_z:

$$\mathbf{\Delta}(\mathbf{k},\mathbf{r}) = \Delta^{\uparrow}(\mathbf{k},\mathbf{r})|\uparrow\uparrow> + \Delta^{\downarrow}(\mathbf{k},\mathbf{r})|\downarrow\downarrow> + \Delta^{0}(\mathbf{k},\mathbf{r})(|\uparrow\downarrow> + |\downarrow\uparrow>) \tag{5.8}$$

Due to the large exchange field and the high upper critical field (compared with the Pauli limitation) in these systems, it is expected that the $S_z = 0$ component of the triplet state should be negligible, and only the "equal spin pairing" components will be considered:

$$\mathbf{\Delta}(\mathbf{k},\mathbf{r}) = \Delta^{\uparrow}(\mathbf{k},\mathbf{r})|\uparrow\uparrow> + \Delta^{\downarrow}(\mathbf{k},\mathbf{r})|\downarrow\downarrow> \tag{5.9}$$

In Ref.[39] the attractive interactions responsible for the formation of the bound state between two electrons is assumed to be mediated by the magnetic polarization of the media, like in equation (4.4)):

$$H_{pairing} = -\frac{1}{2}\mu_B^2 I^2 \int d^3\mathbf{r}d^3\mathbf{r}' S_i(\mathbf{r})\chi_{ij}(\mathbf{r}-\mathbf{r}')S_j(\mathbf{r}') \tag{5.10}$$

where $S_i(\mathbf{r})$ is the spin density operator, $\chi_{ij}(\mathbf{r})$ the system susceptibility and I an exchange constant. For triplet states with only "equal spin pairing" components in (5.9), this form

of interactions leads to the linear equations for the order parameter:

$$\begin{cases} \Delta^{\uparrow}(\mathbf{k},\mathbf{q}) = -T\sum\limits_{n}\sum\limits_{k'} V^{\uparrow\uparrow}(\mathbf{k},\mathbf{k}')G^{\uparrow}G^{\uparrow}\Delta^{\uparrow}(\mathbf{k}',\mathbf{q}) + V^{\uparrow\downarrow}(\mathbf{k},\mathbf{k}')G^{\downarrow}G^{\downarrow}\Delta^{\downarrow}(\mathbf{k}',\mathbf{q}) \\ \Delta^{\downarrow}(\mathbf{k},\mathbf{q}) = -T\sum\limits_{n}\sum\limits_{k'} V^{\downarrow\uparrow}(\mathbf{k},\mathbf{k}')G^{\uparrow}G^{\uparrow}\Delta^{\uparrow}(\mathbf{k}',\mathbf{q}) + V^{\downarrow\downarrow}(\mathbf{k},\mathbf{k}')G^{\downarrow}G^{\downarrow}\Delta^{\downarrow}(\mathbf{k}',\mathbf{q}) \end{cases} \tag{5.11}$$

where the order parameter is in the momentum representation:

$$\Delta^{\uparrow,\downarrow}(\mathbf{k},\mathbf{q}) = \int \Delta^{\uparrow,\downarrow}(\mathbf{k},\mathbf{r})e^{i\mathbf{qr}}d^3\mathbf{r} \tag{5.12}$$

and $G^{\uparrow,\downarrow}G^{\uparrow,\downarrow} = G^{\uparrow,\downarrow}(\mathbf{k}',\omega_n)G^{\uparrow,\downarrow}(-\mathbf{k}'+\mathbf{q},-\omega_n)$ are normal metal Green functions:

$$G^{\uparrow,\downarrow}(\mathbf{k}',\omega_n) = \frac{1}{i\omega_n - \xi^{\uparrow,\downarrow}_{\mathbf{k}'}} \tag{5.13}$$

The pairing interactions are expressed as:

$$\begin{cases} V^{\uparrow\uparrow}(\mathbf{k},\mathbf{k}') = -\mu_B^2 I^2 \chi^u_{zz} \\ V^{\downarrow\downarrow}(\mathbf{k},\mathbf{k}') = -\mu_B^2 I^2 \chi^u_{zz} \\ V^{\uparrow\downarrow}(\mathbf{k},\mathbf{k}') = -\mu_B^2 I^2 (\chi^u_{xx} - \chi^u_{yy} - 2i\chi^u_{xy}) \\ V^{\downarrow\uparrow}(\mathbf{k},\mathbf{k}') = -\mu_B^2 I^2 (\chi^u_{xx} - \chi^u_{yy} + 2i\chi^u_{xy}) \end{cases} \tag{5.14}$$

where χ^u_{ij} is the odd part of the static susceptibility of the system, defined as:

$$\chi^u_{ij}(\mathbf{k},\mathbf{k}') = -\frac{1}{2}[\chi_{ij}(\mathbf{k}-\mathbf{k}') - \chi_{ij}(\mathbf{k}+\mathbf{k}')] \tag{5.15}$$

Equation(5.14) states that the pairing interactions $V^{\uparrow\uparrow}$ and $V^{\downarrow\downarrow}$, respectively responsible for the formation of the $|\uparrow\uparrow>$ and $|\downarrow\downarrow>$ states, depend only on the odd part of the longitudinal magnetic susceptibility χ^u_{zz}. However the mixing of the two "equal spin pairing" components (controlled by $V^{\uparrow\downarrow}$ and $V^{\downarrow\uparrow}$) depend on the other components of the susceptibility tensor χ^u_{xx}, χ^u_{yy} and χ^u_{xy}.

In UCoGe, the longitudinal susceptibility is much larger than the transverse ones (as is indicated by the Ising type spin fluctuations observed in NMR study[57]). Thus, in a first approximation the two "equal spin pairing" components can be considered as decoupled, and the field dependence of the strength of the total pairing interaction $\lambda(H)$ will be above all determined by the field dependence of $\chi^u_{zz}(\mathbf{k},\mathbf{k}')$.

Coming back to the first simplification (neglecting the $S_z = 0$ component), it is shown in Ref.[39] that the $S_z = 0$ component is not necessary zero even if the band splitting is strong. It is controlled by non diagonal components of the susceptibility tensor:

$$\begin{aligned} V^{\uparrow 0}(\mathbf{k},\mathbf{k}') &= -\mu_B^2 I^2(\chi^u_{xz} - i\chi^u_{yz}) \\ V^{\downarrow 0}(\mathbf{k},\mathbf{k}') &= -\mu_B^2 I^2(-\chi^u_{xz} - i\chi^u_{yz}) \end{aligned} \tag{5.16}$$

through the equation:

$$\Delta^{0}(\mathbf{k},\mathbf{q}) = -T\sum_{n}\sum_{k'} V^{0\uparrow}(\mathbf{k},\mathbf{k}')G^{\uparrow}G^{\uparrow}\Delta^{\uparrow}(\mathbf{k}',\mathbf{q}) + V^{0\downarrow}(\mathbf{k},\mathbf{k}')G^{\downarrow}G^{\downarrow}\Delta^{\downarrow}(\mathbf{k}',\mathbf{q}) \tag{5.17}$$

It will be in general non zero if the χ^u_{iz}, $i \neq z$ are not negligible.

The work of in Ref.[39] does not contain explicit evaluations of the upper critical field, which requires heavy calculations based on a precise knowledge of the p-wave superconducting order parameter. However, it gives a complete prediction of the field and angular dependence of the pairing interactions in the case of ferromagnetic superconductors, through the variations of the magnetic susceptibilities $\chi_{ij}(\mathbf{k})$ and the parameters of the gradient term γ_{ij}. The pairing strength, parametrized by a constant of interaction λ (noted g in Ref.[39]), is considered to be in the weak coupling limit, and the superconducting critical temperature T_{sc} is taken to depend on λ with the BCS-type formula $T_{sc} = \epsilon \exp(-\frac{1}{\lambda})$. Strong coupling effects, such as the renormalization of the quasiparticle effective mass, is thus not contained in the present theoretical work. In the following sections we will discuss the field dependence of pairing strength $\lambda(H)$ predicted by this theory in their explicit forms, for magnetic field along different crystal axes, and compare these theoretical predictions with the analyses based on the experimental results performed in Chapter 4.

5.2 Field dependence of pairing interactions of UCoGe for field along the c-axis

We first look at the case where the magnetic field is applied along the easy magnetization axis (**z**-axis). In this situation, the longitudinal susceptibility $\chi_{zz}(\mathbf{k})$ is given by equation (5.7):

$$\chi_{zz}(\mathbf{k}) = \frac{1}{2(\alpha_z + 6\beta_z M_z^2 + \gamma_{ij} k_i k_j)}$$

If we forget about the mixing of the two "equal spin pairing" components, equation (5.14) gives the superconducting pairing strength (λ) as a function of magnetic field through the field dependence of the magnetization (M_z):

$$\lambda(H) \propto \frac{1}{(2\alpha_z + 12\beta_z M_z^2 + 2\gamma k_F^2)^2} \tag{5.18}$$

which can be written as:

$$\lambda(H) = \lambda(0) \frac{\left(1 + (\xi_{mag} k_F)^2\right)^2}{\left(\frac{3}{2}\frac{M_z^2}{M_0^2} - \frac{1}{2} + (\xi_{mag} k_F)^2\right)^2} \tag{5.19}$$

where once again M_z is the magnetization along z-axis under field, M_0 the spontaneous moment and k_F is the momentum at the Fermi surface. The parameter ξ_{mag}, defined as

$$\xi_{mag}^2 = \frac{2\gamma}{4\beta_z M_0^2}, \tag{5.20}$$

is related to the gradient term in the free energy in equation (5.3), and typically corresponds to the coherence length of the long range ferromagnetic order. Equation (5.19) allows to calculate the theoretical prediction from the Mineev's theory of $\lambda(H)$ for $\mathbf{H}//\mathbf{c}$ in UCoGe with the help of experimental magnetization measurements. Figure 5.2 presents

the magnetization (M) of UCoGe for $\mathbf{H}//\mathbf{c}$, measured on the same sample as used in the thermal conductivity study (S^c_{16}). The measurements were performed by Carley Paulsen at Néel Institute in Grenoble, with a the high field (8 T), low temperature (100 mK) SQUID magnetometer. With these results, $\lambda(H)$ can be calculated according to the equation (5.19), with $\xi_{mag}k_F$ being the only adjustable parameter. Figure 5.3 presents the calculated $\lambda(H)$ for $\mathbf{H}//\mathbf{c}$, which is compared with the $\lambda(H)$ obtained in the previous chapter, both from the strong coupling calculations and from the normal phase specific heat data (section 4.4). If the gradient term and the $\mathbf{k}$-dependence of the susceptibilities is not considered ($\xi_{mag}k_F = 0$), equation (5.19) leads to a suppression of pairing strength in UCoGe under magnetic field along the $\mathbf{c}$-axis too strong compared with results of the analyses in chapter 4. However, if $\xi_{mag}k_F$ is fixed at 3.2, the theoretical prediction of equation (5.19) is in perfect agreement with previous $\lambda(H)$ results. This large $\xi_{mag}k_F$ value probably indicates that the ferromagnetism in UCoGe has a strong itinerant nature. ($\xi_{mag} \sim 3.2k_F^{-1}$ is about three times the interatomic distance.)

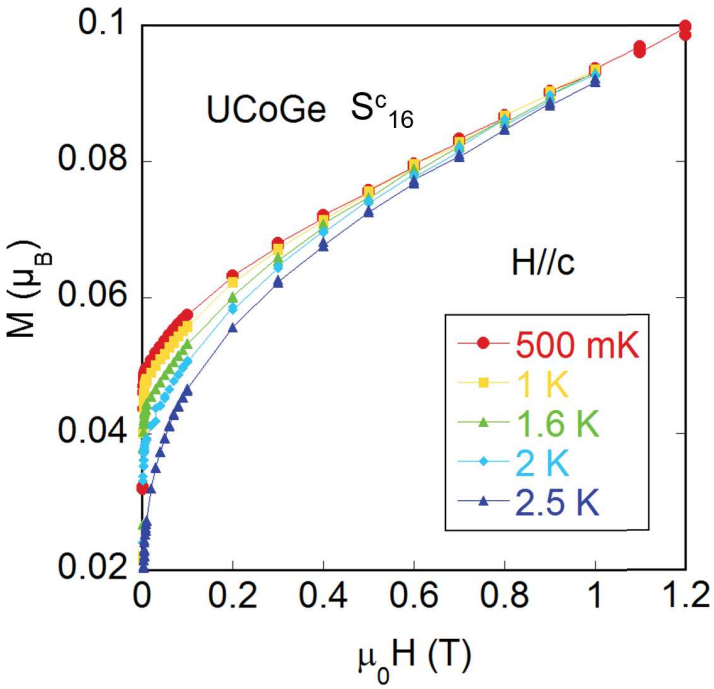

Figure 5.2 | Field dependence of the magnetization in UCoGe, for $\mathbf{H}//\mathbf{c}$ at different temperatures, measured on the same sample used for the thermal conductivity measurements of H_{c2}. The measurements were performed by C. Paulsen at Néel Institute in Grenoble.

In a more rigorous and complete analysis, the splitting of the spin up and spin down bands needs to be considered. The "single band model" approximation used in equation (5.19) is valid, if the polarization of the up and down spin bands is small enough to be neglected, or if the transverse susceptibilities χ_{aa}, χ_{bb} are much smaller than χ_{cc}, and the mixing of the two states is weak compared with the pairing strength of each state. In UCoGe the latter condition is realized. However, it is possible to take explicitly the two-band effect into account. Analyses of the influence of a two band state on $\lambda(H)$ are presented in Appendix A. They show that taking the band splitting into account does not quantitatively change the situation, and gives completely consistent results with the

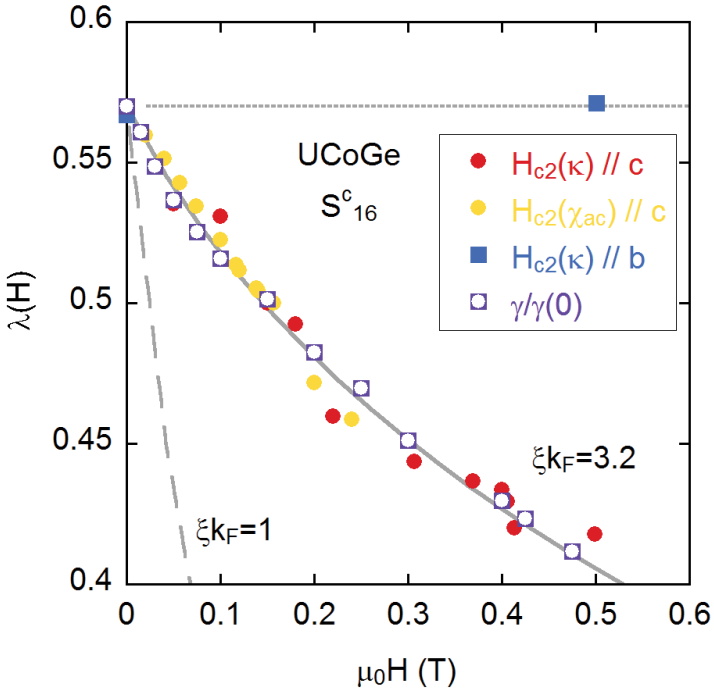

Figure 5.3 | Field dependence of the pairing strength $\lambda(H)$ for $\mathbf{H}//\mathbf{c}$ in UCoGe. Yellow and red circles: $\lambda(H)$ obtained from strong coupling calculations in Chapter 4.4, with the experimental H_{c2} curve. Open violet squares: $\lambda(H)$ obtained from field dependence of the Sommerfeld coefficient. Lines: $\lambda(H)$ predicted by Mineev's theory [39] (equation (5.19)), based on magnetization measurements in figure 5.2 performed on the same sample: solid line, for the optimized value of $\xi_{mag}k_F = 3.2$; dash-dotted line for $\xi_{mag}k_F = 1$ (localized magnetism limit).
The low field regime of $\lambda(H)$ for $\mathbf{H}//\mathbf{b}$ is also presented. Blue squares: $\lambda(H)$ from H_{c2}. Doted line: prediction from equation (5.26) based on the measured field variation of T_{Curie} obtained from Ref.[30], with $\xi_{mag}k_F = 3.2$.

"single band"approximation within a 10% modification of the parameter $\xi_{mag}k_F$.

5.3 Magnetic field in transverse directions

We now look at the case where the field direction is perpendicular to the spontaneous magnetization direction, for example with $\mathbf{H} = H_y\hat{\mathbf{y}}$. For the equilibrium state, minimizing the Landau free energy in equation (5.1) with respect to M_y gives:

$$M_y = \frac{H_y}{2\alpha_y + 2\beta_{yz}M_z^2} \tag{5.21}$$

Thus a finite magnetic moment along the field H_y will be induced, in addition to the spontaneous magnetic moment M_z in the ferromagnetic state. Injecting the equation (5.21) into the equation (5.2), the Landau free energy function F_M can be rewritten in a simple form as:

$$F_M = \tilde{\alpha}_z M_z^2 + \tilde{\beta}_z M_z^4 - \frac{H_y^2}{\alpha_y} \tag{5.22}$$

The new coefficients $\tilde{\alpha}_z$ and $\tilde{\beta}_z$ are defined as:

$$\begin{aligned}\tilde{\alpha}_z &= \alpha_z + \frac{\beta_{yz} H_y^2}{4\alpha_y^2} \\ \tilde{\beta}_z &= \beta_z - \frac{\beta_{yz}}{\alpha_y}\frac{\beta_{yz} H_y^2}{4\alpha_y^2}\end{aligned} \tag{5.23}$$

Putting the equation (5.5) into the $\tilde{\alpha}_z$ expression, we have:

$$\begin{aligned}\tilde{\alpha}_z &= \alpha_{z0}(T - T^0_{Curie}) + \frac{\beta_{yz} H_y^2}{4\alpha_y^2} \\ &= \alpha_{z0}(T - T_{Curie}(H_y))\end{aligned} \tag{5.24}$$

which means that the Curie temperature $T_{Curie}(H_y)$ is reduced by H_y from its zero field value T^0_{Curie}, as

$$T_{Curie}(H_y) = T^0_{Curie} - \frac{\beta_{yz} H_y^2}{4\alpha_{z0}\alpha_y^2} \tag{5.25}$$

If we neglect the effect of the band splitting, and make the same "single band" approximation as in the case of $\mathbf{H} = H_z\hat{\mathbf{z}}$, the pairing interaction $\lambda(H)$ will be determined by the longitudinal spin fluctuations χ_{zz} as before (equation (5.14)). Calculating χ_{zz} by deriving the F_M in equation (5.22), we find:

$$\lambda(H_y) = \lambda(0)\frac{(1 + (\xi k_F)^2)^2}{\left(\frac{T - T_{Curie}(H_y)}{T - T_{Curie}(0)} + (\xi k_F)^2\right)^2} \tag{5.26}$$

Thus the superconducting pairing strength in transverse external field is predicted to depend on the variation of the Curie temperature $T_{Curie}(H)$.

Experimentally, in UCoGe and URhGe, T_{Curie} is indeed observed to decrease with magnetic field applied along one of the two transverse direction ($\mathbf{H}//\mathbf{b}$), and T_{Curie} and follows roughly a H^2 dependence. The re-entrant superconductivity phenomenon appears when $T_{Curie}(H_b)$ decreases to zero. In both systems T_{Curie} is observed to be almost constant for $\mathbf{H}//\mathbf{a}$. At first sight, the prediction from equation (5.26) is consistent with our analyses in the previous chapter, which show that λ increases steadily with field along the **b**-axis and remains practically constant for $\mathbf{H}//\mathbf{a}$. However, calculating explicitly $\lambda(H)$ with the experimental data of $T_{Curie}(H)$ for $\mathbf{H}//\mathbf{b}$ in UCoGe, it is difficult to reach even qualitative agreements.

It is to be mentioned that in the expression of $\lambda(H_b)$ in equation (5.26), many simplifications have been made. In reality, not only the splitting of the spin up and down bands should be considered, but the **d**-vector of the p-wave superconducting order parameter should be rotated. This is to say, as a transverse external field H_b is applied in addition to the spontaneous exchange field h (noted B_{exch} before) along the **c**-axis due to ferromagnetic order, the principal axis of the "equal spin pairing" triplet state will be rotated by θ ($\tan\theta = H_b/h$). Taking the rotation of the **d**-vector into account adds in the influence from the components of the susceptibility tensor other than χ_{zz}. A detailed discussion on these effects is lengthy and is presented in Annexe A. With the above two effects taken into account, the field dependence of $\lambda(H)$ predicted by the Mineev's theory cannot give

satisfying explanation for the $\lambda(H)$ for $\mathbf{H}//\mathbf{b}$ in UCoGe deduced from the experimental H_{c2} data.

One of the possible reasons for this deviation is that, as the pairing interaction is significantly enhanced under magnetic field applied along the **b**-axis, the strong-coupling effects, which are not taken into account in the present weak-coupling theory, may play an important role. More importantly, in transverse external magnetic field, the phenomenological description for ferromagnetism in Ref.[39] leads to approximately constant transverse susceptibilities: $\chi_{yy} \sim 1/(\alpha_y + \gamma_{ij} k_i k_j)$. But experimentally, significant increase of the transverse spin fluctuations along the **b**-axis is observed (in URhGe)[71]. The enhanced transverse susceptibilities likely play an important role in the pairing mechanism in the high field region, and may even lead to a change of the p-wave order parameter. This will be further discussed in Chapter 6.

5.4 Effect of $\lambda(H)$ in URhGe

The theoretical framework in Ref.[86] does not contain any element specific to the system UCoGe, and should apply equally to other ferromagnetic superconducting systems, notably the sister compound URhGe. However, apart from the re-entrant superconducting phase induced by magnetic field along the **b**-axis, which is similar to the S-shape H_{c2} along the same field direction in UCoGe, the low field superconducting phase of URhGe[38] shows an H_{c2} behavior completely different from that of UCoGe (see figure 5.4). The anisotropy of H_{c2} between $\mathbf{H}//\mathbf{c}$ and $\mathbf{H}//\mathbf{a}$, **b**, is only of a factor 3, far from the 20 fold difference in UCoGe. H_{c2} along all three field directions is observed to have a downward curvature, as is expected in a usual case of superconductivity. Thus, most of the remarkable features of H_{c2} in UCoGe are not present in URhGe. At first sight, it seems that the effect of strong suppression of the pairing interaction for $\mathbf{H}//\mathbf{c}$, which is the origin of the usual H_{c2} behavior of UCoGe, is completely absent in the case of URhGe.

One important difference between the two systems is that compared with URhGe, UCoGe lies much closer to the ferromagnetic instability and is much more sensitive to external magnetic fields. The table below summarizes the main magnetic properties of the two systems (data taken from Ref.[15]):

	T_{Curie} (K)	M_0 (μ_B)	χ_a	χ_b (μ_B/T) 1.5 K	χ_c
UCoGe	2.5	0.05	0.0024	0.006	0.029
URhGe	9.5	0.4	0.006	0.03	0.01

In the Mineev's framework, according to equation (5.19), the field dependence of λ for field along the easy magnetization axis (z-axis) is governed by the variation of $(M_z/M_0)^2 - 1$, proportional to $\chi_z H/M_0$ at very low fields. Compared with UCoGe, URhGe has a about 8 times larger spontaneous moment M_0, and a magnetic susceptibility along the **c**-axis (**z**-axis) about 3 times smaller. As a consequence, the effect of the suppression of pairing interaction by magnetic field along the **c**-axis in URhGe is about 24 times weaker than in UCoGe, so it should not change the H_{c2} behavior of URhGe in the same drastic way as in UCoGe.

We then try to estimate the amplitude of the predicted variation of $\lambda(H)$ for $\mathbf{H}//\mathbf{c}$ in URhGe and its consequences on H_{c2} in an explicit way .

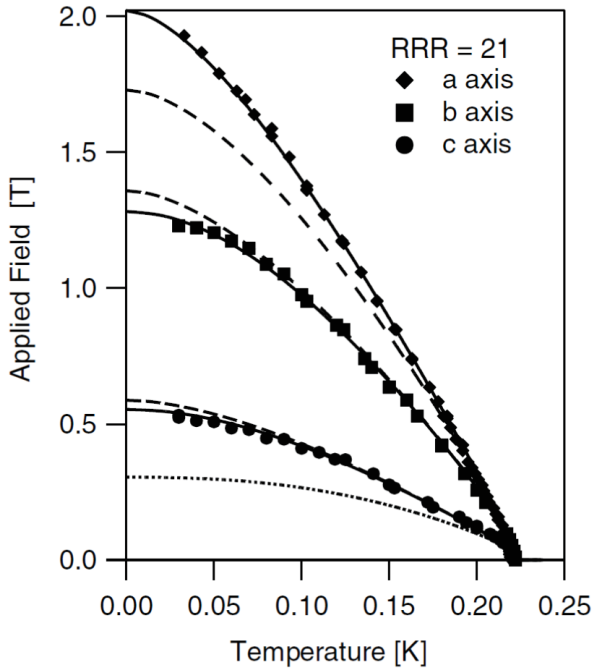

Figure 5.4 | H_{c2} of the low field superconducting phase of URhGe.[38]

In URhGe the field dependence of the Sommerfeld coefficient $\gamma(H)$ has been obtained for all three field directions with the temperature dependence of the magnetization[87], by using the Maxwell relation: $(\partial\gamma/\partial H)_T = (\partial^2 M/\partial T^2)_H$, which are presented in figure 5.5. $\gamma(H)$ for **H**//**a** and **b** in URhGe are observed to be almost constant when the field is small. For **H**//**b**, a 60% enhancement in $\gamma(H)$ is observed at H_R =12 T, which can be associated with the appearance of the re-entrant superconducting phase. For **H**//**c**, $\gamma(H)$ decreases steadily with magnetic field, by about 40% at 5 T. If we consider like in the case of UCoGe, that the variation of γ under field in URhGe is related uniquely to the change of superconducting pairing interactions, this reduction of γ means that the suppression of λ by field along the **c**-axis in URhGe is not negligible.

Estimation of $\lambda(0)$ from $\gamma(H)$ for H//b

We now associate the field evolution of Sommerfeld coefficient $\gamma(H)$ will the field dependence of the pairing strength $\lambda(H)$ and the H_{c2}.

Since in URhGe the effect of $\lambda(H)$ suppression for **H**//**c** is much weaker than in UCoGe, the effect of orbital limitation cannot be neglected as in UCoGe. Thus it is no longer possible to estimate the value of $\lambda(0)$ with the data of $\gamma(H)$ for **H**//**c** as is done in Chapter 4.3. However, it is possible in this case to estimate $\lambda(0)$ with the help of the $\gamma(H)$ data for **H**//**b**. The method is described in the following.

Figure 5.6a presents the same kind of strong-coupling calculations for H_{c2} as is done for UCoGe in Chapter 4.4, in order to extract the field dependence of $\lambda(H)$ for the re-entrant superconducting phase in URhGe. Ω is adjusted with the superconducting critical temperature T_{sc}. The averaged Fermi velocity $< v_F >$ is fixed at 3100 m/s, to reproduce the initial slope of H_{c2} for **H**//**b**. The value of $\lambda(0)$ is a free parameter in the calculations. Depending on $\lambda(0)$, we extract different field dependences of λ for **H**//**b**. $\lambda(0)$ is chosen so as to reproduce the strong maximum of $\gamma(H)$ at H_R: this is shown in figure 5.6b,

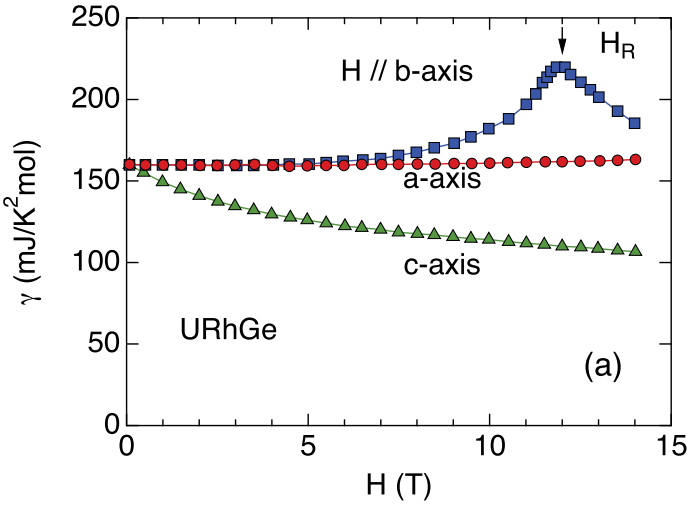

Figure 5.5 | Field dependence of the Sommerfeld coefficient $\gamma(H)$ in URhGe for field along all its three cristal axes, obtained from magnetization measurements through the Maxwell relation[87].

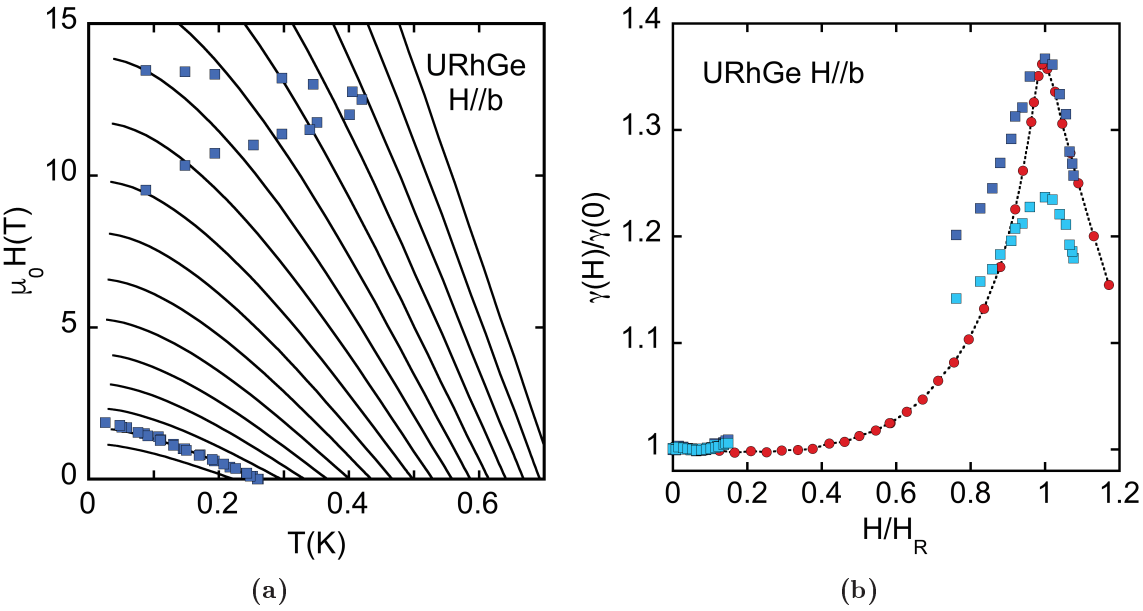

Figure 5.6 | **(a)**: Strong coupling calculation of $\mathbf{H_{c2}}$ in URhGe. Blue squares: data of $H_{c2}//\mathbf{b}$ in URhGe from Ref.[34]. Full lines: series of calculations of H_{c2} with fixed values of the strong coupling constant λ, which changes from 0.7 (left) to 1.5 (right) by steps of 0.05. $\Omega = 5.3$ K and $v_F = 3100$ m/s have been adjusted to match the $T_{sc} = 0.26$ K and initial slope for $\lambda = 0.75$ and $\mu^* \sim 0.1$. **(b)**: Adjustment of λ_0 in URhGe. Red circles: Sommerfeld coefficient for $\mathbf{H}//\mathbf{b}$ from Ref.[87], normalized to its value at zero field. Dark blue squares: $\gamma(H)/\gamma(0)$ for $\mathbf{H}//\mathbf{b}$ deduced from the calculations of H_{c2} presented in (a) for $\lambda(0) = 0.75$. Light blue squares: same ratio, but with the calculations of H_{c2} for $\lambda(0) = 0.6$. It shows that the amplitude of variation of the specific heat coefficient is a selective criterium for the determination of $\lambda(0)$ in this system.

where we trace the $\gamma(H)/\gamma(0)$, deduced from the $\lambda(H)$ which are extracted from H_{c2} for different values of $\lambda(0)$, according to the relation:

$$\gamma(H) = \frac{\gamma(0)}{1+\lambda(H)}(1+\lambda(H)).$$

We see that the enhancement of $\gamma(H)/\gamma(0)$ at H_R is very sensitive to the value of $\lambda(0)$, and by comparison with the the experimental data from Ref.[87] we obtain $\lambda(0) = 0.75$.

Evaluation of $\lambda(H)$ for H//c

Inversely, with the zero-field value of $\lambda(0) = 0.75$ estimated above (with the data for **H**//**b**), the field dependence of the pairing strength $\lambda(H)$ for **H**//**c** can be from the $\gamma(H)$ data, using:

$$\lambda(H) = \frac{\gamma(H)}{\gamma(0)}(1+\lambda(0)) - 1 \tag{4.14}$$

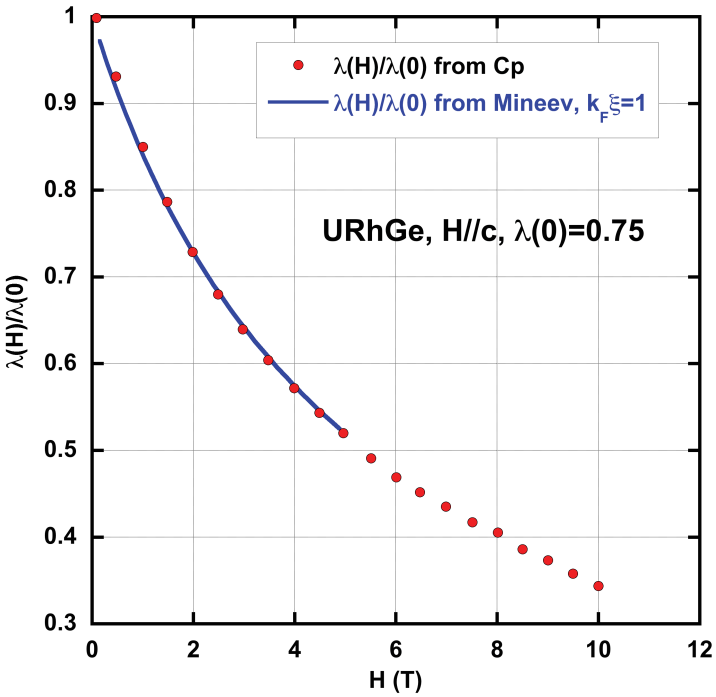

Figure 5.7 | Field dependence of normalized pairing strength $\lambda(H)/\lambda(0)$ for **H**//**c** in URhGe. Red circles: calculated with the $\gamma(H)$ data for **H**//**c** in figure 5.5, according to equation (**??**). Blue solid line: Predicted by Mineev's theory according to equation (5.19), with $\xi_{mag}k_F = 1$. The magnetization data taken from Ref.[87].

Figure 5.7 presents the $\lambda(H)$ for **H**//**c** in URhGe, calculated with the $\gamma(H)$ data for **H**//**c** shown in figure 5.5 (Ref.[87]). The blue line shows the prediction of $\lambda(H)$ of Mineev's theory, calculated with equation (5.19) and with the magnetization data $M(H)$ taken again from Ref.[87]. Comparison between $\lambda(H)$ obtained from $\gamma(H)$ and the theoretical prediction gives an excellent agreement, if $\xi_{mag}k_F$ is fixed at around 1. The smallness of this parameter compared with the case of UCoGe, where $\xi_{mag}k_F \sim 3.2$, suggests that the ferromagnetism in URhGe is closer to the localized limit. This seems to be reasonable,

owing to the larger ordered moment in URhGe and the first order transition occurring at H_R for **H**//**b**, which can be described as a re-orientation of localized magnetic moments along transverse magnetic field. In UCoGe, for the same field direction, although the Curie temperature is also suppressed at field around 12 T, no specific anomaly is observed in $M(H)$ around this field (at least for temperatures above 5.3 K)[88].

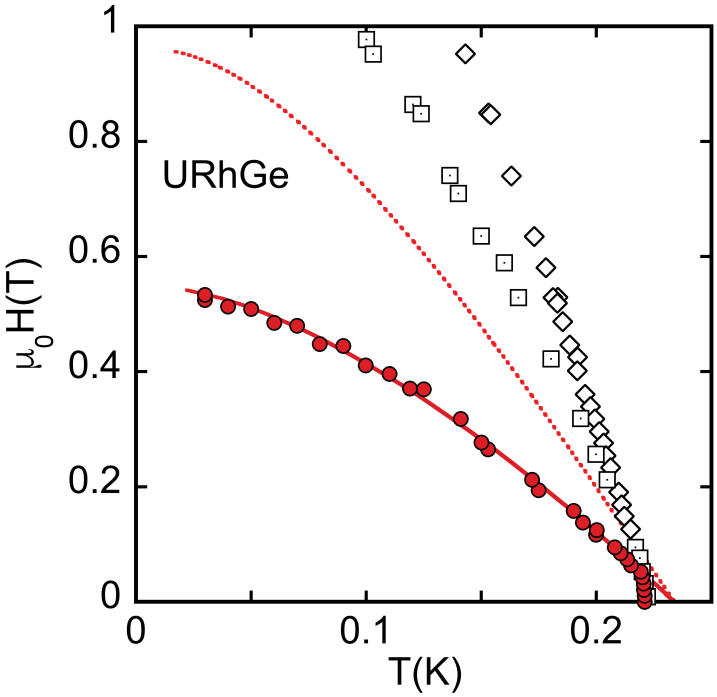

Figure 5.8 | Upper critical field of URhGe for **H**//**c** calculated based on the same strong coupling model as used in Chapter 4.
Red solid line: H_{c2} calculated with the $\lambda(H)$ obtained from the specific heat coefficient in figure 5.7. Red broken line: H_{c2} calculated with the same parameters, but supposing that $\lambda(H)$ fixed at $\lambda(0) = 0.75$. The markers show the experimental data from Ref.[38] for comparison: Red filled circles: **H**//**c**; Squares: **H**//**b**; Diamonds: **H**//**a**.

Figure 5.8 displays H_{c2} for **H**//**c** in URhGe (red solid line) calculated with $\lambda(H)$ in figure 5.7. The calculations are based on the same (s-wave) strong-coupling model used in Chapter 4.4. T_{sc} is shifted up to 0.26 K (linear extrapolation) to take into account the demagnetization effects. Ω is fixed at 5.3 K for T_{sc} to fit this extrapolated value. The averaged Fermi velocity $< v_F >$ is adjusted at 3700 m/s to match the slope of H_{c2} for **H**//**c**. For this value, the calculated H_{c2} for **H**//**c** is found to be in good agreement with the experimental H_{c2} of Ref.[38] (red circles) in the whole temperature range. The calculation of H_{c2} for **H**//**c** with λ fixed at its zero field value $\lambda = 0.75$ is also presented in figure 5.8 as the red broken line. All the other parameters except $\lambda(H)$ are fixed at the same values as used in the previous case. Compared with the H_{c2} calculated with λ fixed at its zero-field value (dotted line in Figure 5.8), the field dependence of $\lambda(H)$ for **H**//**c** in URhGe leads to a 40% reduction of $H_{c2}(0)$. The experimental H_{c2} for **H**//**a** and **b** of URhGe [38] are also presented with respectively the white open squares and diamonds in figure 5.8. One can see that the anisotropy between the **c** and **b**-axis would be very close to that between the **b** and **a**-axis, if there were no suppression of the pairing interaction for **H**//**c**.

As a conclusion, the reduction of λ by field along the **c**-axis exists equally in URhGe and leads to about a 40% reduction of $H_{c2}(0)$. Compared to UCoGe, this effect in URhGe is simply not strong enough to inverse the curvature of H_{c2}. Thus the difference between these two systems is purely quantitative, and arises from the different amplitudes of the field dependence of their magnetization.

5.5 Conclusion

This chapter shows that the field dependence of the pairing interaction, used in Chapter 4.4 to explain the H_{c2} and the normal phase properties of UCoGe, can also be deduced from the theory of Mineev[39]. This theory uses a general Landau free energy formalism to describe the magnetism in the orthorhombic ferromagnetic systems, and p-wave superconductivity is deduced microscopically based on pairing interaction mediated by magnetic susceptibilities.

For the simple case of $\mathbf{H}//\mathbf{c}$ where the pairing interactions are strongly suppressed by magnetic field, this phenomenological approach describes well the magnetic state of UCoGe. The theory leads to the field dependence of the pairing interaction in quantitative agreement with what is obtained with the analyses based on H_{c2} and Sommerfeld coefficient $\gamma(H)$ in the previous chapter, with only one (controlled) adjustable parameter. The same theory remains valid in the case of URhGe. The H_{c2} of URhGe, which seemed to be in striking contrast to the case of UCoGe, can also be understood in a quantitatively consistent way. These analyses show that UCoGe is a unique example among numerous unconventional superconductors, where change of the pairing interaction reflects itself in such a strong way in the superconducting and normal phase properties, that quantitative comparison with theory is possible. This gives a clear proof for the ferromagnetic origin of the pairing mechanism in this compound, and provides precious information about the general problem of magnetically mediated pairing mechanism.

For field perpendicular to the easy axis ($\mathbf{H}//\mathbf{b}$) in UCoGe, however, the magnetic state is much more complicated and the theory in Ref.[39] seems not to be sufficient. The next chapter will present experimental findings in this special case, which give hints for a new physical phenomenon happening in UCoGe.

Chapter 6

Superconductivity in transverse magnetic field in UCoGe

As shown in Chapter 1, when a magnetic field around 12 T is applied along the **b**-axis of URhGe, a re-entrant superconducting phase appears, with its maximum transition temperature higher than that in the low field superconducting phase[32]. The appearance of the re-entrant phase is associated with a field-induced magnetic instability (H_R), at which the ferromagnetic order is suppressed ($T_{Curie} \rightarrow 0$)(see figure 6.1)[34]. Neutron scattering measurements have shown that H_R corresponds to a (first-order) transition where the magnetic moments orient completely along the **b**-axis[32].

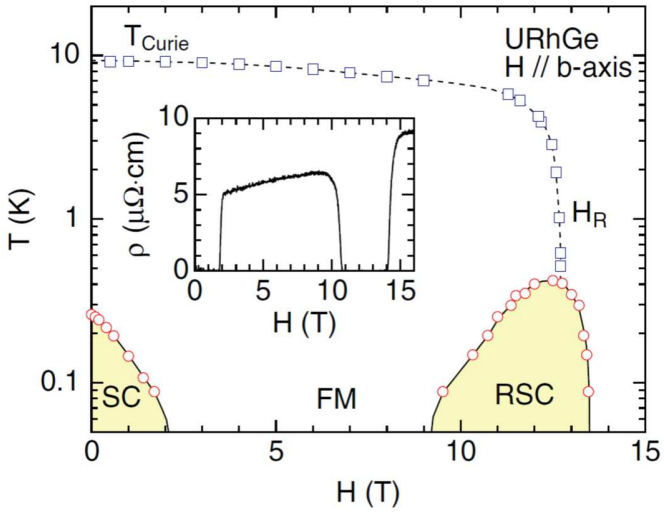

Figure 6.1 | Re-entrant superconducting phase and field-induced ferromagnetic instability at $H_R = 12$ T, for $\mathbf{H}//\mathbf{b}$ in URhGe[34].

Many studies have investigated the nature and the origin of the re-entrant superconducting state in URhGe[71, 89, 56, 44, 33]. Shubnikov-de Hass measurements suggest a Fermi surface change along with the appearance of the re-entrant superconducting phase[44]. NMR studies have shown the importance of the transverse magnetic fluctuations (along the **b**-axis) in this field region, in contrast to the dominating longitudinal fluctuations (along the **c**-axis) in the low field region[71, 89]. The question remains whether or not the pairing state in the re-entrant phase is the same as in the low field phase. In Ref.[56] a change of the p-wave order parameter around H_R has been discussed

theoretically, notably the possibility is mentioned, that a p-wave state with "$S_z = 0$" component appears in the high field region allowed by the cancellation between the external and exchange fields (see discussions on the Jaccarino-Peter effect in Chapter 3.3.2). This would definitely which would make the re-entrant phase different from the low field phase, where an "equal-spin-pairing" p-wave state is most likely realized[38].

In UCoGe for the same field direction, the situation is very similar. The Curie temperature is observed to be suppressed at a field around 12 T for $\mathbf{H}//\mathbf{b}$, accompanied by an enhancement of superconductivity which is reflected in the particular S-shape H_{c2}. Due to these resemblance, one might ask whether the scenario for $\mathbf{H}//\mathbf{b}$ in UCoGe is similar to the case of URhGe, and whether despite the continuous H_{c2} for $\mathbf{H}//\mathbf{b}$ in UCoGe, some change occurs due to a new mechanism for the formation of superconductivity. Up to now these questions remain mostly uninvestigated experimentally. This chapter presents some observations that for the first time give indications about a change in the superconducting phase under transverse magnetic field in UCoGe.

6.1 Upper critical field for H//b of UCoGe: bulk vs resistivity

In Chapter 3 the H_{c2} of UCoGe probed with thermal conductivity (κ/T) is consistent with the resistivity (ρ) measurements, for magnetic field along the **a** and **c** axes. The bulk transition measured by thermal conductivity for these two field directions are observed to be close to the temperature at which the resistivity goes to zero ($T_{\rho=0}$), apart from the low field region where the presence of filamentary superconductivity shifts the resistivity transition to higher temperatures (figure 3.9). However, this is no longer true for $\mathbf{H}//\mathbf{b}$ (figure 6.2): the H_{c2} measured with thermal conductivity crosses the resistivity transition ($T_{\rho=0}$) at around 9 T and it becomes even higher than the onset of resistivity transition for fields above 12 T. This is an anomalous behavior, for resistivity transitions are expected to occur at higher temperature than the bulk transition: in superconducting samples, there should be many percolating superconducting paths.

Due to the smallness of κ/T change in the superconducting state at high fields, it is not easy to determine the superconducting transition temperature from the thermal conductivity measurements.

In the κ/T curves in figure 3.6 the superconducting transition is marked by a kink, which becomes weaker and broader when magnetic field increases, and is difficult to detect on the raw data. The transition signatures are clearer on the derivative of κ/T with respect to the temperature ($(\kappa/T)'$), some of the which are presented in figure 6.3. The superconducting transition is marked by an increase of $(\kappa/T)'$ from the smooth (linear) variation in the normal phase. When the sample is completely inside the superconducting phase, the temperature dependence of κ/T is stronger and $(\kappa/T)'$ has higher values. However, since the temperature dependence of κ/T is not measured continuously in our study, $(\kappa/T)'$ can only be obtained with a large noise level, which makes accurate determination of H_{c2} difficult.

In Chapter 3, the H_{c2} is obtained by fitting the Lorenz ratio $L/L_0 = (\kappa\rho)/(TL_0)$, calculated with the extrapolated normal phase resistivity data. In the fit, L/L_0 is considered to be the sum of two contributions: the non-electronic part, fitted by a polynomial function of order 3, and the normalized electronic contribution to the thermal conductivity

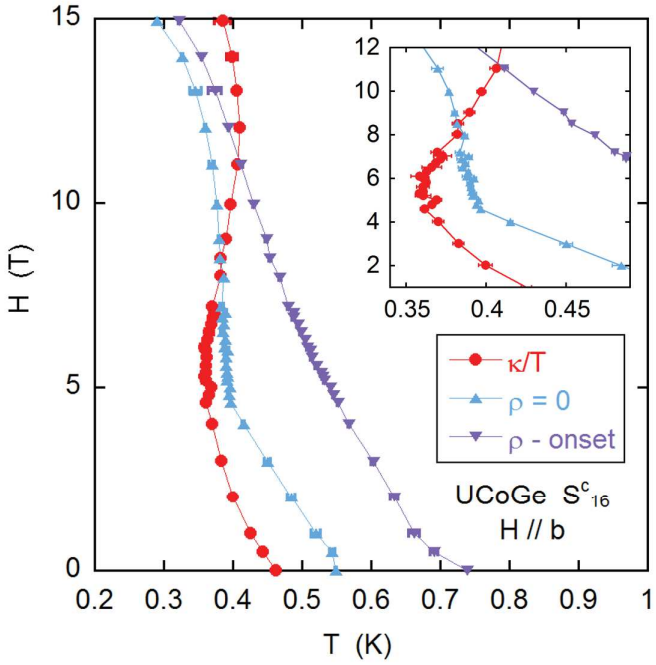

Figure 6.2 | H_{c2} for **H**//**b** of UCoGe, probed with thermal conductivity (red circles) and resistivity measurements (blue triangles for $T_{\rho=0}$ and purple triangles for the onset), measured with the sample S^c_{16} (same as figure 3.11). The inset shows a zoom around the minimum of H_{c2} measured with thermal conductivity.

(noted $\kappa/\kappa^{(n)}$ in this chapter), fitted with a function that equals 1 in the normal phase and decreases with temperature in the superconducting phase. The details of the fit have been presented in Chapter 3.2.1.

Figure 6.3 presents $\kappa/\kappa^{(n)}$ as a function of temperature along with the corresponding fit, for different magnetic fields along the **b**-axis along the **a**-axis, to be compared with $(\kappa/T)'$ and the normalized resistivity (ρ/ρ_n). The superconducting transition temperature given by the fit is indicated by the vertical dashed lines. They show that the fit determination is consistent with the $(\kappa/T)'$ curves. They also show that for all the measured fields for **H**//**a**, and for **H**//**b** up to around 7 T, the bulk transition (the vertical dashed line) lies close to the end of the resistivity transition ($T_{\rho=0}$), but for fields above 8 T along the **b**-axis, the resistivity transition shifts to lower temperature compared with the bulk transition. Thus the crossing of the bulk H_{c2} and the transition lines determined by resistivity in figure 6.2 is a robust phenomenon.

As discussed in Chapter 3.1, in many high-Tc superconductors, it is common to see that the resistivity transition ($T_{\rho=0}$) lies lower than the bulk superconducting transition. In these systems, thermally excited vortex motions leads to finite resistivity inside the superconducting phase, and the criteria $T_{\rho=0}$ corresponds to an irreversibility line above which the vortices are moving in the presence of an electrical current. In heavy fermion superconductors, whose T_{sc} are considerably lower, it is quite unusual to observe this phenomenon of vortex motion. (A rare example: the very pure (RRR = 670) URu_2Si_2 system[90], see figure 6.7)

Compared to the high-Tc superconductors, however, the situation in UCoGe is very different. In high-Tc superconductors, the resistivity transition broadens significantly

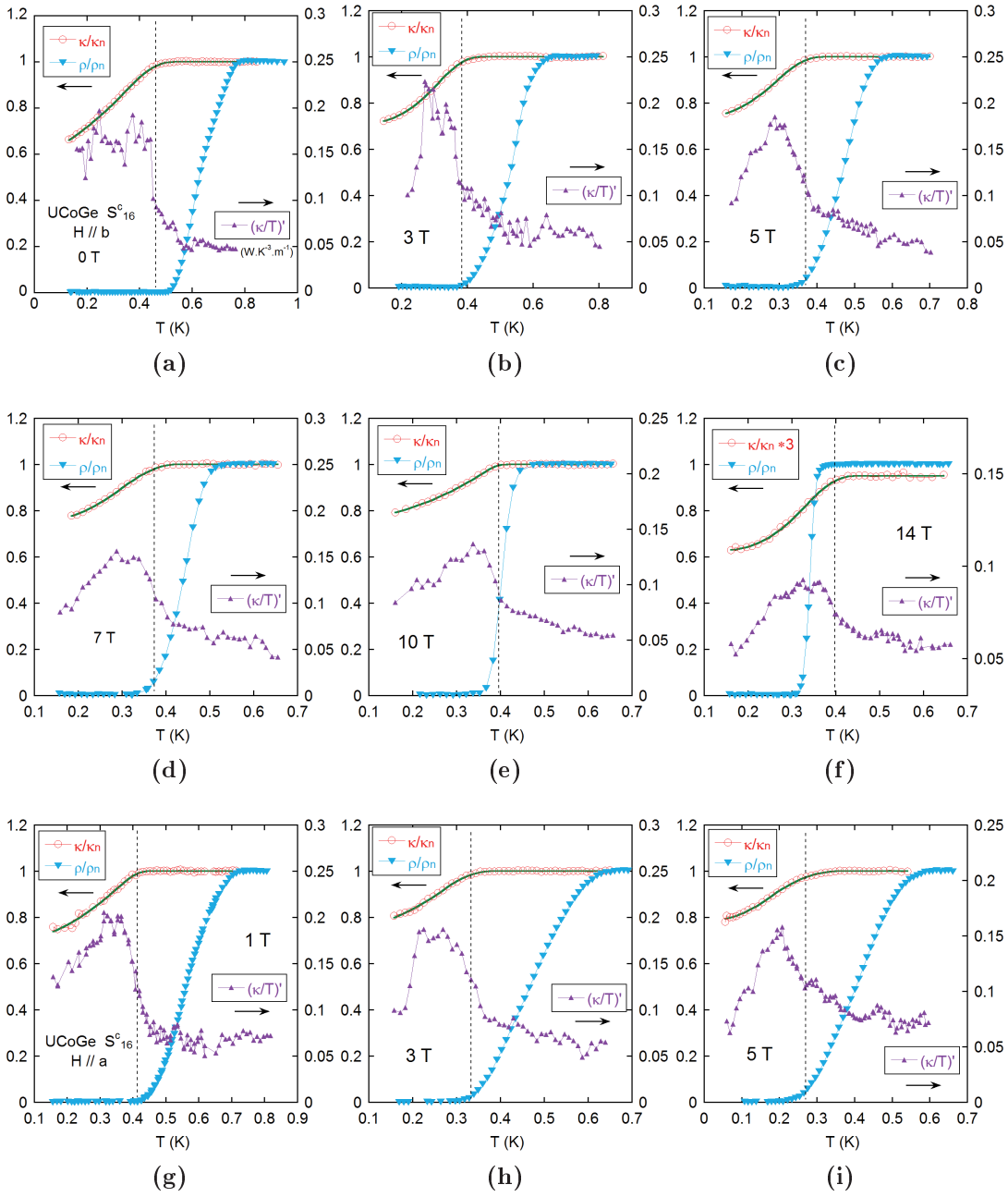

Figure 6.3 | Superconducting transition in κ/T and ρ of UCoGe, measured on the sample S^c_{16}, for different magnetic fields along the **b**-axis (**(a)** to **(f)**) and along the **a**-axis (**(g)** to **(i)**). Red circles: normalized electronic contribution to the thermal conductivity κ/κ_n. Blue triangles: resistivity normalized to the normal phase values (ρ/ρ_n). Purple triangles: Derivative of κ/T with respect to temperature, in unit of J K^{-3} m^{-1}, scale on the right. The vertical dashed line indicates the superconducting transition temperature given by the fit for the κ/κ_n data (green solid line).

under magnetic field, while in UCoGe, the resistivity transition becomes broader under magnetic field along the **a**-axis but becomes sharp under magnetic field along the **b**-axis (see figure 3.5 in Chapter 3.2.1). We will discuss this point in detail in the next section.

6.2 Resistivity transition width for H//b

The fit used in Chapter 3.2.1 gives one method to determine the completeness ($T_{\rho=0}$) and the onset (T_{onset}) of the resistivity transition. One can also use more classical criteria such as the temperatures at which the sample resistance reaches 90% and 10% of its normal phase value ($T_{10\%}$ and $T_{90\%}$). Figure 6.4 presents the $T_{\rho=0}$ and T_{onset} for **H//b** obtained with the fit, and the transition lines obtained with the $T_{10\%}$ and $T_{90\%}$ criteria, which show a good consistency between them. The inset presents the resistivity transition width, given by $T_{onset} - T_{\rho=0}$ or $T_{90\%} - T_{10\%}$, as a function of magnetic field. For fields below 3 T, some double-transition structure is present in the resistivity curve, which makes it difficult to fit perfectly the shape of the resistivity transition. This leads to the disagreement between the transition width given by the fit, and the one given by $T_{10\%}$ and $T_{90\%}$. However, above 3 T the two methods give consistent transition temperatures, and in both cases a sudden decrease in the transition width at around 5 T can be observed.

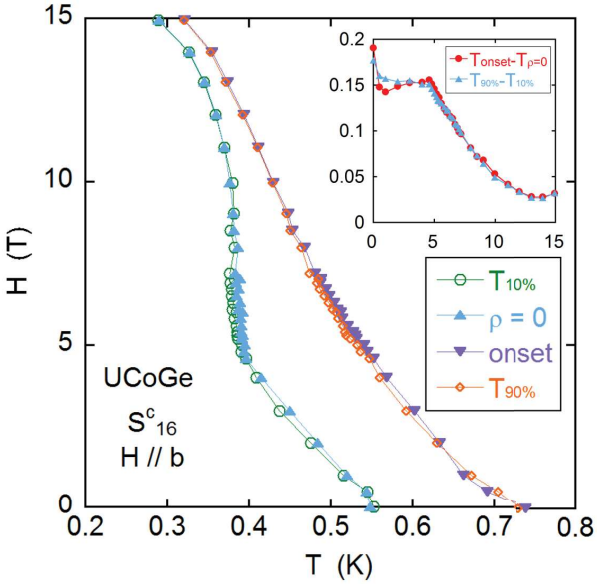

Figure 6.4 | H_{c2} of UCoGe for **H//b** probed with resistivity according to different criteria (sample S^c_{16}). Blue filled triangles and purple filled triangles: $T_{\rho=0}$ and T_{onset} given by the fit; green open circles: $T_{10\%}$; orange open diamonds: $T_{90\%}$. The inset shows the transition width as a function of field. Red circles: given by the fit. Blue triangles: $T_{90\%} - T_{10\%}$.

Resistivity of UCoGe in magnetic field along the **b**-axis has been previously measured by Dai Aoki on two other samples (S^a_{30} and S^c_{35}, both the in transverse field configuration), up to 16 T. The measurements on the sample S^a_{30} have been published in Ref.[30]. Figure 6.5 presents the measurements on the sample S^c_{35}. In all three samples the resistivity transition becomes sharp in magnetic field along the **b**-axis. Figure 6.6a presents the field dependence of the resistivity transition width, given by $T_{90\%} - T_{10\%}$, of the three samples, and figure 6.6b presents their H_{c2} probed with resistivity with the $T_{10\%}$ (filled markers) and $T_{90\%}$ (open markers) criteria. In both sample S^c_{16} and S^c_{35}, $T_{90\%} - T_{10\%}$ is constant or increases slightly for field below 4 T (except close to 0 T), but decreases suddenly at 5 T. For sample S^a_{30} the resistivity transition has a more complicated form for magnetic field

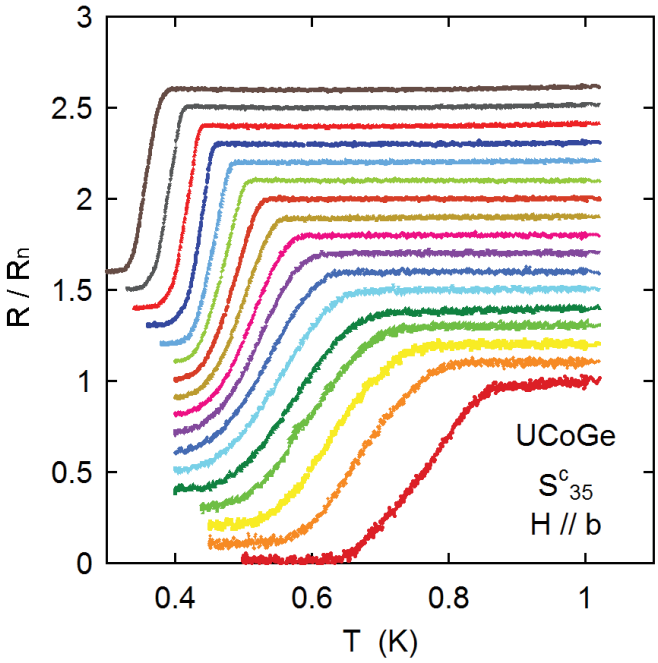

Figure 6.5 | Resistivity normalized by the normal phase value ρ/ρ_n as a function of temperature of UCoGe (sample S^c_{35}, previously measured by D.Aoki, unpublished data) under different magnetic field along the **b**-axis: every tesla from 0 T (on the right) to 16 T (on the left). The curves are shifted to be seen clearly.

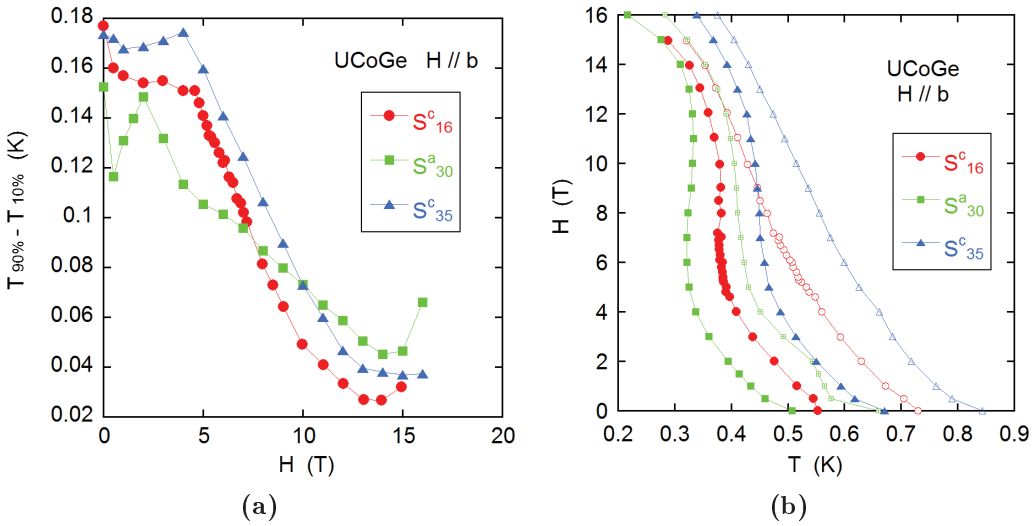

(a) **(b)**

Figure 6.6 | **(a)**: Field dependence of the resistivity transition width, given by $T_{90\%} - T_{10\%}$, of UCoGe for **H**//**b**, measured on sample S^c_{16} and two samples previously measured by D. Aoki (sample S^a_{30}, noted #1 in Ref.[30] and S^c_{35}, unpublished data). **(b)**: H_{c2} of UCoGe for **H**//**b** probed with resistivity on three samples. Different colors correspond to the different samples. The filled marks correspond to the $T_{10\%}$ criteria and the open marks correspond to the $T_{90\%}$ criteria.

below 4 T and the field dependence of $T_{90\%} - T_{10\%}$ shows irregularities in this region. But it shares the global tendency that the resistivity transition gets sharp under field along

the **b**-axis.

The evolution of the resistivity transition width under magnetic field may be associated with the curvature of the H_{c2}. We expect that at fields where the slope of H_{c2} is large, the superconducting transition will be sharp, because a non-homogeneous distribution of the magnetic field in different parts of the sample will lead to a smaller dispersion of T_{sc}. In this sense the resistivity transition should be the sharpest where the H_{c2} shows a minimum or maximum. However, this is in complete contradiction with the evolution of $T_{90\%} - T_{10\%}$ in figure 6.6a, because in the whole field range between 5 T and 10 T where H_{c2} is almost vertical, $T_{90\%} - T_{10\%}$ decreases steadily, while for field above 10 T where the H_{c2} strongly curves towards lower temperature and its slope becomes small, $T_{90\%} - T_{10\%}$ remains around the minimum value instead of increasing strongly.

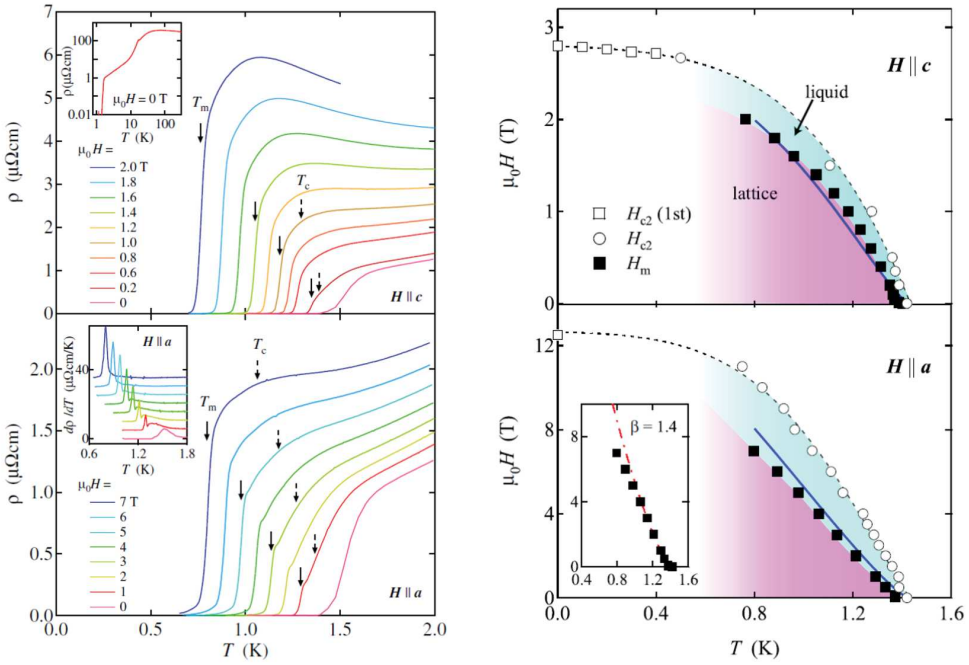

Figure 6.7 | (a): Temperature dependence of the resistivity of an ultraclean URu_2Si_2 sample (RRR = 670) for **H**//**c** (upper panel) and **H**//**a** (lower panel)[90]. The solid arrows indicate the vortex melting transition defined as a peak of $d\rho/dT$ in the inset of the lower panel. The dashed arrows indicate the superconducting transition T_c determined by thermal conductivity measurements. **(b)**: H-T phase diagram of URu_2Si_2 for **H**//**c** (upper panel) and **H**//**a** (lower panel). Open symbols represent the H_{c2} lines determined by thermal conductivity measurements. Filled squares present the vortex melting transition between a vortex solid (pink) and a vortex liquid (sky blue) phase.

The behavior of the resistivity transitions in UCoGe under magnetic field along the **b**-axis is similar to what is observed in another heavy fermion system URu_2Si_2[90]. Figure 6.7a presents the temperature dependence of the resistivity of an ultraclean URu_2Si_2 sample (RRR = 670) for **H**//**c** and **H**//**a** and figure 6.7b presents the H-T phase diagram for superconductivity of URu_2Si_2 for these two field directions. It is observed that the H_{c2} probed with thermal conductivity measurements is higher in temperature than the

resistivity measurements, and the latter appears in an abrupt way under magnetic field. This is actually what is observed in UCoGe when a magnetic field above 8 T is applied along the **b**-axis. In Ref.[90] the authors associate this sharp transition in resistivity with a melting transition (T_m), above which the vortices enter a liquid phase, and the sample has finite resistivity even if it is superconducting.

However, the resemblance of these two systems raises other questions: for URu_2Si_2, the phenomenon has been observed in high quality samples, where the vortex pinning is weak. We do observe the same behavior in a much less clean sample in UCoGe (RRR = 16 instead of RRR = 670) This questions the pinning mechanism: is it controlled by impurities? Is is similar in the two systems? Second, in URu_2Si_2 the resistivity transition appears sharp, and lies lower than the bulk superconducting transition given by thermal conductivity, as soon as small magnetic field (0.6 T) is applied. Moreover, the same behavior is observed both for the field in the basal plane or along the **c**-axis. In UCoGe, this behavior appears only in magnetic field above 8 T for $\mathbf{H}//\mathbf{b}$. For the other two field directions, such behavior is not observed: for $\mathbf{H}//\mathbf{a}$, the H_{c2} given by thermal conductivity follows the $T_{\rho=0}$ line of resistivity up to 5 T, and the resistivity transition width continues to broaden up to 8 T in our measurements, and up to 16 T in previous studies in Ref.[30]. This suggests that a change in the mixed state of UCoGe is triggered by high magnetic fields only along the **b**-axis.

These questions strongly motivate investigations on the vortex state of UCoGe, in magnetic field along its **b**-axis. In our experiment, efforts have been made to study the superconducting critical current and the effect of increasing electrical current on the resistivity. But due to the limitation of the thermal conductivity set-up, (above all to the associated heating effect that strongly influences the sample resistance when close to a superconducting transition), these measurements did not reach firm conclusions. Understanding these phenomena thus requires future experiments specifically designed to probe the vortex motions for $\mathbf{H}//\mathbf{b}$ in UCoGe.

6.3 Thermal conductivity in the superconducting phase

Another experimental indication pointing to a change of the superconducting phase in UCoGe under magnetic field along the **b**-axis, comes from the thermal conductivity data inside the superconducting phase. Figure 6.8 presents the electronic contributions to the thermal conductivity normalized to the normal phase values (κ/κ_n), as a function of the temperature divided by the superconducting transition temperature (T/T_{sc}), under different magnetic fields along the **b**-axis.

For fields below 9 T, κ/κ_n inside the superconducting phase increases only slightly with field. It is even independent of magnetic field within the measurements errors, for fields between 5 T and 8 T. However, for fields above 9 T, κ/κ_n increases steadily with field and approaches 1 quickly (the superconducting transition signal shrinks).

Magnetic field influences thermal conductivity inside the superconducting phase both by changing the quasiparticle mean free path and by changing the density of the excited quasiparticles due to the shift of the electron energy (Doppler effect). For a low quality sample the former effect is weak, as elastic scattering processes from the impurities dominate the quasiparticle transport. For the latter, the field dependence of κ/T will depend on the superconducting order parameter, or more exactly, on the nodal structure of the superconducting gap[91, 92, 93]. Figure 6.9 presents the field dependence of κ/κ_n

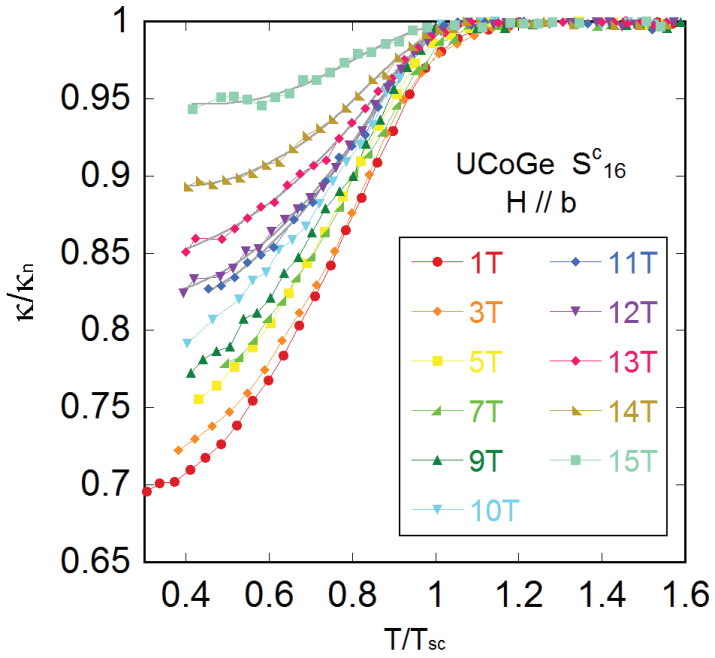

Figure 6.8 | Electronic contributions to the thermal conductivity normalized to its normal phase values κ/κ_n, as a function of temperature divided by the superconducting transition temperature T/T_{sc}, under different magnetic fields along the **b**-axis of UCoGe (sample # 1). For field above 10 T, the gray solid lines present the fit used in Chapter 3.2.1 to determine H_{c2}.

in the $T = 0$ limit, for different superconducting systems[91]. For an s-wave superconductor in the clean limit which has nodeless superconducting gap (Nb [94]), at $T = 0$ the quasiparticles are localized inside the vortex cores with a much reduced mean free path ($\xi_0 << l$). Thus $\kappa/\kappa_n(0)$ increases barely with magnetic field, until it is very close to H_{c2}. For superconductors that presents nodes on the gap, due the (Doppler) energy shift under magnetic field, the system will have finite density of states at zero temperature under field, and $\kappa/\kappa_n(0)$ increases more strongly with magnetic field: in the unconventional superconductor UPt_3[95], $\kappa/\kappa_n(0)$ is linearly in field. In multigap superconductors MgB_2[96] and $PrOs_4Sb_{12}$[91], $\kappa/\kappa_n(0)$ shows a double jump structure, due to the different field scales for the suppression of the small and the large gaps.

Unfortunately, in our study, the measurements were not performed down to low enough temperature to be able to give precise values of $\kappa/\kappa_n(0)$ for $\mathbf{H}//\mathbf{b}$. For most of the fields the κ/T measurements are preformed down to 150 mK, because below this temperature the mechanical vibrations from the pulse-tube unit lead to increasing large noise level on the sample thermometers (see Chapter 2.1.2). However, it is possible to obtain the field dependence of $\kappa/\kappa_n(0)$ qualitatively. The fit used to determine H_{c2} in Chapter 3.2.1 gives one way to obtain $\kappa/\kappa_n(0)$. Some of these fits are presented in figure 6.8 together with the raw κ/κ_n data. It fits the κ/κ_n data in the superconducting phase with a linear decrease then followed by a parabolic rounding for T close to zero, with the slope fixed at zero at $T = 0$. However, the extrapolation to zero with quadratic fit is rather arbitrary. To see the robustness of the conclusion drawn from this analysis, we also present the value extrapolated linearly with the slope right below T_{sc} inside the superconducting phase. Figure 6.10a presents the field dependence of $\kappa/\kappa_n(0)$ given by the fit, and the one

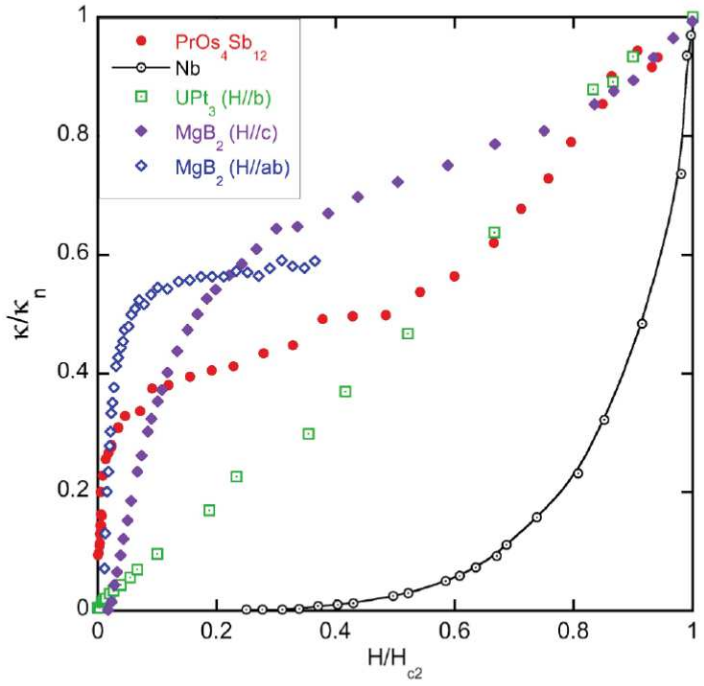

Figure 6.9 | κ/κ_n at the $T = 0$ limit as a function of magnetic field, in a conventional s-wave (nodeless gap) superconductor (Nb), two heavy fermion superconductors (UPt_3 and $PrOs_4Sb_{12}$) and a multiband conventional superconductor MgB_2. Figure from Ref.[91].

obtained with linear extrapolation. In both cases $\kappa/\kappa_n(0)$ stays almost constant for fields between 5 T and 8 T but start to increase steadily with field above 8 T. Figure 6.10b presents the $\kappa/\kappa_n(0)$ obtained from the above two fits, as a function of $H/H_{c2}(0)$, where the $H_{c2}(0)$ values, which depend on the applied field through the superconducting pairing strength $\lambda(H)$, are given by the strong-coupling calculations in Chapter 4.3. On the same graph, the field dependence of $\kappa/\kappa_n(0)$ for $\mathbf{H}//\mathbf{c}$ is also presented for comparison. The data is obtained from the low temperature measurements on a high quality sample (S^b_{150}) in Ref.[28], and the $H_{c2}(0)$ is re-calculated in a similar way with the strong coupling calculations (in Ref.[28], the field dependence of the pairing interaction, thus of $H_{c2}(0)$, is not considered). The result for $\mathbf{H}//\mathbf{c}$ is very comparable with the case of a multiband superconductor (indicated by the solid line).

Due to the incertitudes in the extrapolation of $\kappa(0)$, we can only discuss qualitatively the κ/κ_n vs $H/H_{c2}(0)$ for $\mathbf{H}//\mathbf{b}$. Nonetheless, the sudden upturn of $\kappa/\kappa_n(0)$ at field around 9 T seems robust, and it is a phenomenon specific to this field direction. It gives a new indication that a change of the superconducting phase might occur under magnetic field along the **b**-axis. It could be for example related to the appearance of new nodal structure coming from a change of the superconducting order parameter, or a change of the nodal direction in the superconducting gap with respect to the magnetic field, which leads to an increased amount of quasiparticles excited under field. It could also arise from a change in the type of vortices, which can be very diverse in p-wave superconductors. For example, in superfluid ^{3}He, depending on the ratio of orbital to paramagnetic limitation (i.e: rotating velocity versus applied field), many different vortices may appear, some of which with no "normal core" (called continuous vortices), see figure 7 in Ref.[97]. Such vortices would be expected to be very weakly pinned, which might explain the sudden

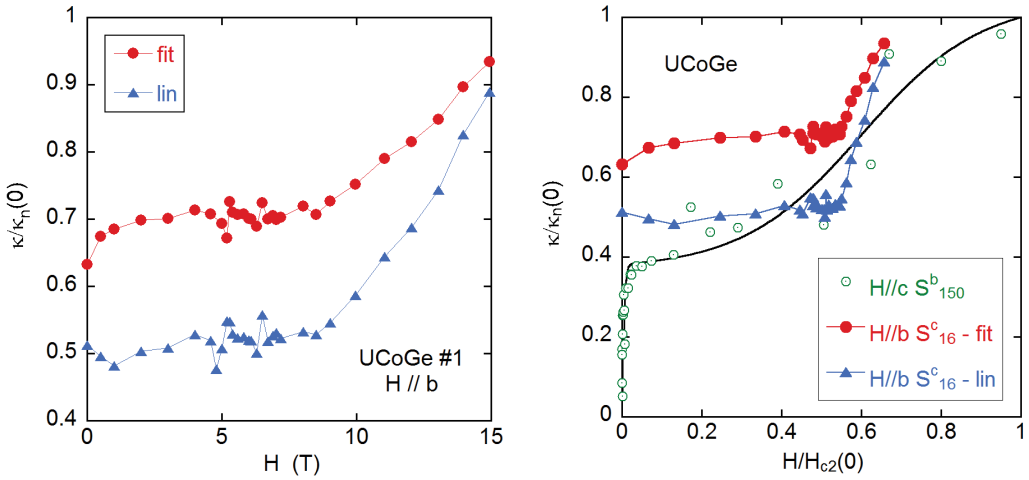

(a) (b)

Figure 6.10 | **(a)**: $\kappa/\kappa_n(0)$ as a function of field for $\mathbf{H}//\mathbf{b}$ in UCoGe. Red circles: given by the fit in Chapter 3.2.1. Blue triangles: obtained with linear extrapolations of the κ/κ_n below T_{sc} (sample S^c_{16}). **(b)**: $\kappa/\kappa_n(0)$ as a function of $H/H_{c2}(0)$ for $\mathbf{H}//\mathbf{b}$ in UCoGe (sample S^c_{16}), with the $H_{c2}(0)$ given by the strong coupling calculations in Chapter 4.3. $\kappa/\kappa_n(0)$ for $\mathbf{H}//\mathbf{c}$ in UCoGe from the low temperature measurements on a high quality sample S^b_{150} in Ref.[28] is equally presented for comparison, with the $H_{c2}(0)$ re-adjusted with the analysis in Chapter 4.4 in this study. The solid line is a guide for the eye.

drop of the critical current.

6.4 Discussions and perspectives

The above discussions present two features that might shed light on the understanding of superconductivity in magnetic field $\mathbf{H}//\mathbf{b}$ in UCoGe.

The first one is the crossing of the H_{c2} from bulk probe (thermal conductivity) and the H_{c2} from resistivity at 8 T, together with the narrowed resistivity transition above this field: it can be most naturally associated with a vortex-liquid state as is observed in URu_2Si_2[90]. However, to confirm this explication, we need more detailed studies of the vortex state in this case. The reason for which this behavior appears only at field above 8 T for $\mathbf{H}//\mathbf{b}$, and not in the other field directions or at lower fields, remains unknown.

The second feature is the field dependence of $\kappa/\kappa_n(0)$. Although our measurements present only the qualitative evolution of $\kappa/\kappa_n(0)$ under field, it shows clearly that $\kappa/\kappa_n(0)$ remains little changed below 8 T for field along the **b**-axis in UCoGe and increases drastically with magnetic field above 8 T.

The interpretation for these phenomena is still open. But both of them suggest that a change occurs inside the superconducting phase at magnetic field around 8 T. It could be associated to a modification of the nodal structure in the superconducting gap, which leads to different field dependence of heat transport, or a change in the properties of the vortices that could be induced by a symmetry change of the p-wave order parameter.

The situation in UCoGe for $\mathbf{H}//\mathbf{b}$ being similar to the case of URhGe, such kind of change of superconducting state is somehow awaited.

In URhGe the importance of transverse magnetic fluctuations at field around H_R have been experimentally proved by NMR studies, which suggest at the same time their role in the formation of re-entrant superconductivity. This makes the re-entrant phase different from the low field phase, where the magnetic fluctuations are strongly Ising-type along the spontaneous axis (**c**-axis). Although direct measurements of the transverse magnetic fluctuations have not been performed in UCoGe[75], it is natural to consider that in UCoGe, a similar situation might be present. Notably, the discussions on the pairing strength under **H**//**b** in Chapter 5.2 reveals that without taking into account the enhancement of the transverse magnetic fluctuations (along the **b**-axis), the predicted increase of the pairing strength λ with field along **b**-axis is too weak compared with that extracted from the experimental H_{c2} (with the strong coupling calculations in Chapter4.4).

What is more, under transverse magnetic fields (**H**//**a** and **b**), the spin directions of the paired electrons are not expected to be aligned along the **c**-axis (parallel to the spontaneous exchange field in the ferromagnetic state) as in zero field. They are supposed to be rotated with transverse external magnetic field, depending on the amplitude of the external field with respect to the internal exchange field [39, 56].

This is a strong difference from the case **H**//**c**, where only Ising-type longitudinal magnetic fluctuations are present[72, 57]. This deep change of the pairing mechanism could easily drive a change of p-wave order parameter with respect to the zero field or **H**//**c** case. So the continuous H_{c2} for **H**//**b** in UCoGe might nevertheless result from the junction of two different superconducting phases, similar to the case of URhGe. In our study, efforts have been made to investigate such a scenario by measuring closely the H_{c2} around the minimum at around 5 T, and to try to detect a kink (change of slope) in H_{c2} that could reflect such a transition (see inset of figure 6.2). Unfortunately this cannot be detected clearly from our measurements within the error bars associated with the H_{c2} determination by thermal conductivity.

To clarify the above scenario, it is necessary to study the superconducting state of UCoGe under **H**//**b** with other experimental methods, especially with bulk sensible tools and microscopic measurements. For example it would be very useful to study the vortex state in this case with tunneling spectroscopy methods? The results presented here only give a first hint about the existence of such a change of state inside the superconducting phase under **H**//**b** in UCoGe.

Chapter 7

Miscellaneous

This chapter discuss about three independent problems in UCoGe and UBe_{13}, which are not directly related to the other parts of this study. The results presented here show the progress made in each of these subjects. Section 7.1 deals with thermal conductivity measurements in the normal phase of UCoGe, which is a following of the PhD work of M.Taupin [49]. Section 7.2 presents specific heat measurements of UCoGe up to 16 T for magnetic fields along the **c**-axis, which are related to field induced Fermi surface changes. Section 7.3 presents the first results on the other system, UBe_{13}, and the quest to high quality single crystals for this compound.

7.1 Thermal conductivity in the normal phase of UCoGe

It has been mentioned in Chapter 4.1 that the normal phase of UCoGe is characterized by the presence of magnetic fluctuations which are strongly suppressed by magnetic field along its **c**-axis. NQR and NMR studies have clearly shown the existence of these Ising-type spin fluctuations and their response to external field. The Sommerfeld coefficient γ equally decreases strongly with magnetic field along **c**-axis within a very narrow field range. This section will discuss about the influence of the magnetic fluctuations on the normal phase electrical and heat transport properties in UCoGe. In particular, it will focus on an extra contribution to the thermal transport in UCoGe that has magnetic origin[98].

7.1.1 Previous studies

Normal phase thermal conductivity in UCoGe has been studied on several samples in Ref.[49, 98], under magnetic field along the **c**-axis. At temperature near T_{Curie} $(2-3\,\mathrm{K})$, strong negative magnetoresistance for $\mathbf{H}//\mathbf{c}$ is observed in all these samples, regardless of their quality, both in the longitudinal or transverse configuration. Based on quantitative analyses of the thermal conductivity (κ) and resistivity (ρ) data on different samples, Ref.[98] points out the existence of some extra contributions to the thermal transport, other than the electrons and the phonons, which are strongly suppressed by magnetic field along **c**-axis. These contributions (κ_{extra}) are thus considered to have magnetic origin, and are associated by the authors with the spin fluctuations observed in the NMR studies[72].

Figure(7.1a) presents the temperature dependence of the thermal conductivity (κ/T) of UCoGe[98] (and resistivity ρ in the inset), under magnetic field at 0, 2 and 6 T for $\mathbf{H}//\mathbf{c}$, measured on the sample S^c_{16}, (same sample used for the thermal conductivity

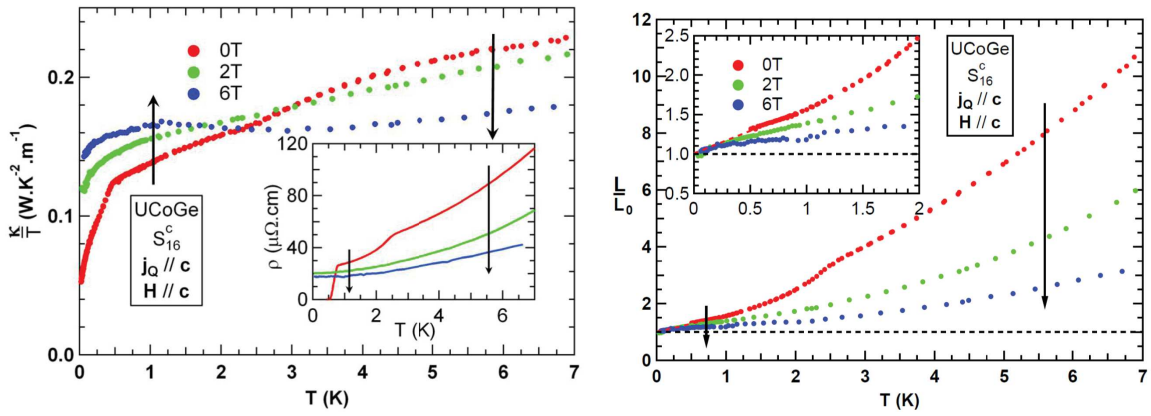

Figure 7.1 | Thermal conductivity measurements[98] under magnetic field **H**//**c** of UCoGe performed on S^c_{16}, (**j**//**c**, RRR = 16) The red, green and blue circles represent respectively the data at 0, 2 and 6 T for **H**//**c**. ((**a**)): Temperature dependence of thermal conductivity κ/T and of resistivity ρ in the inset. ((**b**)): Temperature dependence of Lorentz ratio L/L_0. The inset presents a zoom on the low temperature part.

measurements in chapter 3). We recall that in Ref.[98, 49] and in this study, the UCoGe sample S^i_x is a bar-shaped sample with the current direction along the i axis and RRR equal to x. Strong negative magnetoresistance is observed in the whole temperature range.

As introduced in Chapter2.1.1, thermal conductivity in a metal is the sum of the heat conduction through different channels in parallel (electrons, phonons,etc):

$$\kappa = \kappa_{elec} + \kappa_{phonon} + ... \tag{7.1}$$

The electronic part of the thermal conductivity κ_{elec} can be evaluated with the resistivity data with the Wiedemann-Franz law. Since resistivity decreases with **H**//**c** in sample S^c_{16} in the whole temperature range, κ_{elec} should increase with magnetic field. However, the total thermal conductivity κ decreases with magnetic field for $T > 3$ K. This suggests the existence of an extra contribution (different from the electrons and the phonons) to the thermal conductivity, strongly suppressed by **H**//**c**.

To quantify this extra contribution to thermal transport, the Lorentz ratio L/L_0 is calculated, i.e. is the ratio between the total thermal conductivity κ and the electronic contribution to the thermal conductivity κ_{elec} estimated with Wiedemann-Franz law (cf. Chapter(2.1.1)):

$$\frac{L}{L_0} = \frac{\kappa\rho}{L_0 T} \tag{7.2}$$

where L_0 is the Lorenz number. Figure(7.1b) presents the the temperature dependence the Lorentz ratio L/L_0 on sample S^c_{16}. The large value of L/L_0 (more than 10) at 7 K shows the smallness of the electrons' contribution in thermal conductivity, due to the large residual resistivity of this sample. Under magnetic field, L/L_0 is strongly suppressed, both due to the suppression of κ_{extra}, and to the increase of κ_{elec} along with the negative magnetoresistance.

The existence of this field-dependent extra contribution κ_{extra} is a robust phenomenon and is observed in all samples studied in Ref.[98], regardless of their quality. In all the cases, it is strongly suppressed by the magnetic field along **c**-axis, but remains little changed under transverse magnetic field (**H**//**b**).

Comparison between different samples in Ref.[98] suggests that this κ_{extra} are strongly anisotropic with the current direction. Figure 7.2 presents κ_{extra}/T at zero field in several samples S^c_{16}, S^a_{65}, S^c_{110} and S^b_{150}. In all samples κ_{extra}/T has similar behaviors in the paramagnetic phase (for $T > T_{Curie}$). However, for temperatures below about 1.5 K, κ_{extra}/T is much stronger in the sample S^b_{150}. This could sign an anisotropy of the magnetic fluctuations, which would have much stronger weight for $\mathbf{q}//\mathbf{b}$. An open question is to know whether the large increase of κ_{extra}/T below 1.5 K starts specifically below T_{Curie}, which means that it could be associated with excitations appearing in the ferromagnetic phase.

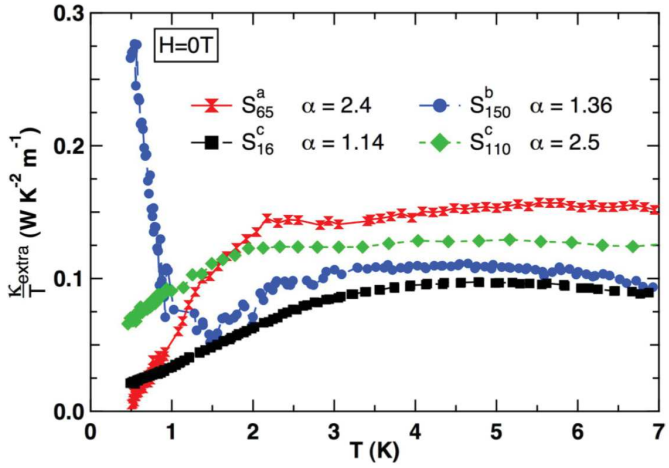

Figure 7.2 | The extra contribution to thermal conductivity in UCoGe in samples with different current direction[98]. Temperature dependence of κ_{extra}/T of four samples of UCoGe: S^c_{16} (black), S^a_{65} (red), S^c_{110} (green) and S^b_{150} (blue). In the analyses in Ref.[98] an empirical model is used to correct deviations from the Wiedemann-Franz law in high quality samples, which is parametrized by the number α associated with each sample.

However, a precise analysis for this κ_{extra} in Ref.[98] has been difficult because of the high quality of the measured samples (large RRR). In such cases, the electrons have a large contribution to the thermal transport, and are strongly influenced by the inelastic scattering process, which leads to deviations from the Wiedemann-Franz law. Ref.[98] uses an empirical model to take into account of this deviation, and a parameter α is associated with each sample in the analyses.

This complication motives us to study the current direction dependence of this κ_{extra} in UCoGe on low quality samples. In low quality samples, the large residual resistivity of the sample makes the electronic contributions to thermal conductivity small compared with κ_{phonon} and κ_{extra}, and as the elastic scattering process from the impurities dominate the low temperature electronic transport properties, the electronic contributions to κ/T can be well estimated with the Wiedemann-Franz law.

For this purpose, thermal conductivity and resistivity measurements have been performed on two low quality samples: sample S^b_4 and S^a_{11}. The results are presented and discussed in the following.

7.1.2 Results and discussions

Figure 7.3 and 7.4 present thermal conductivity and resistivity measurements of UCoGe under magnetic fields along the **c**-axis, respectively on sample S_4^b (RRR = 4, with **j**//**b**), and sample S_{11}^a (RRR = 11, with **j**//**a**).

Compared with sample S_{16}^c in figure 7.1a, these two samples are measured in a transverse configuration, with the magnetic field perpendicular to the current direction. In such case, the magnetic field influences the electron motion through the orbital effect, which reduces their mean free time and favors positive magnetoresistance. Yet negative magnetoresistance is still observed in both samples in a large temperature range, especially for field below 1.5 T (see figure 7.4d). On the other hand, like the results on sample S_{16}^c in figure 7.1a, the values of κ/T decreases with magnetic field in almost the whole temperature range, despite the presence of negative magnetoresistance. Thus the measurements in these two samples support once again the existence of an extra contribution κ_{extra} to the thermal conductivity strongly suppressed by **H**//**c**.

With these data there is no promising way to separate the magnetic contributions κ_{extra} from the phonon contributions κ_{phonon}. Figure 7.5 presents the temperature dependences of the sum of these two non-electronic contributions ($\kappa/T - \kappa_{elec}/T$), along with the Lorentz ratio (L/L_0), at different magnetic fields along the **c**-axis in samples S_4^b and S_{11}^a. L/L_0 increases up to respectively around 10 and 9 in the two samples, at T =7 K and at zero field, consistent with the large residual resistivity in the two samples (respectively about 45 $\mu\Omega$.cm and 30 $\mu\Omega$.cm). Under magnetic field L/L_0 is strongly suppressed in both samples, similar to sample S_{16}^c in figure 7.1a.

The amplitude of the non-electronic contributions to the thermal conductivity $\kappa/T - \kappa_{elec}/T$ in these two samples present similar temperature dependence and have close values at T =7 K (about 0.25 W K^{-2} m^{-1} in both cases). Under magnetic field along the **c**-axis, it has a stronger reduction in sample S_4^b (about a 40% reduction at 7 K for H = 6 T) than in S_{11}^a (only about a 15% reduction at 7 K for H = 6 T). This difference in response to magnetic field may be related to the different current directions in the samples: for sample S_4^b, **j**//**b** and for sample S_{11}^a, **j**//**a**.

However, the very large magnetic contribution, observed in sample S_{150}^b in figure 7.2, which has an amplitude more than 0.25 W K^{-2} m^{-1} at 0.5 K at zero field, is not observed in our sample S_4^b (same current direction: **j**//**b**). Thus the anisotropic behavior of κ_{extra} below 1.5 K reported in Ref.[98] is not confirmed by the measurements on this poor quality sample S_4^b. It remains to be understood, whether the difference between sample S_{150}^b in Ref.[98] and sample S_4^b in this study is related to the high quality of the sample S_{150}^b (RRR= 150), which makes its behavior special: in S_{150}^b κ/T is significantly enhanced at low temperature due to the large electronic contribution, and it reaches 1.1 W K^{-2} m^{-1}) at 0.5 K; or does this difference originate from the too low quality of sample S_4^b, which presents a superconducting transition in resistivity at much lower temperature than the other samples, and has a barely noticeable ferromagnetic transition. It is well known that in UCoGe ferromagnetic order (T_{Curie}) is even more sensitive to sample quality than T_{sc}: probably in sample S_4^b, the magnetic excitations (notably in the ordered phase) are strongly affected by impurities ans inhomogeneities. The answers to these questions await still future experiments to study the normal phase thermal transport properties in other UCoGe samples, with medium quality and with heat current flowing along the **b**-axis.

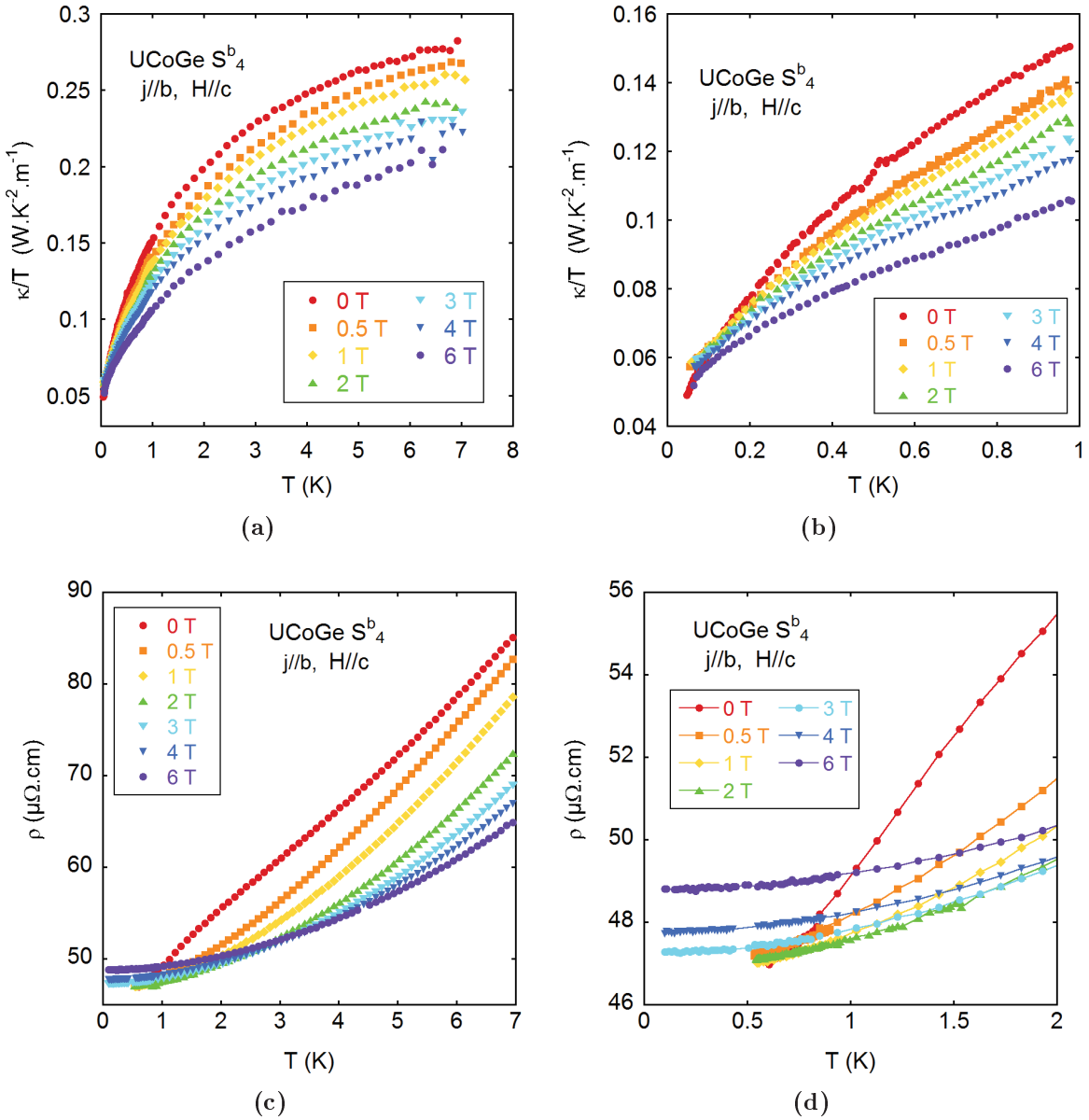

Figure 7.3 | **(a)**: Temperature dependence of thermal conductivity κ/T in sample S_4^b of UCoGe, with RRR= 4 and the current direction **j**//**b**, under different magnetic fields along the **c**-axis. **(b)**: Zoom of the low temperature part of the κ/T curves. **(c)**: Temperature dependence of resistivity ρ in sample S_4^b of UCoGe. **(d)**: Zoom of the low temperature part of the ρ curves.

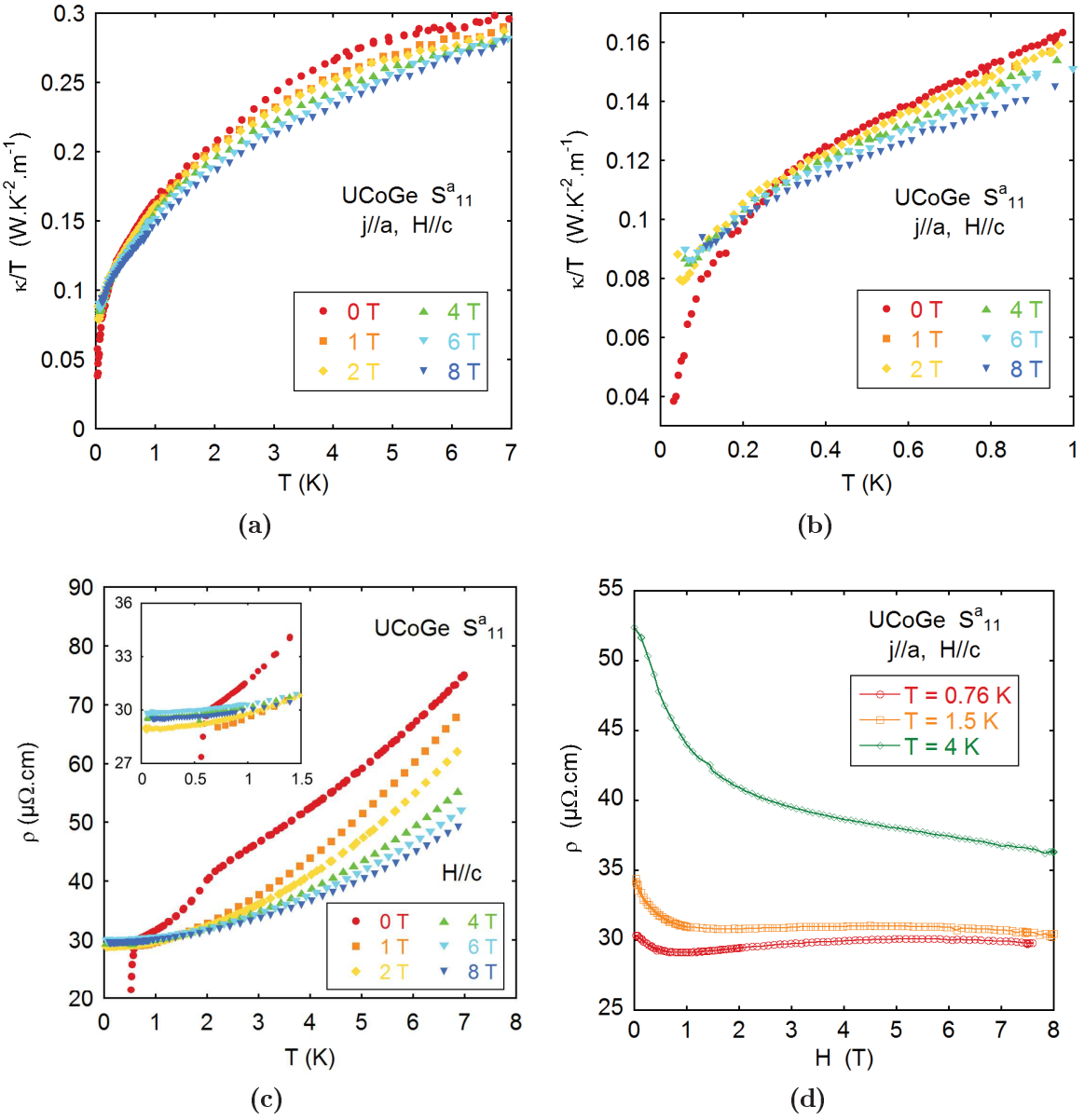

Figure 7.4 | (a): Temperature dependence of thermal conductivity κ/T in sample S^a_{11} of UCoGe, with RRR= 9 and the current direction **j**//**a**, under different magnetic fields along the **c**-axis. **(b)**: Zoom of the low temperature part of the κ/T curves. **(c)**: Temperature dependence of resistivity ρ in sample S^a_{11} of UCoGe. The inset shows a zoom for the low temperature part. **(d)**: Magnetoresistance for **H**//**c** of UCoGe at different temperatures up to 8 T on sample S^a_{11}. Magnetic field is perpendicular to the current direction.

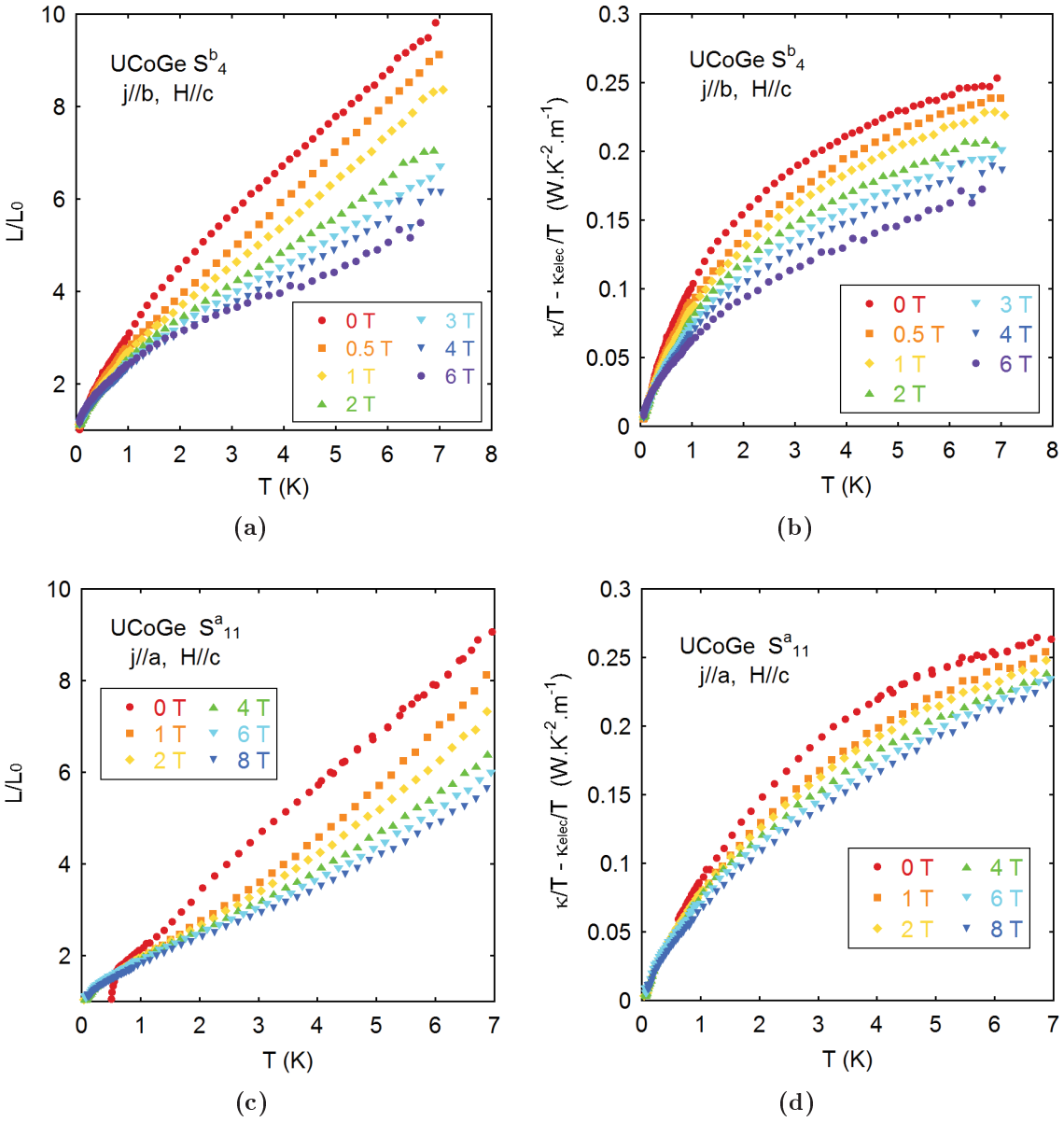

Figure 7.5 | **(a)**: Temperature dependence of the Lorentz ratio L/L_0 of UCoGe sample S^b_4, under magnetic fields along the **c**-axis. **(b)**: Non-electronic contributions (phonons, magnectic fluctuations, ...) to the thermal conductivity of sample S^b_4. **(c)**: L/L_0 ratio of UCoGe sample S^a_{11} under magnetic field **H**//**c**. **(d)**: Non-electronic contributions to the thermal conductivity of sample S^a_{11}.

7.2 High field properties for H//c in UCoGe

7.2.1 Physical background

UCoGe under high magnetic field along the **c**-axis is an interesting case, because a series of field-induced anomalies have been observed in the transport properties. They were first observed as small kinks in the magnetoresistance for **H**//**c** in Ref.[99], and were then studied with other experimental probes which are more sensitive to Fermi surface changes. Figure 7.6 presents the field dependence of the Hall coefficient ρ_{xy} and thermopower S (Seebeck effect) in UCoGe for **H**//**c** [100], both of which show clear anomalies at $H_1 \sim 4$ T, $H_2 \sim 9$ T, $H_3 \sim 14$ T and $H_4 \sim 16$ T, etc.

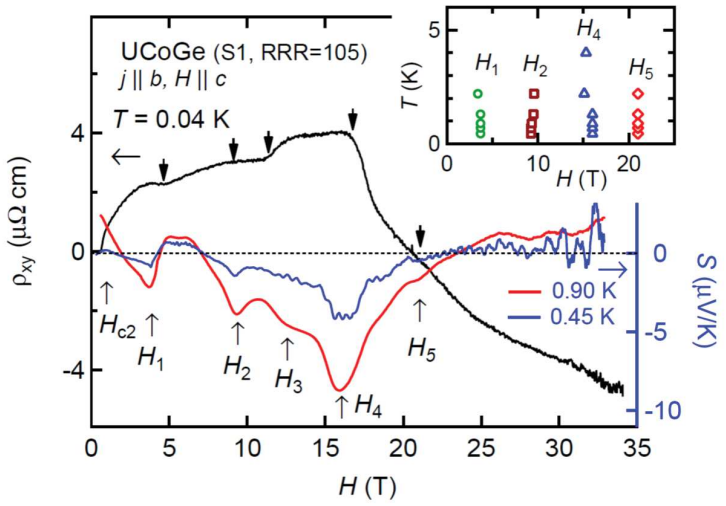

Figure 7.6 | The series of field-induced anomalies H_1 to H_5, marked by the arrows, in transport properties of UCoGe under magnetic field along **c**-axis. Black line: Hall resistance ρ_{xy} (scale on the left); red and blue lines: Seebeck coefficient S (scale on the right).[100]

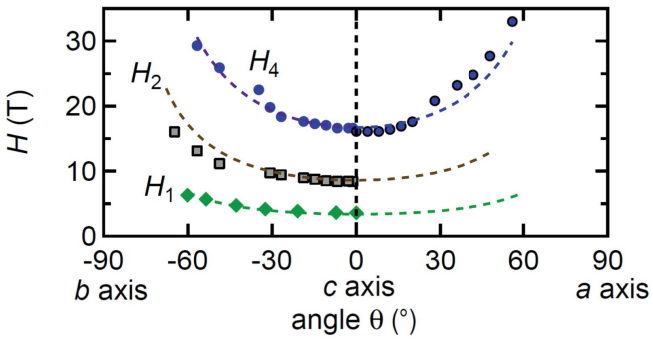

Figure 7.7 | Angular dependence of H_1, H_2 and H_4 from **c**-axis to **a** and **b** axes. Dashed lines are fits with $H \propto 1/\cos\theta$ (θ the angle between the field direction and the **c**-axis.[100]

Figure 7.7 presents the angular dependence of the H_1, H_2 and H_4 anomalies, both from the **c**-axis to the **a** and **b** axes, obtained with thermopower or magnetoresistivity measurements (presented in figure 7.6)[100]. The values of these anomalies under field

follow a $1/\cos\theta$ relation, with θ being the angle between the field direction and the **c**-axis of UCoGe. This angular dependence means that the changes associated with these anomalies occur when the field component along **c**-axis reaches well-defined values, and are insensitive to field components perpendicular to this easy magnetization axis. For the H_2 anomaly close to 9 T, this angular dependence has been also observed in the magnetoresistance measurements in two other (earlier) studies[101, 102].

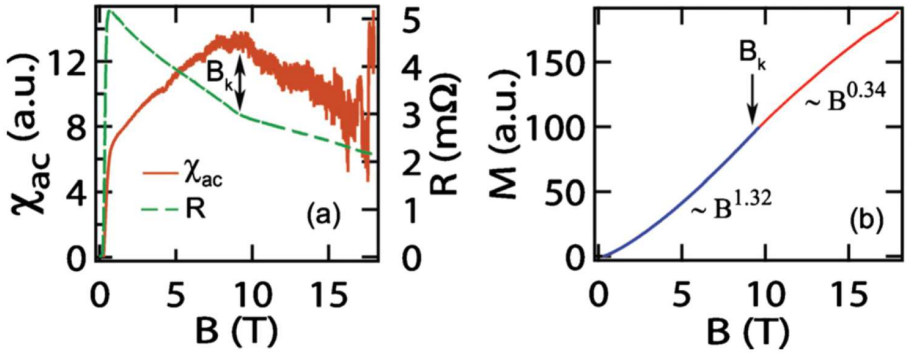

Figure 7.8 | (a): Field dependence of ac-susceptibility of UCoGe for **H**//**c**, at 40 mK (red solid line), and magnetoresistance in the same case (green dashed line)[101]. The H_2 anomaly is marked as B_k in the figure. **(b)**: Magnetization obtained by integration of the χ_{ac} data, which shows a reflection point at B_k.

The field dependence of the ac-susceptibility (χ_{ac}) for **H**//**c** in UCoGe has been measured, at 40 mK in Ref.[101] (figure 7.8). The H_1 anomaly is barely visible, and appears possibly as a small kink at around 4 T. The H_2 anomaly is marked as a maximum in χ_{ac}, or an inflection point in $M(H)$ obtained by integration of the χ_{ac} data. A sudden strong increase of χ_{ac} starts at about 16 T, coinciding with the H_4 anomaly, but this last feature is not certain due to the large noise in the measurements.

Strong experimental indications for the nature of these field-induced anomalies have been found in the quantum oscillation studies in the PhD work of G. Bastien and A. Gourgout, and presented in Ref.[100]. Figure 7.9 presents the quantum oscillations in UCoGe observed in resistivity, Hall coefficient and thermopower measurements, under magnetic field along the **c**-axis above and below the H_2 anomaly around 9 T. The oscillation pattern changes at the H_2 anomaly and the two observed frequencies (β and γ) jump to a higher value. More significant changes occur at higher fields, which is summarized in figure 7.9b. For magnetic field above H_4, the two frequencies observed at low field are replaced by a much higher frequency (α), which corresponds to a much larger Fermi surface pocket. These results show that the series of field induced anomalies in the transport properties in UCoGe for **H**//**c** are accompanied by changes in the Fermi Surface. In particular, topological changes of the Fermi surface, also referred to as Lifshitz transitions, are suggested. In such a case, a new Fermi surface pocket may appear (or disappear) with magnetic field, or alternatively, two small pockets of Fermi surface may join each other and make a bigger one.

Up to now the band calculations in UCoGe cannot account for these changes. In order to better understand these field induced transitions in the Fermi surface, we measured the specific heat of UCoGe under magnetic field along its **c**-axis up to 16 T, the results will be presented and discussed in the following. Previously C_p/T in UCoGe for **H**//**c** have been measured only up to 9 T[34].

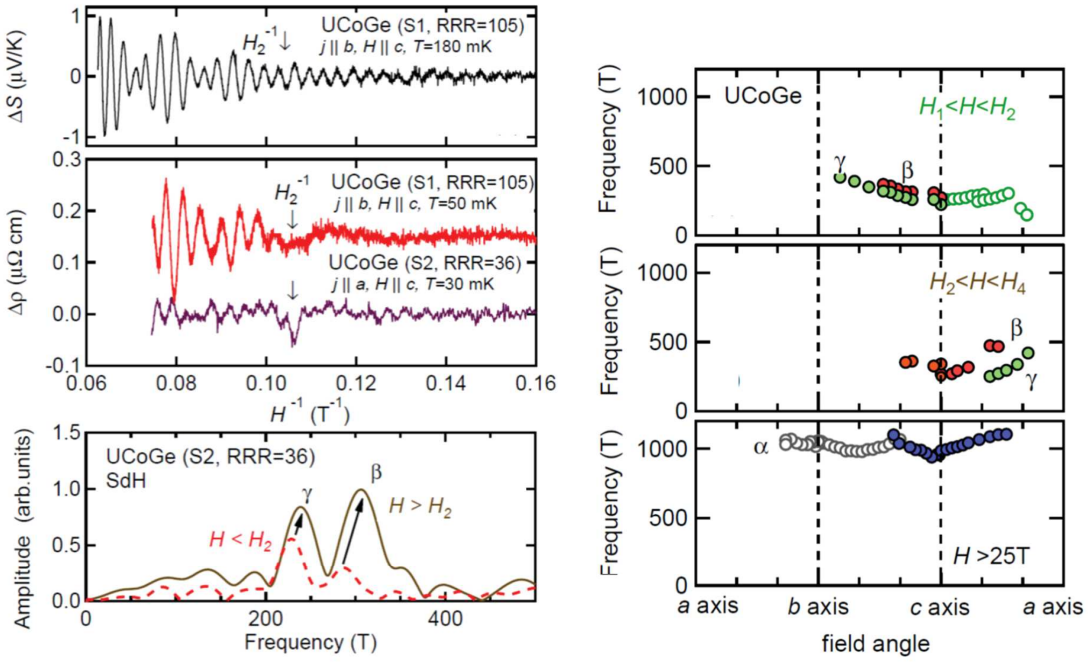

Figure 7.9 | Quantum oscillation pattern and frequencies in resistivity and thermopower measurements in different field ranges for **H**//**c** in UCoGe [100].

7.2.2 Specific heat measurements of UCoGe under H//c

Specific heat of UCoGe under magnetic field along the **c**-axis has been measured on a high quality sample S_{95}^{ab} (a square-shaped sample in the (**a**,**b**) plane, RRR= 95), with the classical relaxation method. The experiment is performed in a dilution refrigerator, equipped with a 16 T superconducting magnet. Figure 7.10 presents the field dependence of the specific heat divided by temperature (C_p/T) at several fixed temperatures T = 500 mK, 650 mK,685 mK and 1 K. At T = 500 mK (close to the superconductivity critical temperature T_{sc}), C_p/T close to 0 T is influenced by the onset of the superconducting transition. In the curves for all four temperatures, the H_1 anomaly near 4 T in the transport properties appears as a smooth minimum in $C_p/T(H)$, with no sign of irregularity. The H_2 anomaly near 9 T is marked with a visible maximum. Around the H_4 anomaly (14 T), $C_p/T(H)$ shows a kink and is followed by a strong upturn.

The last anomaly H_4 is not directly observable in the $C_p/T(H)$ curve at 500 mK, due to the strong nuclear contributions. The importance of this contribution can be better observed in figure 7.11a and 7.11b. Figure 7.11a presents C_p/T as a function of magnetic field in UCoGe at 200 mK. For magnetic field below 1 T, a small feature can be seen due to the superconducting transition. Above 1 T, C_p/T is strongly enhanced by the increasing magnetic field by almost an order of magnitude at 16 T, and follows a H^2 dependence. Figure 7.11b presents C_p/Tas a function of temperature, with magnetic field fixed at 12 T and 16 T. A low temperature tail is observed in these two curves. Such behaviors are typically expected for a Schottky anomaly associated with the Zeeman splitting of the nuclear spin under magnetic field. As this contribution is particularly large at 200 mK, it can be estimated with the data in figure 7.11a.

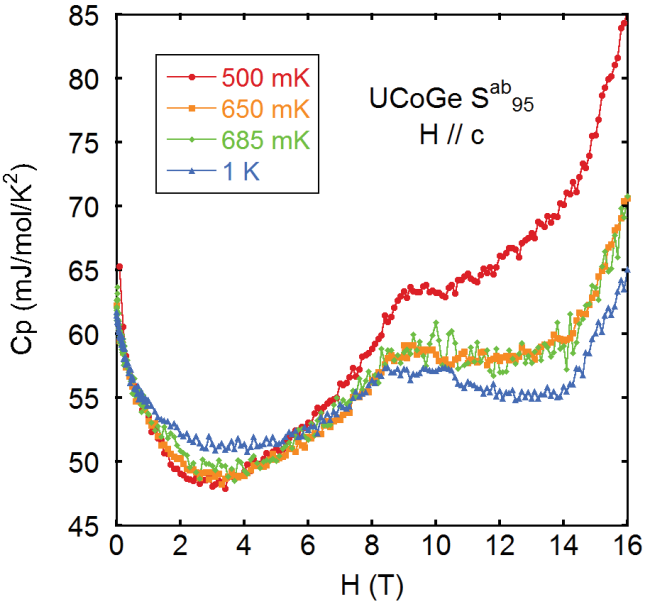

Figure 7.10 | Specific heat divided by temperature as a function of magnetic field for **H**//**c** in UCoGe, measured on sample S^{ab}_{95}. The temperature for different curves is fixed respectively at 500 mK (red circles), 650 mK (orange squares), 685 mK (green diamonds) and 1 K (blue triangles).

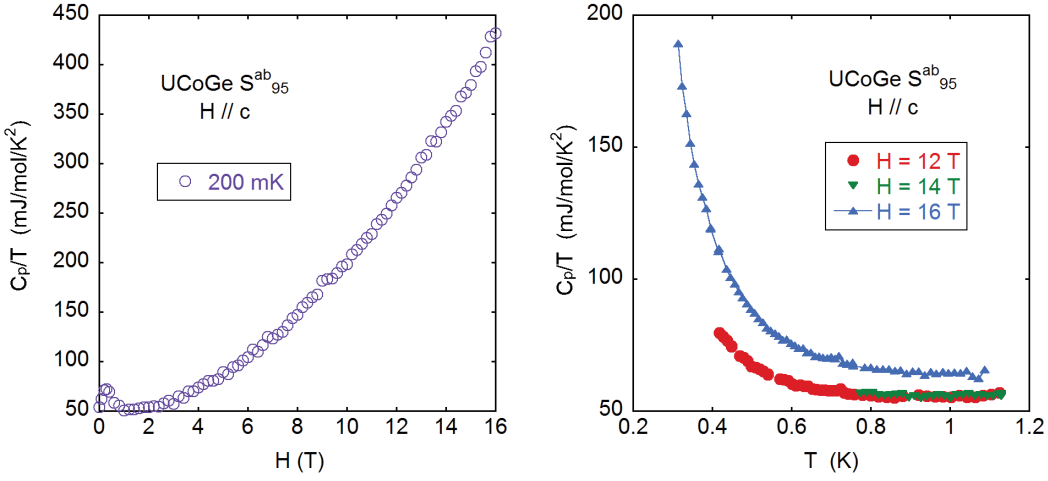

(a) **(b)**

Figure 7.11 | **(a)**: Field dependence of specific heat over temperature C_p/T for **H**//**c** in UCoGe, measured on sample S^{ab}_{95}, with temperature fixed at 200 mK. The large value of C_p/T at high field shows the domination of the nuclear contribution in this case. **(b)**: Temperature dependence of specific heat over temperature C_p/T for **H**//**c** in UCoGe, measured at respectively $H = 12$ T, 14 T and 16 T.

7.2.3 Corrections of the nuclear contribution

A Schottky anomaly in specific heat is associated with the thermal excited transitions in a two-level system. It is given by

$$C_p^{Schottky} = R \left(\frac{\Delta}{T}\right)^2 \frac{\exp(\Delta/T)}{[(1+\exp(\Delta/T)]^2} \tag{7.3}$$

where $R = 8.314$ J K^{-1} mol^{-1}, is the ideal gas constant, and Δ corresponds to the energy splitting of the two level system (Δ in Kelvin).

For a nuclear spin, a small splitting of the nuclear energy levels appears under magnetic field due to the Zeeman splitting and the hyperfine interactions, and is proportional to the field: $\Delta = \beta H$, with β a constant of unit K/T. When the temperature is much larger than Δ, this Schottky anomaly of the nuclear specific heat contribution is approximately given by:

$$C_p^{nuclear} = \frac{1}{4} R\beta^2 \frac{H^2}{T^2} \tag{7.4}$$

which corresponds to the enhancement of C_p/T at low temperature and at high magnetic field observed in figure 7.11a and 7.11b.

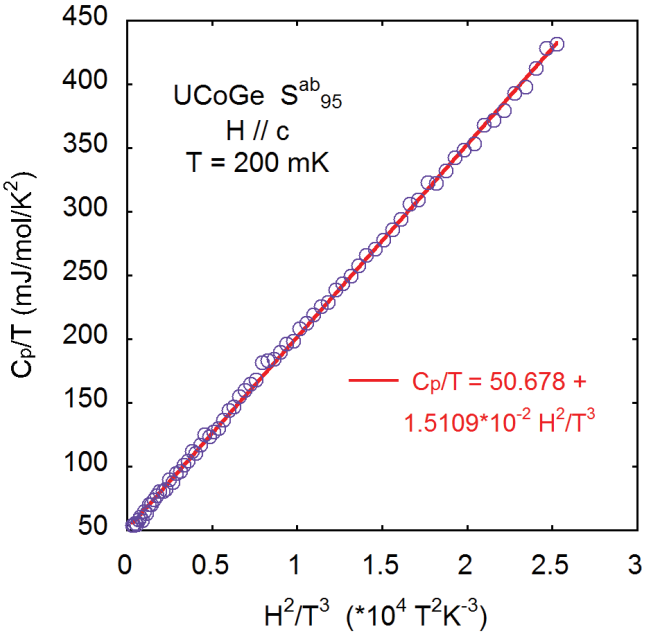

Figure 7.12 | The specific heat divided by temperature as a function of H^2/T^3 for $\mathbf{H}//\mathbf{c}$ in UCoGe. The solid line corresponds to a linear fit of the data (equation in the figure).

Figure 7.12 presents the C_p/T as a function of H^2/T^3 for $\mathbf{H}//\mathbf{c}$ in UCoGe, with the measurements at around 200 mK in figure 7.11a: the data are calculated with the exact temperature of the sample at each field, and the points for field below 1 T which show the superconducting transition have been removed. The results show a perfect linear dependence, and can be fit as the sum of a constant electronic contributions and a field and temperature dependent nuclear contribution:

$$C_p = C_p^{elec} + C_p^{nuclear} = \gamma\, T + \frac{1}{4} R\beta^2 \frac{H^2}{T^2} \tag{7.5}$$

The coefficients are found to be: $\gamma = 50.68$ mJ mol^{-1} K^{-2} and $\beta = 0.00270$ K T^{-1}.

With the β value estimated, the energy gap (Δ) associated with the Schottky anomaly can be explicitly calculated. With the highest field in our measurements (16 T), $\Delta = \beta H$ equals 43 mK, much lower than the lowest temperature of the measurements (200 mK). Calculation with the complete expression in equation(7.3) shows that the "high temperature" approximation used in equation(7.5) leads to an error of order 1% at most, and is thus justified.

7.2.4 Discussions

With the Schottky anomaly from the nuclear contributions removed, it is possible now to extract the specific heat of the electrons. Figure(7.13) shows the field dependence of the electronic specific heat divided by the temperature of UCoGe.

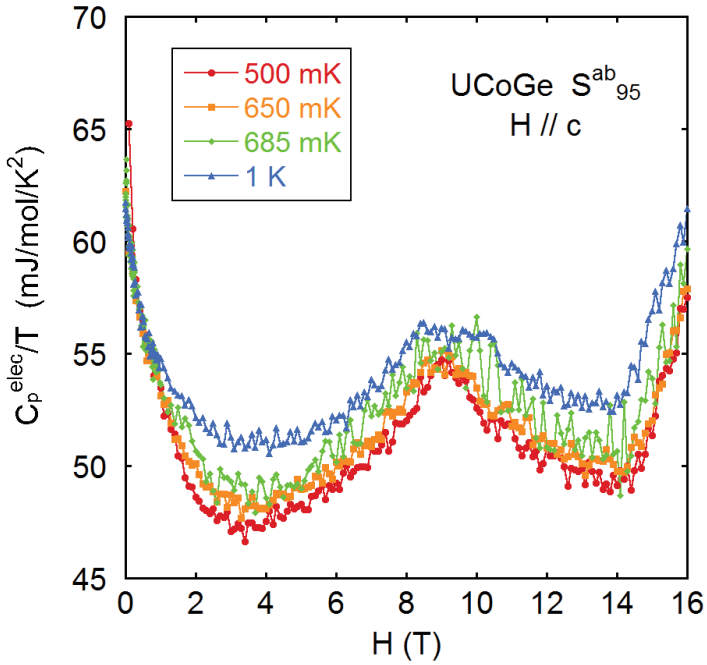

Figure 7.13 | The electronic specific heat divided by temperature (C_p^{elec}/T) as a function of magnetic field for **H**//**c** in UCoGe, measured on sample #2 (RRR= 95). The temperature for each measurement is fixed respectively at 500 mK (red circles), 650 mK (orange squares), 685 mK (green diamonds) and 1 K (blue triangles).

It can be observed that the field dependence of C_p^{elec}/T is similar at all four temperatures, marked by a strong decrease in the narrow field range below 2 T (about 20%), a broad minimum around 4 T (H_1), a peak-like maximum at around 9 T (H_2), and a sudden upturn at around 14 T (H_4). In the whole field range, C_p^{elec}/T increases slightly with temperature (for temperature between 500 mK and 1 K), and this temperature dependence is the strongest for field around the minimum at 4 T.

As a conclusion, the features observed in the field dependence of C_p^{elec}/T for **H**//**c** in UCoGe are consistent with the anomalies seen in transport properties, and give thermodynamic information about these transition: no discontinuities in $C_p^{elec}/T(H)$ can be observed, indicating that these transitions do not correspond to first or second order transitions. This point is also supported by the magnetization measurements, which shows

a smooth $M(H)$ behavior in the field range for $\mathbf{H}//\mathbf{c}$ in UCoGe[88]. As C_p^{elec}/T for a metallic system is proportional to the density of states at the Fermi level $\mathcal{N}(E_F)$:

$$C_p/T = \frac{\pi^2}{3} k_B^2 \mathcal{N}(E_F), \tag{7.6}$$

these features in $C_p^{elec}/T(H)$ are possibly related to field-induced changes in the band structure. Notably they are compatible with the topological changes of the Fermi surface suggested by the transport studies[100], which consist in 5/2-order transitions[103].

7.3 Characterization of single and polycrystals of UBe_{13}

7.3.1 Background

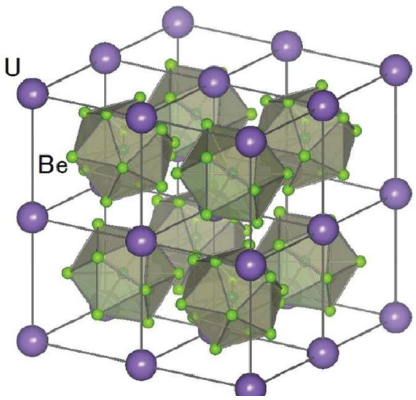

Figure 7.14 | Crystal structure of UBe_{13}. Figure from Ref.[104].

UBe_{13} is the first discovered uranium-based heavy fermion superconductor[105]. It shows many fascinating normal phase and superconducting properties, and continues to be a system of interest today more than 30 years after its discovery[106, 107, 108]. The upper critical field in UBe_{13} has a large initial slope of almost -50 T/K, and shows a change of curvature at around $0.5T_{sc}$ [109]. Despite numerous experimental and theoretical efforts, the main questions concerning superconductivity in this compound are still unsolved, such as the symmetry of the unconventional superconducting order parameter, the puzzling H_{c2} behavior, and the origin of the pairing mechanism.

UBe_{13} crystallizes in a cubic $NaZn_{13}$-type structure, presented in figure 7.14. The uranium atoms form a simple cubic lattice. Each of the cubic cell center is occupied by 13 beryllium atoms: 12 forming a regular icosahedron cage and the last one lying in the cage center. The distance between nearest neighbor uranium atoms is 5.13 Å, much larger than the Hill's limit (3.5 Å)[110], indicating small overlap between the $5f$ orbitals.

The early studies suggest the existence of two variants of UBe_{13}[111]. Most good-quality samples, including poly- and single crystals, are found to have a T_{sc} closely distributed around 0.9 K (the H-type). On the other hand, some single crystals are found to have a T_{sc} significantly lower, distributed around 0.75 K (the L-type). Figure 7.15a presents the specific heat of the H- and L-type UBe_{13}[111]. Apart from the lower T_{sc}, the L-type UBe_{13} shows an even higher jump of C_p/T at T_{sc}. It has a temperature-dependent

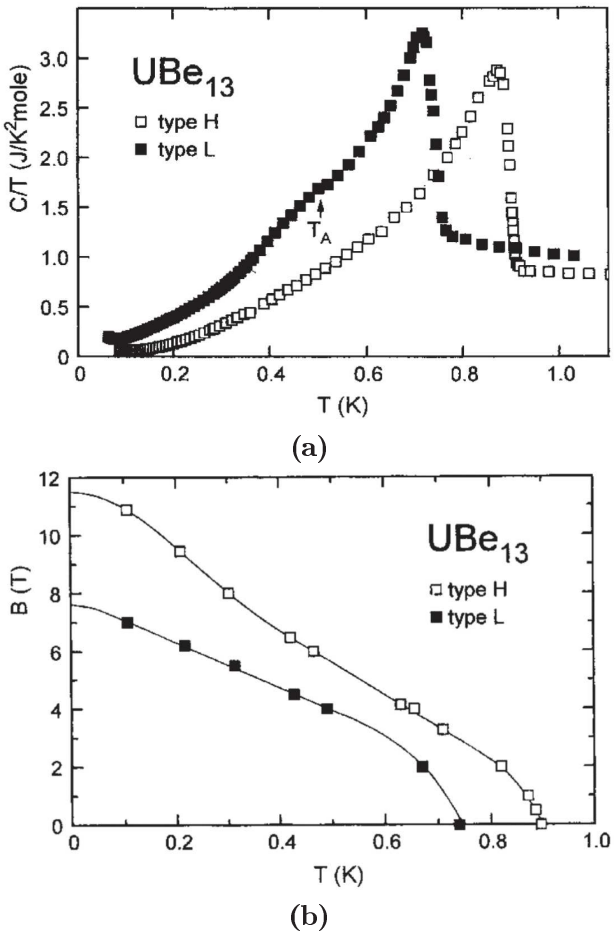

Figure 7.15 | Specific heat over temperature (C_p/T) as a function of temperature ((**a**)) and the upper critical field (H_{c2}) ((**b**)) of the two variants of UBe_{13}[111]. Filled markers: L-type UBe_{13}; Open markers: H-type UBe_{13}

C_p/T in the normal phase above T_{sc}, with values exceeding 1 J K^{-2} mol^{-1}, while in H-type samples, C_p/T is almost constant for temperature below 0.75 K down to T_{sc}, and is of order 0.75 J K^{-2} mol^{-1}. Figure 7.15b presents the upper critical field of the H- and L-type UBe_{13}[111]. Both variants present a huge initial slope of H_{c2} of about -50 T/K. However, a change of curvature at about $0.5T_{sc}$ is observed only in the H-type UBe_{13}, while in the L-type, the H_{c2} has an almost linear behavior for $T < 0.5T_{sc}$. Since the L-type characteristics are only found in the single crystals, the difference between the two variants of UBe_{13} is possibly related to the sample preparation process.

It is also known that the normal and superconducting properties of UBe_{13} are sensitive to small amount of doping. Small substitution of U by thorium ($U_{1-y}Th_yBe_{13}$) leads to a nonmonotonic change of the critical temperature and an extra specific heat anomaly inside the superconducting phase[114]. Small amount of boron substitutions also have a strong effect on the properties of UBe_{13}. Figure 7.16 presents the specific heat measurement on $U(Be_{1-x}B_x)_{13}$ polycrystals[112, 113]. It can be seen that less than 0.3% of B substitution is enough to change significantly the C_p/T: T_{sc} is shifted to lower temperature, and the C_p/T jump at T_{sc} becomes much higher. At the same time, in the normal phase C_p/T increases upon cooling, unlike in the undoped polycrystals where C_p/T is almost constant

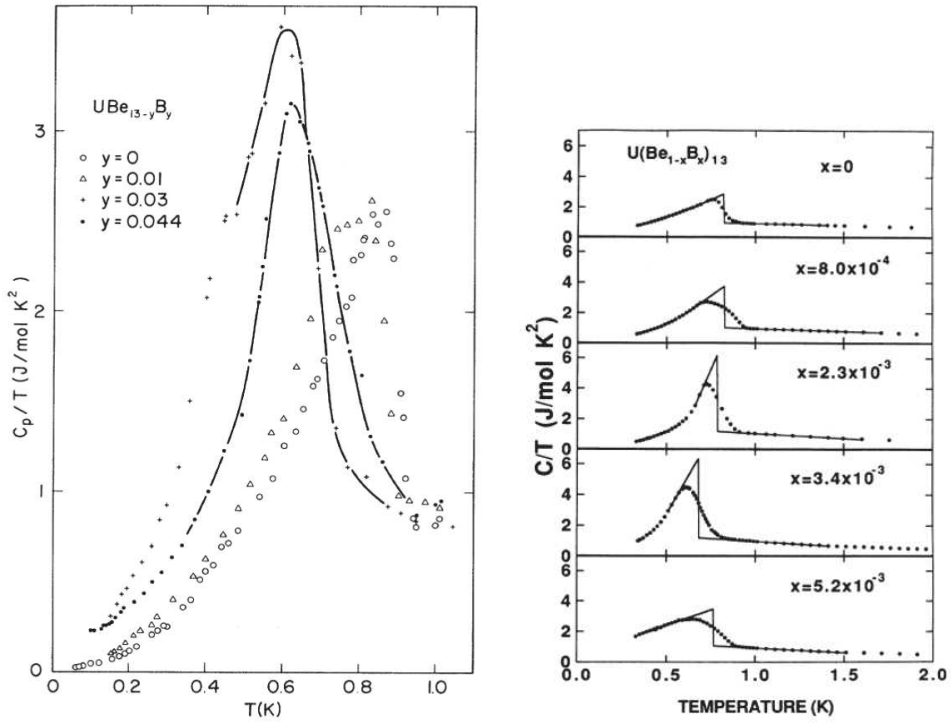

(a) (b)

Figure 7.16 | Effect on C_p/T of boron substitution in UBe_{13}[112, 113].

at temperature right above T_{sc}.

C_p/T in boron doped polycrystals of UBe_{13} resembles closely the L-type UBe_{13} samples (single crystals) in figure 7.15a. The origin of this extreme sensitivity of superconducting and normal phase properties to substitutions is still unknown. However, these results suggest that the difference between L- and H-types crystals could come from impurities absorbed by the sample during the flux growth.

The aim of this part is to study how the different factors in the preparation process, both for single and polycrystalline UBe_{13} samples, might change their physical properties. By analyzing these effects, we hope to find a way to obtain high quality UBe_{13} single crystals. The results on different samples are presented in the next section. The strategy for this quest was discussed regularly with Gérard Lapertot, who grew all the samples (poly- and single crystals) at CEA Grenoble, and performed the Scanning Electron Microscope (SEM) and Laue X-ray characterizations. We did the specific heat and resistivity measurements on these samples. Note that due to the large specific heat of UBe_{13}, the measurements are often limited to small-mass samples (sometimes below 0.5 mg). As the mass measurements are associated with an error of order 0.05 mg, this leads to a large error bar on the mass determination, thus on the absolute value of the C_p/T results.

7.3.2 Results and discussions

Polycrystals

We first present the results on the polycrystals.

Figure 7.17a presents the C_p/T measurements on a polycrystalline sample P_1 (sample

number : U-LAP-0020-1) (the letter "P" stands for a polycrystal), and on the sample P_1' (U-LAP-0020-700) which is cut from the same polycrystal and is further annealed at 700°C during 370 hours. The unannealed sample has a low T_{sc} of 0.7 K. With annealing, T_{sc} raises to 0.88 K, compatible with the T_{sc} in H-type UBe_{13}[115, 116]. In the normal phase, both samples have an almost constant C_p/T. γ ($\gamma = C_p/T$ in the normal phase) of the annealed P_1' is around 0.6 J K^{-2} mol^{-1}, lower than in other reported single crystals (about 0.75 J K^{-2} mol^{-1}) [115, 116], probably due to the error in the sample mass determination.

Figure 7.17b presents the resisitivty (ρ) measurements on the annealed sample P_1', with geometric factor obtained by supposing that the room temperature resistivity equals 135 $\mu\Omega$ cm as in Ref.[105]. It shows a strange behavior compared with usual UBe_{13}[105, 117]. At around 1 K, ρ at 0 T becomes smaller than at 2 T, while monotonous negative magnetoresistance is expected at this temperature in UBe_{13}[109, 116, 118]. Two maximums can be observed on the temperature dependence of ρ up to 300 K (in the inset), contrary to the reference behavior, and the maximum of ρ at around 2 K is significantly reduced compared with the usual value (higher than 220 $\mu\Omega$ cm)[105, 117] (see figure 7.22a).

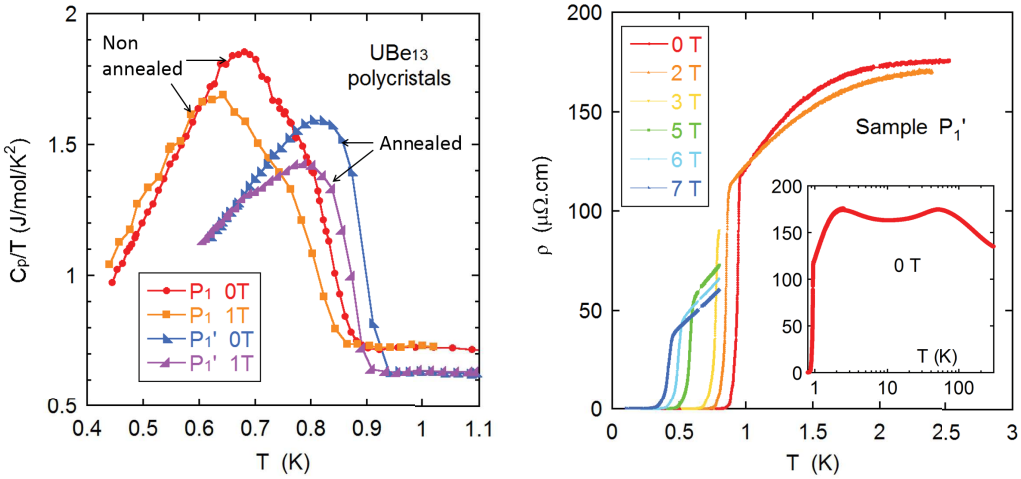

(a) (b)

Figure 7.17 | (a): C_p/T vs T at 0 T and 1 T of the polycrystal sample P_1 (U-LAP-0020-1) (not annealed) and P_1' (U-LAP-0020-700, annealed at 700°C during 370 hours). **(b):** Resistivity measurements on the annealed polycrystal P_1', at different magnetic fields. Note the $\rho(T)$ behavior at 0 T is significantly different from the classical behavior of UBe_{13} (see figure 7.22a). The inset gives $\rho(T)$ up to magnetoresistance 300 K at zero field (T in log).

The Scanning Electron Microscope (SEM) images presented in figure 7.18 help to understand this strange behavior of resistivity in sample P_1'. Figure 7.18a and figure 7.18b show respectively the SEM image for the annealed (P_1') and non annealed sample (P_1). The luminous traces in these images correspond to zones with higher electron border scattered intensity, which in the occurrence most likely correspond to zones rich in uranium atoms (or even pure uranium!). It can be observed that the annealed sample P_1' presents much more such uranium-rich traces than the the unannealed sample P_1. Figure 7.18c displays a zoom on the sample P_1', which shows that these traces form complete percolating paths.

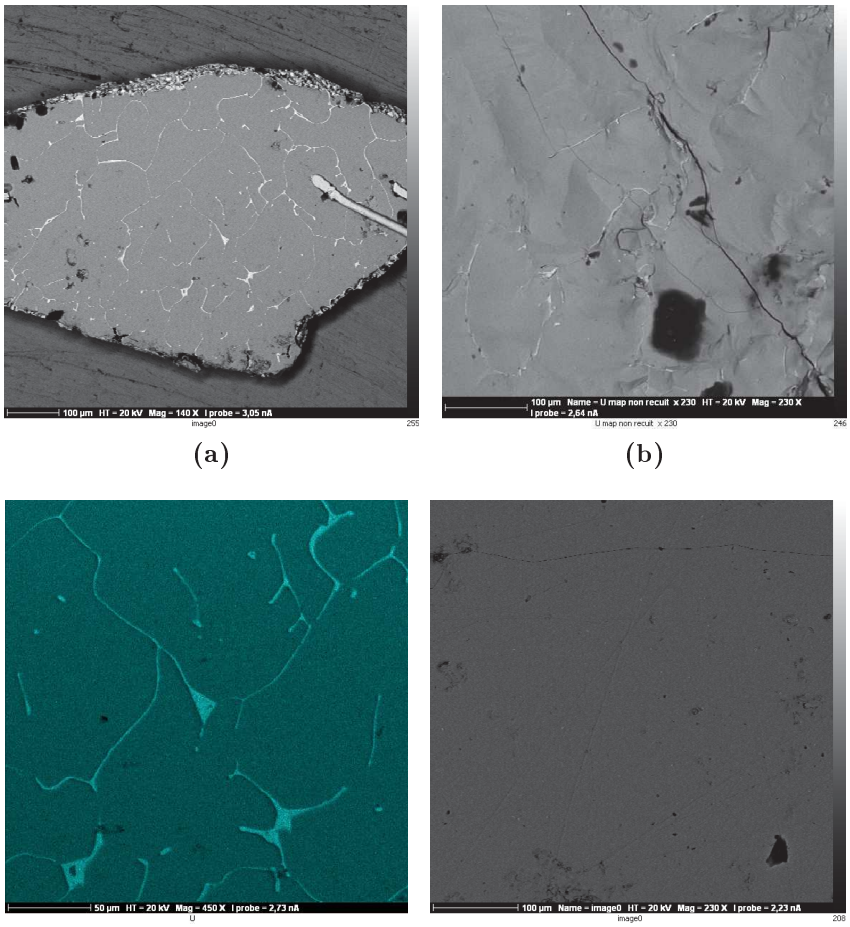

Figure 7.18 | Scanning Electron Microscope (SEM) images (border scattered intensity) for the polycrystals samples. **(a)**: annealed sample P_1' (U-LAP-0020-700), with normal composition of U and Be composition (1 : 13) **(b)**: unannealed sample P_1 (U-LAP-0020-1), with normal composition of U and Be material composition (1 : 13) **(c)**: U elemental analysis, zoom for the annealed sample P_1'. **(d)**: annealed sample P_2 (U-LAP-0029), with extra Be material at the beginning (U : Be = 1 : 13.5)

Due to the high vapor pressure of the beryllium metal, it is possible that during the sample synthesis small quantities of Be material are lost by vaporization, which leaves in the polycrystalline sample excess uranium metal. After annealing, this uranium migrates and aggregates, and forms these macroscopic filaments which modify significantly the sample resistance. Of course, further loss of Be materials during the annealing is also possible. To avoid this complication, all the annealing procedures were limited at a low temperature (700°C).

One solution to this problem is to put an extra amount of Be material from the beginning, when melting the sample. Figure 7.19 shows the C_p/T of a polycristalline sample P_2 (U-LAP-0029), made with uranium and beryllium materials casted as 1 : 13.5, and annealed at 700°C during 370 hours. Like the annealed sample P_1', it has a high T_{sc} of 0.9 K and shows a similar behavior of H-type UBe_{13}, but has a larger γ in the normal phase 0.72 J K^{-2} mol^{-1}. Figure 7.18d shows the SEM image (border scattered intensity) of sample P_2, which presents no trace of uranium-rich parts.

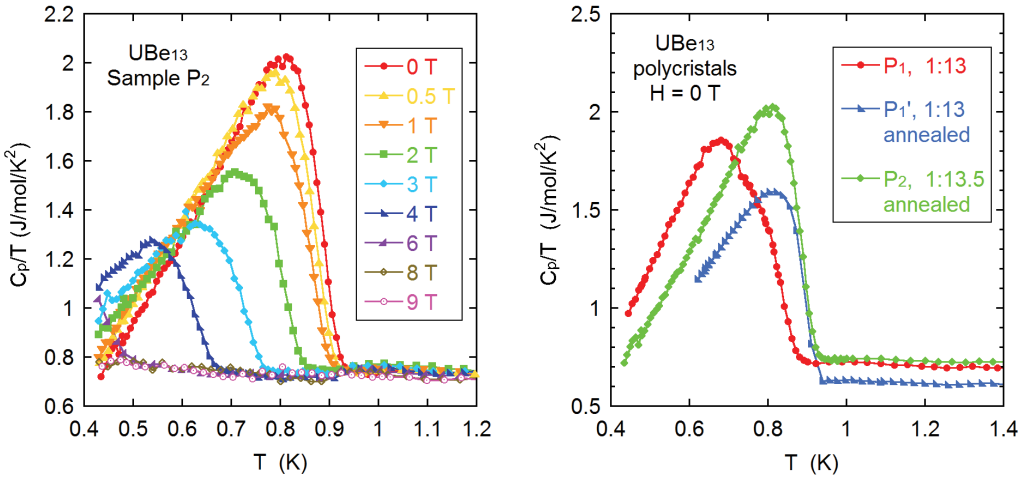

(a) (b)

Figure 7.19 | **(a)**: C_p/T vs T at different magnetic fields of sample P_2 (U-LAP-0029), with the starting composition U : Be = 1 : 13.5, and annealed at 700°C duing 370 hours. **(b)**: Comparison of normalized C_p/T at zero field between the unannealed sample P_1 and the annealed P_1' and P_2.

Single crystals

We now turn to the single crystals prepared with the flux method.

Figure 7.20a and figure 7.20b present the C_p/T at zero field of different single crystals (S_1-S_7, the letter "S" stands for a single crystal). All these samples are obtained with the flux method, but with differences in their preparation processes. The details of the preparation and their physical properties are summarized in table 7.2.

Sample	T_{sc} (K)	γ_n (J.mol^{-1}K^{-2})	$\Delta C/C$	Mass (mg)	Preparing details
S_1	0.794	1.10	2.78	2.35	Standard: Al flux, $-2°$/h, U:Be = 1:13
S_2	0.769	0.86	2.20	0.40	U:Be = 1:20
S_3	0.816	0.90	2.93	0.34	With cooling rate ($-1°$/h)
S_4	0.788	1.11	2.66	0.65	U:Be = 1:10
S_5	0.800	0.95	2.52	0.69	Start with the polycrystal P_1' Using Al 6N
S_6	0.601	1.15	1.72	2.70	Ga flux
S_7	0.681	1.10	1.70	2.22	Ga-Al flux

Table 7.1 | Preparation details and properties of the single crystals from the flux method.

The C_p/T of sample S_1 (U-LAP-0016) at different magnetic fields are presented in figure 7.21. It shows a similar behavior to the sample reported in the recent Ref.[107] (also a single crystal with Al-flux method), and the "L-type" UBe_{13} single crystals[111]: compared with the H-type UBe_{13}[115], they have a lower T_{sc} (0.794 K for sample S_1) and an enhanced C_p jump (the maximum of C_p equals 3.7 J/mol/K^2 for sample S_1 at zero field and about 3.6 J/mol/K^2 in Ref.[107]; in H-type UBe_{13} in Ref.[115], it is about

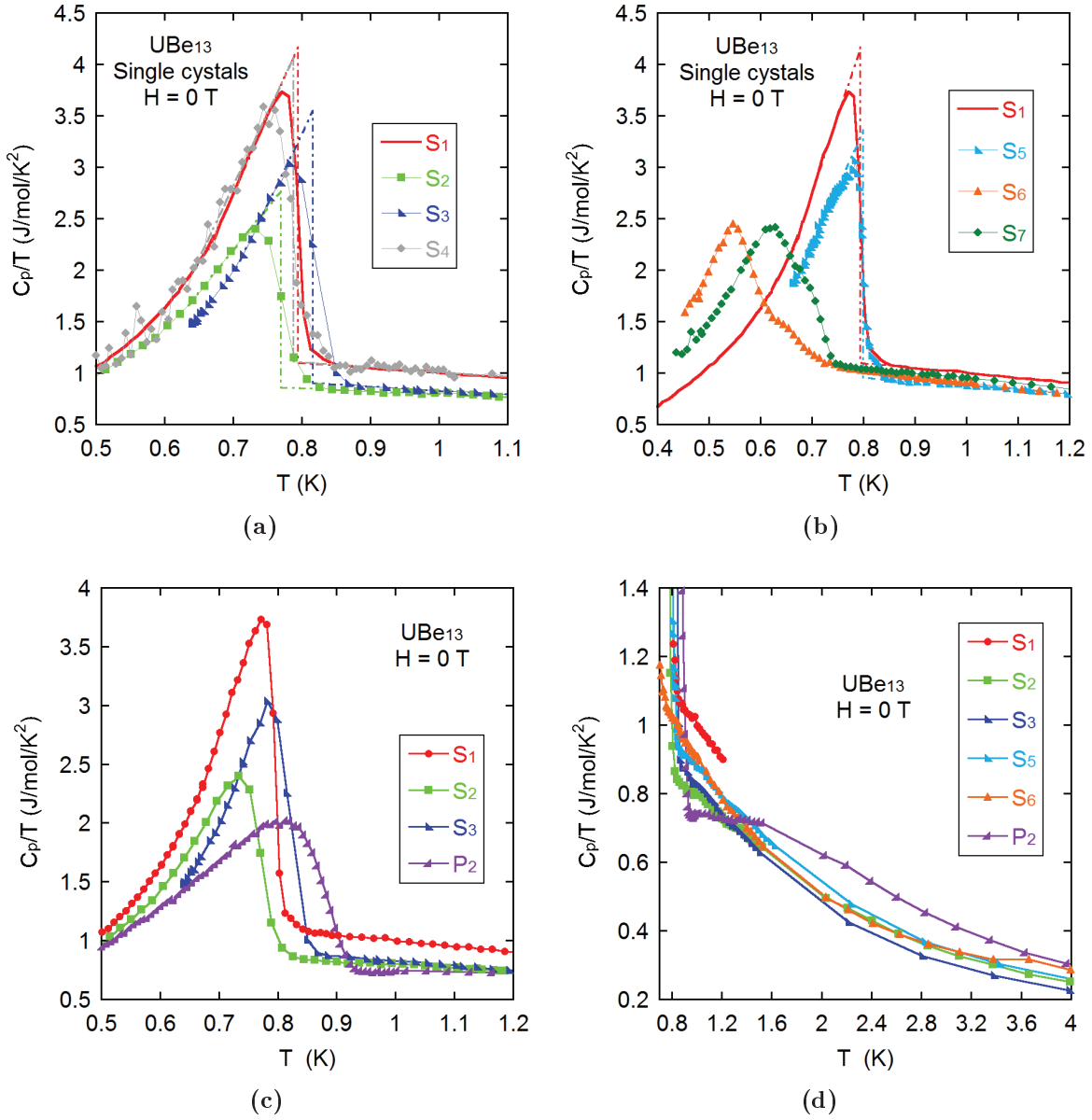

Figure 7.20 | **(a)**: C_P/T as a function of temperature at zero magnetic field, of different UBe_{13} single crystals, S_1, S_2 (extra Be), S_3 ($-1°$/h cooling rate), S_4 (deficit Be). **(b)**: C_P/T as a function of temperature at field, of different UBe_{13} single crystals (S_1 (Al flux), S_5 (ultra clean Al flux, with 6N purity), S_6 (Ga flux), S_7(Ga-Al flux)). **(c)**: Comparison between the single crystals from Al flux (S_1, S_2 and S_3) and the polycrystal sample P_2, at the C_P/T jump at the superconducting transition. **(d)**: Comparison between the single crystals and the polycrystalline sample P_2 in the normal phase.

2.7 J/mol/K^2); in the normal phase, C_p/T decreases both with temperature and with magnetic field, while in H-type UBe_{13}[115], C_p/T is almost constant in temperature and field.

Sample S_2 (U-LAP-0026) is obtained with an extra amount of beryllium material in the Al flux: initially the quantity (in mole) of U and Be materials is in a 1 : 20 ratio. This leads to a reduced $\Delta C/C$ than in sample S_1 (normal initial composition, U and Be casted as 1 : 13). It shows also a lower normal phase C_p/T, probably due to its small

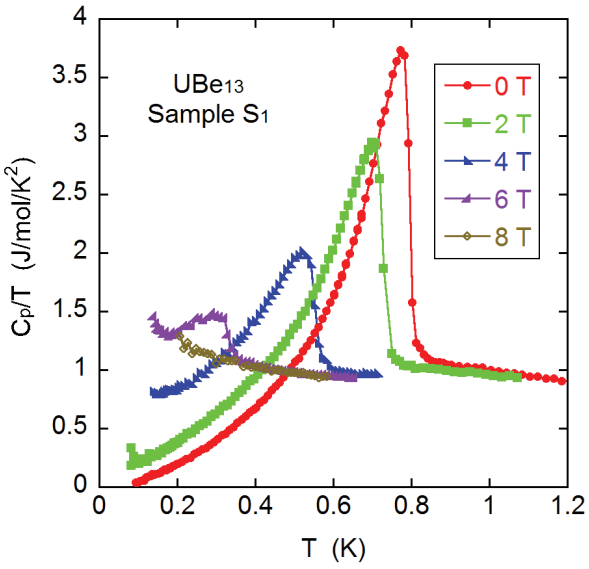

Figure 7.21 | C_p/T as a function of temperature at different magnetic fields on single crystal sample S_1 (U-LAP-0016).

mass and thus the large uncertainty in mass determination. Sample S_4 (U-LAP-0025) is obtained with a deficit in the amount of Be (U and Be materials casted as 1:10) and shows no difference from sample S_1.

Sample S_3 (U-LAP-0019) is prepared in the same initial conditions as for sample S_1, but with a 2 times slower cooling rate ($-1°$/h) than for S_1 and the other samples ($-2°$/h). Compared with sample S_1, its T_{sc} is slightly higher (0.816 K).

Sample S_5 (U-LAP-0021-2) is obtained with ultra clean Al flux (6N purity), starting with a part of the polycrystal P_1 (U-LAP-0020) and with a slow cooling rate ($-1°$/h). Compared with S_1, using purer Al for the flux leads to a reduction of $\Delta C/C$, but the overall behavior remain unchanged: T_{sc} is almost the same, and C_p/T is temperature dependent in the normal phase.

Samples S_6 (U-LAP-0027) and S_7 (U-LAP-0028) are obtained with an alternative flux (respectively Ga and a mixture of Ga and Al flux). Compared with the samples obtained with Al flux, they have a lower T_{sc}. They do not show an enhanced C_p/T jump at T_{sc}, and the maximum of C_p/T is only around 2.5 J/mol/K^2. In the normal phase, however, C_p/T is still temperature dependent.

Figure 7.20c compares the C_p/T of the single crystals and the polycrystalline sample P_2. Compared with P_2 which presents an H-type behavior of UBe_{13}, all the single samples obtained from the flux method show the "L-type" behavior: a lower T_{sc} and an enhanced C_p/T jump at T_{sc}. A zoom on the normal phase (figure 7.20d) shows the difference in the temperature dependence of C_p/T between the two cases.

Resistivity (ρ) measurements have been performed on sample S_1 and S_5. Figure 7.22b presents ρ as a function of temperature up to 300 K (T in log) of sample S_1 (U-LAP-0016), compatible with previous results[105, 117]. The geometric factor was adjusted to reproduce the same resistivity at room temperature as in Ref.[105] ($\rho(T$=300 K) = 135 $\mu\Omega$ cm). Figure 7.22a presents the resistivity of sample S_1 in the low temperature region at different fields, with the field dependence of the residual resistivity linearly

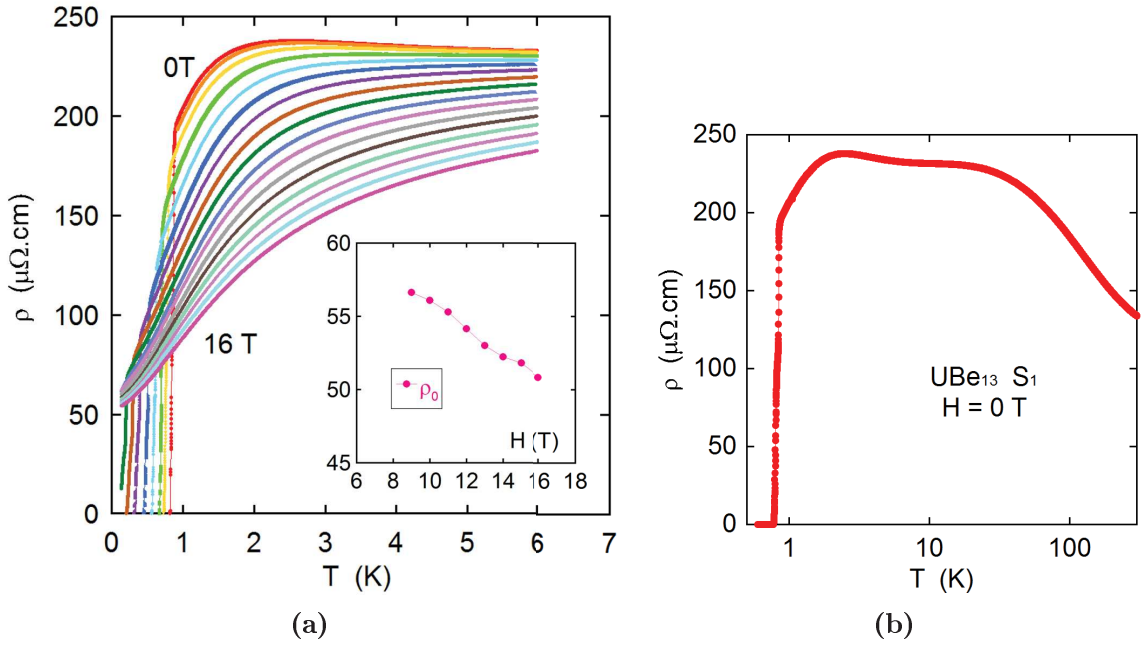

Figure 7.22 | (a): Resistivity as a function of temperature of UBe_{13} measured on the single crystal S_1 (U-LAP-0016), at different magnetic field: from 0 T (above) to 16 T (below). The inset shows the field dependence of ρ at the $T = 0$ limit, obtained with linear extrapolation. **(b)**: ρ at zero field as a function of temperature (in log) from low temperature to 300 K. The geometric factor is adjusted to the resistivity at 300 K: 135 $\mu\Omega$ cm according to Ref.[105].

extrapolated at $T = 0$ presented in the inset. It is not easy to define the residual resistivity $\rho(T = 0)$ in the low field region: at zero field ρ is significantly enhanced around the coherence temperature T^* at around 2 K, and has strong temperature dependence down to T_{sc}. Under magnetic field, however, the maximum of ρ around T^* is strongly suppressed, and one can estimate the residual resistivity by extrapolating the $\rho(T)$ data for fields above 10 T. For sample S_1, the residual resistivity for field between 10 and 16 T is more than $50 - 55$ $\mu\Omega$ cm. For sample S_5, low temperature measurements up to 13.6 T also show a residual resistivity of around 50 $\mu\Omega$ cm (not shown). These values are about 2 times higher than for the previously reported H-type single-crystalline samples: in Ref.[109, 116, 118], the residual resistivity in this high field region is found to range from 15 $\mu\Omega$ cm to 25 $\mu\Omega$ cm.

Figure 7.23 presents the H_{c2} of two single crystals S_1 (blue) and S_2 (green), and that of the annealed polycrystal P_1', measured with specific heat and resistivity. The H_{c2} of these single crystals again resembles very much the "L-type" H_{c2} presented in figure 7.15b[111]: it lies much lower than H-type behavior in Ref.[109] and shows no clear change of curvature at around $T_{sc}/2$. By contrast, H_{c2} in the annealed polycrystal P_1' shows the same trend as in Ref.[109]

Annealing effects

In order to understand the differences between these single crystals and the usual UBe_{13} behavior, we further performed the following investigations.

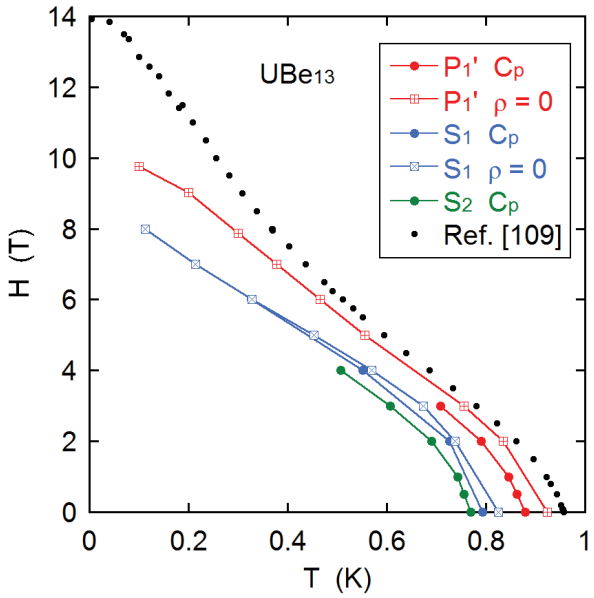

Figure 7.23 | Upper critical field of the annealed polycrystal P_1' and two single crystals S_1 (blue, U-LAP-0016) and S_2 (green, U-LAP-0026), measured with specific heat (filled circles) and resistivity ($\rho = 0$ criteria, the open squares). The H_{c2} reported in Ref.[109] (by resistivity) is presented with the black points for comparison.

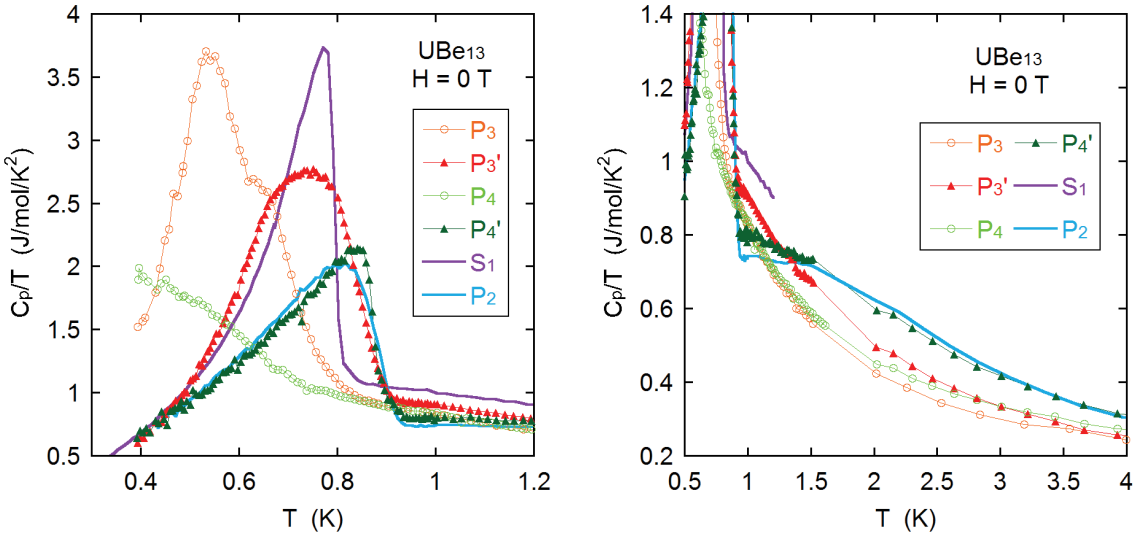

Figure 7.24 | C_p/T behavior of two polycrystals with 1% boron and aluminum substitutions, before and after annealing at 700°C during 370 hours. P_3 (U-LAP-0024) and P_3' (U-LAP-0030) correspond to the bare and annealed 1% B-doped sample. P_4 (U-LAP-0023) and P_4' (U-LAP-0031) correspond to the bare and annealed 1% Al-doped sample. The single crystal S_1 and the undoped annealed polycrystal P_2 (U-LAP-0029) are equally presented for comparison. **(a)** presents the superconducting transitions, and **(b)** gives a zoom at the normal phase.

Considering the sensitivity of UBe_{13} to small amount of doping, one possible origin for the "L-type" behavior in the single crystals is due to the impurities introduced by the flux method. To study this possibility we measured two polycrystalline samples P_3 and P_4, respectively with 1% substitution of boron and aluminum on the beryllium atoms. Figure 7.24a presents the C_p/T of these doped samples, before and after annealing at 700°C during 370 hours. C_p/T of single crystal S_1 and the undoped annealed polycrystal P_2 are equally presented for comparison. It shows that B-doping leads to an enhanced C_p/T jump at T_{sc} and lowered T_{sc}, as is observed previously in the single crystals with Al flux. With Al doping the superconducting transition broadens significantly and shifts to lower temperature. In both cases, in the normal phase C_p/T becomes temperature dependent, contrary to the undoped polycrystals in figure 7.17a and figure 7.19.

For the B-doped sample, after annealing (sample P_3') T_{sc} shifts to a usual value (0.86 K), and the enhanced C_p/T maximum is reduced. However, the normal phase behavior is not changed with annealing, and C_p/T is always strongly temperature dependent. For the Al-doped sample, after annealing, not only the usual T_{sc} is found, but the usual temperature-independent normal phase behavior is recovered: P_4' no longer shows any sign of doping and shows exactly the same behavior than the undoped sample P_2. Like the annealing effect on the undoped crystal P_1, it is possible that the the impurities move and aggregate during the annealing process, and get out of the bulk UBe_{13} phase, and as a consequence the effects of doping disappear. Then, one may question if Al migrates more freely than B during annealing.

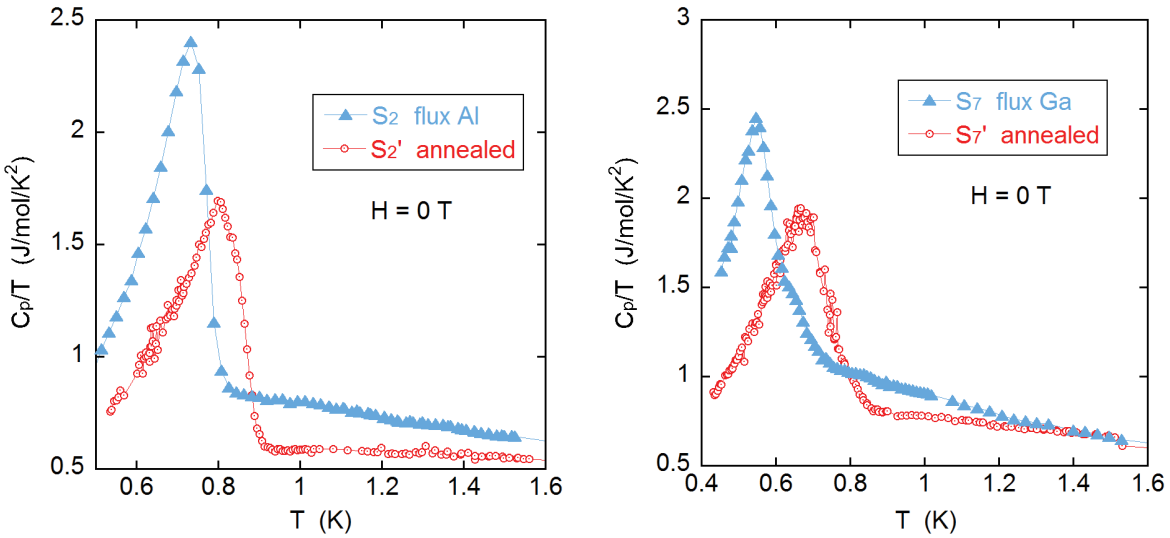

Figure 7.25 | C_p/T of two single crystals before (blue) and after (red) annealing at 700°C during 730 hours. **(a)**: sample S_2 with Al flux (U-LAP-0034, ancient U-LAP-0026); **(b)**: sample S_2 with Ga flux (U-LAP-0035, ancient U-LAP-0027).

In general, one considers that single crystals obtained by flux do not need to be annealed, owing to the very homogeneous chemical environment and absence of the temperature gradient at the grown surface during the synthesis. But this might be wrong if Al is

migrating into the crystal during the growth: it might then be removed by post-annealing, as would be the case for the doped polycrystals. To test this scenario we annealed several single crystals to see how their properties change.

Although performed under vacuum, after annealing, the surfaces of the single crystals are covered with a soft, non-crystalline layer, that presents no metallic glare as the initial single crystals do. This is probably due to oxidation. On flat surfaces, this layer can be removed by scrubbing carefully.

Figure 7.25 presents C_p/T of two single crystals S_2 (from Al flux, with extra amount of Be at the beginning) and S_7 (from Ga flux), before and after annealing at 700°C during 730 hours. In both cases, annealing leads to a higher T_{sc} as for the polycrystals, and in the normal phase, both the absolute value of the γ coefficient and its temperature dependence are reduced. The low C_p/T in the normal phase in the annealed samples are possibly related to an overestimation of the sample mass due to the oxidation problem.

7.3.3 Summary

The specific heat measurements on different samples reveal a strong contrast between the single crystals obtained from the flux method and polycrystalline samples, both in terms of the critical temperature T_{sc}, the specific heat jump at T_{sc}, and the temperature and field dependence of C_p/T in the normal phase.

The single crystals, obtained from Al or alternative flux method, show different behaviors depending on the details of the preparation procedure. However, they all share the "L-type" behavior[111]: a lower T_{sc} (ranging from 0.6 to 0.8 K), an enhanced C_p/T jump at T_{sc}, and a marked temperature dependence of C_p/T in the normal phase down to T_{sc}.

The single crystals have nice cubic crystal forms with shiny metallic surface. Both the Laue X-ray spectra and distinct specific heat jump at the superconducting transition, demonstrate that they have good homogeneity. However, their large residual resistivity show that they probably have sizable impurity contents.

The polycrystals show quite different behavior. The unannealed polycrystalline samples show low homogeneity and have low T_{sc}, as well as a specific heat jump slightly higher than in the same annealed polycrystals. Annealing increases significantly their quality. The annealed polycrystalline samples show H-type behavior[115] and have higher T_{sc} than the single crystals. With doping (with boron or aluminum) the "L-type" behavior observed in the single crystals also emerges in polycrystals. Annealing reduces the effect of doping significantly: for the Al doped sample, after annealing the normal undoped behavior is recovered.

Annealing the single crystals equally exerts large effects on their C_p/T behavior. Several tests show that T_{sc} of the single crystals is raised up to reference value (around 0.9 K) after annealing, and that the enhanced C_p/T jump at T_{sc} is reduced and in the normal phase the temperature dependence of C_p/T becomes negligible (below 0.5 K). Thus the "L-type" behaviors observed in single crystals disappear with annealing. Figure 7.26 summarizes this final finding. C_p/T of the annealed single crystal S_2' have been multiplied by an arbitrary factor 1.3 (it could come from a probable overestimation of the sample mass), to be compared with the polycrystalline sample P_2. It demonstrates that after annealing, the C_p/T of single crystals becomes close to that of polycrystalline samples.

These results suggest that the "L-type" behavior of the single crystals might be due to the Al impurities introduced by the flux method itself, and could be removed with post-annealing. Thus to obtain high quality UBe_{13} single crystals, one should first obtain

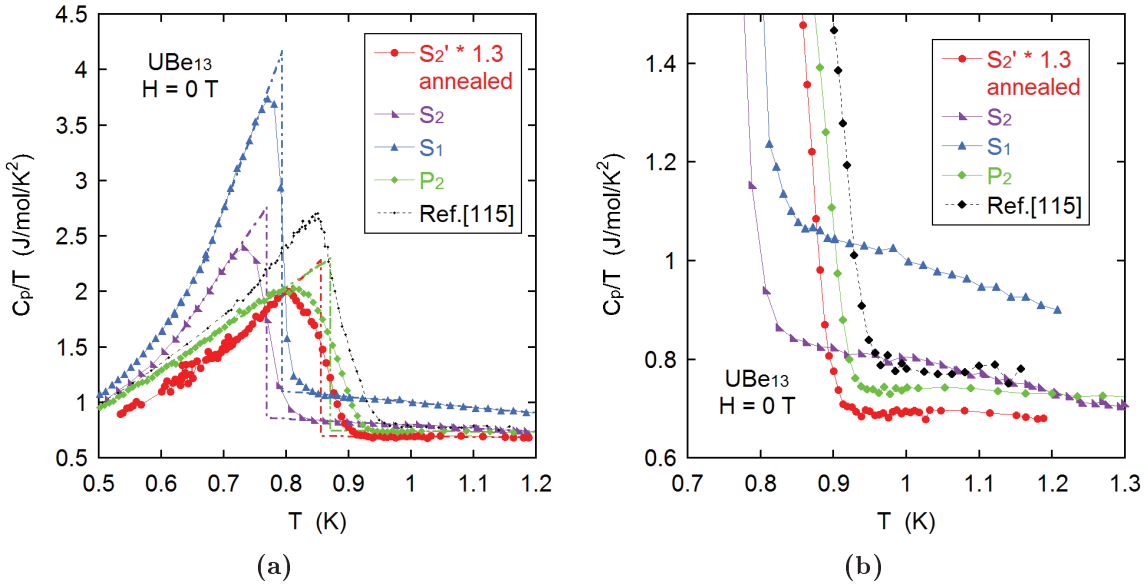

Figure 7.26 | C_p/T behavior of sample S_2 before (purple) and after (red) annealing, compared with the typical single crystal S_1 (blue) and the polycrystal P_2 (green). The black points show the classical UBe_{13} reported in Ref.[115]. **(a)** presents the superconducting transitions, the dashed line shows the fit based on entropy conserving analyses, **(b)** presents a zoom on the normal phase.

single crystals in the optimal conditions, i.e. with small extra amount of Be in the starting material and with a low cooling rate, then perform a long term annealing process, limited at 700°C. The optimal length of the annealing is still under investigation at the time of the writing of this manuscript, as well as the effect of the annealing on the single crystal residual resistivity (ρ_0): we do expect that ρ_0 should strongly decrease with annealing, if migration of Al outside the bulk of the crystal is indeed the reason for the sample "improvement".

Sample	No.	T_c (K)	γ_n (J.mol^{-1}K^{-2})	$\Delta C/C$	Mass (mg)	Preparing details
S_1	LAP 0016	0.794	1.10	2.78	2.35	standard
S_2	LAP 0026	0.769	0.86	2.20	0.40	U:Be = 1:20
S_3	LAP 0019	0.816	0.90	2.93	0.34	cooling rate $-1°$/h
S_4	LAP 0025	0.788	1.11	2.66	0.65	U:Be = 1:10
S_5	LAP 0021-2	0.800	0.95	2.52	0.69	start with the polycrystal P_1' Al 6N
S_6	LAP 0027	0.601	1.15	1.72	2.70	Ga flux
S_7	LAP 0028	0.681	1.10	1.70	2.22	Ga-Al flux
P_1	LAP 0020	0.775	0.72	2.29	0.77	standard
P_1'	LAP 0020-700	0.879	0.63	1.94	0.55	LAP 0020 annealed
P_2	LAP 0029	0.871	0.75	2.08	0.63	U:Be = 1:13.5 LAP 0022 annealed
P_3	LAP 0023				1.35	doped 1% Al
P_3'	LAP 0031	∼0.9			1.31	LAP 0023 annealed doped 1% Al
P_4	LAP 0024	∼0.65			2.27	doped 1% B
P_4'	LAP 0030	∼0.8			0.91	LAP 0024 annealed doped 1% B
S_2'	LAP 0034	0.856	0.53	2.28	0.34	LAP 0026 annealed U:Be = 1:20
S_5'	LAP 0033					LAP 0021-2 annealed
S_6'	LAP 0035	∼0.75			2.53	LAP 0027 annealed Ga flux
S_7'	LAP 0036					LAP 0028 annealed Ga-Al flux

Table 7.2 | Preparation details and properties of UBe_{13} samples.

Appendix A

Discussions on the two-band effect and the case of transverse field on the Mineev's theory

In the work of V. Mineev [119, 39], superconductivity is derived from a microscopic model, and ESP (Equal Spin Pairing) states are realized due to strong polarization of the Fermi sea in the exchange field driving the ferromagnetism. This naturally leads to a "two-band solution" for the superconductivity order parameter, where pairing is realized in the spin up or spin down bands. The splitting of the two bands can be characterized by a dimensionless parameter u, which corresponds to the relative change of the density of states ($N^{\uparrow,\downarrow}$) weighted by the particular choice of superconducting order parameter. For example, for $\Psi = (\hat{k_x}\eta_x^{\uparrow}, \hat{k_x}\eta_x^{\downarrow})$,

$$u = \frac{| < \hat{k_x}^2 N^{\uparrow}(k_x) > - < \hat{k_x}^2 N^{\downarrow}(k_x) > |}{< \hat{k_x}^2 N^{\uparrow}(k_x) > + < \hat{k_x}^2 N^{\downarrow}(k_x) >} \tag{A.1}$$

Eq.(5.19) presented in Chapter 5 is a simplified version of these solutions, valid when the polarization is strong (u close to 1), or when the spin susceptibilities have a strong uniaxial anisotropy. This last point is well verified in UCoGe, which explains why we could safely ignore the complexity of the two-band solution. However, it is also easy to quantify numerically the importance of these corrections. The theoretical work of Ref.[39] does not evaluate explicitely H_{c2}, which requires heavy calculations depending on the precise order parameter. But at the level discussed in our paper, it gives an expression for the coupling constant of ESP states (Eq.(117) in Ref.[39]) taking multiband effects into account. In all cases, T_{sc} is determined by a pairing constant λ:

$$\lambda = \frac{\lambda_{11} + \lambda_{22}}{2} + \sqrt{\frac{(\lambda_{11} - \lambda_{22})^2}{4} + \lambda_{12}\lambda_{21}} \tag{A.2}$$

The various λ_{ij} depend on the susceptibilities, but also on the band polarization (u), and on the orientation of the d-vector (representing the spin triplet superconducting order parameter): ($\mathbf{d} \times \mathbf{d}^*$) is parallel to the average spin of the superconducting condensate, which should follow the effective field $\mathbf{H_m} = \mathbf{h} + \mathbf{H}$ with $\mathbf{h}$ the exchange field ($//\mathbf{c}$) and $\mathbf{H}$ the applied field.Noting ϕ the angle between $\mathbf{h}$ and $\mathbf{H}$ $\left(\tan\phi = \frac{H_y}{h}\right)$, χ_i the static susceptibility $\chi(\mathbf{H} = \mathbf{0}, \mathbf{q} = \mathbf{0})$ for the magnetization response along the field applied on

axis-i, and taking also an isotropic **k**-dependence for all susceptibilities (characterized by $a = \xi_{mag} k_F$), we get for the λ_{ij} from Eq.(117), (168)-(170) in Ref.[39]:

$$\begin{aligned}
\lambda_{11} &= \left[g_z \cos^2\phi + B \sin^2\phi\right](1+u) \\
\lambda_{22} &= \left[g_z \cos^2\phi + B \sin^2\phi\right](1-u) \\
\lambda_{12} &= \left[(A-g_z)\sin^2\phi + (A-B)\cos^2\phi\right](1-u) \\
\lambda_{21} &= \left[(A-g_z)\sin^2\phi + (A-B)\cos^2\phi\right](1+u)
\end{aligned} \tag{A.3}$$

Combining Eq.(A.3) with Eq.(A.2), we have:

$$\begin{aligned}
\lambda = \bar{\lambda}_0 \Big(& g_z \cos^2\phi + B \sin^2\phi + \\
& \sqrt{u^2 \left[g_z \cos^2\phi + B \sin^2\phi\right]^2 + (1-u^2)\left[(g_z - A)\sin^2\phi + (B-A)\cos^2\phi\right]^2} \Big)
\end{aligned} \tag{A.4}$$

where

$$\bar{\lambda}_0 = \frac{\lambda(0)}{1 + \sqrt{u^2 + (1-u^2)(B-A)^2}} \tag{A.5}$$

and

$$\begin{aligned}
g_z(\mathbf{H}) &= \frac{(1+a^2)^2}{(\Theta(\mathbf{H}) + a^2)^2} \\
\Theta(\mathbf{H}//\mathbf{c}) = 1/2\left(3\frac{M_z^2}{M_0^2} - 1\right); \quad & \Theta(\mathbf{H} \perp \mathbf{c}) = \frac{T_{Curie}(H) - T_{sc}}{T_{Curie}(0) - T_{sc}} \\
A = \frac{(1+a^2)^2}{\left(\frac{\chi_z}{2\chi_x} + a^2\right)^2}; \quad & B = \frac{(1+a^2)^2}{\left(\frac{\chi_z}{2\chi_y} + a^2\right)^2}
\end{aligned} \tag{A.6}$$

Very generally, when there is no polarization ($u = 0$), Eq.(A.4) is independent of the rotation of the **d**-vector, and it reduces to:

$$\lambda = \lambda_0 \frac{g_z + B - A}{1 + B - A} \tag{A.7}$$

A.1 Consequences for H//c:

For $\mathbf{H}//\mathbf{c}$, the **d**-vector remains perpendicular to the **c**-axis ($\phi = 0$). So Eq.(A.4) takes a simple form, even with finite polarization u:

$$\lambda = \bar{\lambda}_0 \left(g_z + \sqrt{u^2 g_z^2 + (1-u^2)(B-A)^2}\right) \tag{A.8}$$

The change in the field dependence of λ given by Eq.(A.8), compared to the expression $\lambda = \lambda_0 g_z$ ($u = 1$) used for the discussion in the main paper, arises from the term $(B-A)$ which depends on the susceptibilities along **b** and **a** axis respectively, and is field independent. This term, which tends to diminish the field dependence of λ, will have the largest influence when there is no polarization ($u = 0$).

Collecting values of χ_a and χ_b from the literature[42, 87, 88], and our own data for $\chi_c \approx 0.11\ \mu_B$/T at 0.5 K, we get the following estimations for the ratios $\chi_c/2\chi_b \sim 8.5$ and $\chi_c/2\chi_a \sim 20$. Fig.A.1 displays the worst case, computed from Eq.(A.7) ($u = 0$), when the influence of the two-band effect is the strongest. The difference between the one-band and the two-band calculation of $\lambda(H)$ is compensated, in the required field range (0-0.6 T), by a 10% change of $\xi_{mag}k_F$. With a finite polarization u, the required change is even lower. This justifies the use the "one-band approximation" in the main paper for the whole discussion of H_{c2} in UCoGe along the **c**-axis.

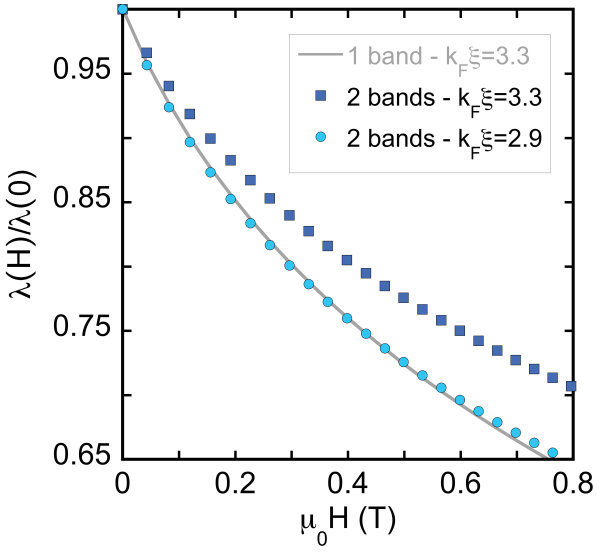

Figure A.1 | One vs two band calculations for UCoGe - H//c.
Grey full line: one band calculation of $\lambda(H)$ as presented in the main paper from the theoretical expressions in Ref.[39]. It is based on the experimental magnetization data (Fig.5.2), and a value of the the parameter $a = \xi_{mag}k_F \sim 3.3$. Dark blue squares: two-band calculation (from Ref.[39]), with the same magnetization data and same value of a, as well as with the experimental values of the susceptibility anisotropies between the **b**-**c** and **a**-**c** axis (see text). Light blue circle: same two-band calculation, but with a lower value of $a \sim 2.9$. One can see that the more exact two-band calculation yield the same field dependance as the one-band calculation, in the field range of $H_{c2}(0)//\mathbf{c}$, with only a 10% adjustment of the value of a.

A.2 Consequences for H//b:

As regards now the situation for field along the **b**-axis, on top of the polarization, we also need the (related) value of the exchange field "h", required to determine the rotation angle ϕ of the **d**-vector. Starting with the one-band model ($u = 1$) with rotation of the **d**-vector, Fig.A.2 shows that Eq.(A.4) predicts a decrease of λ for $\mathbf{H}//\mathbf{b}$. This counter-intuitive result is easily understood. In such a case, the expression for λ reduces to $\lambda(H)/\lambda(0) = g_z \cos^2\phi + B\sin^2\phi$, and the increase of g_z due to the suppression of T_{Curie} does not compensate the increasing weight of the fluctuations along **b** (B is much smaller than g_z since $\chi_b \ll \chi_c$) even with a large value of the exchange field (15 T chosen for the

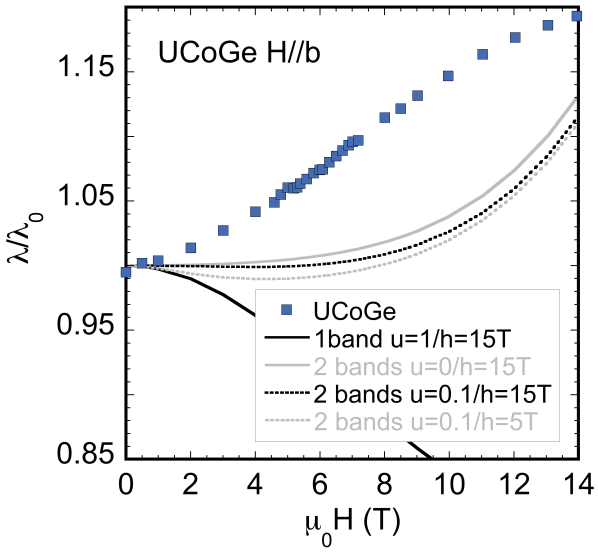

Figure A.2 | Comparison theory/experiment for H//b in UCoGe.
Blue squares: data for $\lambda(H)//\mathbf{b}$ as deduced from the H_{c2} data (see main paper). Full black line: one band calculation of $\lambda(H)$ according to Ref.[39], taking now account of the rotation of the **d**-vector, for a large exchange field of 15 T. λ should then decrease under field, as the rotation of **d** prevents to take full advantage of the fluctuations along the **c**-axis. Full grey line: two-band calculation, with the same exchange field but still no polarization: this is the most favorable case, and an increase of λ is predicted for $\mathbf{H}//\mathbf{b}$, but the quantitative agreement is poor. Black dotted and grey lines: same two bands calculation, with 10% polarization of the bands, and respective exchange fields of 15 and 5 T. The agreement is even worse, and naturally, smaller exchange field accentuate the decrease of λ due to the rotation of the **d**-vector.

curve of Fig.A.2). The situation is better in a two-band model with negligible polarization (for the same 15 T exchange field, $u = 0$, see Fig.A.2). In this case, λ has again the simple expression (A.7), independent of the angle ϕ, and it increases due to the suppression of T_{Curie}. The positive point is that one recovers an increase of λ along **b**, however not the right value for the initial (positive) curvature, and more seriously, not the saturation of the increase at higher fields. This increase is controlled by the T_{Curie} suppression, and no change of the values of the parameters can alter this behavior. Including the effect of a finite polarization only further increases this behavior. This is notably the case at low fields, where the trend to a decrease of λ is recovered (as for the one band case), the faster, the weaker the exchange field is (as it drives a faster rotation of the spins): see the calculations for 10% polarization and an exchange field of 15 or 5 T in Fig.A.2. As a summary, for the case of $\mathbf{H}//\mathbf{b}$ in UCoGe, when a two-band model is considered (as it should), the theory of Ref.[39] predicts indeed a pairing strength increasing with field, as is experimentally expected. But quantitative agreement of $\lambda(H)$ for this field direction is hard to obtain, featuring the complexity of magnetism in this case.

UCoGe is probably not the best system to discuss the physics at play for field along the **b**-axis: the case of URhGe is much better documented experimentally, and an important information is provided again by very recent NMR experiments in (Co-doped) URhGe[71]. It has been observed that in this compound, both the longitudinal (T_1) and transverse (T_2)

nuclear relaxation times, probing respectively the fluctuations transverse and along the effective $\mathbf{H_m}$ field, strongly increase when a field is applied along the **b**-axis. This means that both fluctuations along **c** and along **b**-axis are reinforced on field increase along **b**. This last effect cannot be deduced from the model based on a Landau description of the ferromagnetic state[39], but could be captured in more microscopic models of the ferromagnetic state[56], where the reinforcement of superconductivity along the **b**-axis originates from the appearance of soft magnon modes.

Conclusion

Since their discovery, the three orthorhombic ferromagnetic superconductors, UGe_2, URhGe and UCoGe, have attracted much attention, due to the coexistence of ferromagnetism and superconductivity in these systems, and the interplay between these two orders.

The main focus of this thesis is on the upper critical field of UCoGe. As is shown by previous resistivity studies[30], the H_{c2} of UCoGe presents many particular aspects: the huge anisotropy between field along the **c**-axis (spontaneous magnetization axis) and the two transverse field directions, the extremely sharp angular dependence around the **a** and **b**-axes, and the unusual upward curvatures in H_{c2} for the three field directions, not to speak of the S-shape H_{c2} for $\mathbf{H}//\mathbf{b}$. The first part of this thesis presents the H_{c2} measurements with thermal conductivity and other experimental methods, which confirm with bulk-sensitive probes all the special features of H_{c2} in UCoGe.

The second part of this study tries to answer the questions raised by the particular H_{c2} in UCoGe. To understand this behavior, it is necessary to take into account a new (predicted) phenomenon specific to the ferromagnetic superconductors: the field dependence of the pairing interaction.

For the case of $\mathbf{H}//\mathbf{c}$, both the "2D" anisotropy and the upward curvature in H_{c2} can be explained if a strong suppression of the pairing interaction under field along the **c**-axis is considered. This aspect is supported by many experimental observations which prove that the longitudinal magnetic fluctuations in UCoGe is strongly suppressed by $\mathbf{H}//\mathbf{c}$, and can be further compared quantitatively with the field dependence of the Sommerfeld coefficient in the specific heat, in the normal phase of UCoGe. What is more, such a behavior is predicted by a general microscopic theory for (orthorhombic) ferromagnetic superconductors[39]. It predicts that for field along the easy magnetization axis (**c**-axis in UCoGe), the field dependence of the pairing interaction is associated to the variation of the magnetization. With experimental magnetization measurements, the theoretical prediction in Ref.[39] can then be compared quantitatively with the experimental data.

These analyses provide a quantitative and well-controlled clarification for the "simple" case of $\mathbf{H}//\mathbf{c}$ in UCoGe. Based on the same physical framework, it is even possible to explain why the particular H_{c2} behavior of UCoGe is not observed in the sister compound URhGe, despite the strong resemblance of the two systems.

Hence UCoGe is a rare case (if not unique) among unconventional superconductors, where a prediction of a microscopic theory (with a precise magnetically mediated pairing mechanism) can be compared quantitatively to experiments. Such a fulfillment is possible only because in UCoGe the change of the pairing interaction (under magnetic field along the **c**-axis) is so important, that it has a significant and dominant impact on both the superconducting properties (H_{c2}) and the normal phase behavior ($\gamma(H)$). This gives a strong prove that the pairing mechanism in UCoGe originate from ferromagnetic fluctuations.

On the contrary to the well-understood case of **H**//**c**, the case of transverse magnetic fields (**H**//**b**) is much more complex. In this case the theory in Ref.[39] seems to be at its limit, probably due to the fact that it cannot fully account for the complicated magnetism in the transverse field configuration. This study presents some experimental findings, which show that a change in the superconducting order parameter under **H**//**b** possibly occurs in UCoGe, and the continuous (S-shape) H_{c2} in this case may nonetheless come from two different superconducting states, similar to the case of URhGe.

The enhancement of the transverse fluctuations might be a key element to understand the case of **H**//**b** in UCoGe (and in URhGe, for the re-entrant phase), since it leads to a situation different from the zero field or the **H**//**c** case, where only the longitudinal fluctuations are important. This might alter the pairing mechanism, and possibly leads to a change of the p-wave pairing state. To fully understand the case of **H**//**b** in these systems it is above all important to investigate the magnetic state in the transverse field configuration, both with experiments (NMR, neutrons, etc) and with more complete theoretical models. In particular, it will be interesting to study the vortex state in UCoGe for **H**//**b**, for example with critical current or STM measurements.

As an additional part of this study, the last chapter presents some thermal conductivity and specific heat measurements on the normal phase of UCoGe, to study respectively the role of the spin fluctuations in thermal transport, and a series of field-induced changes in the band structure of UCoGe. This chapter also presents the first results of the other system studied: UBe_{13}. They show that the L-type UBe_{13} behavior observed in some single crystals might originate from the Al impurities introduced by the flux method. Further annealing helps to remove the Al impurities, and is thus a promising method to get high quality UBe_{13} single crystals.

Conclusion en français

Depuis leur découvertes, les trois supraconducteurs ferromagnétiques orthorhombiques, UGe_2, URhGe et UCoGe, ont attiré beaucoup d'attention, en raison de la coexistence du ferromagnétisme et de la supraconductivité dans ces systèmes, et de l'interaction entre ces deux ordres.

Le sujet principal de cette thèse est le champ critique supérieur de UCoGe. Comme le montrent les études en résistivité précédentes[30], le H_{c2} de UCoGe présente de nombreux aspects particuliers: une énorme anisotropie entre le champ le long de l'axe **c** (axe d'aimantation spontanée) et les deux directions du champ transversales, la dépendance angulaire de l'H_{c2} extrêmement forte autour des axes **a** et **b**, les curvatures positives inhabituelles dans H_{c2} pour tous les trois directions de champ, sans parler de la forme S dans le H_{c2} pour $\mathbf{H}//\mathbf{b}$. La première partie de cette thèse présente des mesures de H_{c2} avec la conductivité thermique et d'autres méthodes expérimentales, qui confirment avec des sondes sensibles caractéristiques spéciales de H_{c2} dans UCoGe.

La deuxième partie de cette étude tente de répondre aux questions soulevées par le H_{c2} de UCoGe. Pour comprendre ce comportement, il est nécessaire de prendre en compte un nouveau phénomène (prédit) spécifique au supraconducteurs ferromagnétique: la dépendance en champ de l'interaction d'appariement.

Pour le cas de $\mathbf{H}//\mathbf{c}$, on peut expliquer à la fois l'anisotropie "2D" et la courbure positive dans H_{c2}, Si l'on considère une forte suppression de l'interaction d'appariement sous le champ le long de l'axe **c**. Cet aspect est observé dans de nombreuses observations expérimentales qui prouvent que les fluctuations magnétiques longitudinales. Dans UCoGe est fortement supprimée par $\mathbf{H}//\mathbf{c}$, et peut être davantage comparée quantitativement avec la dépendance en champ du coefficient Sommerfeld de la chaleur spécifique, dans la phase normale de UCoGe. De plus, un tel comportement est prédit par une théorie microscopique pour les supraconducteurs ferromagnétiques (orthorhombiques) [39]. Il en déduit que pour le champ le long de l'axe facile d'aimantation (l'axe **c** dans UCoGe), la dépendance en champ de l'interaction d'appariement est associée à la variation de l'aimantation. Avec des mesures expérimentales d'aimantation, la théorie dans le Ref.[39] peut ensuite être comparée quantitativement avec les données expérimentales.

Ces analyses fournissent une clarification quantitative et bien contrôlée pour le cas "simple" de $\mathbf{H}//\mathbf{c}$ dans UCoGe. Basé sur le même cadre physique, il est même possible d'expliquer pourquoi le comportement particulier de H_{c2} de UCoGe n'est pas observé dans le composé URhGe, malgré la forte ressemblance des deux systèmes.

Par conséquent UCoGe est un cas rare (sinon unique) parmi les supraconducteurs non conventionnels, ouu on peut comparer la prédiction d'une théorie microscopique (avec un mécanisme d'appariement via les susceptibilité magnétiques) quantitativement aux expériences. Une telle réalisation n'est possible que parce que dans UCoGe le changement de l'interaction d'appariement (sous champ magnétique le long de l'axe **c**) est si important, qu'il a un impact significatif et dominant, aussi bien sur les propriétés supra-

conductrices (H_{c2}) que sur la phase normale ($\gamma(H)$). Cela donne une forte preuve pour que le mécanisme d'appariement dans UCoGe provient des fluctuations ferromagnétiques.

Contrairement au cas bien compris de $\mathbf{H}//\mathbf{c}$, le cas des champs magnétiques transversaux ($\mathbf{H}//\mathbf{b}$ surtout) est beaucoup plus complexe. Dans ce cas, la théorie de Ref.[39] semble être à sa limite, probablement en raison du fait qu'elle ne peuvent pas entièrement tenir compte du magnétisme complexe dans la configuration du champ transversal. Cette étude présente quelques résultats expérimentaux qui montrent qu'un changement dans le paramètre d'ordre supraconducteur sous $\mathbf{H}//\mathbf{b}$ peut se produire dans UCoGe, et le continu (S-forme) H_{c2} dans ce cas peut néanmoins provenir de deux différents états supraconducteurs, comme dans le cas de l'URhGe.

L'augmentation des fluctuations transversales pourrait être un élément clé pour comprendre le cas de $\mathbf{H}//\mathbf{b}$ dans UCoGe, et dans URhGe, pour la phase réentrante. Elle conduit à une situation différente du champ nul ou du cas de $\mathbf{H}//\mathbf{c}$, ouu seules les fluctuations longitudinales sont importantes. Cela peut modifier le mécanisme d'appariement et peut éventuellement entraîner un changement de l'ordre de paramètre supraconductrice p-wave. Pour bien comprendre le cas de $\mathbf{H}//\mathbf{b}$ dans ces systèmes, il est avant tout important de étudier l'état magnétique sous champ transversal, à la fois avec des expériences (RMN, Neutrons, etc.) et avec des modèles théoriques plus complets. En particulier, il sera intéressant d'étudier l'état de vortex dans UCoGe pour $\mathbf{H}//\mathbf{b}$, par exemple avec des mesures de courant critique ou de STM.

Le dernier chapitre de cette étude présente des mesures de la conductivité thermique et de la chaleur spécifiques de la phase normale de UCoGe, pour étudier respectivement le rôle des fluctuations de spin dans le transport thermique et une série de changements induits par le champ dans la structure de bande de UCoGe. Ce chapitre présente également les premiers résultats sur l'autre système étudié: UBe $_{13}$. Ils montrent que le comportement de type L UBe_{13} observé dans certains monocristaux peut provenir du Al introduites par la méthode du flux. Un recuit supplémentaire aide à éliminer les impuretés Al, et donc consiste à une méthode prometteuse pour obtenir des monocristaux UBe_{13} de haute qualité.

Bibliography

[1] W. A. Fertig, D. C. Johnston, L. E. DeLong, R. W. McCallum, M. B. Maple, and B. T. Matthias. Destruction of superconductivity at the onset of long-range magnetic order in the compound $ErRh_4B_4$. *Phys. Rev. Lett.*, 38:987–990, Apr 1977.

[2] P. W. Anderson and H. Suhl. Spin alignment in the superconducting state. *Phys. Rev.*, 116:898–900, Nov 1959.

[3] A.I. Buzdin, L.N. Bulaevskii, and S.V. Panyukov. Existence of superconducting domain walls in ferromagnets. 60(1):174–179–, 1984.

[4] L.N. Bulaevskii, A.I. Buzdin, M.L. Kulic, and S.V. Panjukov. Coexistence of superconductivity and magnetism theoretical predictions and experimental results. *Advances in Physics*, 34(2):175–261, 1985.

[5] S. S. Saxena, P. Agarwal, K. Ahilan, F. M. Grosche, R. K. W. Haselwimmer, M. J. Steiner, E. Pugh, I. R. Walker, S. R. Julian, P. Monthoux, G. G. Lonzarich, A. Huxley, I. Sheikin, D. Braithwaite, and J. Flouquet. Superconductivity on the border of itinerant-electron ferromagnetism in UGe_2. *Nature*, 406(6796):587–592, August 2000.

[6] Dai Aoki, Andrew Huxley, Eric Ressouche, Daniel Braithwaite, Jacques Flouquet, Jean-Pascal Brison, Elsa Lhotel, and Carley Paulsen. Coexistence of superconductivity and ferromagnetism in URhGe. *Nature*, 413(6856):613–616, October 2001.

[7] T Akazawa, H Hidaka, T Fujiwara, T C Kobayashi, E Yamamoto, Y Haga, R Settai, and Y Onuki. Pressure-induced superconductivity in ferromagnetic UIr without inversion symmetry. *Journal of Physics: Condensed Matter*, 16(4):L29, 2004.

[8] N. T. Huy, A. Gasparini, D. E. de Nijs, Y. Huang, J. C. P. Klaasse, T. Gortenmulder, A. de Visser, A. Hamann, T. Görlach, and H. v. Löhneysen. Superconductivity on the border of weak itinerant ferromagnetism in UCoGe. *Phys. Rev. Lett.*, 99:067006, Aug 2007.

[9] H. Kotegawa, S. Kawasaki, A. Harada, Y. Kawasaki, K. Okamoto, G. q. Zheng, Y. Kitaoka, E. Yamamoto, Y. Haga, Y. Onuki, K.M. Itoh, and E.E. Haller. The microscopic coexistence of superconductivity and ferromagnetism in UGe_2: ^{73}Ge-NMR/NQR study. *Journal of Magnetism and Magnetic Materials*, 272-276, Supplement:E27 – E28, 2004. Proceedings of the International Conference on Magnetism (ICM 2003).

[10] A. de Visser, N. T. Huy, A. Gasparini, D. E. de Nijs, D. Andreica, C. Baines, and A. Amato. Muon spin rotation and relaxation in the superconducting ferromagnet UCoGe. *Phys. Rev. Lett.*, 102:167003, Apr 2009.

[11] Tetsuya Ohta, Taisuke Hattori, Kenji Ishida, Yusuke Nakai, Eisuke Osaki, Kazuhiko Deguchi, Noriaki K. Sato, and Isamu Satoh. Microscopic coexistence of ferromagnetism and superconductivity in single-crystal UCoGe. *Journal of the Physical Society of Japan*, 79(2):023707, 2010.

[12] A. Pogrebna, T. Mertelj, N. Vujicic, G. Cao, Z. A. Xu, and D. Mihailovic. Coexistence of ferromagnetism and superconductivity in iron based pnictides: a time resolved magnetooptical study. *Scientific Reports*, 5:7754–, January 2015.

[13] C. Paulsen, D. J. Hykel, K. Hasselbach, and D. Aoki. Observation of the meissner-ochsenfeld effect and the absence of the meissner state in UCoGe. *Phys. Rev. Lett.*, 109:237001, Dec 2012.

[14] E.-M. Anton, S. Granville, A. Engel, S. V. Chong, M. Governale, U. Zülicke, A. G. Moghaddam, H. J. Trodahl, F. Natali, S. Vézian, and B. J. Ruck. Superconductivity in the ferromagnetic semiconductor samarium nitride. *Phys. Rev. B*, 94:024106, Jul 2016.

[15] Dai Aoki and Jacques Flouquet. Ferromagnetism and superconductivity in uranium compounds. *Journal of the Physical Society of Japan*, 81(1):011003, 2012.

[16] F. Steglich, J. Aarts, C. D. Bredl, W. Lieke, D. Meschede, W. Franz, and H. Schäfer. Superconductivity in the presence of strong pauli paramagnetism: $CeCu_2Si_2$. *Phys. Rev. Lett.*, 43:1892–1896, Dec 1979.

[17] N. D. Mathur, F. M. Grosche, S. R. Julian, I. R. Walker, D. M. Freye, R. K. W. Haselwimmer, and G. G. Lonzarich. Magnetically mediated superconductivity in heavy fermion compounds. *Nature*, 394(6688):39–43, July 1998.

[18] H. Q. Yuan, F. M. Grosche, M. Deppe, C. Geibel, G. Sparn, and F. Steglich. Observation of two distinct superconducting phases in $CeCu_2Si_2$. *Science*, 302(5653):2104–2107, 2003.

[19] G. Knebel, D. Aoki, D. Braithwaite, B. Salce, and J. Flouquet. Coexistence of antiferromagnetism and superconductivity in $CeRhIn_5$ under high pressure and magnetic field. *Phys. Rev. B*, 74:020501, Jul 2006.

[20] Andrew Huxley, Ilya Sheikin, Eric Ressouche, Nolwenn Kernavanois, Daniel Braithwaite, Roberto Calemczuk, and Jacques Flouquet. UGe_2: A ferromagnetic spin-triplet superconductor. *Phys. Rev. B*, 63:144519, Mar 2001.

[21] C. Pfleiderer and A. D. Huxley. Pressure dependence of the magnetization in the ferromagnetic superconductor UGe_2. *Phys. Rev. Lett.*, 89:147005, Sep 2002.

[22] F. Hardy, A. Huxley, J. Flouquet, B. Salce, G. Knebel, D. Braithwaite, D. Aoki, M. Uhlarz, and C. Pfleiderer. phase diagram of the ferromagnetic superconductor URhGe. *Physica B: Condensed Matter*, 359-361:1111 – 1113, 2005. Proceedings of the International Conference on Strongly Correlated Electron Systems.

[23] E. Slooten, T. Naka, A. Gasparini, Y. K. Huang, and A. de Visser. Enhancement of superconductivity near the ferromagnetic quantum critical point in UCoGe. *Phys. Rev. Lett.*, 103:097003, Aug 2009.

[24] E Hassinger, D Aoki, G Knebel, and J Flouquet. Pressure-phase diagram of UCoGe by ac-susceptibility and resistivity measurements. *Journal of Physics: Conference Series*, 200(1):012055, 2010.

[25] Gaël Bastien, Daniel Braithwaite, Dai Aoki, Georg Knebel, and Jacques Flouquet. Quantum criticality in the ferromagnetic superconductor UCoGe under pressure and magnetic field. *Phys. Rev. B*, 94:125110, Sep 2016.

[26] V. P. Mineev. Superconducting states in ferromagnetic metals. *Phys. Rev. B*, 66:134504, Oct 2002.

[27] V. P. Mineev and T. Champel. Theory of superconductivity in ferromagnetic superconductors with triplet pairing. *Phys. Rev. B*, 69:144521, Apr 2004.

[28] M. Taupin, L. Howald, D. Aoki, and J.-P. Brison. Superconducting gap of UCoGe probed by thermal transport. *Phys. Rev. B*, 90:180501, Nov 2014.

[29] Tetsuya Ohta, Yusuke Nakai, Yoshihiko Ihara, Kenji Ishida, Kazuhiko Deguchi, Noriaki K. Sato, and Isamu Satoh. Ferromagnetic quantum critical fluctuations and anomalous coexistence of ferromagnetism and superconductivity in UCoGe revealed by Co-NMR and NQR studies. *Journal of the Physical Society of Japan*, 77(2):023707, 2008.

[30] Dai Aoki, Tatsuma D. Matsuda, Valentin Taufour, Elena Hassinger, Georg Knebel, and Jacques Flouquet. Extremely large and anisotropic upper critical field and the ferromagnetic instability in UCoGe. *Journal of the Physical Society of Japan*, 78(11):113709, 2009.

[31] I. Sheikin, A. Huxley, D. Braithwaite, J. P. Brison, S. Watanabe, K. Miyake, and J. Flouquet. Anisotropy and pressure dependence of the upper critical field of the ferromagnetic superconductor UGe_2. *Phys. Rev. B*, 64:220503, Nov 2001.

[32] F. Levy, I. Sheikin, B. Grenier, and A. D. Huxley. Magnetic field-induced superconductivity in the ferromagnet URhGe. *Science*, 309(5739):1343–1346, 2005.

[33] Atsushi Miyake, Dai Aoki, and Jacques Flouquet. Field re-entrant superconductivity induced by the enhancement of effective mass in URhGe. *Journal of the Physical Society of Japan*, 77(9):094709, 2008.

[34] Dai Aoki, Tatsuma D. Matsuda, Frederic Hardy, Christoph Meingast, Valentin Taufour, Elena Hassinger, Ilya Sheikin, Carley Paulsen, Georg Knebel, Hisashi Kotegawa, and Jacques Flouquet. Superconductivity reinforced by magnetic field and the magnetic instability in uranium ferromagnets. *Journal of the Physical Society of Japan*, 80(Suppl.A):SA008, 2011.

[35] Dai Aoki and Jacques Flouquet. Superconductivity and ferromagnetic quantum criticality in uranium compounds. *Journal of the Physical Society of Japan*, 83(6):061011, 2014.

[36] E. Helfand and N. R. Werthamer. Temperature and purity dependence of the superconducting critical field, H_{c2}. II. *Phys. Rev.*, 147:288–294, Jul 1966.

[37] N. R. Werthamer, E. Helfand, and P. C. Hohenberg. Temperature and purity dependence of the superconducting critical field, H_{c2}. III. electron spin and spin-orbit effects. *Phys. Rev.*, 147:295–302, Jul 1966.

[38] F. Hardy and A. D. Huxley. p-wave superconductivity in the ferromagnetic superconductor URhGe. *Phys. Rev. Lett.*, 94:247006, Jun 2005.

[39] V. P. Mineev. Superconductivity in Uranium Ferromagnets. *ArXiv e-prints*, May 2016.

[40] R. Berman. *Thermal Conductivity In Solids*. Oxford University Press, 1976.

[41] Terry M. Tritt. *Thermal Conductivity: Theory, Properties, and Applications*. Kluwer Academic/Plenul Publishers, 2004.

[42] N. T. Huy, D. E. de Nijs, Y. K. Huang, and A. de Visser. Unusual upper critical field of the ferromagnetic superconductor UCoGe. *Phys. Rev. Lett.*, 100:077002, Feb 2008.

[43] C. Pfleiderer, M. Uhlarz, S. M. Hayden, R. Vollmer, H. v. Lohneysen, N. R. Bernhoeft, and G. G. Lonzarich. Coexistence of superconductivity and ferromagnetism in the d-band metal $ZrZn_2$. *Nature*, 412(6842):58–61, July 2001.

[44] E. A. Yelland, S. M. Hayden, S. J. C. Yates, C. Pfleiderer, M. Uhlarz, R. Vollmer, H. v. Löhneysen, N. R. Bernhoeft, R. P. Smith, S. S. Saxena, and N. Kimura. Superconductivity induced by spark erosion in $ZrZn_2$. *Phys. Rev. B*, 72:214523, Dec 2005.

[45] T. T. M. Palstra, B. Batlogg, R. B. van Dover, L. F. Schneemeyer, and J. V. Waszczak. Dissipative flux motion in high-temperature superconductors. *Phys. Rev. B*, 41:6621–6632, Apr 1990.

[46] S. Belin, T. Shibauchi, K. Behnia, and T. Tamegai. Probing the upper critical field of κ-(BEDT-TTF)$_2$Cu(NCS)$_2$. *Journal of Superconductivity*, 12(3):497–500, 1999.

[47] A. Carrington, A. P. Mackenzie, and A. Tyler. Specific heat of low-T_c $Tl_2Ba_2CuO_{6+\delta}$. *Phys. Rev. B*, 54:R3788–R3791, Aug 1996.

[48] G. Grissonnanche, O. Cyr-Choiniére, F. Lalibert´, S. Ren´ de Cotret, A. Juneau-Fecteau, S. Dufour-Beausj́our, M. E. Delage, D. LeBoeuf, J. Chang, B. J. Ramshaw, D. A. Bonn, W. N. Hardy, R. Liang, S. Adachi, N. E. Hussey, B. Vignolle, C. Proust, M. Sutherland, S. Krämer, J. H. Park, D. Graf, N. Doiron-Leyraud, and Louis Taillefer. Direct measurement of the upper critical field in cuprate superconductors. *Nat Commun*, 5:–, February 2014.

[49] MathieuTaupin. *Study of the magnetic heavy fermions UCoGe and $YbRh_2Si_2$ by transport measurements*. PhD thesis, University of Joseph-Fourier Grenoble I, 2013.

[50] Ludovic Howald. *Superconductivity and quantum criticality in $CeCoIn_5$, URhGe and UCoGe*. PhD thesis, Univertity of Grenoble, 2011.

[51] P.G.de Gennes. *Superconductivity of Metals and Alloys*. Advanced Book Program, 1999.

[52] Kazuhiko Deguchi, Eisuke Osaki, Seiko Ban, Nobuyuki Tamura, Yasuyuki Simura, Toshiro Sakakibara, Isamu Satoh, and Noriaki K. Sato. Absence of meissner state and robust ferromagnetism in the superconducting state of UCoGe: Possible evidence of spontaneous vortex state. *Journal of the Physical Society of Japan*, 79(8):083708, 2010.

[53] Stephan Blundell. *Magnetism in Condensed Matter*. Oxford University Press, 2001.

[54] V. Jaccarino and M. Peter. Ultra-high-field superconductivity. *Phys. Rev. Lett.*, 9:290–292, Oct 1962.

[55] H. W. Meul, C. Rossel, M. Decroux, Ø Fischer, G. Remenyi, and A. Briggs. Observation of magnetic-field-induced superconductivity. *Phys. Rev. Lett.*, 53:497–500, Jul 1984.

[56] K. Hattori and H. Tsunetsugu. p-wave superconductivity near a transverse saturation field. *Phys. Rev. B*, 87:064501, Feb 2013.

[57] T. Hattori, Y. Ihara, Y. Nakai, K. Ishida, Y. Tada, S. Fujimoto, N. Kawakami, E. Osaki, K. Deguchi, N. K. Sato, and I. Satoh. Superconductivity induced by longitudinal ferromagnetic fluctuations in UCoGe. *Phys. Rev. Lett.*, 108:066403, Feb 2012.

[58] Kurt Scharnberg and Richard A. Klemm. Upper critical field in p-wave superconductors with broken symmetry. *Phys. Rev. Lett.*, 54:2445–2448, Jun 1985.

[59] Christopher Lorscher. *Novel properties of ferromagnetic p-wave superconductors*. PhD thesis, University of Central Florida, 2014.

[60] L. N. Bulaevskii, O. V. Dolgov, and M. O. Ptitsyn. Properties of strong-coupled superconductors. *Phys. Rev. B*, 38:11290–11295, Dec 1988.

[61] F. Thomas, B. Wand, T. Luhmann, P. Gegenwart, G. R. Stewart, F. Steglich, J. P. Brison, A. Buzdin, L. Glemot, and J. Flouquet. Strong coupling effects on the upper critical field of the heavy-fermion superconductor UBe_{13}. *Journal of Low Temperature Physics*, 102(1):117–132, 1996.

[62] S. V. Shulga, S.-L. Drechsler, G. Fuchs, K.-H. Müller, K. Winzer, M. Heinecke, and K. Krug. Upper critical field peculiarities of superconducting YNi_2B_2C and $LuNi_2B_2C$. *Phys. Rev. Lett.*, 80:1730–1733, Feb 1998.

[63] S. V. Shulga, S. . Drechsler, H. Eschrig, H. Rosner, and W. E. Pickett. The upper critical field problem in MgB_2. *eprint arXiv:cond-mat/0103154*, March 2001.

[64] Emanuel Maxwell. Isotope effect in the superconductivity of mercury. *Phys. Rev.*, 78:477–477, May 1950.

[65] D. J. Scalapino, J. R. Schrieffer, and J. W. Wilkins. Strong-coupling superconductivity. i. *Phys. Rev.*, 148:263–279, Aug 1966.

[66] R.D.Parks. *Superconductivity*, volume 1. Marcel Dekker, INC., New York, 1969.

[67] K. Miyake, S. Schmitt-Rink, and C. M. Varma. Spin-fluctuation-mediated even-parity pairing in heavy-fermion superconductors. *Phys. Rev. B*, 34:6554–6556, Nov 1986.

[68] N. F. Berk and J. R. Schrieffer. Effect of ferromagnetic spin correlations on superconductivity. *Phys. Rev. Lett.*, 17:433–435, Aug 1966.

[69] S. Lefebvre, P. Wzietek, S. Brown, C. Bourbonnais, D. Jérome, C. Mézière, M. Fourmigué, and P. Batail. Mott transition, antiferromagnetism, and unconventional superconductivity in layered organic superconductors. *Phys. Rev. Lett.*, 85:5420–5423, Dec 2000.

[70] D. Fay and J. Appel. Coexistence of p-state superconductivity and itinerant ferromagnetism. *Phys. Rev. B*, 22:3173–3182, Oct 1980.

[71] Y. Tokunaga, D. Aoki, H. Mayaffre, S. Krämer, M.-H. Julien, C. Berthier, M. Horvatic, H. Sakai, S. Kambe, and S. Araki. Reentrant superconductivity driven by quantum tricritical fluctuations in URhGe: Evidence from ^{59}Co NMR in $URh_{0.9}Co_{0.1}Ge$. *Phys. Rev. Lett.*, 114:216401, May 2015.

[72] Y. Ihara, T. Hattori, K. Ishida, Y. Nakai, E. Osaki, K. Deguchi, N. K. Sato, and I. Satoh. Anisotropic magnetic fluctuations in the ferromagnetic superconductor UCoGe studied by direction-dependent ^{59}Co NMR measurements. *Phys. Rev. Lett.*, 105:206403, Nov 2010.

[73] Y Tada, S Fujimoto, N Kawakami, T Hattori, Y Ihara, K Ishida, K Deguchi, N K Sato, and I Satoh. Spin-triplet superconductivity induced by longitudinal ferromagnetic fluctuations in UCoGe: Theoretical aspect. *Journal of Physics: Conference Series*, 449(1):012029, 2013.

[74] L. Glemot, J. P. Brison, J. Flouquet, A. I. Buzdin, I. Sheikin, D. Jaccard, C. Thessieu, and F. Thomas. Pressure dependence of the upper critical field of the heavy fermion superconductor UBe_{13}. *Phys. Rev. Lett.*, 82:169–172, Jan 1999.

[75] Taisuke Hattori, Kosuke Karube, Kenji Ishida, Kazuhiko Deguchi, Noriaki K. Sato, and Tomoo Yamamura. Relationship between ferromagnetic criticality and the enhancement of superconductivity induced by transverse magnetic fields in UCoGe. *Journal of the Physical Society of Japan*, 83(7):073708, 2014.

[76] P. Monthoux and G. G. Lonzarich. Magnetically mediated superconductivity in quasi-two and three dimensions. *Phys. Rev. B*, 63:054529, Jan 2001.

[77] Satoshi Fujimoto. Asymptotically exact solution for superconductivity near ferromagnetic criticality. *Journal of the Physical Society of Japan*, 73(8):2061–2064, 2004.

[78] P. Monthoux, D. Pines, and G. G. Lonzarich. Superconductivity without phonons. *Nature*, 450(7173):1177–1183, December 2007.

[79] Shin-ichi Fujimori, Takuo Ohkochi, Ikuto Kawasaki, Akira Yasui, Yukiharu Takeda, Tetsuo Okane, Yuji Saitoh, Atsushi Fujimori, Hiroshi Yamagami, Yoshinori Haga, Etsuji Yamamoto, Yoshifumi Tokiwa, Shugo Ikeda, Takashi Sugai, Hitoshi Ohkuni,

Noriaki Kimura, and Yoshichika Ônuki. Electronic structure of heavy fermion uranium compounds studied by core-level photoelectron spectroscopy. *J. Phys. Soc. Jpn.*, 81(1):014703–, December 2011.

[80] M Samsel-Czekala, S Elgazzar, P M Oppeneer, E Talik, W Walerczyk, and R Troc. The electronic structure of UCoGe by ab initio calculations and XPS experiment. *Journal of Physics: Condensed Matter*, 22(1):015503, 2010.

[81] Jing-Xin Yu, Yan Cheng, Bo Zhu, and Huan Yang. Electronic structure, optical and thermodynamic properties of orthorhombic UCoGe under pressure. *Physica B: Condensed Matter*, 406(14):2788 – 2794, 2011.

[82] Shin-ichi Fujimori, Takuo Ohkochi, Ikuto Kawasaki, Akira Yasui, Yukiharu Takeda, Tetsuo Okane, Yuji Saitoh, Atsushi Fujimori, Hiroshi Yamagami, Yoshinori Haga, Etsuji Yamamoto, and Yoshichika Ônuki. Electronic structures of ferromagnetic superconductors UGe_2 and UCoGe studied by angle-resolved photoelectron spectroscopy. *Phys. Rev. B*, 91:174503, May 2015.

[83] A. D. Huxley, S. Raymond, and E. Ressouche. Magnetic excitations in the ferromagentic superconductor UGe_2. *Phys. Rev. Lett.*, 91:207201, Nov 2003.

[84] S Raymond and A Huxley. Spin dynamics of the ferromagnetic superconductor UGe_2. *Physica B: Condensed Matter*, 350:33 – 35, 2004. Proceedings of the Third European Conference on Neutron Scattering.

[85] C. Stock, D. A. Sokolov, P. Bourges, P. H. Tobash, K. Gofryk, F. Ronning, E. D. Bauer, K. C. Rule, and A. D. Huxley. Anisotropic critical magnetic fluctuations in the ferromagnetic superconductor UCoGe. *Phys. Rev. Lett.*, 107:187202, Oct 2011.

[86] V. P. Mineev. Superconductivity in uranium compounds. *Phys. Rev. B*, 90:064506, Aug 2014.

[87] F. Hardy, D. Aoki, C. Meingast, P. Schweiss, P. Burger, H. v. Löhneysen, and J. Flouquet. Transverse and longitudinal magnetic-field responses in the ising ferromagnets URhGe, UCoGe, and UGe_2. *Phys. Rev. B*, 83:195107, May 2011.

[88] W. Knafo, T. D. Matsuda, D. Aoki, F. Hardy, G. W. Scheerer, G. Ballon, M. Nardone, A. Zitouni, C. Meingast, and J. Flouquet. High-field moment polarization in the ferromagnetic superconductor UCoGe. *Phys. Rev. B*, 86:184416, Nov 2012.

[89] Hisashi Kotegawa, Kenta Fukumoto, Toshihiro Toyama, Hideki Tou, Hisatomo Harima, Atsushi Harada, Yoshio Kitaoka, Yoshinori Haga, Etsuji Yamamoto, Yoshichika Ônuki, Kohei M. Itoh, and Eugene E. Haller. ^{73}Ge-nuclear magnetic resonance/nuclear quadrupole resonance investigation of magnetic properties of URhGe. *Journal of the Physical Society of Japan*, 84(5):054710, 2015.

[90] R. Okazaki, Y. Kasahara, H. Shishido, M. Konczykowski, K. Behnia, Y. Haga, T. D. Matsuda, Y. Onuki, T. Shibauchi, and Y. Matsuda. Flux line lattice melting and the formation of a coherent quasiparticle bloch state in the ultraclean URu_2Si_2 superconductor. *Phys. Rev. Lett.*, 100:037004, Jan 2008.

[91] G. Seyfarth, J. P. Brison, M.-A. Méasson, J. Flouquet, K. Izawa, Y. Matsuda, H. Sugawara, and H. Sato. Multiband superconductivity in the heavy fermion compound $PrOs_4Sb_{12}$. *Phys. Rev. Lett.*, 95:107004, Sep 2005.

[92] H Shakeripour, C Petrovic, and Louis Taillefer. Heat transport as a probe of superconducting gap structure. *New Journal of Physics*, 11(5):055065, 2009.

[93] C. Kübert and P. J. Hirschfeld. Quasiparticle transport properties of d-wave superconductors in the vortex state. *Phys. Rev. Lett.*, 80:4963–4966, Jun 1998.

[94] J. Lowell and J. B. Sousa. Mixed-state thermal conductivity of type II superconductors. *Journal of Low Temperature Physics*, 3(1):65–87, 1970.

[95] H. Suderow, J. P. Brison, A. Huxley, and J. Flouquet. Thermal conductivity and gap structure of the superconducting phases of UPt_3. *Journal of Low Temperature Physics*, 108(1):11–30, 1997.

[96] A. V. Sologubenko, J. Jun, S. M. Kazakov, J. Karpinski, and H. R. Ott. Thermal conductivity of single-crystalline MgB_2. *Phys. Rev. B*, 66:014504, Jun 2002.

[97] Olli V. Lounasmaa and Erkki Thuneberg. Vortices in rotating superfluid ^{3}He. *Proceedings of the National Academy of Sciences*, 96(14):7760–7767, 1999.

[98] M. Taupin, L. Howald, D. Aoki, J. Flouquet, and J. P. Brison. Existence of anisotropic spin fluctuations at low temperature in the normal phase of the superconducting ferromagnet UCoGe. *Phys. Rev. B*, 89:041108, Jan 2014.

[99] Dai Aoki, Ilya Sheikin, Tatsuma D. Matsuda, Valentin Taufour, Georg Knebel, and Jacques Flouquet. First observation of quantum oscillations in the ferromagnetic superconductor UCoGe. *Journal of the Physical Society of Japan*, 80(1):013705, 2011.

[100] G. Bastien, A. Gourgout, D. Aoki, A. Pourret, I. Sheikin, G. Seyfarth, J. Flouquet, and G. Knebel. Lifshitz Transitions in the Ferromagnetic Superconductor UCoGe. *ArXiv e-prints*, September 2016.

[101] E. Steven, A. Kiswandhi, D. Krstovska, J. S. Brooks, M. Almeida, A. P. Gon¸calves, M. S. Henriques, G. M. Luke, and T. J. Williams. Robust properties of the superconducting ferromagnet UCoGe. *Applied Physics Letters*, 98(13), 2011.

[102] T. V. Bay, A. M. Nikitin, T. Naka, A. McCollam, Y. K. Huang, and A. de Visser. Angular variation of the magnetoresistance of the superconducting ferromagnet UCoGe. *Phys. Rev. B*, 89:214512, Jun 2014.

[103] A.A. Varlamov, V.S. Egorov, and A.V. Pantsulaya. Kinetic properties of metals near electronic topological transitions (2 1/2-order transitions). *Advances in Physics*, 38(5):469–564, 1989.

[104] Yusei Shimizu. *Study on superconducting symmetry of uranium heavy-electron compound UBe13 by very-low temperature precise magnetization and specific-heat measurements*. PhD thesis, University of Hokaido, 2012.

[105] H. R. Ott, H. Rudigier, Z. Fisk, and J. L. Smith. UBe_{13}: An unconventional actinide superconductor. *Phys. Rev. Lett.*, 50:1595–1598, May 1983.

[106] A. Hiess, A. Schneidewind, O. Stockert, and Z. Fisk. Signature of superconductivity in UBe_{13} as seen by neutron scattering: Superconducting and magnetic energy scales. *Phys. Rev. B*, 89:235118, Jun 2014.

[107] Yusei Shimizu, Shunichiro Kittaka, Toshiro Sakakibara, Yoshinori Haga, Etsuji Yamamoto, Hiroshi Amitsuka, Yasumasa Tsutsumi, and Kazushige Machida. Field-orientation dependence of low-energy quasiparticle excitations in the heavy-electron superconductor UBe_{13}. *Phys. Rev. Lett.*, 114:147002, Apr 2015.

[108] V G Storchak, J H Brewer, D G Eshchenko, P W Mengyan, O E Parfenov, A M Tokmachev, P Dosanjh, Z Fisk, and J L Smith. Spin gap in heavy fermion compound UBe_{13}. *New Journal of Physics*, 18(8):083029, 2016.

[109] J. P. Brison, J. Flouquet, and G. Deutscher. Low-temperature magnetoresistivity and upper critical field in UBe_{13}. *Journal of Low Temperature Physics*, 76(5):453–464, 1989.

[110] H.H.Hill. *Plutonium 1970 and Other Actinides: Proceedings of the 4th International Conference on Plutonium and Other Actinides*. Number ptie. 2 in Nuclear metallurgy. Metallurgical Society of AIME, Edited by W.N.Miner, 1970.

[111] C. Langhammer, R. Helfrich, A. Bach, F. Kromer, M. Lang, T. Michels, M. Deppe, F. Steglich, and G.R. Stewart. Evidence for the existence of two variants of UBe_{13}. *Journal of Magnetism and Magnetic Materials*, 177:443 – 444, 1998.

[112] H. R. Ott, E. Felder, Z. Fisk, R. H. Heffner, and J. L. Smith. Influence of boron impurities on the superconducting phase transition of $U_{1-x}Th_xBe_{13}$. *Phys. Rev. B*, 44:7081–7084, Oct 1991.

[113] W. P. Beyermann, R. H. Heffner, J. L. Smith, M. F. Hundley, P. C. Canfield, and J. D. Thompson. Effects of boron substitution on the superconducting state of UBe_{13}. *Phys. Rev. B*, 51:404–409, Jan 1995.

[114] H. R. Ott, H. Rudigier, E. Felder, Z. Fisk, and J. L. Smith. Influence of impurities and magnetic fields on the normal and superconducting states of UBe_{13}. *Phys. Rev. B*, 33:126–131, Jan 1986.

[115] JP Brison, A Ravex, J Flouquet, Z Fisk, and JL Smith. Field-dependence of the specific-heat of UBe_{13}. *Journal of Magnetism and Magnetic Materials*, 76 & 77:525–526, 1988.

[116] P. Gegenwart, C. Langhammer, R. Helfrich, N. Oeschler, M. Lang, J.S. Kim, G.R. Stewart, and F. Steglich. Non-fermi liquid normal state of the heavy-fermion superconductor UBe_{13}. *Physica C: Superconductivity*, 408 - 410:157 – 160, 2004. Proceedings of the International Conference on Materials and Mechanisms of Superconductivity. High Temperature Superconductors {VII} – {M2SRIO}.

[117] Brison, J.P., Laborde, O., Jaccard, D., Flouquet, J., Morin, P., Fisk, Z., and Smith, J.L. Normal and superconducting properties of UBe_{13}. *J. Phys. France*, 50(18):2795–2810, 1989.

[118] U. Rauchschwalbe, U. Ahlheim, F. Steglich, D. Rainer, and J. J. M. Franse. Upper critical magnetic fields of the heavy fermion superconductors $CeCu_2Si_2$, UPt_3, and UBe_{13}: Comparison between experiment and theory. *Zeitschrift für Physik B Condensed Matter*, 60(2):379–386, 1985.

[119] V. P. Mineev. Magnetic field dependence of pairing interaction in ferromagnetic superconductors with triplet pairing. *Phys. Rev. B*, 83:064515, Feb 2011.

Résumé des chapitres en français

Chapitre 1

Chapitre 1 donne une introduction brève sur les supreconducteurs ferromagnétiques UGe_2, URhGe et UCoGe.

Chapitre 2

Chapitre 2 donne une introduction sur les deux methodes expérimentales utilisées dans cette étude: la conductivité thermique et la chaleur spécifique. Il explique des difficultés expérimentales rencontrées dans ces expériences en détail, notamment sur l'orientation de la direction du champ dans les mesures de la conductivité thermique sur UCoGe, et la correction de la thermométrie pour les mesures de chaleur spécifique au PPMS.

Chapitre 3

Ce chapitre présente les mesures du H_{c2} de UCoGe avec la conductivité thermique, qui est une sonde volumique pour la transition supraconductrice, et d'autres méthodes expérimentales. Ces mesures montrent que les aspects particuliers dans le H_{c2} de UCoGe, observés dans les mesures de résistivité, sont bien très propriétés robustes de la supraconductivité. Une discussion est portée sur ces points particuliers, montrant qu'ils ne sont pas compatibles avec les théories classiques de la supraconductivité.

Chapitre 4

Ce chapitre discute le comportement de H_{c2} dans UCoGe en considérant un aspect particulier dans les systèmes supraconductrices ferromagnétiques: la dépendence en champ des interactions d'appariement. Il explique comment un tel effet peut influencer le comportement de H_{c2} d'une manière explicite, et discute cet effet dans UCoGe avec un modèle simple de supracoductivité en couplage fort. Un tel phenomène peut bien expliquer les différents aspects dans H_{c2} de UCoGe, et en plus soutenus par les propriétés dans la phase normale.

Chapitre 5

Ce chapitre discute la dépendance en champ d'intraction d'appariement avec la théorie de Mineev, une theorie microscopique pour la supraconductivité p-wave induit par les

susceptibilités magnétiques. Pour **H**//**c**, la théorie de Mineev déduit une dépendance en champ de l'interaction d'appariement qui est consistent avec celle obtenue en analysant les données expérimentales, dans le chapitre 4. En même temps, ce modèle théorique permet d'expliquer d'une manière quantitative la différence du comportement du H_{c2} dans URhGe et dans UCoGe. Pour **H**//**b**, la comparaison entre la théorie de Mineev et l'expérimental n'est pas conclusive, qui suggère la nécessité d'une description de l'état magnétique sous champ transversal dans ce système avec un modèle théorique plus complet.

Chapitre 6

Ce chapitre présente quelques observations expérimentales dans les mesures de la conductivité thermique et de la résistivité, pour le cas **H**//**b** dans UCoGe, qui suggèrent qu'un changement de l'état supraconductrice probablement se passe sous champ magnétique transversal (**H**//**b**) dans ce composé, tout comme dans la phase ré-entrante du composé jumeau URhGe.

Chapitre 7

Indépendant du rest de cette étude, ce dernier chapitre présente des mesures de la conductivité thermique et de la chaleur spécifiques de la phase normale de UCoGe, pour étudier respectivement le rôle des fluctuations de spin dans le transport thermique et une série de changements induits par le champ dans la structure de bande de UCoGe. Ce chapitre présente également les premiers résultats sur l'autre système étudié: UBe_{13}. Ils montrent que le comportement de type L UBe_{13} observé dans certains monocristaux peut provenir du Al introduites par la méthode du flux. Un recuit supplémentaire aide à éliminer les impuretés Al, et donc consiste à une méthode prometteuse pour obtenir des monocristaux UBe_{13} de haute qualité.

Abstract

This thesis mainly discuss the upper critical field of the ferromagnetic superconductor UCoGe. Thermal conductivity and other experimental methods have been used to confirm the numerous particular behaviors of H_{c2} in UCoGe, previously observed in resistivity studies. These features, including the strong anisotropy and the anomalous curvatures, cannot be interpreted in terms of classical theories for H_{c2}. Instead, a phenomenon specific to the ferromagnetic superconductors - the field dependence of the pairing interaction, needs to be considered. We show that this effect can be consistently analyzed with normal phase properties, and is quantitatively compared with existing theory. This leads to a net clarification for the case of $\mathbf{H}//\mathbf{c}$ in UCoGe, and at the same time explains the different behavior of H_{c2} in UCoGe and URhGe. These results strongly support the magnetic origin of superconductivity in these systems. For $\mathbf{H}//\mathbf{b}$, we show convergent experimental observations that suggest a possible change of the superconducting state induced by the transverse magnetic field in UCoGe. Independent from the rest of the study, the last chapter presents some experimental results on the normal phase of UCoGe and on the other heavy-fermion system UBe_{13}.

Key words: Unconventional superconductivity, magnetism, pairing mechanism, heavy fermion, UCoGe, UBe_{13}.

Résumé en Français

Cette thèse discute essentiellement sur le champ critique supérieur du supraconducteur ferromagnétique UCoGe. La conductivité thermique et d'autres méthodes expérimentales ont été utilisées pour confirmer les nombreux comportements particuliers de H_{c2} dans UCoGe, précédemment observés dans des études de résistivité. Ces caractéristiques, y compris une anisotropie forte et des courbures anormales, ne peuvent pas être interprétées en termes de théories classiques pour H_{c2}. Au lieu de cela, un phénomène spécifique aux supraconducteurs ferromagnétiques - la dépendance en champ de l'interaction d'appariement doit être considéré. Nous montrons que cet effet peut être analysé de façon cohérente avec des propriétés de la phase normales et peut être aussi comparé quantitativement avec une théorie existante. Ceci conduit à une clarification nette pour le cas de $\mathbf{H}//\mathbf{c}$ dans UCoGe, et explique en même temps le comportement différent de H_{c2} dans UCoGe et URhGe. Ces résultats soutiennent fortement l'origine magnétique de la supraconductivité dans ces systèmes. Pour $\mathbf{H}//\mathbf{b}$, nous montrons que certaines observations expérimentales convergentes suggèrent un possible changement d'état supraconducteur induit par le champ magnétique transversal dans UCoGe. Indépendamment du reste de l'étude, le dernier chapitre présente quelques résultats expérimentaux sur la phase normale de UCoGe et sur l'autre système de fermions lourds UBe_{13}.

Mots clés: Supraconductivité non conventionnelle, magnétisme, mécanisme d'appariement, fermions lourds, UCoGe, UBe_{13}.